Boiling on a Tube Bundle: Heat Transfer, Pressure Drop and Flow Patterns

PAR

Eugene VAN ROOYEN

ÉCOLE POLYTECHNIQUE
FÉDÉRALE DE LAUSANNE

Suisse
2011

"Men are nearly always willing to believe what they wish."

Julius Caesar

Acknowledgements

Abstract

The complexity of two-phase flow boiling on a tube bundle presents many challenges to the understanding of the physical phenomena taking place. It is important to quantify these numerous heat flow mechanisms in order to better describe the performance of tube bundles as a function of the operational conditions. In the present study, the bundle boiling facility at the Laboratory of Heat and Mass Transfer (LTCM) was modified to obtain high-speed videos to characterise the two-phase regimes and some bubble dynamics of the boiling process. It was then used to measure heat transfer on single tubes and in bundle boiling conditions. Pressure drop measurements were also made during adiabatic and diabatic bundle conditions.

New enhanced boiling tubes from Wolverine Tube Inc. (Turbo-B5) and the Wieland-Werke AG (Gewa-B5) were investigated using R134a and R236fa as test fluids. The tests were carried out at saturation temperatures T_{sat} of 5^oC and 15^oC, mass flow rates from 4 to 35 kg/m^2s and heat fluxes from 15 to 70 kW/m^2, typical of actual operating conditions. The flow pattern investigation was conducted using visual observations from a borescope inserted in the middle of the bundle. Measurements of the light attenuation of a laser beam through the intertube two-phase flow and local pressure fluctuations with piezo-electric pressure transducers were also taken to further help in characterising the complex flow. Pressure drop measurements and data reduction procedures were revised and used to develop new, improved frictional pressure drop prediction methods for adiabatic and diabatic two-phase conditions.

The physical phenomena governing the enhanced tube evaporation process and their effects on the performance of tube bundles were investigated and insight gained. A new method based on a theoretical analysis of thin film evaporation was used to propose a new correlating parameter. A large new database of local heat transfer coefficients were obtained and then utilised to generate improved prediction methods for pool boiling and bundle boiling, including a method for predicting the onset of dryout.

Keywords: boiling mechanism, bundle boiling, flow pattern, heat transfer, pool boiling, pressure drop, two-phase flow, visualisation and Wilson Plot

Version abrégée

La complexité des écoulements diphasique en ébullition dans un faisceau de tubes présente de nombreux défis pour la compréhension des phénomènes physiques. Il est important de quantifier l'effet des flux de chaleur sur les nombreux mécanismes afin de mieux décrire les performances des tubes en fonction des conditions opératoires. Pour cette étude, l'installation "Bundle boiling" au Laboratoire de Transfert de Chaleur et de Masse (LTCM) a été utilisée pour mesurer le transfert de chaleur par ébullition sur des tubes simples et disposés en faisceau. Des mesures de pertes de charge ont également été réalisées pour des conditions adiabatiques et non adiabatiques.

Deux nouveaux tubes améliorés fabriqués par Wolverine Tube Inc. (Turbo-B5) et Wieland-Werke AG (Gewa-B5), ont été étudiés en ébullition avec les fluides R134a et R236fa. Les tests ont été effectuées à des conditions opératoire classiques: températures de saturation T_{sat}, débits et flux de chaleur allant respectivement de 5 à 15 ^{o}C, de 4 à 35 kg/m^2s et de 15 à 70 kW/m^2. Une étude visuelle des differents écoulements a été menée à l'aide d'un endoscope inséré dans l'arrangement de tubes. Des mesures de l'atténuation de la lumière d'un faisceau laser à travers l'écoulement diphasique et des mesures de fluctuation de la pression locale par capteur piézo-électrique ont aussi été faites afin d'aider à la caractérisation de l'écoulements.

Les phénomènes physiques qui régissent l'évaporation sur les tubes améliorés et leurs effets sur les performances du faisceau de tubes ont été étudiés. Une nouvelle méthode basée sur une analyse théorique de l'évaporation en couche mince a été utilisée pour proposer un nouveau paramètre de corrélation. Une nouvelle base de données de coefficients locaux de transfert de la chaleur a été obtenue et ensuite utilisée pour concevoir de meilleures méthodes de prédiction pour l'ébullition en vase et l'évaporation dans un faisceau de tubes, ainsi que pour prévoir la formation de zones sèches. Les mesures de perte de charge et la réduction des données ont été révisées et utilisées pour développer de nouvelles prédictions des pertes de charge en conditions adiabatiques et non adiabatiques.

Mots-clés: ébullition améliorée, ébullition en faisceau de tubes, ébullition en vase, écoulement diphasique, mécanisme de l'ébullition, méthode de Wilson, modèle d'écoulement, perte de charge et transfert de chaleur

Contents

List of Figures

List of Tables

Nomenclature

Roman Symbols

A Area, $[m^2]$ / Hamaker constant, $[Pa\,m^3]$

a Minor restriction width, $[m]$ / Prediction method dummy variable

b Prediction method dummy variable / y-intercept

B_i Bias of ith measurement

Bo Bond number, $\frac{g(\rho_l - \rho_v)D^2}{\sigma}$, $[-]$

C Sensible heat flux constant / Pool boiling constant / Constant in two-phase multiplier correlations

c Prediction method dummy variable / Constant

Cap Capillary number, $\frac{\mu_l u_v}{\sigma}$, $[-]$

$C_{i/o}$ Wilson plot coefficient, $[-]$

Co Convection number, $(\frac{1}{x-1})^{0.8}(\frac{\rho_v}{\rho_l})^{0.5}$, $[-]$

C_o Drift flux model distribution parameter, $[-]$

c_p Isobaric specific heat, $[\frac{J}{kg \cdot K}]$

C_{sf} Rohsenow (1952) pool boiling constant

C_{tg} Bubble growth constant in Chien and Webb (1998b)

D Diameter, $[m]$

d Prediction method dummy variable / Stephan and Abdelsalam (1980) break-off-diameter

NOMENCLATURE

e Prediction method dummy variable

Eu Euler number, $\frac{\Delta p}{\rho u^2}$, $[-]$

F Two-phase convection multiplier, $[-]$

f Frequency, $[Hz]$ / Friction factor, $[-]$ / Minimisation function

f   focal length, $[mm]$

Fr Froude number, $\frac{G}{\rho_l \sqrt{gD}}$, $[-]$

G Mass flux, $[\frac{kg}{m^2 s}]$

g Gravitational acceleration, $[\frac{m}{s^2}]$

G_{t-s} Tube specific factor in Christians (2010), $[-]$

h Specific enthalpy, $[\frac{J}{kg}]$ / height $[m]$

h   Heat transfer coefficient, $[\frac{W}{m^2 K}]$

I_R Interface resistance to mass transfer, $[-]$

J Interface evaporative mass flux, $[\frac{kg}{m^2 s}]$

j Phase superficial velocity, $[\frac{m}{s}]$

J_P Variable used in near-wall evaporation, $[\frac{s}{m}]$

J_T Variable used in near-wall evaporation, $[\frac{kg}{m^2 s K}]$

K Curvature, $[\frac{1}{m}]$

k Thermal conductivity, $[\frac{W}{mK}]$ / Geometry constant, $[-]$

K_{BB} Bundle boiling multiplier, $\frac{h_{BB}}{h_{pb}}$, $[-]$

K_{ff} Falling film multiplier, $\frac{h_{ff}}{h_{pb}}$, $[-]$

L Length, $[m]$

l_H Length used for near-wall evaporation, $[m]$

M Molecular weight, $[\frac{kg}{kmol}]$

m Slope of a straight line / Error example variable

$\dot{m}$ Mass flow-rate, $\left[\frac{kg}{s}\right]$

N Number / Number of minor restrictions

n Sample size

N_a Number of active nucleation sites

N_R Number of tube rows

N_{tubes} Number of tubes in a single row

Nu Local Nusselt number, $\frac{hD}{k_l}$, $[-]$

P Tube pitch, [m] / Power, $[W]$

p Pressure, $[Pa]$

Pr Prandtl number, $\frac{\mu c_p}{k}$, $[-]$

p_r Reduced pressure, $\frac{p}{p_{cr}}$, $[-]$

P_i Precision of ith measurement

Q Heat, $[W]$

q Heat flux, $\left[\frac{W}{m^2}\right]$

R Uncertainty variable / Thermal resistance, $\left[\frac{m^2 K}{W}\right]$

r Radius, $[m]$

Re Reynolds number, $\frac{\rho u D}{\mu}$ or $\frac{GD}{\mu}$ or $\frac{4\Gamma}{\mu}$, $[-]$

Ri Richardson number, $\frac{(\rho_l - \rho_v)^2 ga}{G^2}$, $[-]$

R_a Roughness parameter, μm

r_w Wall resistance, $\frac{ln\frac{D_{or}}{D_i}}{2\pi l k_w}$, $\left[\frac{K}{W}\right]$

S Samples

S Velocity slip ratio, $[-]$ / Curvilinear coordinate along tube / Coriolis meter constant / Boiling suppression factor

T Temperature, $[K]$

t Time, $[s]$

TSF Tube specific factor, $[-]$

U Overall heat transfer coefficient, $[\frac{W}{m^2 K}]$ / Drift velocity, $[\frac{m}{s}]$

u Velocity, $[\frac{m}{s}]$

U_{gs} Dimensionless superficial velocity, $[-]$

V Volume, $[m^3]$

W_{bundle} Width of bundle, $[m]$

We Weber number, $\frac{\rho_l u_l^2 D_o}{\sigma}$, $[-]$

W_i York *et al.* (2004) method weighting function, $[-]$

x Vapour quality, [-] / Coordinate along tube axis, $[m]$

X_i Uncertainty variable / Wilson plot x-axis variable, $[m^2 K W^{n-1}]$

X_{tt} Lockhart-Martinelli parameter, $(\frac{1-x}{x})^{0.9}(\frac{\rho_g}{\rho_l})^{0.5}(\frac{\mu_l}{\mu_g})^{0.1}$, $[-]$

y Horizontal coordinate normal to tube axis, $[m]$

Y_i Wilson plot y-axis variable, $[m^2 K W^{n-1}]$

z Vertical coordinate normal to tube axis, $[m]$

Greek Symbols

α Thermal diffusivity, $\frac{k}{\rho c_p}$, $[\frac{m^2}{s}]$

δ Uncertainty / Film thickness, $[m]$

Δ Difference

Γ Refrigerant film flow rate on one side of tube, $[\frac{kg}{ms}]$

λ Consolini (2008) friction factor multiplier / Wavelength, $[nm]$

Λ Consolini (2008) multiplier

μ Dynamic viscosity, $[Pa\,s]$

ω Weighting function

Φ Two-phase multiplier, $[-]$

ϕ Angle, $[rad]$ / Near-wall film conduction variable, $[\frac{kg}{m^2 sK}]$

π Dimensionless group

$\Re$ Specific gas constant, $[\frac{J}{kgK}]$

ρ Density, $[\frac{kg}{m^3}]$

σ Surface tension, $[\frac{Ns}{m}]$ / Standard deviation

τ Mean wall shear stress, $[Pa]$

υ Kinematic viscosity, $[\frac{m^2}{s}]$ / Evaporation coefficient, $[-]$

ε Void fraction, $[-]$ / Prediction error

υ_i Vapour bubble velocity $[\frac{m}{s}]$

ξ Gaddis and Gnielinski (1985) correlation terms

Superscripts

a Wilson plot Reynolds number exponent

m Exponent

n Cooper (1984) pool boiling exponent

p Wilson plot Reynolds number exponent

Subscripts

a Absorbed

0 Initial condition

1 Final condition

2ϕ Two-phase

NOMENCLATURE

adiab   Adiabatic

ann   Annulus-side

avg   Average

b   Bubble / Boiling

BB   Bundle boiling

bottom   Bottom

buld   Bulk

c   Convective

calc   Calculated

cb   Convective boiling

con   Contracting

cr   Critical

Cu   Copper

d   Departure / Diagonal direction

δ Related to film thickness

diab   Diabatic

diret   Direct heat transfer measurement

dry   Onset of dryout

e   Evaporative

ε Void fraction related

exp   Experimental / Expanding

f   Frictional / End of near-wall region / Fluid

ff   Falling film

g Gas phase

gap Minor restriction

$GB5$ Wieland Gewa-B5

gni Gnielinski

gu Vapour phase relative component

H Homogenous

h Hydraulic

hex Hexagonal

i Inside / Inner / Interval number / Interface

in Inlet

int Interface

l Liquid phase / Laminar

lv Liquid-vapour

lu Liquid phase relative component

m Mean / Momentum / Meniscus

$meas$ Measured

min Minimum

NcB NcB

o Outside / Outer

oa Overall

$one\,side$ Flow on only one side of the tube

$onset$ Onset of dryout

out Outlet

p Pressure related / Pore

pb Pool boiling

pre Pre-heater

$pred$ Predicted

r Reduced / Root

ref Refrigerant / Reference

sat Saturated

ss Stainless steel

s Static / Shell-side

$super$ Wall superheat

$TB5$ Wolverine Turbo-B5

$test$ Test section

tf Thin film

tot Total

$trans$ Transition

$tube$ Flow per tube

t Tunnel / Total

v Vapour phase

w Wall

$water$ Water

WP Wilson plot

z Vertical direction

Acronyms

A Annular flow

B Bubbly flow

BB Bundle boiling

C Churn flow

CFC Chlorofluorocarbon

CHF Critical heat flux

$CMOS$ Silicone technology

Ct Churn-turbulent flow

D Dispersed flow

DC Direct current

F Froth flow

FF Falling film

fps Frames per second

FS Full scale

GOF Goodness of fit, R^2

GWP Global Warming Potential

$HCFC$ Hydrochlorofluorocarbons

I Intermittent flow

$LTCM$ Heat transfer laboratory at EPFL

M Mist flow

ODP Ozone Depletion Potential

ODS Ozone Depleting Substance

PDF Probability density function

NOMENCLATURE

PSD Power spectral density

RMS Root mean square

RTD   Resistance temperature detector

S Slug flow

TC Themocouple

Chapter 1

Introduction

1.1 Background

Energy is one of the most valuable resources on the planet earth. Research on how to improve the use of energy and energy conversion has become important in diverse fields of application. In the future, the wise use of energy resources will be crucial for a sustainable existence and thus research in the field of energy intensive systems is invaluable.

Boiling heat transfer enhancement is one of the major issues in modern thermal technologies. Heat transfer enhancement is applied in, amongst other industries, refrigeration, chemical engineering, air conditioning and heat pipes (Thome, 1990). The economic aspects of heat transfer enhancement are not only related to the size and mass of heat exchangers but also their operating costs. By optimising thermal performance with respect to the driving energy, primarily to overcome the pressure drops, heat transfer strategies become more economical to operate. Currently, research effort is therefore aimed at developing new enhancement geometries, obtaining valuable test data with the refrigerants and process fluids of interest and development of new local thermal-fluid design methods.

In a wider context, new refrigerants have been introduced as a result of directives imposed by environmental concerns to minimise the damaging effects of refrigerants on the ozone layer or to limit the greenhouse effect. The protection of the stratospheric ozone layer began in 1985 with the negotiation of the Vienna Convention. The details of this convention are contained in the Montreal Protocol (UNEP, 2000), which became effective in 1989 and made provision for the regular review of control measures based on information from the scientific, environmental, technical and economic sectors. The tropospheric abundances of most ozone-depleting substances (ODS), as well as stratospheric chlorine, are currently stable or decreasing due to actions taken

1. INTRODUCTION

under the Montreal Protocol (Figure 1.1). Due to the time it takes for surface emissions to reach the stratosphere there is a time lag in the decrease of stratospheric concentrations (GAW, 2006). Based on these facts, it was stated that "The Montreal Protocol is working, and the ozone-layer depletion from the Protocol's controlled substances is expected to begin to ameliorate within the next decade or so."

Figure 1. Ozone-Depleting Substances, the Ozone Layer, and UV Radiation: Past, Present, and Future.

(a) Production of ozone-depleting substances (ODSs) before and after the 1987 Montreal Protocol and its Amendments, from baseline scenario A1. Chlorofluorocarbons (CFCs) are shown in black; additional ODSs from hydrochlorofluorocarbons (HCFCs) are in gray. Note: HCFCs, which have been used as CFC replacements under the Protocol, lead to less ozone destruction than CFCs.

(b) Combined effective abundances of ozone-depleting chlorine and bromine in the stratosphere. The range reflects uncertainties due to the lag time between emission at the surface and the stratosphere, as well as different hypothetical ODS emission scenarios.

(c) Total global ozone change (outside of the polar regions; 60°S-60°N). Seasonal, quasi-biennial oscillation (QBO), volcanic, and solar effects have been removed. The black line shows measurements. The gray region broadly represents the evolution of ozone predicted by models that encompass the range of future potential climate conditions. Pre-1980 values, to the left of the vertical dashed line, are often used as a benchmark for ozone and UV recovery.

(d) Estimated change in UV erythemal ("sunburning") irradiance for high sun. The gray area shows the calculated response to the ozone changes shown in (c). The hatched area shows rough estimates of what might occur due to climate-related changes in clouds and atmospheric fine particles (aerosols).

Figure 1.1: Results presented on the state of ozone-depleting substances in the atmosphere with predictions of future levels (GAW, 2006)

The Kyoto Protocol is another international treaty, which calls for the reduction of greenhouse gasses that result in global warming. In 2001 the United States of America, responsible for a quarter of the global CO_2 emissions, announced that it would abandon the Kyoto Protocol. Nevertheless, the treaty came into effect in 2005 after ratification by more than 125 nations and as of July 2010, 191 states have signed and ratified the protocol. The protocol sets binding targets for industrialized countries and the European community for reducing greenhouse gas emissions. However, most of the signature nations have not moved fast enough to fulfill their lofty pledges. Significant advances in energy hungry industries, such as refrigeration, are needed to achieve such goals.

1.2   Justification for the study

The complexity of fluid flows over the shell side of tube bundles and the development of new refrigerating fluids and fluid-tube enhancement combinations require further in-depth research by the scientific community. The experimental approach remains the main tool of investigation in the multi-phase field to characterise the complex interactions taking place and thereby improving the design process and system efficiencies.

Due to the phasing out of these ODS refrigerants and the introduction of new enhanced boiling tubes, a whole new set of experiments are required to develop a new thermal database and to investigate heat transfer enhancing mechanisms. The challenge is to develop unified and accurate heat transfer models which will hopefully be of general application, even for new fluids. A method of determining the flow pattern and additional information on two-phase flows and transition boundaries are necessary for improving such models.

The test facility at the Heat and Mass Transfer Laboratory (LTCM), is well equipped and allows for numerous local boiling data to be obtained. In a previous study on bundle boiling in the LTCM laboratory, Robinson and Thome (2003) proposed a local boiling heat transfer model based on void fraction from their data. They were not able to obtain local flow pattern data and therefore were not able to relate their model to observed physical phenomena. The study that followed by Agostini in 2008, also in the LTCM laboratory, focused on implementation of several flow pattern identification methods at locations inside the bundle for plain tube surfaces.

1.3   Objectives of study

The questions emerging from the work of Agostini (2008), pertaining to the flow patterns inside the bundle and the instrumentation setup that he pioneered, were further investigated and developed here. The current study evaluated the latest generation of enhanced micro-structure boiling tubes provided by two leading global manufacturers. In this study a novel experimental approach was followed to validate new measurement methods and then to apply them to these enhanced boiling tubes.

The objectives of this study were:

- To investigate boiling on two enhanced tubes (*Wolverine Turbo-B5* and *Wieland Gewa-B5)* with two different refrigerants (R134a and R236fa).

- To improve the visualisation of the flow in order to provide quantitative data to better characterise the two-phase phenomena.

- Measurement of two-phase pressure drops over the enhanced tubes with each refrigerant. The adiabatic data would serve as a starting point for the prediction methods for the diabatic pressure drop.

- Measurement of local heat transfer coefficients for both tubes and refrigerants. Combined with a good visualisation technique and the existing database for plain tubes the new enhanced tube data will lead to an important and informative database that can be used to further improve the understanding of mechanisms active inside tube bundles during evaporation.

- Theoretical analysis of the thin film evaporation process to further our understanding of the contribution of this process to the enhancement of heat transfer.

- The development of new heat transfer and pressure drop methods based on the database and observations made of the two-phase flow structure and the results of the theoretical analysis.

- Identification and prediction of the onset of dryout in the tube bundle, with its substantial fall in heat transfer.

1.4   Structure of this thesis

The thesis is comprised of nine chapters. Chapter 2 is an update of available scientific literature relevant to this study. This chapter includes reviews of studies done in the past that highlight important thermal aspects and thereby clarify the rationale and direction of this study. In Chapter 3 the experimental apparatus and methods are presented in detail. Thereafter, a discussion of results commences with flow pattern and flow structure related results in Chapter 4, followed by pressure drop and heat transfer results in Chapters 5 and 6, respectively. Chapter 7 discusses the theoretical analysis of evaporation of a thin film and defines a new correlating relationship for boiling heat transfer. The new prediction methods are presented in Chapter 8 before concluding remarks in Chapter 9.

Chapter 2

Literature study

2.1 Introduction

The basic understanding of heat transfer and pressure drop with the aim to develop prediction methods related to physical effects, begins with a thorough investigation of the hydrodynamics of the phases involved and their interaction with the fixed structure of the tube bundle.

There is a general lack of understanding of the two-phase flow patterns for flows over tube bundles and how they affect heat transfer in tube bundles. Various measurement methods have been implemented in the past to help clarify the complex flow patterns. This chapter provides a brief review of some previous investigations and then develops a set of visualisation and measurement tools to use in a tube bundle to quantify the flow patterns, and then investigate their relationship to void fraction, pressure drop and heat transfer.

The remainder of this chapter is dedicated to presenting the milestones in bundle boiling investigation over the past years. A review of boiling mechanisms commonly associated with enhanced tubes is given to provide the fundamentals for the new prediction methods developed later in the study.

2.2 Flow patterns and transitions for two-phase flow in bundles

2.2.1 Flow pattern maps in bundles

Early studies relied purely on visual observations of flow patterns (mostly air and water as test fluids) and more recently advanced instrumentation has been included. A pioneering study on the different flow patterns observed in tube bundles was done by Diehl (1957). The National

2. LITERATURE STUDY

Engineering Laboratory (NEL) performed an extensive study on heat exchangers (NEL report, 1975) with Sutherland and Murray (1969) studying pressure drop and heat transfer. They presented a series of flow images but no classification of the flow patterns. Grant and Murray (1972) reported bubbly, slug and spray flow in another test section for up and downward flows. The air-water investigations conducted at NEL were summarised by Grant and Chisholm (1979).

Using air-water in an upward flow bundle, Kondo and Nakajima (1980) and Kondo (1984) identified bubbly, froth and slug flows. They did not define a new flow map but confirmed the work by Grant and Chisholm (1979). After studying flow pattern and tube vibration, Pettigrew *et al.* (1989a,b,c) proposed a new flow map with the Martinelli parameter and gas phase dimensionless velocity as the control parameters. They also compared their visual observations with the NEL report (1975). As stated by Ulbrich and Mewes (1994), the three flow pattern maps proposed by Grant and Murray (1972), Grant and Chisholm (1979) and Pettigrew *et al.* (1989a,b,c) are practically identical and differ only in the coordinate system used. Lian *et al.* (1992) studied tube bundle vibrations and observed bubbly, churn turbulent and dispersed droplet flow regimes.

Visual observation and statistical methods were used by Ulbrich and Mewes (1994) who proposed a classification into bubbly, intermittent and dispersed flows on a flow pattern map with liquid and vapour superficial velocities as the coordinate axes (Figure 2.1a). Visual observation of vertical (upward, downward) and horizontal flow in a tube bundle was carried out by Xu *et al.* (1998b,a) who identified bubbly, turbulent, churn and intermittent flows.

Noghrehkar *et al.* (1999) pointed out that the use of only visual observations as a flow regime indicator could lead to false conclusions. They used the probability density function (PDF) of local void fraction fluctuations as a flow regime indicator (Figure 2.1b). Applying the PDF method, they identified flow patterns near the shell wall that differed from those in the bundle core. For the staggered arrangement that they investigated, the bubbly-intermittent transition occurred at higher gas flow rates compared to inline tubes.

Burnside *et al.* (2005) and Iwaki *et al.* (2005) found that flow regime identification was oriented towards a characterisation of the velocity fields inside the bundle using particle image velocimetry. They tested a very short bundle butted up against a plexiglass end plate in order to view the flows.

Aprin *et al.* (2007) ran a series of void fraction measurement experiments in a tube bundle with the following evaporating test fluids: n-pentane, iso-butane and propane. They found the diabatic transitions much lower when compared to the adiabatic results of Noghrehkar *et al.* (1999) and the intermittent regime much narrower. Similar to previous flow pattern maps the transitions
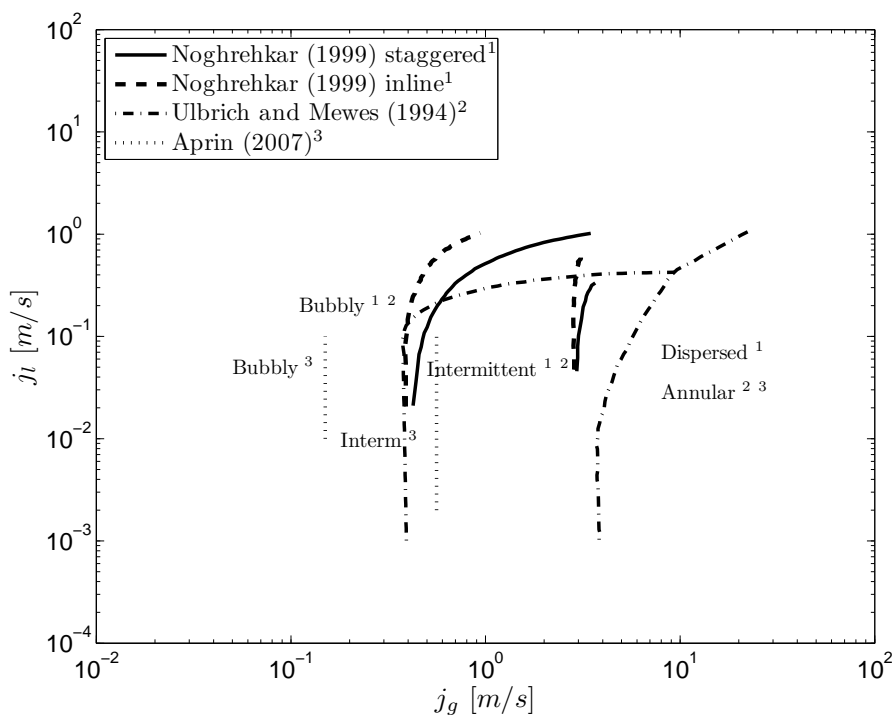
(a)
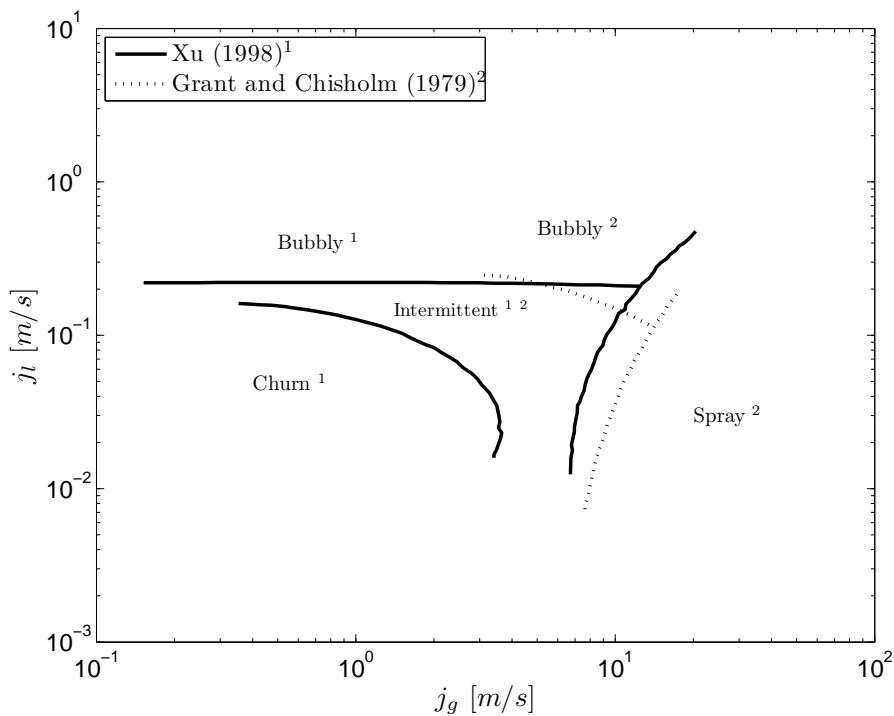
(b)

Figure 2.1: Shell side flow pattern map by (a) Noghrehkar *et al.* (1999), Ulbrich and Mewes (1994) and Aprin (2003) using additional flow pattern indicators and (b) by Xu *et al.* (1998b) and Grant and Chisholm (1979) from visual observations

were found not to be a function of liquid superficial velocity for the lower liquid flow rates tested. Their study showed that the physical properties of the fluid, such as the liquid and vapour density, play a major role together with mass flux and heat flux. The analysis of flow pattern and bubble diameter provided a possible measure to classify flow patterns. They found that the mean bubble diameter was smaller than the minimum space between the tubes for void fractions lower than 0.35. When the bubbles reached a size corresponding to the minimum space between the tubes, the flow became chaotic. Alternative passages of small and large vapour structures occurred that corresponded to the two peaks of the intermittent regime in a probability density function of void fraction. As the void fraction increased further the bubbles grew bigger and closer to each other. The interfaces between the vapour slugs were broken and a continuous vapour phase, in which liquid droplets could be involved, was generated. For this annular-dispersed flow, which appeared for void fractions higher than 0.56, an average size of bubble ranging from 2.5 to 7 times the tube clearance was observed. The effects of the obstacles and the tortuosity induce flow transitions at lower void fractions. Due to the agitation and the dynamic effects of the two-phase flow in a tube bundle, the width of the transition zone between the bubbly and the annular-dispersed flow increased.

(a)   (b)
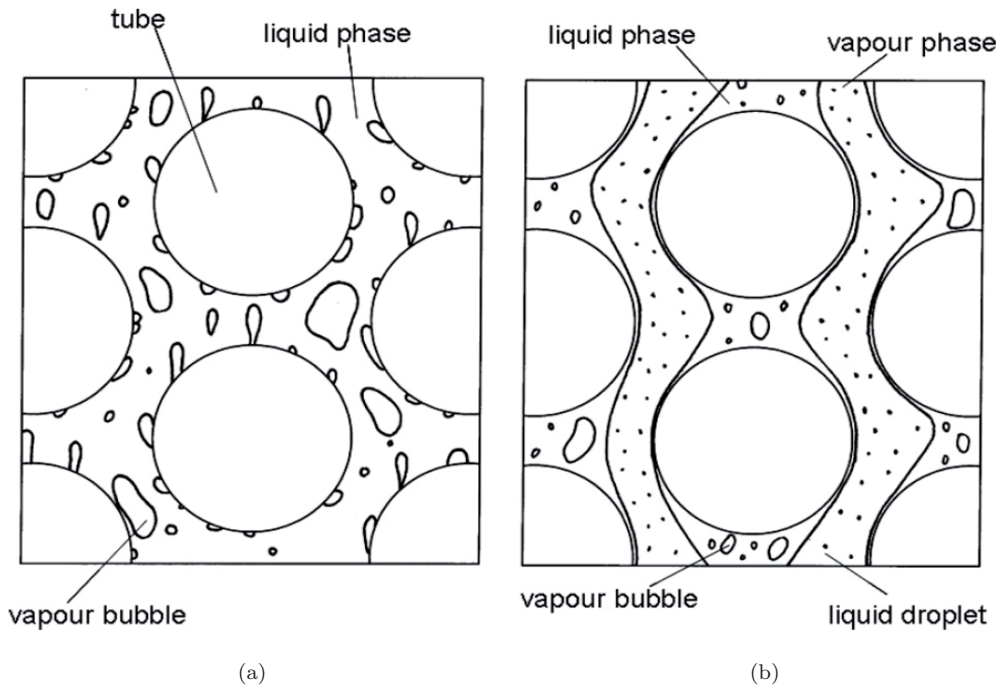
Figure 2.2: Flow patterns in bundles as defined in the study of Aprin *et al.* (2007) for (a) bubbly and (b) annular regimes

Bubbly flow can be characterised by a vapour phase distributed as discrete bubbles in the continuous liquid phase (Figure 2.2a). The bubbles are initiated from nucleation sites on the tube walls in diabatic evaporation tests. Kondo and Nakajima (1980) and Ulbrich and Mewes (1994) noted that bubbles are uniform in size with a characteristic diameter lower than the intertube space. Aprin *et al.* (2007) defined annular-dispersed flow as a continuous gas phase in which the liquid droplets are carried (Figure 2.2b). The vapour phase congregates into channels between the tubes of the bundle and occupies a larger fraction of the flow area. The liquid phase stays in the recirculation zone between the tubes, and displays an irregular movement with surface waves around the tube walls. Intermittent flow is characterised by a combination of bubbly and annular-dispersed flows.

Huang *et al.* (2008) used wavelet analysis on a 20 mm staggered tube bundle in cross-flow for diabatic tests with R134a, and defined six energy levels based on their measurements. Differential pressure measurements were analysed over five tube rows (135 mm). The distribution of the energy levels differed for each flow regime and this was used to classify each flow regime. However, they failed to provide a generically applicable classification of the flow regimes that was independent of their measurement technique. The decomposition of signals into different frequency bands and energy levels can potentially be applied to local measurements to track the flow regime developments through the bundle at different positions.

Two recent papers review flow patterns in tube bundles, one by Khushnood *et al.* (2004) who focused on vibrations in tube bundles and the other by Ribatski and Thome (2007) who compared flow maps derived by subjective and objective methods. The focus of Ribatski and Thome (2007) was on void fraction as one of the most important parameters inside tube bundles. Their analysis unveils important discrepancies between the different methods, in particular when visual observations are not backed up by more objective measurements of flow pattern.

2.2.2 Flow pattern measurement techniques

Flow pattern recognition is achieved by the analysis of various experimental parameters. Some of the methods mentioned here have been applied to in-tube flow, yet a similar response is expected from different flow patterns in tube bundles.

Reviews on flow measurement techniques have been provided by Rajković *et al.* (1996), Noghrehkar *et al.* (1999) and Bertola (2003). The detailed study of Jones Jr. and Zuber (1975) on chordal void fraction, measured with X-rays, and statistical analysis for two-phase flow including PDF and power spectral density (PSD), lead to the classification of three major flow patterns

and an objective method of flow pattern identification. Their experiments were carried out in an air-water facility under adiabatic conditions. They pointed out that considerable fundamental information regarding the structure of two-phase flow may be obtained from the statistical behaviour of the void fraction. A series of papers by Akagawa *et al.* (1971a,b,c) preempted this hypothesis. The use of PDF analysis allowed a clear distinction between bubbly and annular flows with high count peaks at low and high void fractions respectively (Figure 2.3a and b). Slug-like, or intermittent flows appeared as a combination of the two distributions with twin peaks, one at a low void fraction and one at a high void fraction (Figure 2.3c). The Vince and Lahey Jr. (1982) study was a detailed extension of the Jones Jr. and Zuber (1975) approach using statistical moments, whereas the Lowe and Rezkallah (1999) study used a capacitance sensor and found flow pattern information comparable to that of Jones Jr. and Zuber (1975). Furthermore, their analysis continued with the characterisation of transitions between flow regimes by PDF analysis and visual observation.
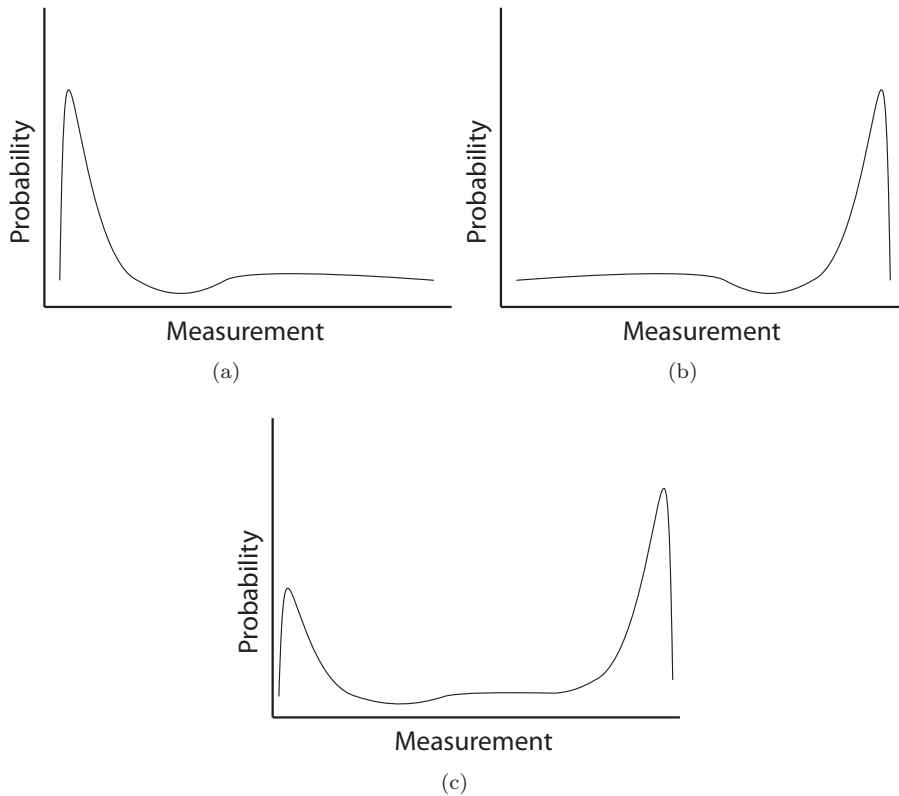
Figure 2.3: Indicative PDF results of typical distributions found for (a) bubbly, (b) annular and (c) slug-type flows

Jain and Roy (1983) developed a challenging experimental technique by combining piezo-electric pressure transducer measurements with a linearized dual-beam X-ray system for void fraction measurements. The fluid was a single component boiling flow and not an air-water mix. Importantly, the authors developed two redundant objective experimental techniques for two-phase flow identification and carried out a detailed analysis of the obtained data.

Lin and Hanratty (1987) described how a pair of pressure transducers could be used to detect the presence of slugs. They proposed that the differential pressure drop was more suited for detecting flow patterns that are steady than those that are intermittent. Therefore, two local strain gauge pressure transducers were used. They also employed cross-correlation analysis to determine the propagation of the pressure wave.

The present study in this thesis is built on the findings from these investigations. Unsteady intermittent flow behaviour was expected and therefore local piezo-electric pressure transducers were installed at different locations in the bundle to track the flow development. Furthermore, it was expected that the flow would either have a weak relation between these locations or it would be chaotic (no relation). The present study attempted to utilize two independent flow pattern detection methods by using the laser light attenuation technique in conjunction with the piezo-electric transducers.

2.3 Void fraction in tube bundles

Void fractions in two-phase flows over tube bundles are far more difficult to measure than those for internal channel flows and thus much less is known about this flow geometry. Mass velocities of industrial interest also tend to be much lower than for internal flows. As a consequence, for vertical two-phase flows across tube bundles the frictional pressure drop tends to be small compared to the static head of the two-phase fluid. The void fraction thus becomes the most important parameter for evaluating the two-phase pressure drop since it is directly related to the local two-phase density of the shell-side flow. In particular, for thermosyphon evaporators, the circulation rate depends directly on the two-phase pressure drop across the tube bundle and hence the difference in void fraction is of primary importance. Furthermore, in flooded type evaporators with close temperature approaches, such as in refrigeration and heat pump applications, the effect of the two-phase pressure drop on the local saturation temperature may be crucial in evaluating the temperature difference for incremental thermal design methods (*i.e.* step-wise calculation of thermal performance).

A distinction was made between the studies that used void fraction for flow pattern iden-
tification (discussed in Section 2.2.2) and those that measured void fraction for the purpose of
developing predictive methods. Although both are often linked, this section only refers to the
prediction methods (Table 2.1).

As pointed out by Ribatski and Thome (2007), several authors recorded void fraction values
significantly different from those predicted by the homogeneous flow model. In the case of ho-
mogeneous flow, the velocity ratio is equal to unity and the void fraction is easily predicted. For
tube bundle flow, and especially at low liquid velocities, the slip ratio can be much higher because
the vapour phase buoyancy dominates.

2.3.1 Void fraction prediction methods

The method of Ishihara *et al.* (1980) (equation 2.1) is based on the two-phase frictional multiplier
of the liquid (right hand side of equation 2.1) which is defined as a function of the Martinelli
parameter (equation 2.4). Cornwell *et al.* (1980) also proposed a void fraction method based on
the Martinelli parameter (equation 2.2), whereas Fair and Klip (1982) proposed a method based
on a different two-phase friction multiplier (equation 2.3):

$$\frac{1}{1-\varepsilon} = 1 + \frac{8}{X_{tt}} + \frac{1}{X_{tt}^2} \tag{2.1}$$

$$\frac{1}{1-\varepsilon} = 1 + \left(\frac{6}{X_{tt}}\right)^{0.71} \tag{2.2}$$

$$\frac{1}{(1-\varepsilon)^2} = 1 + \frac{20}{X_{tt}} + \frac{1}{X_{tt}^2} \tag{2.3}$$

All equations are based on the following Martinelli parameter:

$$X_{tt} = \left(\frac{1-x}{x}\right)^{0.9} \left(\frac{\rho_v}{\rho_l}\right)^{0.5} \left(\frac{\mu_l}{\mu_v}\right)^{0.1} \tag{2.4}$$

The prediction method of Schrage *et al.* (1988) used a function of liquid Froude number as a
multiplier in the homogeneous model. This model of Schrage *et al.* (1988) was one of the earliest
models that included the important effect of mass flux directly:

$$\frac{\varepsilon}{\varepsilon_H} = 1 + 0.123 \left(\frac{ln\,x}{Fr_l^{0.191}}\right) \tag{2.5}$$

$$\text{with} \quad Fr_l = \frac{G}{\rho_l(gD)^{0.5}}$$

Dowlati *et al.* (1996) proposed a void fraction model based on data from R113 flow at mass velocities higher than 50 kg/m^{2}s. The method is based on dimensionless gas phase superficial velocity and two constants ($C_1 = 30$ and $C_2 = 50$):

$$\varepsilon = 1 - \frac{1}{(1 + C_1 j_g^* + C_2 j_g^*)^{0.5}} \tag{2.6}$$

$$\text{with} \quad j_g^* = \frac{\rho_g^{0.5} j_g}{\sqrt{gD(\rho_l - \rho_g)}}$$

The Feenstra *et al.* (2000) method is based on dimensionless parameters that were identified and used to fit to their database. The detailed equations for this method are given in the data reduction in Section 3.7.1. Ribatski and Thome (2007) reviewed the models proposed in the literature and found that the Feenstra *et al.* (2000) model is the most suitable void fraction prediction method for tube bundles.

2.4 Frictional pressure drop in tube bundles

2.4.1 Friction factor

The Darcy friction factor as used for tube-side flow is:

$$f = \frac{\Delta p_f}{\frac{density\,velocity^2}{2}} \frac{Diameter}{Length} \tag{2.7}$$

For tube bundles the friction factor most commonly used is:

$$f = \frac{\Delta p_f}{4G^2} \frac{2\rho}{N_R} \tag{2.8}$$

In this equation the velocity component is substituted by mass flux (G) and the dimensionless length ratio is accommodated by the number of tubes (N_R), roughly equal to height over tube diameter.

2.4.2 Single phase pressure drop prediction methods

The pressure drop for single phase flow over tube bundles was formulated by Žukauskas and Ulinskas (1983) to be:

$$\Delta p_f \quad = \quad EuN_R\frac{G^2}{2\rho} \tag{2.9}$$

for $3 < Re \leq 10^3$

$$\frac{Eu}{k_1} \quad = \quad 0.795 + \frac{0.247\,10^3}{Re} + \frac{0.335\,10^3}{Re^2} - \frac{0.155\,10^4}{Re^3} + \frac{0.241\,10^4}{Re^4}$$

for $10^3 < Re < 2.10^6$

$$\frac{Eu}{k_1} \quad = \quad 0.245 + \frac{0.339\,10^4}{Re} - \frac{0.984\,10^7}{Re^2} + \frac{0.132\,10^{11}}{Re^3} - \frac{0.599\,10^{13}}{Re^4}$$

where the geometric factor k_1 is a function of the aspect ratio $\left(\frac{a}{b}\right)$. For a triangular equilateral array, $\left(\frac{a}{b}\right) = \left(\frac{2}{\sqrt{3}}\right)$ and $k_1 \approx 1$, the influence of this parameter can be neglected.

Gaddis and Gnielinski (1985) approached the problem by considering a superposition of laminar and turbulent components in the ξ term (equation 2.10). N is assumed to be the number of minor restrictions encountered by the fluid and is equal to N_R in the present study's geometry:

$$\Delta p_f \quad = \quad \xi_i N\frac{G^2}{2\rho} \tag{2.10}$$

$$\text{with} \quad \xi_i \quad = \quad \underbrace{\xi_{i,l} f_{zn,l}}_{l} + \underbrace{(\xi_{i,t} f_{z,t} + f_{n,t})[1 - e^{\left(-\frac{Re+200}{1000}\right)}]}_{t}$$
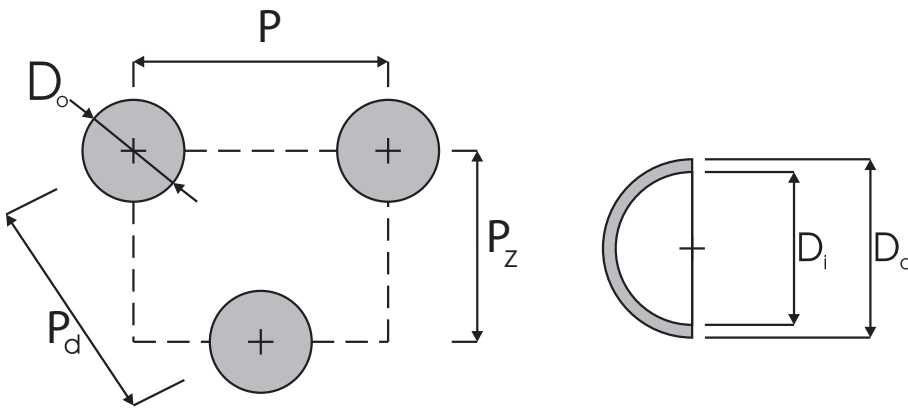
Figure 2.4: Tube bundle geometry for a unit cell

The correlations for the ξ terms were developed for generic tube bundle geometries. Since different tube bundles are geometrically and fluid-dynamically dissimilar, the arrangement factors

(f) are dependent on the geometry of the tube bundle. The relative transverse (a) and longitudinal (b) spacings are used as classifiers. The parameters P, P_z, P_d are the transverse, longitudinal and diagonal spacings divided by the tube diameter in order to obtain the non-dimensional parameters a, b and c (Figure 2.4):

$$a = \frac{P}{D_o} \qquad b = \frac{P_z}{D_o} \qquad c = \frac{P_d}{D_o}$$

The equivalent hydraulic diameter of the tube bundle can be computed as follows for a unit cell with the above geometry (outlined by the dashed line or an equilateral triangle):

$$D_h = \frac{4\, \dot{\text{Flow Area}}}{\text{Heated Perimeter}} = \left(\frac{4ab}{\pi} - 1 \right) D_o \tag{2.11}$$

The following distinctions were made:

$$b \geq \frac{1}{2}\sqrt{2a+1} \qquad \text{Staggered with narrowest cross section perpendicular to the flow direction}$$

$$b < \frac{1}{2}\sqrt{2a+1} \qquad \text{Staggered with narrowest cross section along the diagonal}$$

The pressure drop coefficient for the laminar term is expressed as:

$$\xi_{i,l} = \frac{f_{a,l}}{Re} \quad \text{where} \quad Re = \frac{GD_o}{\mu_{2\phi}} \tag{2.12}$$

The arrangement factor for the laminar term for a staggered tube layout with the narrowest cross section along the diagonal is:

$$f_{a,l} = \frac{280\pi[(b^{0.5} - 0.6)^2 + 0.75]}{(4ab - \pi)a^{1.6}}$$

For the turbulent component:

$$\xi_{i,t} = \frac{f_{a,t}}{Re^{0.25}} \tag{2.13}$$

and for a staggered arrangement with the narrowest cross section along the diagonal:

$$f_{a,t} = 2.5 + \frac{1.2}{(a - 0.85)^{1.08}} + 0.4 \left(\frac{b}{a} - 1 \right)^3 - 0.01 \left(\frac{a}{b} - 1 \right)^3$$

The coefficient $f_{zn,l}$ accounts for the effect of temperature dependency on the physical constant and the number of tube rows for the laminar component. The turbulent term, $f_{z,t}$ accounts for the temperature dependency. The parameter $f_{n,t}$ incorporates the effects of inlet and outlet pressure drops in turbulent flows when the number of tube rows is small. The number of rows seems to be relevant only in the case of non-isothermal flows when the factor will act for $N_R < 10$.

2.4.3 Two-phase pressure drop prediction methods

Ishihara *et al.* (1980) and Xu *et al.* (1998b) based their two-phase correlations on the Martinelli parameter to represent the two-phase friction multiplier. The two-phase multiplier accounts for the ratio between the two-phase pressure drop and the single phase liquid pressure drop:

$$\Phi_f = \frac{\Delta p_{2\phi}}{\Delta p_f} = 1 + \frac{C}{X_{tt}} + \frac{1}{X_{tt}^2} \tag{2.14}$$

For two-phase flow Ishihara *et al.* (1980) set the parameter C to a value of 8 (for the data reduction, the single phase pressure drop Δp_f was predicted by the method of Žukauskas and Ulinskas (1983)). Instead of using a constant value of C, Xu *et al.* (1998b) proposed an empirical equation for C based on the dimensionless superficial velocity and the vapour quality.

$$
\begin{aligned}
C &= 24.45 U_{gs}^{-0.654} \left(\frac{x}{1-x} \right)^{0.336} \\
U_{gs} &= \frac{Gx}{\sqrt{\rho_g g D_o (\rho_l - \rho_g)}}
\end{aligned}
\tag{2.15}
$$

The Consolini *et al.* (2008) method is based on the homogeneous pressure drop with a two-phase multiplier. The homogeneous friction factor for tube bundles ($f_f = Eu/4$) of Žukauskas and Ulinskas (1983) can be computed in terms of the Euler number with two-phase properties based on void fraction as follows:

$$\rho_{2\phi} = \rho_f(1-\varepsilon) + \rho_g \varepsilon \qquad \text{and} \quad \mu_{2\phi} = \mu_f(1-\varepsilon) + \mu_g \varepsilon \tag{2.16}$$

The friction factor (f) and Reynolds number (Re) were defined as:

$$f_{2\phi} = \frac{1}{4} \frac{\Delta p_{2\phi}}{G^2 N_R} 2\rho_{2\phi} \qquad \text{and} \qquad Re = \frac{G D_o}{\mu_{2\phi}} \tag{2.17}$$

Then the homogeneous friction factor is correlated to a two-phase friction factor $f_{2\phi}$, through a multiplier λ:

$$\lambda = \frac{f_{2\phi}}{f_H} \tag{2.18}$$

where:

$$\lambda = \Lambda + (1-\Lambda)(2x-1)^2 \qquad \text{with} \qquad \Lambda = \left(\frac{G}{G_{ref}} \right)^{-1.5} \tag{2.19}$$

and $G_{ref} = 400 \ kg/m^2 s$. At this point $f_{2\phi}$ is evaluated and the two-phase frictional pressure drop is calculated.

The Consolini *et al.* (2008) method is based on diabatic data for plain and enhanced tubes with large quality variations throughout the bundle. The prediction was not tube specific, indicating that there were only small differences in the friction factor for the two tube classes. No adiabatic data were correlated to compare against. The Consolini *et al.* (2008) method was adapted by Agostini (2008) through improvements in the λ multiplier (equation 2.20). This method is based on adiabatic data for plain tubes and improves the representation of the actual trends in friction factor:

$$
\begin{aligned}
\lambda = \frac{f_{2\phi}}{f_H} &= e\left[-\left(\frac{(x - C_2)}{0.3}\right)^2 + C_1\right] \\
\text{with:} \quad C_1 &= -25.015\Lambda + 24.193 \\
C_2 &= -1.168\Lambda + 1.4521 \\
\Lambda &= \left(\frac{G}{G_{ref}}\right)^{0.1}
\end{aligned}
\tag{2.20}
$$

The comparison with diabatic data did not provide satisfactory results since the mean vapour quality used in such evaluations does not represent the local conditions. A smaller discretisation of vapour quality by assuming smaller sections of Δz could improve such a comparison.

Table 2.1: Hydrodynamic studies in bundle boiling indicating the main research topic, such as flow patterns (FP), void fraction (VF) and pressure drop (PD) and other basic parameters of each study

Author	Topic	Flow pattern	Diameter	P/D	Bundle geometry	Fluid	Heat flux	G	Vapour quality
Diehl (1957)	FP	A M	19.05	1.25-1.33	Stag/Inline	AW and mixtures		<1110	0.006-0.99
Sutherland and Murray (1969)	FP	B I	19		-	AW		200-886	0.00035-0.091
Grant and Murray (1972)	FP	B I D	19	1.25	Stag	AW		58-1124	0.003-0.94
Grant and Murray (1974)	FP	B S	19	1.25	Stag	AW		17-1124	0.002-0.93
Grant and Chisholm (1979)	FP, VF	B I S	19	1.25	Stag	AW		20-1120	0.002-0.94
Cornwell et al. (1980)	VF	-	19.05	1.3	Inline	R113	Diab.	95	
Ishihara et al. (1980)	VF, PD	Collated dataset							
Kondo and Naka-jima (1980)	FP, VF	B F S	25	1.08-1.4	Stag	AW		3-60	0.005-0.9
Kondo (1984)	FP	B F S	25	1.08-1.4	Stag	AW		3-35	0.005-0.9
Schrage et al. (1988)	VF	-	7.9	1.3	Inline	AW		54-683	0-0.65
Pettigrew et al. (1989a)	FP	B I	19.05	1.32-1.47	Stag/Inline	AW		28-1200	0-1

Author	Topic	Flow pattern	Diameter	P/D	Bundle geometry	Fluid	Heat flux	G	Vapour quality
Dowlati et al. (1990)	VF	-	12.7 and 19.05	1.3-1.75	Stag/Inline	AW		27-818	0-0.3
Hahne et al. (1990)	FP	B S	-	-	Stag/inline	R11		-	-
Lian et al. (1992)	FP	B Ct D-droplet	25.4	1.75	Inline	AW		100-600	0-1
Dowlati et al. (1992)	VF	-	12.7 and 19.05	1.3-1.75	Stag/Inline	AW		56-795	0.001-0.89
Ulbrich and Mewes (1994)	FP	B I D	20	1.5	Inline	AW		1.6-650	0.0001.0.89
Dowlati et al. (1996)	VF, PD		12.7 and 19.05	1.3	Stag/Inline	R113	0-80	50-790	0-0.5
Xu et al. (1998b)	FP, VF, PD	B Ct I	9.79	1.28	Inline	AW		37-658	0.001-0.94
Noghrehkar et al. (1999)	FP	B I A	12.7	1.47	Stag/Inline	AW		50-1000	0-085
Feenstra et al. (2000)	VF	-	6.3-19.05	1.3-1.75	Stag/Inline	AW R113		90-1330	
Doo et al. (2004)	FP	TEMA E shell	-	-		R134a		-	-
Burnside et al. (2005)	FP	-	19	1.34	-	AW		-	-
Iwaki et al. (2005)	FP	B	15	1.5	Stag/Inline	AW		G_l= 64-692	<0.02
Huang et al. (2008)	FP	B C A	20	1.35	Stag	R134a	Diab.	4 25	0.02-0.9
Aprin et al. (2007)	FP, VF	B I A	19.05	1.33	Stag	HC	Diab.	9-45	0.1-0.7

Author	Topic	Flow pattern	Diameter	P/D	Bundle geometry	Fluid	Heat flux	G	Vapour quality
Consolini *et al.* (2008)	PD		19	1.17	Stag	R134a, R507A, R410A	6-45	5-40	0.1-0.81
McNeil *et al.* (2010)	FP	Reboiler	-	-		-		-	-
Van Rooyen et al. (2011a)	PD	-	19	1.17	Stag	R134a, R236fa	0-22	5-40	0.1-0.81

2.5 Boiling heat transfer

The size of equipment needed for a given heat load can be reduced if an already high nucleate boiling heat flux can be further enhanced. Recent advances in enhancing nucleate boiling heat flux have included the development of enhanced surfaces with high density interconnected artificial cavities of the re-entrant type. The enhanced surfaces have led to an order of magnitude increase in already high nucleate-boiling heat transfer coefficients (Thome, 1990, Dhir, 1998).

Prediction of boiling heat transfer has been studied thoroughly over the last half century (Kolev, 1995, Pioro *et al.*, 2004). When predicting heat transfer performance one has several options to chose from. Many processes, still too complicated for accurate modelling, are predicted by simplified empirical correlations. As understanding increases, dimensionless groups, representing physical processes, have become part of these empirical correlations. Dhir (2006) classified two types of studies: empirical and mechanistic. Moghaddam and Kiger (2009b) distinguished three types of prediction methods for nucleate boiling: convection models, transient conduction and composite mechanisms. Mechanistic models (discussed in Appendix C) that are based, as far as possible, on modelling the processes exactly, are not yet general enough for the complex surfaces. The pool boiling performance of any tube, smooth or enhanced, can not yet be well predicted by a general boiling model (Poniewski and Thome, 2008).

The pool boiling performance is critical in understanding boiling heat transfer on a tube and often also serves as the basis for the convective prediction methods. If an accurate, general pool boiling prediction method can be devised, many existing methods for convection could implement this directly. This section presents an overview of prediction methods for single tube pool boiling and convective bundle boiling.

2.5.1 Empirical pool boiling correlations for smooth and enhanced tubes

Prediction methods have remained empirical to some extent, but an effort has always been made to highlight the importance of physical properties or dimensionless groups that are well correlated to the data.

For smooth surfaces, Rohsenow (1952) proposed a physical model of semi-empirical nature based on intuitive arguments concerning the supposed physics of nucleate pool boiling (equation 2.21). Rohsenow (1952) suggested that heat transfer enhancement is due to local liquid circulation at the surface caused by bubbles detaching from the surface. A mass flux was defined based on vapour generation and a Reynolds number was defined with bubble detachment diameter as characteristic dimension. A Jakob number, the ratio between latent heat and sensible heat,

Reynolds number and Prandtl number were correlated by three empirical constants that were a function of fluid and surface relations. Over the years many studies have used this relationship, including some recent work by Jabardo *et al.* (2004) and Ribatski *et al.* (2008). All these studies have added to the database of fluids and surface material used.

$$\frac{c_{pl}\Delta T}{h_{lv}} = C_{sf} \cdot \left(\frac{q}{h_{lv}\mu_l} \left[\frac{\sigma}{g(\rho_l - \rho_v)} \right]^{\frac{1}{2}} \right)^m \cdot \frac{c_{pl}\mu_l}{k_l}^n \tag{2.21}$$

Stephan and Abdelsalam (1980) used dimensional analysis to define π-groups and a statistical regression method to identify the strongest π-group to correlate with their database. They correlated separate equations for water, hydrocarbons, cryogenic fluids and refrigerants and all combined (equation 2.22). The dimensionless groups were based on fluid and solid properties, but no consideration was given to heater geometry (roughness), yielding:

$$Nu = 0.23\,\pi_1^{0.674}\,\pi_2^{0.297}\,\pi_3^{0.371}\,\pi_4^{-1.73}\,\pi_5^{0.35} \tag{2.22}$$

The π-groups are arranged in order of their influence on the Nusselt number and given below:

$$\pi_1 = \frac{qd}{k_l T_{sat}} \qquad\qquad \pi_2 = \frac{\rho_v}{\rho_l}$$

$$\pi_3 = \frac{h_{lv}d^2}{\alpha_l^2} \qquad\qquad \pi_4 = \frac{\rho_l - \rho_v}{\rho_l}$$

$$\pi_5 = \frac{\alpha_l^2 \rho_l}{\sigma d}$$

Cooper (1984) proposed a popular correlation for predicting nucleate pool boiling on smooth, flat surfaces (equation 2.23). He also commented that cylindrical copper boiling surfaces had a 1.6 times higher heat transfer coefficient in comparison with a flat surface. No detailed analysis or explanation was given for this factor. It can be assumed that it is due to sliding bubbles moving around the surface of the tube adding convective, thin film evaporation and transient cooling components to the heat flux that is transferred at the nucleation site. The wall conduction might also play a role. Although the correlation accounts for surface roughness, it does not account for surface wettability:

$$h_{o,pb} = 55p_r^{[0.12-0.08686ln(R_a)]}\left(-0.4343ln(p_r)\right)^{-0.55} M^{-0.5}q_o^{0.67} \tag{2.23}$$

Gorenflo (1993) proposed a fluid specific correlation based on reduced pressure and surface roughness, but related the correlation to the heat flux of a specific reference condition q_o. The main parameters for the correlation were heat flux and reduced pressure:

$$
\begin{aligned}
h_{o,pb} &= h_o F_{PF} \left(\frac{q}{q_o} \right)^{nf} \left(\frac{R_a}{R_{ao}} \right)^{0.133} \\
\text{with:} \quad F_{PF} &= 1.2 p_r^{0.27} + 2.5 p_r + \frac{p_r}{1 - p_r} \\
nf &= 0.9 - 0.3 p_r^{0.3}
\end{aligned}
\tag{2.24}
$$

Ribatski *et al.* (2008) used a correlation based on the Cooper (1984) principle but tailored it for horizontal tubes. The main parameters were heat flux and reduced pressure, but the correlation was also a function of surface roughness and molar mass with a material specific leading coefficient. The value of B accounts for the wall material and was found to be 100 for copper, 110 for brass and 85 for stainless steel:

$$
h_{o,pb} = B \left(q^{0.9 - 0.3 p_r^{0.2}} \right) p_r^{0.45} \left[-log(p_r) \right]^{-0.8} R_a^{0.2} M^{-0.5}
\tag{2.25}
$$

Recent experimental studies of nucleate pool boiling on plain and enhanced tubes were summarised by Christians (2010). The study included data with R134a and R236fa for heat fluxes from 20 to 80 kW/m^2 . The prediction method derived by Christians (2010) from a database of seven enhanced tubes is empirical and based on dimensionless groups that correlate well with the LTCM data set for seven tubes. The enhanced tubes were significantly different from each other, yet only one constant was used to correlate the geometric differences (Table 2.2):

$$
\begin{aligned}
h_{o,pb} &= 99976 \pi_6^{-0.128} G_{t-s}^{1.658} \left(\frac{k_l}{D_o} \right) \\
\pi_6 &= \frac{q_o^2}{h_{lv} p_{sat}^2}
\end{aligned}
\tag{2.26}
$$

No effort was made to explain or quantify the geometric constant and due to the complex interaction of geometry and heat transfer mechanisms this would be difficult without the exact geometry of the tubes and substructures known. The π_6 group was described as an effective rate of bubble generation (which indicates the amount of liquid pumping intake that occurs into the 3D enhancement) and the heat flux dependence on the saturation pressure (also a type of flow rate) (Christians, 2010).

23

Table 2.2: Geometric factor G_{t-s} for each tube

	G_{t-s}
Turbo-Bii (Roques, 2004)	0.118
Gewa-B (Roques, 2004)	0.1141
High Flux (Roques, 2004)	0.2024
Turbo-EDE2 (Habert, 2009)	0.1488
Gewa-B4 (Habert, 2009)	0.1777
Turbo-B5 (Christians, 2010)	0.1584
Gewa-B5 (Christians, 2010)	0.1597

It should be evident from the preceding excerpts that these correlations cannot be universally applied and large deviations between actual data and predictions can occur when conditions for which the correlations were developed are not duplicated. The general trend for smooth tubes is an increase in the heat transfer coefficient with an increase in heat flux. Most studies indicate that the dominant dependence is on heat flux, followed by properties such as the reduced pressure, heater material, surface condition and surface tension. For enhanced tubes the heat transfer coefficients often show a decreasing trend with an increase in heat flux and a greater enhancement factor with respect to smooth tubes at lower heat fluxes. The enhancement advantage diminishes as the heat flux approaches the critical heat flux (CHF) (Yilmaz and Palen, 1984). This indicates a fundamental difference between smooth and enhanced surfaces. The π-group used by Christians (2010) for enhanced tubes hints at the importance of liquid supply into enhanced structures. The following section elaborates on these mechanisms.

2.5.2 Mechanisms of boiling

The studies in the second category of Dhir (2006) are those that focused on detailed investigations of individual subprocesses in the hope that such studies could serve as a basis for the development of mechanistic models. Such models then serve to predict boiling heat fluxes as a function of wall superheat and other independent variables.

The enhanced boiling process is different from normal nucleate boiling in cavities on smooth surfaces. The heat flux on enhanced surfaces has four paths by which it can leave the tube (Thome, 1990):

- As latent heat in vapour formed inside the enhanced passageways;

- As latent heat in bubbles growing on the exterior or while they are emerging from the pores;

- As sensible heat to liquid pumped through the re-entrant passageways; and

- As sensible heat to liquid on the external surface of the tube.

Each of these paths can be divided into mechanisms. Boiling mechanisms in pool boiling have been well studied and over the years many attempts have been made at mechanistic models (Nakayama *et al.*, 1980a, Chien and Webb, 1998b, Ramaswamy *et al.*, 2003, Das *et al.*, 2006, Moghaddam and Kiger, 2009b). All these models gave satisfactory predictions to the respective data sets that they were developed for. Their shortcoming is that there is still no consensus on which combination of mechanisms are present and on what area they act (Moghaddam and Kiger, 2009a). Accordingly, the areas attributed to each mechanism have been scaled differently by each researcher to correct his model. The problem then snowballs in complexity when the geometry of enhanced tubes enters into the mix.

To mechanistically model nucleate boiling, efforts have been devoted to inception, nucleation site density, bubble dynamics (which includes departure diameter, bubble growth and departure rate), interfacial instabilities, fractional area and duration of liquid-solid contacts and the associated heat transfer processes (Dhir, 2001). There will inevitably be interactions among all the mechanisms that remain difficult to quantify (Thome, 1990, Poniewski and Thome, 2008).

An important fundamental component of mechanistic models concerns bubble dynamics. Another component is the nucleation site density. For smooth tubes the nucleation sites are active and a function of the superheat, surface material and fluid with complex interactions. A smooth surface is essentially open to the influx of colder fluid and a distinct cycle develops for bubbles including waiting, growth and departure periods. For enhanced tubes active sites have a different meaning. On enhanced tubes the existence of nucleation sites are less important for the evaporation process. The vapour will escape through a pore somewhere on the tube but the vapour could have been generated in the tunnel by a combination of thin film evaporation, menisci evaporating in the corners of microchannels and nucleate boiling.

The heat transfer processes, like the micro-layer and transient heat transfer, due to the bubble cycle of waiting, growth and departure are integral parts of mechanistic models and link the mechanics of each state to heat flux. The role of natural convection in the areas unaffected by boiling remains contested (Das *et al.*, 2006) and does not represent the physics according to Moghaddam and Kiger (2009b).

For tubular surfaces the external sliding bubble contribution is added. Nishikawa *et al.* (1984) found that for water on flat plates inclined at different angles in partial nucleate boiling, the

downward-facing surfaces had better heat transfer performance than those on an upward-facing horizontal surface or a vertical surface. Cornwell (1990) studied the effect of sliding bubbles on horizontal tubes and demonstrated that a thin liquid film between the wall and the vapour could enhance the heat transfer. However, Cornwell and Schöller (1982) confined their studies to micro-layer evaporation during sliding, neglecting the transient conduction due to sliding which can be as important as the former (Haider and Webb, 1997). Including transient conduction around the sliding bubbles in their model was the approach taken by Luke and Gorenflo (2000) and Das and Roetzel (2004). Thus, any modelling of non-horizontal surfaces requires the incorporation of all the mechanisms involved. One such attempt, for smooth tubes, was the model of Sateesh *et al.* (2005).

For enhanced structures the thin liquid film, liquid menisci in the corners and the cycle of vapour generation, release and liquid replenishment are identified as mechanisms (Nakayama *et al.*, 1980a). For enhanced tubes the common procedure is to quantify the sites where bubbles emerge from the enhancement similar to smooth tube nucleation sites. This has no relation to the nucleation inception that occurs on a smooth tube or possibly inside the enhancement. The abundance of vapour in the tunnels will merely exit the enhancement at a pore site determined by the fluid, pore size, internal pressure and other parameters.

The details for pool boiling mechanisms on flat plates, inclined surfaces and plain tubes will not be discussed further and the following discussion will focus on enhanced tubes. Although some of the mechanisms present on smooth tubes might also be present on enhanced tubes, the differences between the two cases are countless and the plain surfaces do not have direct application in this study. Where it is necessary to recall smooth tube mechanisms, the appropriate reference will be made. The enhanced tube mechanistic studies are discussed in Appendix C.

The insight gained from an accurate mechanistic model for nucleate pool boiling might also lead to an inclusion of convective effects for cases like bundle boiling. On enhanced tubes it might lead to design and optimisation of tube geometries for material, fluid and heat flux combinations that serve a client or application.

2.5.3 Heat transfer in tube bundles

Some important bundle effects and prediction methods are highlighted next. For the sake of brevity the experimental studies and prediction methods available are summarised in Table 2.3. Details on these methods are thoroughly reviewed in Thome (1990), Browne and Bansal (1999), Casciaro and Thome (2001) and Thome (2004).

Several studies have been done on boiling on a single tube with convection of fluid past the tube (Wege and Jensen, 1984, Hwang and Yao, 1986, Cornwell and Einarsson, 1990, Webb and Pais, 1992, Cornwell and Houston, 1994, Dhir, 1998). These studies are useful in the development stages of new refrigerant systems and can be important in isolating and quantifying mechanisms because the bundle effect is not yet included. For the enhanced tubes in the current study the scope of testing was limited to single tube pool boiling and convective bundle boiling.

The main bundle effects are: flow induced convection, tube row effect, onset of dryout and those related to flow pattern (bubbly, dispersed, annular and mist flow), heat flux effect in bundle, vapour quality, mass flux, tube type, tube layout, refrigerant and the effects of oil. The main focus of the present study was to investigate bundle boiling and possible bundle effects. Some noteworthy effects for the purposes of this investigation are briefly elaborated on below.

The major classification of studies can be done by experimental method. Bundle boiling studies aim to obtain overall heat transfer coefficients or local heat transfer coefficients. Experiments are done with electric heating or by a heating fluid inside the tubes. Another important distinction is whether the mass flux is measured and consequently, by means of energy balances, the local vapour quality on the shell-side. From the large amount of data currently available, those obtained with local measurements of heat transfer, mass flux and vapour quality are most useful for comparison.

2.5.3.1 Bundle effects

Row effects Many researchers found an increase in the heat transfer coefficient on smooth tubes as flow moved through the bundle, tube row for tube row (Cornwell *et al.*, 1980, Rebrov *et al.*, 1989, Marto and Anderson, 1992). At low heat fluxes (1 to 10 kW/m^2), the increase in the row effect relative to a single tube is large because the nucleate boiling coefficient is still small and convective heat transfer is important. At heat fluxes above 50 kW/m^2 the bundle and single tube curves coincide to forced convection in cross-flow over a single tube as described earlier, because bubbles from nucleate boiling have become dominant. For enhanced tubes the row effect was found to be weaker (Jensen *et al.*, 1992).

Contrary to these results, Jensen and Hsu (1988) found little or no increment in the heat transfer coefficient with increasing tube row in their 27-row test bundle using forced flow, although the coefficients are larger than those predicted by single tube correlations such as the one of Cooper (1984). Since h_o was found not to be a function of vapour quality in these well executed tests, this study created considerable discussion (Robinson and Thome, 2003). However, critical examination shows that uniformity in h_o can apparently be attributed to the forced convection effect. The bottom tube rows are subjected to a significant fluid velocity similar to a single tube in cross-flow whilst in natural circulation tests, fluid velocities are very small at the lower tube rows with coefficients nearly equal to single tube values. Their tests included mass velocities considerably above present interest, such that convection was dominant throughout the bundle.

Tube layout Liu and Qiu (2002, 2004), Qiu and Liu (2004) and Liao and Liu (2007) ran a series of compact bundle experiments with water and R11. They investigated the effects as pitch to diameter ratios became small and restricted the gap between tubes. Smooth tubes showed heat transfer enhancement in a compact bundle for all fluids compared to enhanced tubes that showed no bundle enhancement. This suggested that the mechanisms created by the subsurface structures are dominant in the enhanced boiling heat transfer process and not strongly affected by the bundle layout. The smooth or open tubes also benefit from being very close together in compact bundles because the superheated liquid layer is maintained (Liu and Qiu, 2002).

Bundle factor In this section heat flux, mass flux, vapour quality and tube type are discussed by referring to the bundle factor, defined as:

$$K_{BB} = \frac{h_{o,BB}}{h_{o,pb}} \quad \text{at the same heat flux} \tag{2.27}$$

A large study was conducted by Jensen *et al.* (1992) covering a wide variety of operating conditions. For plain tubes, substantial bundle factors were observed which increased with local vapour quality and mass velocity. This was more notable at low heat fluxes where the convection contribution to the flow boiling coefficient was larger than at high heat fluxes. For the enhanced tubes (*Wolverine Turbo-B* and *High Flux*), neither showed a marked influence of mass velocity nor vapour quality. The induced convection which was similar in magnitude for all three tubes had more influence on the plain tube bundle.

Gupte and Webb (1995b) conducted experiments on an enhanced tube bundle with R11, R123 and R134a in an equilateral triangular tube layout of Turbo-B and Gewa-SE tubes. They

concluded that the bundle performance was within -10% and +25% of corresponding single tube nucleate pool boiling heat transfer coefficients and therefore no significant convective effects were present. According to data by Memory *et al.* (1995), Turbo-B tube heat transfer in bundle boiling was 1.10-1.47 times higher than pool boiling heat transfer. The High Flux tube, which had the highest performance of all the tubes tested, showed no bundle boiling enhancement.

In the study of Roser *et al.* (1999) on low fin tubes with propane and pentane, the pentane indicated high bundle boiling factors for low heat fluxes and lower bundle boiling factors for higher heat fluxes. Pentane had considerable vapour quality effects. Propane, which has a higher performance at six bar had lower bundle boiling factors and a weak vapour quality effect.

Burnside *et al.* (2005) ran high mass flux experiments on a square bundle with 19 mm electrically heated tubes and observed heat transfer coefficients higher than pool boiling, and the heat transfer coefficients linearly increased with vapour quality for heat fluxes below 40 kW/m^2. For heat fluxes above 40 kW/m^2 the pool boiling performance was similar to the bundle.

Bundle factor results are dependent on accurate pool boiling heat transfer coefficients and pool boiling results are known to be sensitive to the experimental facilities and methods of researches. Furthermore, the uncertainty in the bundle boiling factor is rather large because the uncertainty of both heat transfer coefficients are propagated into the factor. This means that variations of 20% might be meaningless (Gupte and Webb, 1995b). If we assume a reasonable bundle boiling factor uncertainty of 30%, the main conclusions from such a data presentation are that low fin tubes benefit the most from convection, followed by plain tubes, then enhanced tubes. The trend in bundle boiling factor is clearly that a tube with inherently high heat transfer performance (modern enhanced tubes and High Flux tubes) is less likely to show an effect on performance in a bundle with convection.

To conclude, for enhanced boiling tubes the bundle factors are not significant as long as dryout or sub-cooling are avoided. It is hypothesized that the prediction method for enhanced tubes does not depend strongly on bundle convection effects or row effects but merely on the local heat flux, fluid choice and any other secondary effects that would have an impact on nucleate pool boiling performance. This can be attributed to the subsurface micro channels, re-entrant cavities and pores that are responsible for maintaining a subsurface superheated liquid, cyclic pumping of new liquid and thin liquid films with high heat transfer that are shielded from the convective effects, which serve merely to supply liquid to maintain the underlying processes. If the external convection affects these parameters notably then convective effects need to be included

in a prediction method. In comparison, the smooth tubes and low fin tubes, with essentially open structures, benefit from convection to produce enhancement (Kim *et al.*, 2002).

2.5.3.2 Smooth tube bundle prediction methods

Smooth tube prediction methods are mentioned here because the external heat transfer on the outside of enhanced tubes is similar to that on smooth tubes. Bubbles appear from a pore and slide upwards over the tube. The major differences between smooth and enhanced tubes are the amount of bubbles, the actual surface structure and the temperature difference.

Single phase The heat transfer for single phase forced convective flow across a tube bank is governed primarily by the flow velocity, bundle geometry and fluid properties. The heat transfer process can be described empirically by the Nusselt number, the flow velocity by the Reynolds number, the physical properties by the Prandtl number and the bundle geometry by its tube layout and dimensions:

$$Nu = cRe^m Pr^n \frac{Pr}{Pr_w}^{0.25} \tag{2.28}$$

The Reynolds number is based on the tube diameter and maximum velocity in the tube gap. Žukauskas and Ulinskas (1983) have done extensive work on tube bundles, covering Reynolds numbers from 2 to 2 000 000 for staggered and in-line tube banks and reported various case-dependent values for c, m and n. In actual heat exchangers the flow is not ideal and bypass flows can be significant. For more on these effects, one should refer to the Delaware method described by Bell (1981) and also the comprehensive experimental studies completed by Matsushima *et al.* (1986, 1987, 1988). For natural convection on horizontal tube bundles, Shklover and Gusev (1988) reviewed the correlations available.

Bundle boiling methods Several mean bundle boiling methods have been proposed to predict mean bundle heat transfer coefficient (Palen and Small, 1964, Palen and Yang, 1983, Rebrov *et al.*, 1989). An altogether more useful means of designing bundles accurately is with local heat transfer prediction methods that can be used as a function of local mass flux, heat flux and vapour quality conditions.

Hwang and Yao (1986) modified the Chen (1966) correlation for in-tube flow using a new empirical expression for F (F = $f(\text{x},\rho_v,\rho_l)$) and the Bennett *et al.* (1980) expression for the boiling suppression factor S. Y is a dimensionless variable in their equation:

$$
\begin{aligned}
h_o &= Sh_{o,pb} + Fh_l & (2.29) \\
S &= \frac{k_l}{Fh_lY}\left[1 - e\left(\frac{Fh_lY}{k_l}\right)\right] \\
Y &= 0.0205\frac{D}{Bo^*}
\end{aligned}
$$

However, visual observations of bubbly and frothy flow made by Cornwell *et al.* (1980) do not show evidence of a suppression of nucleate boiling in a bundle or single tube in cross flow. Thus, it can be concluded that the boiling suppression factor should be set equal to 1.0 for a tube bundle and the complete effect of convection included in the model through the two-phase flow correction factor F. Cornwell *et al.* (1986) assumed the convective and nucleate boiling contributions to be additive without a boiling suppression factor as:

$$
Nu_b = \frac{h_oD}{k_l} = cRe^mPr^n + CRe_b^{0.67} \tag{2.30}
$$

where the Žukauskas and Ulinskas (1983) parameters are used for c, m and n. The bundle Reynolds number is determined based on the liquid velocity as:

$$
Re_b = \frac{\rho_l u_l D}{\mu_l}
$$

The liquid velocity is determined from the following equations where A_{min} is the minimum crossflow area between the tubes and ε is the void fraction given by Cornwell *et al.* (1980):

$$
\begin{aligned}
u_l &= u_v(\frac{\varepsilon}{1-\varepsilon})(\frac{\rho_v}{\rho_l})(\frac{1-x}{x}) \\
u_v &= \frac{Gx}{\rho_v A_{min}\varepsilon}
\end{aligned}
$$

Based on their tests with R113, they found C = 150 for data at 20 kW/m^2. Use of this expression at other pressures or for other fluids requires a general expression for the nucleate boiling contribution and comparison to more data.

Nakajima (1978) proposed that the bundle boiling coefficient is the summation of nucleate boiling and thin film evaporation, the latter resulting from conduction through thin liquid films created between the tubes and rising bubbles. Their general expression for the local heat transfer coefficient was:

$$\begin{aligned} h_o &= (1-\varepsilon)h_{o,pb} + \varepsilon h_{tf} \\ h_{tf} &= 2326 + 1512 e\left[\left(\frac{-0.5556}{U_v}\right)^{1.5}\right] \end{aligned} \qquad (2.31)$$

However, no convective heat transfer contribution was considered. Also, at the limit when the void fraction equaled 1.0, the model brakes down and predicts thin film evaporation to occur when no liquid was present.

The most general form of the asymptotic model for the prediction of bundle boiling heat transfer coefficients is:

$$h_o = [(Sh_{o,pb})^n + (Fh_l)^n]^{\frac{1}{n}} \qquad (2.32)$$

Webb and Chien (1994a) presented a correlation of this type for convective boiling on plain tube bundles. They utilised their own data for R113 and R123 and also data from two other independent tests with R113. They correlated the data using both an asymptotic model approach (with the boiling suppression factor set to 1.0 and the asymptotic exponent n = 3.0) and a Chen (1966) in-tube flow boiling type of approach (with the boiling suppression factor S from the in-tube model and n = 1). Neither model is satisfactory since they used single tube experimental boiling curves for the nucleate boiling coefficients in their calculations rather than a single tube nucleate boiling correlation.

The Thome and Robinson (2006) prediction method developed for plain tubes uses an asymptotic method for predicting the local bundle boiling heat transfer coefficient:

$$h_o = \left(h_{o,pb}^2 + h_{o,cb}^2\right)^{1/2} \qquad (2.33)$$

where the first term is the nucleate boiling heat transfer coefficient and the second term is the convective boiling heat transfer coefficient. The nucleate boiling term $h_{o,pb}$ is predicted using the Cooper (1984) correlation. A film thickness δ was calculated using the void fraction model of Feenstra $et\ al.$ (2000) and then used to estimate the convective heat transfer coefficients for film flow over the tubes in the bundle:

$$h_{o,cb} = 4.032\, Re_\delta^{0.236} Pr_l^{0.4} \left(\frac{k_l}{\delta}\right) \qquad (2.34)$$

Many studies present different heat transfer trends and dependencies on the basic parameters such as heat flux, mass velocity, vapour quality and refrigerant. Shah (2007) highlights apparent
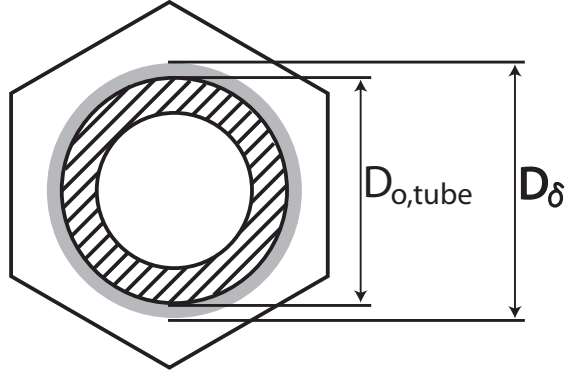
Figure 2.5: Film thickness when liquid is redistributed based on the void fraction and a hexagonal unit element

conflicts in the literature where different authors reported contrasting results. The method of Shah (2007), based on an extensive database, provides a set of equations to define each flow regime. Shah (2007) identified three possible regimes: *intense boiling regime* (heat transfer depends on heat flux), *convective boiling regime* (heat transfer depends on heat flux and mass velocity) and *convective regime* (heat transfer affected by mass velocity).

2.5.3.3 Enhanced tube prediction methods

Gupte and Webb (1995a) assumed and then experimentally validated that the boiling suppression factor (S) equals one. Starting from a heat momentum transfer analogy, they presented a general expression for the two-phase convection multiplier F (equation 2.35), dependent on the Prandtl number and the two-phase friction multiplier defined by Ishihara *et al.* (1980). They concluded that for enhanced tube banks the correlation for the F-factor and h_l are not critical. They validated their method against measurements from Cornwell and Scoones (1988) for R113 on plain tube banks and their own measurements for R11, R123 and R134a on GEWA-SE, Turbo-B and low fin (1024 fins/m) tube banks. For tubes with low nucleate boiling performance (plain tubes) the accuracy of the F-factor dictated the accuracy of the prediction.

$$F = \left[\frac{\Phi_f^2 (Pr_l + 1)}{2} \right]^{0.327} \tag{2.35}$$

A series of experiments by Kim *et al.* (2002) with refrigerant on smooth and enhanced tubes suggested that heat flux has the strongest effect on heat transfer coefficient while mass flux and vapour quality did not influence any trends over their experimental range for enhanced tubes. They proposed a Chen type method, composed of the correlations by Žukauskas and Ulinskas

33

(1983) for h_l, Gupte and Webb (1995a) for F and S $= 1$ for enhanced tubes. Φ_f is the two-phase friction multiplier by Ishihara *et al.* (1980):

Additionally, they also correlated an asymptotic model to their data by setting S $= 1$ and found that n $= 1$ gives the best prediction after backing out the F-factor using their own data:

$$F = 2.70 \left[\frac{\Phi_f^2 (Pr_l + 1)}{2} \right]^{0.202} \tag{2.36}$$

Thome and Robinson (2006) reported methods for predicting heat transfer on plain, low fin and enhanced tubes based on a database with several refrigerants (R134a, R507A and R410A) at low mass fluxes. Enhanced tube heat transfer coefficients were predicted using two multipliers to the pool boiling heat transfer coefficient. A reduced pressure effect (F_p) and a void fraction effect (F_ε) were considered. The void fraction effect was based on the void fraction predicted by the Feenstra *et al.* (2000) method and therefore includes mass flux. For enhanced tubes the convection effects deduced had little effect on the bundle performance of Turbo-BII HP because of its very high nucleate boiling coefficients when compared with the plain and low finned tube bundles. They concluded that there was no strong effect of mass flux or vapour quality on the heat transfer coefficient:

$$
\begin{aligned}
h_{o,BB} &= h_{o,pb} F_p F_\varepsilon \\
F_p &= 1.41 - 2.66 p_r \\
F_\varepsilon &= 1 - 2(0.4 - \varepsilon)^2
\end{aligned}
\tag{2.37}
$$

In summary, there are various bundle boiling methods available but none have been successful in predicting independent data not included in their development. The existing methods do not necessarily reflect all the heat transfer mechanisms involved in bundle boiling. It was concluded by Robinson and Thome (2003) that it was not a promising approach to apply the Chen (1966) prediction method to bundle boiling without a complete rethinking of the heat transfer and flow phenomena involved. Thus the present study will attempt to add more understanding to the complex process of bundle boiling, with particular interest on enhanced boiling.

Table 2.3: Heat transfer studies in boiling on tubes with convection

Author	Diameter	Metal	Bundle geometry	Surface	P/D	Fluid	Mass flux	Heat flux	Vapour quality
Diehl (1957)	12.7	Cu	Inline/ Staggered	Smooth	1.25	AW +solutions	<1000		0.006-1
Cornwell et al. (1980)	19.05	Cu		Smooth	1.33	R113		20	
Cumo et al. (1980)	13.6	SS	Staggered 5x3	Smooth	1.25	R12	41	296	0.13
Polley et al. (1980)	25.4	SS	6x6	Smooth	1.244	R113	450	17	0.002-0.017
Yilmaz and Palen (1984)	19	Cu	-	Smooth enhanced	-	p-xylene, isopropyl	-	-	-
Hwang and Yao (1986)	19.1	SS	16x3	Smooth	1.5	R113	0-817	3-80	0-0.14
Jensen and Hsu (1988)	7.9	SS	27x5	Smooth	1.3	R113	100-675	6.3-37.8	0.001-0.184
Cornwell and Scoones (1988)	25.4	Brass	Inline 5x6	Smooth	1.25	R113	150	6-36	0-0.35
Rebrov et al. (1989)	22	SS	30 rows and 50 rows	Smooth	1.45	R12, R22		10	
Jensen et al. (1992)	19.1	Cu	Staggered 15x5	Smooth	1.17-1.5	R113	51-500	10-40	0-0.74
Jensen et al. (1992)	7.9-25.4	Cu	Staggered 15x5	Enhanced	1.17-1.5	R113	1.7-679	2-296	0-0.88

Author	Diameter	Metal	Bundle geometry	Surface	P/D	Fluid	Mass flux	Heat flux	Vapour quality
Marto and Anderson (1992)	15.9	Cu	Staggered	Smooth	1.2	R113	-	-	-
Cotchin and Boyd (1992)	25.4	Brass	3x60	Smooth	1.33	R113 (oil)	-	-	-
Cornwell and Houston (1994)	Collation	-	1 tube	Smooth	-	Water, Ref, HC	-	<1000	-
Memory et al. (1994)	15.9	Cu	Staggered 15	Enhanced	1.2	R113	-	5-80	-
Webb and Chien (1994b)	16.8	Cu	Staggered	Smooth	1.42	R113	8-37	13-55	0.07-0.88
Gupte and Webb (1995a) Gupte and Webb (1995b)	18.9	Cu	Staggered 15	Enhanced low fin	1.26	R11, R123, R134a		5-45	0.1-0.9
Memory et al. (1995)	15.9	Cu	Staggered	Smooth enhanced	1.2	R114 (oil)	-	2-60	-
Gupta et al. (1995)	19.05	SS	1 / 2 / 3 tubes	Smooth	1.5-6	Water	0-10	10-40	-
Gorenflo et al. (1995)	4-88.4	SS	1 tube	Smooth		Propane, n-butane	-	0.1-100	-
King and Jensen (1995)	15.9	Brass	Inline	Smooth	1.3	R113	-	10-70	-
Cheung et al. (1996)	19.05		Staggered	Low fin	1.37	R134a	-	-	-
Dowlati et al. (1996)	12.7	Cu	Inline 20x5	Smooth	1.3	R113	50-790	-	0-0.5
Fujita et al. (1997)	14		Staggered and inline	Smooth	1.29-1.5	R113	Not local		

36

Author	Diameter	Metal	Bundle geometry	Surface	P/D	Fluid	Mass flux	Heat flux	Vapour quality
Kramer et al. (1997)	-	Cu	-	Enhanced 1 tube	-	Ethanol, water, mixtures	-		-
Cheung et al. (1997)	-			Low fin + EHD		R134a			
Chien and Webb (1998b)	19	Cu	1 tube	Enhanced	-	R11, R123	1-70	-	-
Roser et al. (1999)	19.05	Cu	Staggered 17x5	Smooth	1.33	n-pentane	14-44	<60	<0.6
Tatara and Payvar (2000a) Tatara and Payvar (2000b)	19.05		Staggered 31x 9	Enhanced	1.17	R123, R134a, R22 (oil)		8.2-34	
Kim et al. (2002)	18.8	Cu	Staggered 5x6	Smooth enhanced	1.27	R123 R134a	8-26	10-40	0.1-0.9
Liu and Qiu (2002)	18	Cu	Staggered 17 tubes	Smooth enhanced	1.027-1.22	Water, brine	-	2-300	-
Robinson and Thome (2003)	18.9	Cu	8x3	Smooth enhanced	1.17	R134a, R507A, R410A	5-39	2-35	0.1-0.81
Chien and Wu (2004)	15.9		5x3	Smooth	1.5	R134a, R123	10-40	10-50	0.07-0.24
Liu and Qiu (2004)	18	Cu	Staggered 17	Smooth enhanced	1.027-1.22	R11	-	1-100	-
Burnside and Shire (2005)	19.1	Cu-Ni	Inline 17x5	Smooth	1.33	R113	211-622	10-65	0.004-0.25
Gupta (2005)	19.05	SS	5x3 inline	Smooth	1.5	Water	0-10	10-40	-
Liu and Liao (2006)	18	Cu	Inline	Smooth	1.027-1.22	Water	-	5-100	-

Author	Diameter	Metal	Bundle geometry	Surface	P/D	Fluid	Mass flux	Heat flux	Vapour quality
Liao and Liu (2007)	18	Cu	Staggered 15 tubes	Smooth	1.2-2	Water	-	5-100	-
Shah (2007)	Collated dataset	-	-	Smooth	1.17-1.5	Water, pentane R11, R12, R113, R123, R134a	1.3-1391	1-1000	-
Doo et al. (2008)	-	-	TEMA E-shell	Smooth	-	R134a	100-800	19-44	0.05-0.6
Gorgy and Eckels (2010)	19.05	Cu	1 Tube	Smooth enhanced	-	R134a, R123	-	4-134	-

Chapter 3

Experimental set-up and methods

3.1 Introduction

The existing bundle boiling facility, as used in the study by Agostini (2008), was modified and improved for this study. The flow pattern instrumentation and visualisation systems were improved. The functionality of the facility was also improved by adding some computer control and automation for increased productivity. This chapter gives a complete description of the facility and its instrumentation. General information about the original configuration is available in Robinson and Thome (2003).

3.2 Test facility

The bundle boiling facility consisted of a hermetically sealed, single circulating loop for the refrigerant and a second water loop that acts as a heat source for the boiling process in the test section.

3.2.1 Refrigerant cycle

The existing Laboratory for heat and mass transfer (LTCM) test loop, developed by Robinson and Thome (2003) and modified by Agostini (2008) was adapted to perform the tests conducted in this study. A schematic diagram of the refrigerant loop is depicted in Figure 3.1 and an image of the test stand is given in Figure 3.2.

A magnetically coupled oil free gear pump circulated the refrigerant while a computer controlled the refrigerant mass flow rate. The flow passed through a pre-heater which controlled the inlet vapour quality of the test section by means of an electric heat input with a maximum power

of 25 kW. After the test section and before re-entering the pump, a condenser brought the fluid to subcooled conditions by exchanging heat with a water-glycol mixture.
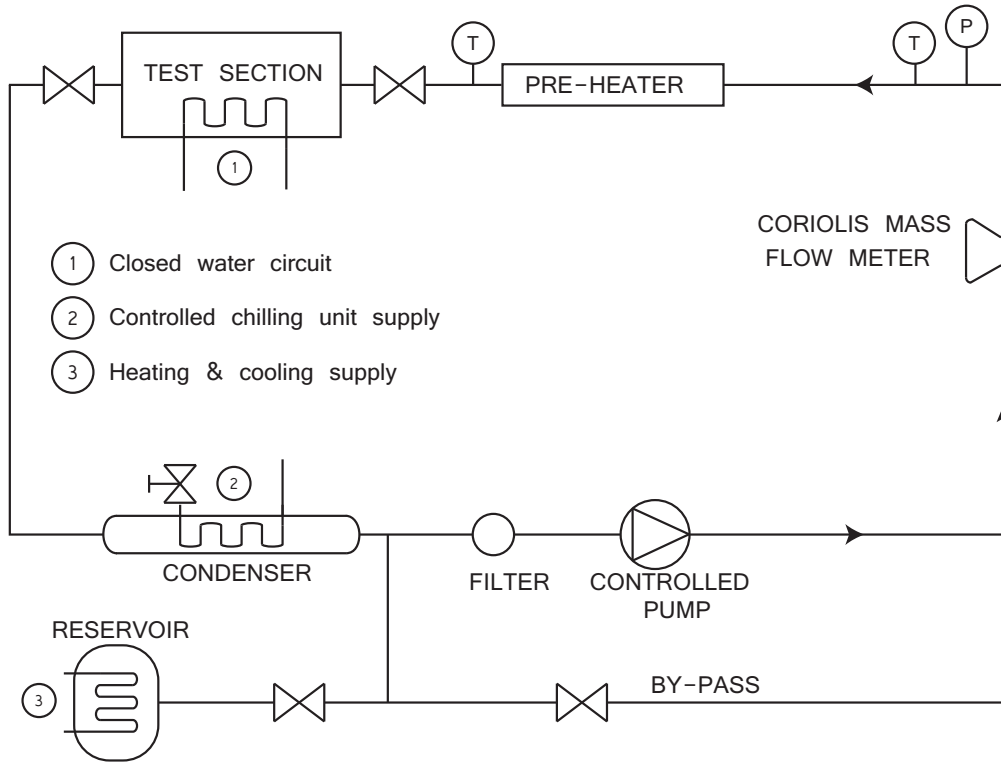
Figure 3.1: Schematic of the refrigerant cycle with all major components

The test section was housed in a reinforced stainless steel box 107 mm wide, 268 mm high and 1 067 mm long. The stainless steel walls of the box had a thickness of 20 mm and was suitable for testing up to 25 bar. The refrigerant entered at the bottom of the test section, being distributed by a perforated tube and a flat perforated distribution plate. Within the test section was a bundle of 20 copper tubes over which the refrigerant flow evaporated. The tube sheet was fixed and the bundle was eight rows high in a staggered, equilateral triangle layout with a pitch of 22.22 mm. The tube length over which the heat transfer occurred measured 1 027 mm. Two types of tube were tested in this study and their respective dimensions are given in Table 6.10.
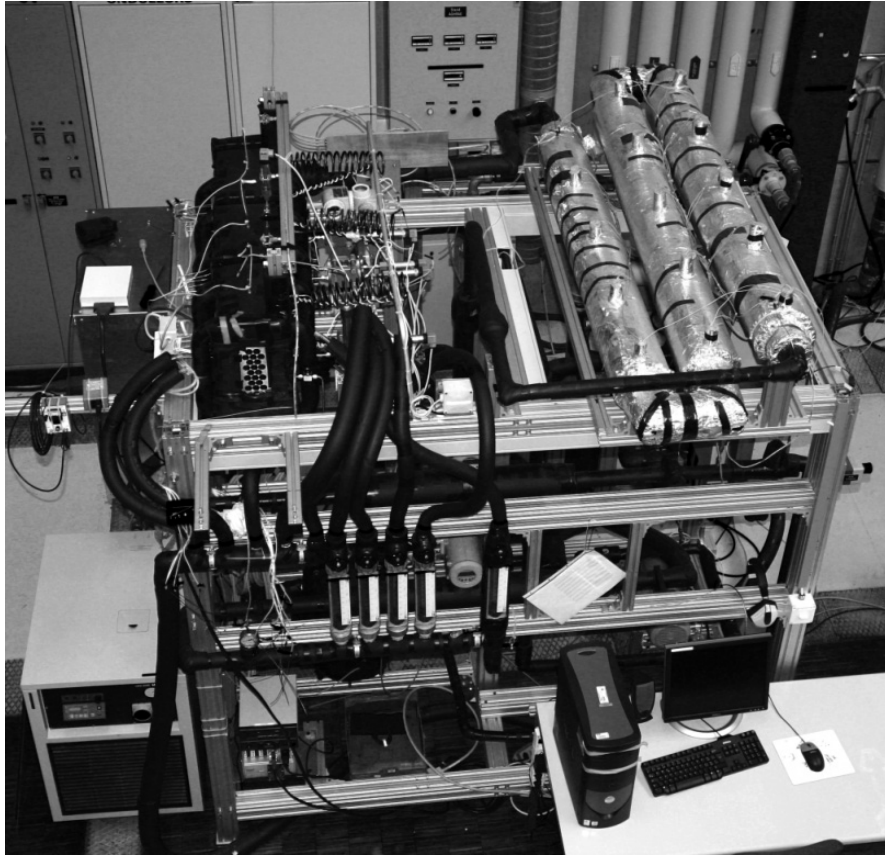
Figure 3.2: Bundle boiling test stand viewed from above

3.2.2 Water cycle

The water circuit (Figure 3.3) supplied the heat for evaporation. The water passed through the test section where it was cooled by the evaporation on the outside of the tubes. Thereafter the water passed through a series of heat exchangers to reheat it. The heat source was a gas boiler with reservoir supplying heat to the test facility. The inlet temperature was computer controlled by setting the flow rate of the heating fluid through the heat exchangers. The mass flow rate of the water through the test section was also computer controlled by setting the appropriate Reynolds number. The computer controlled flow rate and temperature was a part of the new features added to the facility for the present project. The water circuits in the test section were well instrumented to measure the temperature profile.

The tube bundle was subdivided into four groups of five tubes (Figure 3.4), with three tubes

41
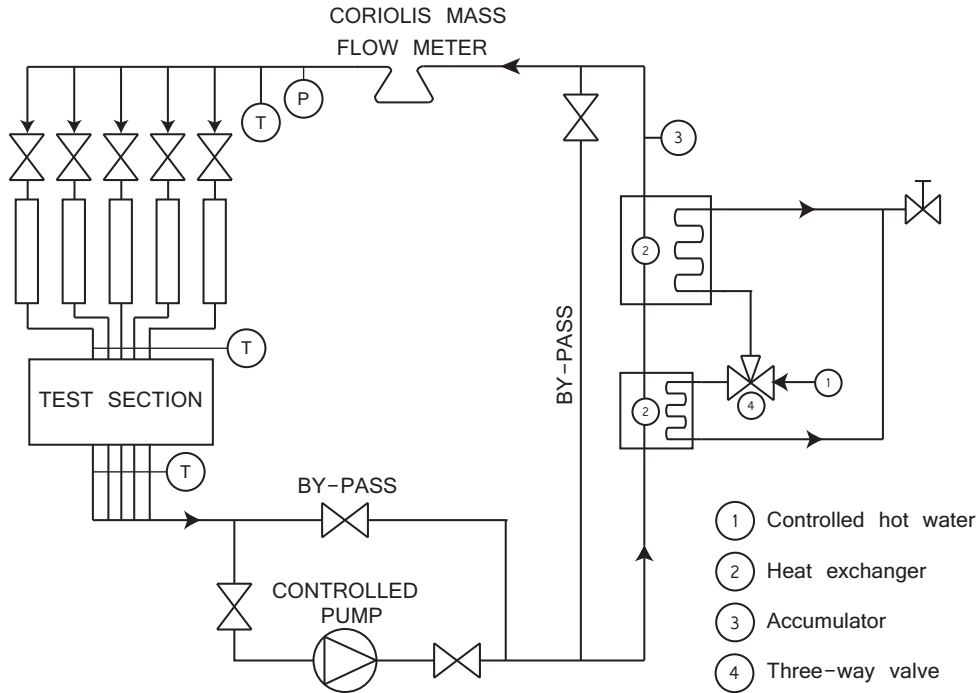
Figure 3.3: Schematic diagram of the water circuit with pump, heat exchangers, flow meters and test section

on the bottom and two tubes on top, per group. Each group of five tubes represented one pass of the water flow along the length of the test section. In the present configuration the two bottom groups were connected to the water circuit producing a two pass water circuit consisting of five tubes in each direction. The water flow was from the bottom group (inlet pass) to the second group (outlet pass) of the test section. The two top groups were not connected to the water circuit. The top and bottom sections created two zones that will be referred to as the diabatic and adiabatic zones, respectively. During adiabatic testing the entire bundle is adiabatic but the bottom section is still referred to as the diabatic section.

Within the two tube passes, there were stainless steel rods of 8 mm diameter centered in each tube. A rectangular copper element was wrapped along the length of the rod in the annulus. The rod increased the heat source water velocity and therefore also the water side heat transfer coefficient. The spiral wrap on the outside of the rod mixed the water to aid in maintaining a uniform water temperature distribution.

To enable measurement of local heat flux in the diabatic section the central tube column
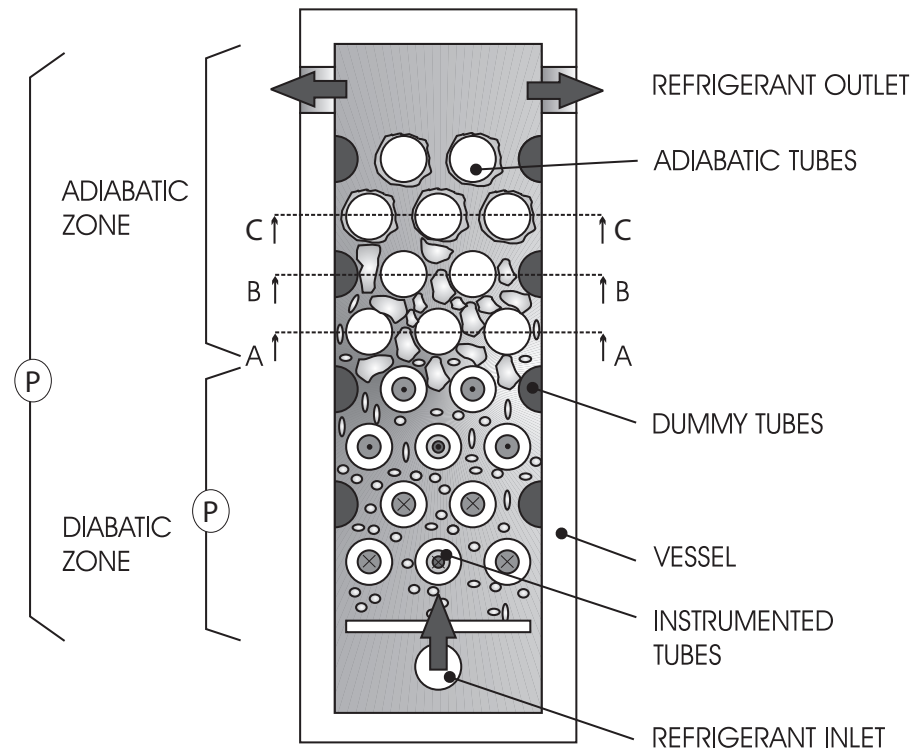
Figure 3.4: Cross-section layout indicating the components of the test section (not to scale)
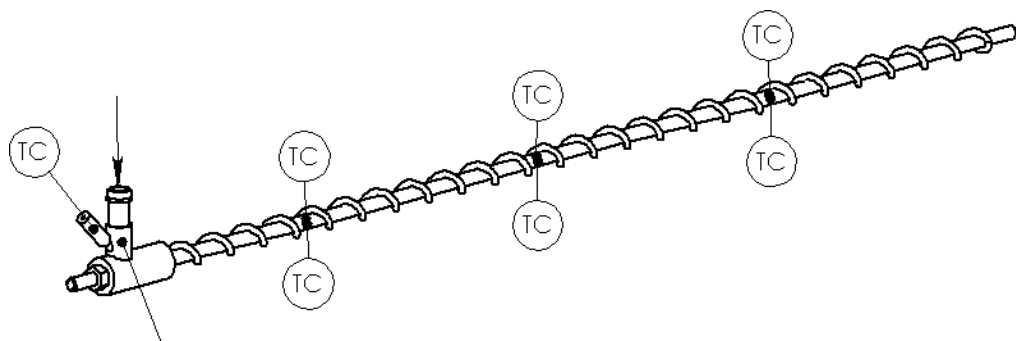
Figure 3.5: Rod insert with helical wire and thermocouples (TC) that create the annulus inside the enhanced tube for the single phase heated water flow

was instrumented with thermocouples along its length to provide local measurements of the water temperature at three locations per pass, totalling six locations with two thermocouples per location (Figure 3.5). One thermocouple faced upward and the other downward. In addition to the thermocouples in the tube, each pass was equipped with an inlet and outlet thermocouple.

3.2.3   Fluid properties

The refrigerants used for testing were R134a and R236fa (Table 3.1). R134a is widely used as a refrigerant in refrigeration systems, heat pumps, air-conditioners, etc. and has been tested extensively (although not with the present enhanced tubes). The chemical formula for R134a is 1,1,1,2-tetrafluoroethane: CH_2FCF_3. R134a was designated as a long term alternative for the CFCs, R12 and R22. R134a has an Ozone Depletion Potential (ODP) of 0 and a Global Warming Potential (GWP) of 1300 (U.S. Environmental Protection Agency, 2010). Notably, R134a is being phased out of automobile cooling systems.

R236fa is commonly used in fire-extinguishers and it is the retrofit for R114 in low pressure centrifugal chillers. Its has a distinctly different set of properties to R134a (Table 3.1) and for this reason it was chosen as the second refrigerant in the study. The chemical formula for R236fa is 1,1,1,3,3,3-hexafluoropropane: $C_3H_2F_6$. R236fa is non-flammable and non-toxic but it has an OPD of 0.05 and a modest GWP of 1700 (U.S. Environmental Protection Agency, 2010).

The liquid viscosity of the fluids vary significantly (50%) and the other fluid properties that might effect enhanced boiling such as surface tension, latent heat of vaporisation and liquid thermal conductivity vary by 10-20%.

Table 3.1: Properties of R134a and R236fa and their relative variation at $T_{sat}=5^oC$

Property	Unit	R134a	R236fa	Relative to R134a [%]
ρ_l	[kg/m^3]	1278.1	1424.6	+11.5
ρ_v	[kg/m^3]	17.131	9.155	-46.6
c_p	[kJ/kg.K]	1.3552	1.2182	-10.1
h_{lv}	[kJ/kg]	194.74	156.99	-19.4
k_l	[mW/m.K]	89.81	79.31	-11.7
μ_l	[μPa·s]	250.11	370.03	+47.9
σ	[mN/m]	10.844	12.415	+14.5
M	[kg/kmol]	102.03	152.04	+49.0
p	[kPa]	349.66	131.64	-62.4
p_{cr}	[kPa]	4060	3196	-21.3

REFPROP 8.0 (NIST, 2007) was used for the refrigerant and water properties. The saturation properties were based on temperature measurements and controls were done against the saturation pressure.

3.3   Data acquisition

All measurements were recorded with a computer equipped with a *National Instruments* data acquisition system. The system was split into two subsystems. Two acquisition cards were installed in the computer, one for high frequency signal measurements (photo-diode and piezo-pressure transducer) and the other one for low frequency response instrumentation such as thermocouples and pressure transducers.

For the low frequency instrumentation, a PCI-6259 acquisition card was used. This card provided 32 differential channels with analogue to digital resolution of 16 bits and a sampling rate of 1 MS/s (Mega samples/second)(Multichannel). A SCXI-1000 chassis with four slots was connected to this card. Each of the four slots had a 32 channel voltage measurement module (SCXI-1102) for a total of 128 acquisition channels. Each channel of this system had a computer programmable gain: 1 for 0 to 10 V signal (pressure transducer and mass flow meter) and 100 for low voltage signals (thermocouples). A 2 Hz low pass filter was automatically applied by the hardware to each channel. Each of the SCXI-1102 modules was connected to a 32 channel isothermal terminal block (TC-2095). The cold junction for every thermocouple was made in this terminal block at the socket. The material of this socket was copper for both poles so that the continuity of the two different specific materials of the thermocouple was broken at this point inside the terminal block. The temperature of the 32 cold junctions was maintained uniform with a metallic plate and was measured by the system via a Resistance Temperature Detector (RTD) installed in the middle of the plate. Additionally, all the terminal blocks were placed in a closed cabinet away from external thermal influences. In order to measure a test parameter of a channel, 100 acquisitions were made in 0.1 s and the mean of these 100 values was calculated during the acquisition. The result was presented as the measured value of this channel. To obtain one steady state data point, 50 measurements were recorded for each channel and averaged.

For the high frequency measurements, a PCI-6143 acquisition card was installed. This card provided eight differential channels with an analogue to digital resolution of 16 bits, a sampling rate of 250 kS/s per channel and an input range of ± 5 V. A shielded I/O connector block (SCB-68) was connected directly to the PCI-6143. The SCB-68 allowed different configurations of connections according to the signal source type. The PCI-6143 was triggered by a digital signal from the high speed camera and this initiated the recording at the set rate and for the set number of samples. The digital trigger was used to synchronize the capture of data by the piezo and laser systems with the video recording for later inspection.

3.3.1   High frequency instrumentation connection

A connection diagram for the SCB-68 is provided in Figure 3.6. The signal from the piezo-electric pressure transducer was a ground referenced signal. It was connected to the building system ground and was therefore already connected to a common ground point with respect to the PCI card. The piezo-electric pressure transducer PCB-ICP-M105C02 was connected to the SCB-68 through a signal conditioner PCB-480E09 with gain settings of 1, 10 and 100. The frequency range was $15 \times 10^{-5} - 100$ kHz in the case of gains of 1 or 10 and $15 \times 10^{-5} - 50$ kHz if the gain was 100. Each channel of the piezo-electric system was powered by a direct current power supply PCB-488E09.

The negative signal from the photo-diode (S-25VL) was connected directly from the negative signal input to the analog input ground which itself was connected to the ground of the data acquisition card. If a return path was not provided the instrumentation amplifier bias current stored up stray capacitances, resulting in uncontrollable drift and possible saturation of the amplifier. An AD620 instrumentation amplifier was used to amplify (gain ≈ 6) the photo-diode signal for the Data Acquisition system (DAQ). The differential output signal of the AD620 was connected to the positive input of the DAQ and its reference signal, or return path, was tied to the reference of the instrumentation amplifier.
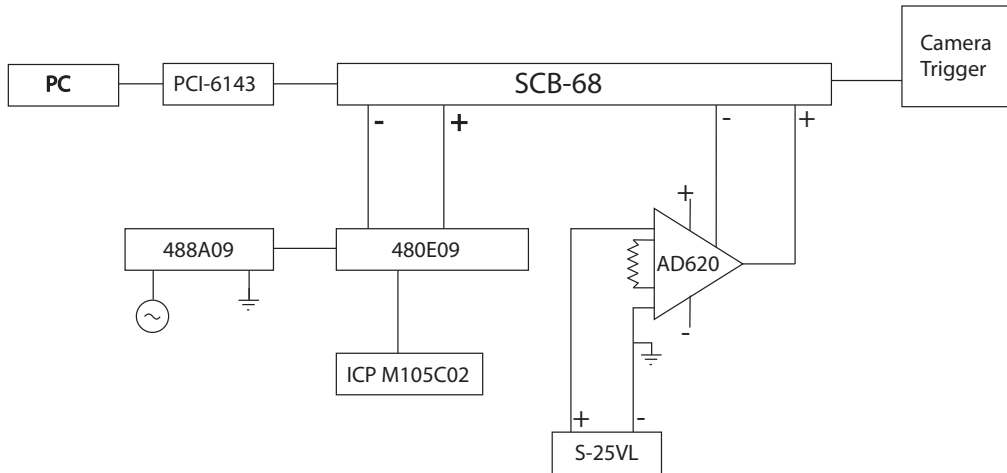
Figure 3.6: PCI-6143 configuration with an example of piezo and photo-diode wiring

3.4 Test section and instrumentation

The lower four rows were kept as the diabatic part of the test section. The improved flow pattern instrumentation was installed in the adiabatic upper four rows of the test section.

In the diabatic zone of the test section thermocouples and pressure transducers (absolute and differential) were responsible for the main measurements. Mass flow rate was measured in the single phase, liquid flow region. In the adiabatic zone of the test section flow pattern measurements were installed, indicated in Figure 3.4 as sections A-A, B-B and C-C. The flow pattern measurement instrumentation that were linked together by synchronization signal were placed in close proximity to each other (Figure 3.7) in an attempt to characterise the flow development.
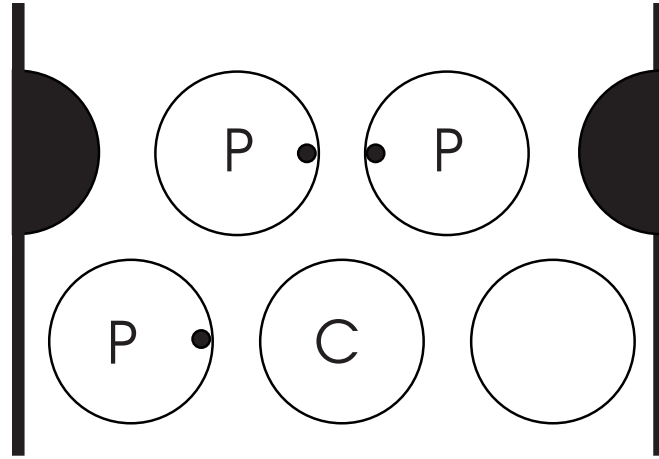
Figure 3.7: The flow measurements taken at four locations at the entry to the adiabatic zone (P: piezo-electric pressure transducer C: camera/borescope)

3.4.1 Fundamental measurements: Temperature, pressure and mass flow

Thermocouples   Type K thermocouples (NiCr/NiMnAl) were used to measure the temperature. They were calibrated in a thermal bath with RTDs as reference. Saturated test conditions were used to monitor the calibration. The saturation pressure and temperature were always within 0.1^{o}C of the measured temperature when compared in the temperature scale.

Pressure transducers   Keller absolute pressure transducers were employed for monitoring the operating conditions. The operating ranges were from $0-10$ bar and $0-40$ bar, with accuracies of

$\pm 0.4\,\%$ of full scale (FS) and $\pm 0.1\,\%$ FS respectively, provided by the supplier. These transducers were calibrated in the laboratory with a hydraulic dead weight balance. The deviation was always smaller than the one specified by the manufacturer.

Endress and Hauser differential pressure transducers with working ranges of ± 30 mbar and ± 40 mbar were installed for pressure drop measurements. The accuracy of the two models used were $\pm 0.075\,\%$ FS and $\pm 0.1\,\%$ FS, respectively. The instruments were calibrated in the laboratory with an alcohol column manometer. The ± 30 mbar pressure transducer was added for this study and measured the pressure from the bottom of the bundle, at the same inlet height as all the other pressure transducers, and the fourth row of tubes at a height of 79 mm above the inlet point.

Flow meter Two Coriolis mass flow meters (one for the refrigerant and the other for the heating water) were installed on the bundle boiling test facility with a range of $0-1.67$ kg/s. The uncertainty in the measurement was provided by the manufacturer using the equation: $\delta\dot{m}/\dot{m} \leq \pm(0.15 + S/\dot{m})\,\%$, where $S = 8.3\,10^{-3}$ kg/s was a constant depending on the mass flow meter.

3.4.2 Piezo-electric pressure transducer

Figures 3.8a and 3.8b are schematic representations of section A-A and B-B (Figure 3.4). A detailed layout of section A-A is presented in Figure 3.9.

The tube to the right in Figure 3.8a was instrumented with a piezo-electric pressure transducer. These components were installed at the same axial position as the laser system and high-speed camera. The instrumentation in section B-B consisted of two piezo-electric pressure transducers facing each other (Figure 3.8b).

The sensing element was made of quartz, housed in a stainless steel casing and functioned in compression. The sensitive area measured 4.95 mm^2, with a diameter of 2.51 mm. The measurement range for an output voltage of ± 5 V was 690 kPa. The sensitivity $(-40/+20\%)$ was 7.3 mV/kPa. The sensor could resist pressures up to 1720 kPa with a resolution of 0.035 kPa and a resonance frequency of ≥ 250 kHz. The accuracy was $\leq 1\,\%$ FS.

3.4.3 Laser two-phase detection

In section C-C, two tubes were used to house the laser system that constitutes the laser-light signal two-phase detector (Figure 3.10). The system was similar to that employed by Revellin *et al.* (2006). A more detailed layout of the laser system in section C-C is presented in Figure 3.11.
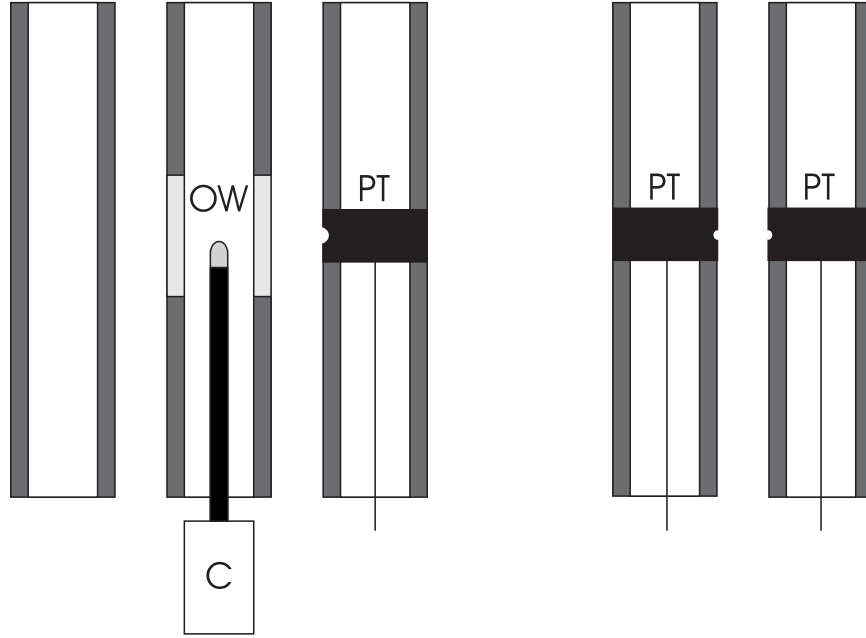
(a) Section A-A (OW: optical window, PT: piezo-electric pressure transducer, C: camera)

(b) Section B-B (PT: piezo-electric pressure transducer)

Figure 3.8: Schematics of instrumentation in section A-A and B-B

The laser was mounted in the tube on the right-hand side. The laser beam was aligned along the tube axis to reach a right angle prism at the midplane. The beam was then reflected by 90°, passing through the optical window and exiting the tube where it encountered the two-phase flow. The beam then passed through the optical window of the second tube and on to a miniature photo-diode. The photo-diode converted the intensity of incident light into voltage, and a wiring system brought the electrical signal outside the test section to the data acquisition system.

3.4.3.1 Laser side

A laser-diode with a wavelength of $\lambda = 635$ nm and a power output of 1 mW was installed. It generated a circular beam profile with a diameter of 3 mm. The laser was driven by a DC power supply of 6.5 V and 0.11 A. The prism was made of BK7 fused silica glass. Its size was 5.0 x 5.0 x 5.0 ± 0.2 mm. It was characterised by a surface quality of $40 - 20$ scratch & dig, a surface flatness of $\lambda/4$ at 633 nm and an angle tolerance of $\pm 5\,arcmin$. The two catheti were uncoated and the hypotenuse was coated with aluminium.
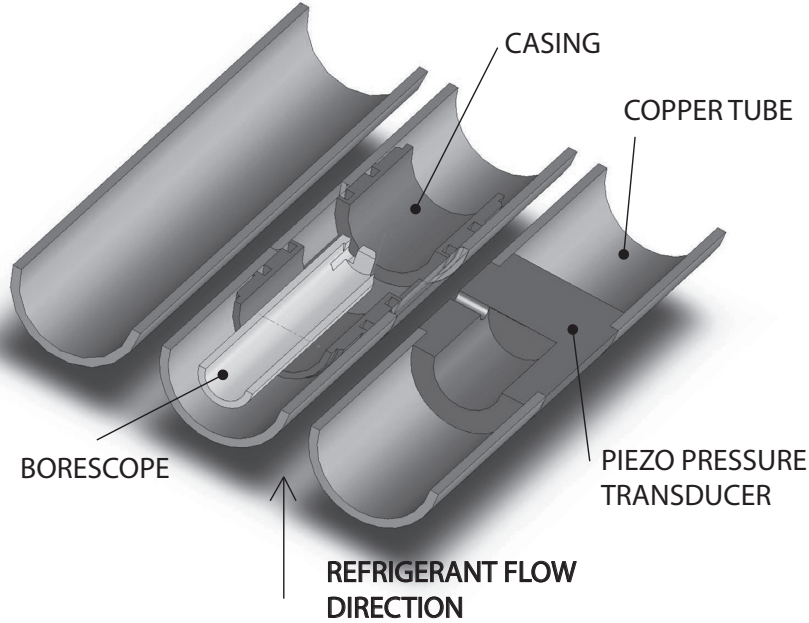
Figure 3.9: Layout of section A-A with camera system and piezo-electric pressure transducer layout

3.4.3.2 Photo-diode side

The photo-diode was sensitive to a spectral range of $\lambda = 350-1100$ nm with a maximum sensitivity at $\tilde{\lambda} = 920$ nm. The S-25VL chip series photo-diode was used. The square radiant sensitive area measures 25 mm^2. The photo-diode used in this study was much larger than the 7.35 mm^2 model used in the previous study (Agostini, 2008) to avoid the laser light beam being deflected off the photosensitive area by the flow, thereby giving a square wave characteristic to the signal.

3.4.4 High-speed camera

The high-speed camera used in this study was a Photron Ultima APX. The camera was capable of frame rates up to 120 000 fps, it had a 10-bit 1024 x 1024 pixel CMOS sensor with 17 μm pixels and adjustable shutter speeds of 16.7 ms to 4 μs. An optical element, with f = 35 mm, was used to connect the borescope to the C-mount on the camera. The resolution of the images was 512 x 512 pixels. The length of video sequences, frame rate and exposure time were set according to requirements with a maximum frame rate of 2000 fps and an exposure time of 1/4 000th of a
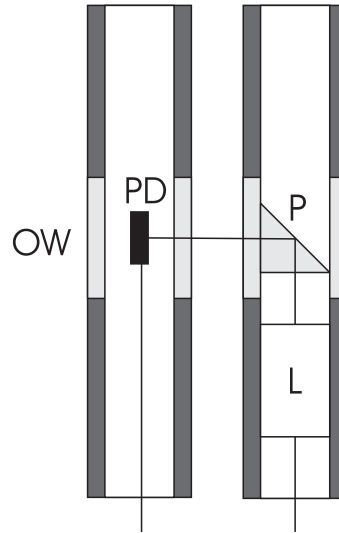
Figure 3.10: Laser system layout in section C-C (OW: optical window, PH: photo-diode, P: prism, L: laser source)

(a) Rear view of the photo-diode fitting
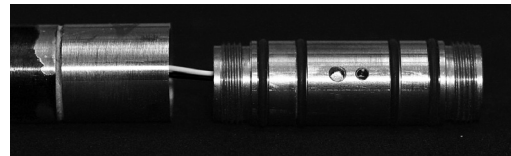
(b) Front view of the photo-diode fitting
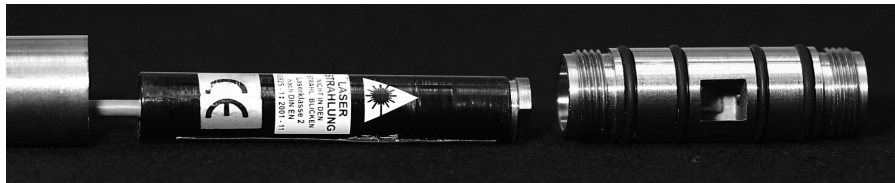
(c) Laser-prism assembly

Figure 3.11: Components making up the laser light attenuation measurement system

second. The video controller was used to send a synchronization signal that triggered the video and high-speed data recording at exactly the same time. The synchronisation was tested up to 30 000 fps.

3.4.5   Visualisation system: light source and optics

The center tube was designed with an optical window to allow access for the borescope with a 360° view around the perimeter. The 440 mm long borescope was connected to the high-speed camera outside the test bundle. The video recordings were made with the camera facing the pressure tap of the piezo-electric transducer in the adjacent tube and the refrigerant flowing in between. Precisely synchronised sequences of video and piezo-electric data were recorded.

EFER endoscopy designed and manufactured the light source and borescope. The light source was a 20 V, 300 W Zenon bulb which focused the light into the connection port of the fibre optical link. The light from the source was guided internally by optical fibres to the tip of the borescope without any connections to minimise losses. The flexible light guide fibre optic cable was 2000 mm long and 7 mm in diameter. The viewing angle of the borescope lens was set to 70° to avoid direct reflections associated with a 90° viewing angle. The field of view was 90° from the lens allowing an image of approximately 24 mm horizontally.

An optical window was used for the borescope and laser two-phase flow detector. The optical window was made from a borosilicate glass tube (glass type 3.3) with an outer diameter $D_o = 19 \pm 0.20\, mm$ and wall thickness of 1.2 ± 0.05 mm. The transmissivity at a wave length of $\lambda = 635$ nm was $> 92\%$.

3.5   Summary of modifications

The improvements and changes made to the test facility during this study include:

- Making the refrigerant flow rate computer controlled.

- Removing the on-off control of the pre-heater elements and installing a rheostat over all elements for steady operation to avoid step inputs.

- The water pump control was connected to the computer control system.

- Manual water inlet temperature control was replaced with a redesigned system of heat exchangers and a computer controlled valve to maintain constant inlet temperature.

- A borescope with built-in light source was specified for the new visualisation system to sacrifice only a single tube and allow diabatic observations.

- Additional piezo-electric pressure transducers were mounted to allow characterisation of flow development in the bundle.
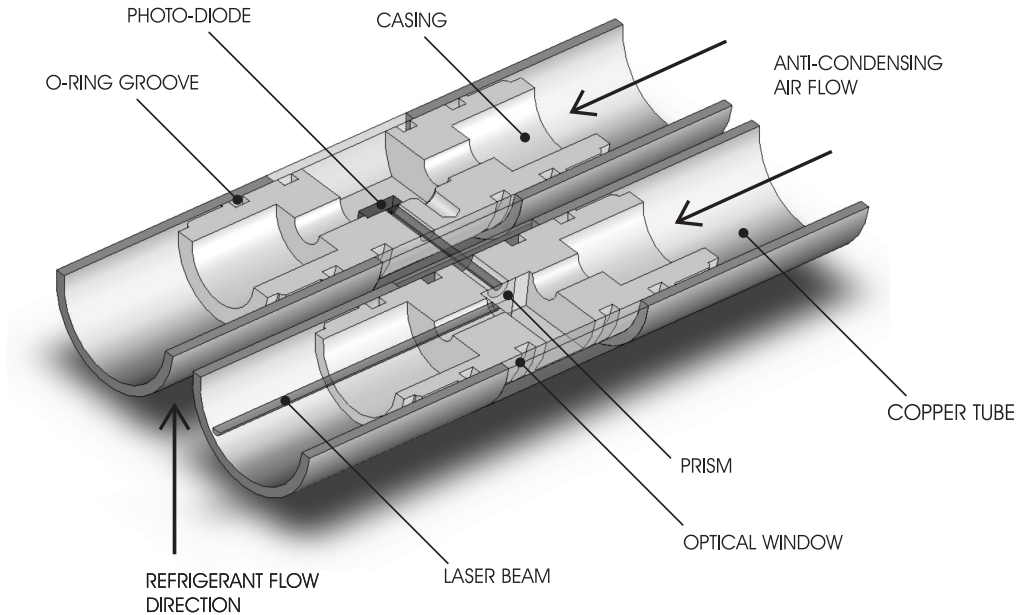
Figure 3.12: Section C-C, laser system layout indicating two tubes housing the laser and photo-diode

- Using the hardware to synchronise the video capture with all other flow pattern related measurements.

- The laser two-phase detector was modified by enlarging the photo-diode and introducing signal amplification to improve the signal detail.

- A differential pressure transducer was added to measure the pressure drop over the diabatic section of the bundle.

3.6 Control methodology and experimental procedure

The objective of the experimental phase of this study was to obtain a complete database for adiabatic and evaporating flows in tube bundles in as wide a variety of conditions as possible with the test facility. A wide range of experimental conditions were investigated with two enhanced tubes and two refrigerants at two saturation temperatures. Accurate measurements were made of the two-phase pressure drop, local heat transfer coefficients, video-recordings of the two-phase flow, and high frequency laser and pressure signals. These measurements were then used to investigate and characterise the two-phase flow.

There were a multitude of factors and settings which could be changed in the system which would affect the working pressure, mass flux and test inlet quality. These were the three main areas that must be controlled in this setup to successfully carry out valid and meaningful experiments. However, altering any one factor could have an effect on more than one of the critical parameters. The methodology for experimentation is stated in the following sections. Due to the complex relationship between the multiple parameters that affect the main test criteria, automating the system would not be a trivial procedure and hence this was not done.

Great care was taken to avoid and check for the presence of non-condensables in the refrigerant cycle. To ensure that there were no leaks, the system was pressurised with nitrogen and controlled for at least 24 hours. If no drop in pressure occurred, the system was accepted as leak-tight. The system was then evacuated (with the use of a vacuum pump) until the internal pressure was not much higher than absolute zero pressure ($<$ 4 mbar). Two 200 mbar pressure transducers were used to monitor the vacuum. The vacuum pump was run for a total of 24 hours whilst controlling the pressure to ensure a clean cycle. At this stage refrigerant charging commenced.

3.6.1 Wilson plot

Experimentally, the procedure for the Wilson plot tests on a single tube was as follows:

1. The tube to be tested was connected to the water loop in a two-pass configuration. The first pass and bottom tube was the only one used for measurements. The top two tubes in the array were connected in a two-pass configuration to the laboratory's cold group, which supplied a mixture of water-glycol at a minimum temperature of -20°C. Condensation took place on these two tubes to compensate for the evaporation on the tube being tested. All the other tubes were removed.

2. The outlets of the test section were closed to create an isolated chamber, and the test section was filled with liquid refrigerant. The liquid level was adjusted to submerge the lowest two boiling tubes.

3. The temperature and flow rate of the water were adjusted to reach the desired heat flux, while the temperature and flow rate of the water-glycol were changed to reach the desired saturation temperature. Once the system stabilized, data acquisition could begin.

4. The water mass flow rate and inlet temperature were adjusted such that the water-side Reynolds number changed, but the heat flux remained constant. This normally also entailed

slight modifications to the water-glycol mass flow rate. This procedure was repeated for different heat fluxes.

3.6.2 Pool boiling

During pool boiling experiments the heating water temperature and Reynolds number were computer controlled. The water-glycol circuit flow rate was also controlled to condense the evaporated fluid and to achieve a steady energy balance. For pool boiling the heat flux was varied within the achievable range to produce a boiling curve. Limitations in pool boiling were determined by the cooling power of the condensing tubes or the measurement accuracy at low heat fluxes.

3.6.3 Convective bundle boiling

During convective bundle boiling the mass flux of the refrigerant was computer controlled. The heating water temperature and Reynolds number were also computer controlled to set the required heat flux. The required power input needed from the pre-heater was calculated based on the selected inlet vapour quality and subcooling at the pump. This was set manually with a rheostat. The saturation pressure was generally set by heating or cooling the reservoir and thereby charging or discharging refrigerant into the closed cycle. The condenser could also affect the saturation pressure but was usually not used for this purpose due to the instability caused in the system. The system limitations were determined by pre-heater power, pump capacity, dryout on the tubes or dryout in the pre-heater.

3.7 Data reduction methods

3.7.1 Void fraction

Combining the continuity equations for the liquid and gas phases and accounting for the definition of cross-sectional vapour quality and slip ratio, $(S = u_g/u_l)$ the void fraction ε is obtained:

$$\varepsilon = \left[1 + S\frac{\rho_g}{\rho_l}\left(\frac{1-x}{x}\right)\right]^{-1} \tag{3.1}$$

By non-dimensional analysis, Feenstra *et al.* (2000) identified four dimensionless groups governing the velocity ratio. Equation 3.2 was obtained by fitting their experimental data as follows:

$$S = 1 + 25.7(Ri \cdot Cap)^{1/2}\left(\frac{D}{P}\right) \tag{3.2}$$

The basic length scale a is assumed to be the narrowest gap between two tubes and the pitch velocity u_g is evaluated with the flow area in the gap and it follows that:

$$Ri = \frac{(\rho_l - \rho_g)^2 g \, a}{G^2} \quad and \quad Cap = \frac{\mu_l u_g}{\sigma} \quad with \quad u_g = \frac{xG}{\varepsilon \rho_g} \tag{3.3}$$

where the Richardson number, Ri is a ratio between buoyancy force and inertial force and the capillary number, Cap is a ratio between the viscous force and the surface tension force.

An iterative procedure is needed for the computation: a guessed value of the vapour velocity, u_g, is imposed and then the parameters defined through equation 3.2 and 3.3 are evaluated to solve the slip ratio. The void fraction ε is solved by equation 3.1. Then a new value of the u_g is computed using the updated ε and:

$$\rho_{2\phi} = \rho_f(1 - \varepsilon) + \rho_g \varepsilon \quad and \quad \mu_{2\phi} = \mu_f(1 - \varepsilon) + \mu_g \varepsilon \tag{3.4}$$

3.7.2 Pressure drop

The two-phase flow pressure drop is comprised of three different components: static (gravitational), momentum (or dynamic) and frictional. For an evaporating, vertical flow at low mass velocities the static component is generally dominant. The momentum component accounts for the change of momentum experienced by the flow during phase change. The static and momentum components require a void fraction model to be accurately calculated. The pressure drop is formulated as:

$$\Delta p_t = \Delta p_s + \Delta p_m + \Delta p_f \tag{3.5}$$

For a discretised domain, where z is the coordinate in the vertical direction, the gravitational (equation 3.6) and momentum (equation 3.7) components can be backed out from the measured test conditions and from the evaluation of the void fraction. The computation of the void fraction makes use of the computed values of the vapour quality in the tube bundle. This is possible through thermal balances over a vertical discretisation of the geometry of the tube bundle. The discretisation of the tube bundle for the thermal balance and thus for the vapour quality and void fraction is depicted in Figure 3.13 where thermal balances are based on the control volumes indicated as $A1$ to $A7$ and identified with the coordinate z from i_0 to i_7:
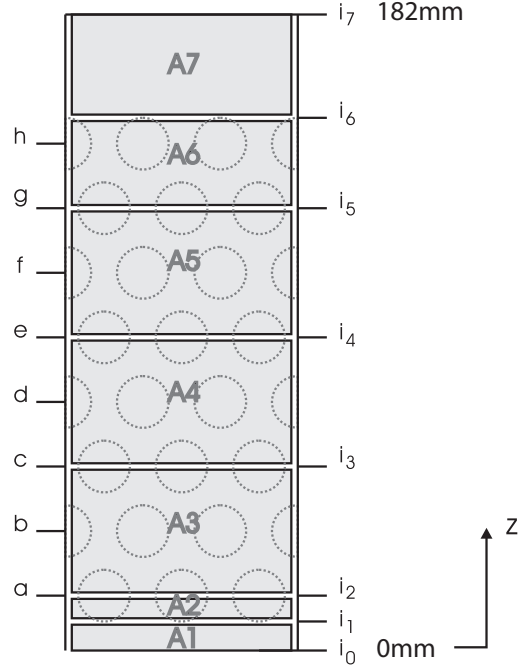
Figure 3.13: Void fraction, vapour quality and pressure drop discretisation schemes

$$\Delta p_s = \sum_i \left[\rho_l \left(1 - \frac{\varepsilon_{i+1} + \varepsilon_i}{2} \right) + \rho_g \left(\frac{\varepsilon_{i+1} + \varepsilon_i}{2} \right) \right] g \Delta z_i \qquad (3.6)$$

$$\Delta p_m = G^2 \left\{ \left[\frac{(1-x)^2}{\rho_l(1-\varepsilon)} + \frac{x^2}{\rho_g \varepsilon} \right]_{i+1} - \left[\frac{(1-x)^2}{\rho_l(1-\varepsilon)} + \frac{x^2}{\rho_g \varepsilon} \right]_i \right\} \qquad (3.7)$$

These equations are valid for a constant area flow with all the fluid entering and leaving in the same direction. The void fraction model is normally subject to the same conditions.

Once all the necessary quantities have been calculated to determine the gravitational and momentum components, the frictional component is backed out from the measured total pressure drop. The differential pressure drop is measured by three transducers with pressure taps running into the side of the bundle and the mean value is used.

3.7.3 Heat transfer

A hot water circuit is used to supply the heating for evaporation. An enthalpy profile method is applied to obtain a local heat flux. This is achieved by instrumenting the water circuit on the inside of the evaporating tubes with pairs of thermocouples in the water annulus at fixed locations coming through the inside of a small diameter stainless steel tube centered within the evaporating

3. EXPERIMENTAL SET-UP AND METHODS

tube (Figure 3.5). A second order fit is made of the temperature profile, $T_{water} = f(S)$, where S is the curvilinear coordinate through the water circuit from which the local heat flux is computed and employed to evaluate the local heat transfer coefficient on the outside of the tube.

According to the first law of thermodynamics for a constant pressure process:

$$\delta Q = \dot{m} c_{p,water} \delta T_{water} \tag{3.8}$$

Considering that

$$dA_o = \pi D_o dS \tag{3.9}$$

the local heat flux is obtained by:

$$q_o = \frac{\delta Q}{\delta A_o} = \frac{\dot{m} c_{p,water}}{\pi D_o} \frac{dT_{water}}{dS} \tag{3.10}$$

The axial conduction along the tube is considered negligible. With the known temperature profile, T_{water}, the heat flux at any position S and the outside temperature, T_{sat}, the local external heat transfer coefficient can be expressed as:

$$h_o = \frac{q_o}{T_{wall,o} - T_{sat}} \tag{3.11}$$

The inside water temperature is measured and not the wall temperature. Therefore the heat transfer coefficients are analysed through a thermal resistance model. The overall resistance is the sum of the external, wall, and internal resistances. In a flooded evaporator, the external convective resistance refers to the evaporating fluid, the internal convective resistance to the fluid (water in the present case) that supplies the heat necessary for the phase change, and the wall resistance is that of the physical metallic tube wall conduction.

Using the outside area over the enhancement D_o as reference:

$$\frac{T_{water} - T_{sat}}{q_o} = \frac{1}{U_o} = \frac{1}{h_o} + \frac{1}{C_i h_{gni,i}} \frac{D_o}{D_i} + R_w \tag{3.12}$$

$$R_w = \frac{D_o}{2k_w} ln\left(\frac{D_{or}}{D_i}\right) \tag{3.13}$$

U_o represents the overall heat transfer coefficient with respect to the reference heat transfer area (A_o). To compute the external heat transfer coefficient (h_0), equation 3.12 is employed. The internal heat transfer coefficient is estimated by the Gnielinski (1976) correlation, corrected through a multiplier C_i determined using the Wilson plot method (Section 6.1).

A rigorous uncertainty analysis of heat transfer and pressure drop results is presented in Appendix A.

3.8   Conclusion

The methods used for experimentation and in the data reduction have been discussed here to maintain a clear and concise discussion in the results section. This chapter, together with the literature study, serves as the reference for all information used during the discussion in the following chapters.

Chapter 4

Flow pattern results

4.1 Introduction

The flow patterns in the bundle were inspected and classified in order to evaluate possible correlations with their effects on heat transfer and pressure drop. Two aspects of flow patterns were evaluated: (a) the macroscopic flow pattern of the external flow over the tubes and (b) the local effects on enhanced tube surfaces related to bubble dynamics. The flow pattern discussion begins with the macroscopic intertube flow pattern video observations and then elaborates on the flow patterns by referring to the data gathered by the instrumentation. The bubble dynamics is an important element of the enhanced surface flow pattern. Some basic measurements of departure diameter and frequency were made for comparison between tubes.

4.2 Flow patterns

The main hypothesis proposed in this study is that the heat transfer of enhanced tubes is unaffected by the position and flow pattern in the bundle. This hypothesis will be investigated in the current chapter and the heat transfer and pressure drop results presented hereafter.

Visual observations of the flow in the bundle were carried out with a borescope. These observations were taken from the center tube at the first adiabatic row above the diabatic section, equal to the fifth row from the bottom of the test bundle. These observations were classified according to the flow patterns previously found, resulting in three identifiable signals from the measurement equipment (Noghrehkar *et al.*, 1999): bubbly flow (Figure 4.1a), annular flow (Figure 4.1c) and intermittent flow (Figure 4.1b) that represents a combination of the first two flow patterns as a transition zone between them. Transition lines were indicated on a superficial velocity plot with
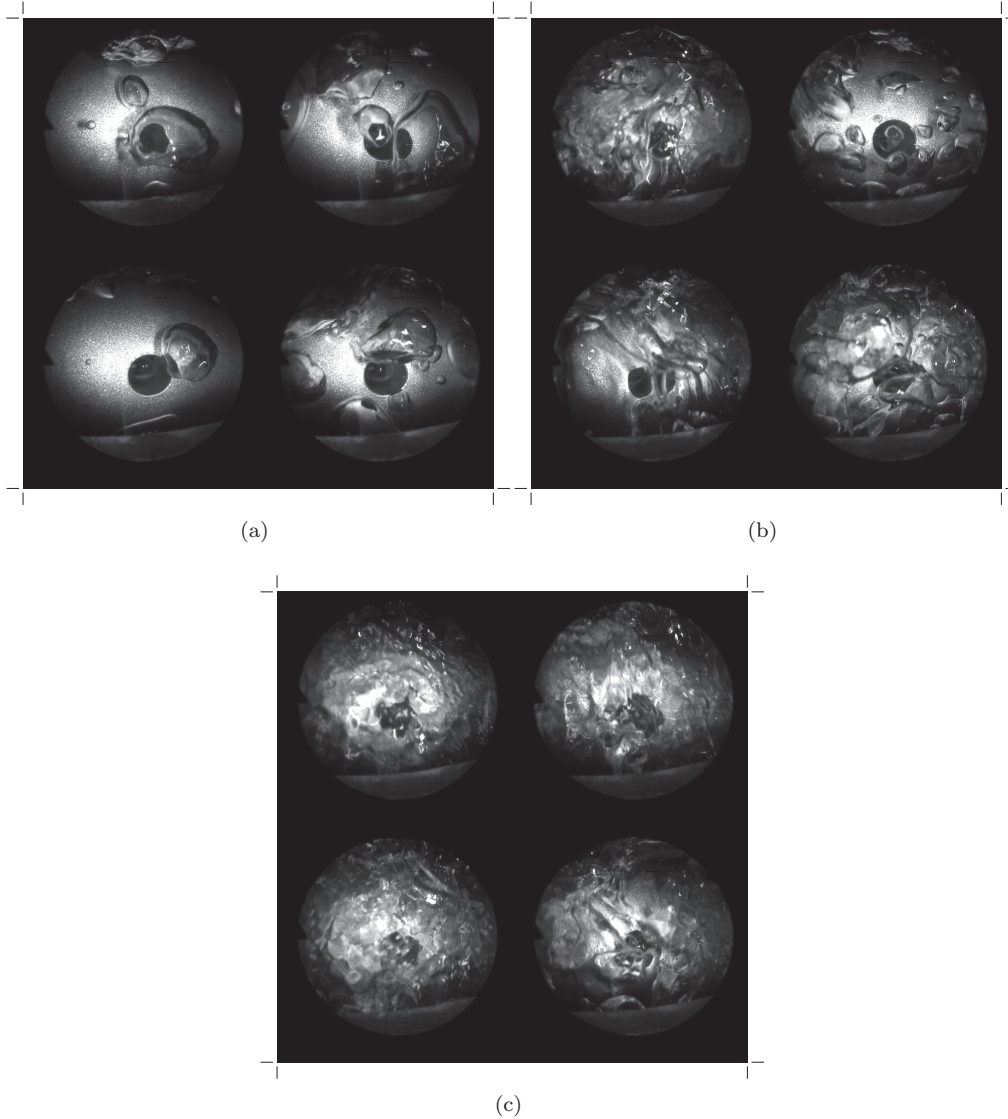
Figure 4.1: Bundle boiling in a *Turbo-B5* tube bundle at (a) bubbly, (b) intermittent and (c) annular flow pattern conditions with R134a at 5ºC observed at row 5 in the adiabatic section

previously mentioned methods (Figure 4.2). The transition lines were not a function of superficial liquid velocity, which agrees with the findings of Noghrehkar *et al.* (1999). The transitions differ significantly from the air-water results of Noghrehkar *et al.* (1999), but fall in a similar range as that of other single fluid flow tested by Aprin *et al.* (2007). The span of the intermittent flow was found to be larger for diabatic flow conditions ($j_g = 0.1$ to 0.8 m/s) than for adiabatic conditions ($j_g = 0.1$ to 0.4 m/s).
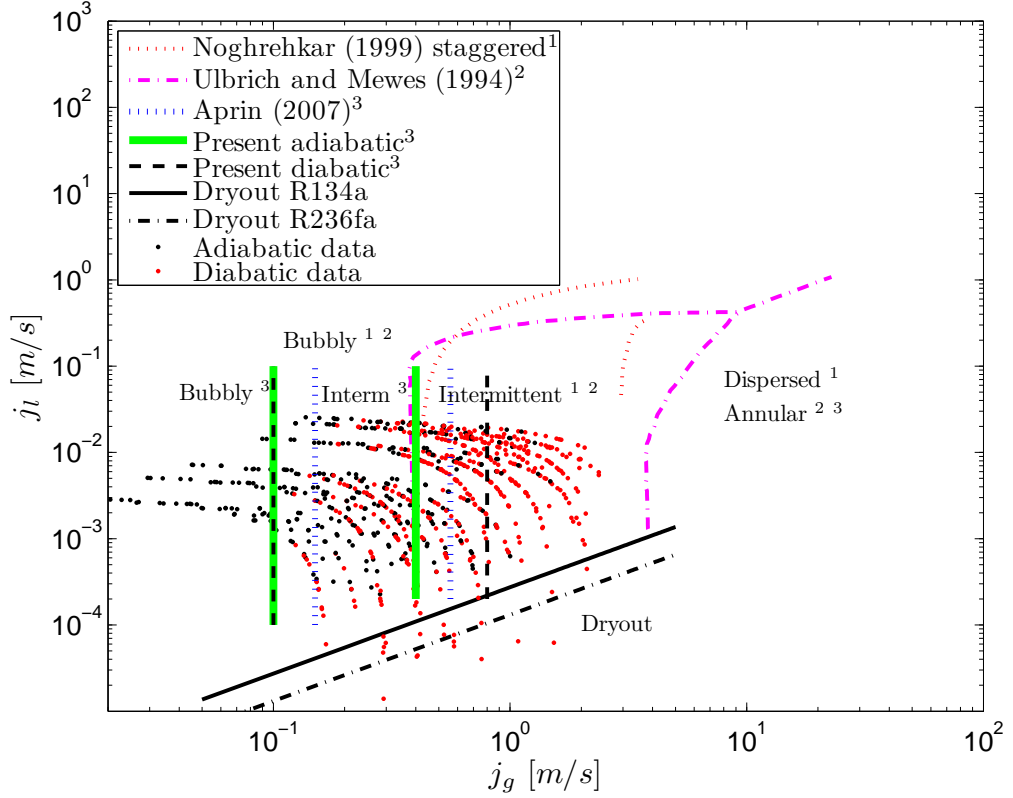
Figure 4.2: Flow pattern map for bundles indicating previous air-water transitions and single component diabatic and adiabatic transitions including the onset of dryout transition

Bubbly flow was present at the lowest vapour qualities and persisted in the bundle for longer at low mass flux. The flow development caused in the bundle by the narrow intertube gap and cyclical external flow was responsible for a change in the local flow pattern as the bubbles coalesced and interacted (Aprin *et al.*, 2007, Ulbrich and Mewes, 1994). The flow development was evident from the lack of a strong relation between the two measurement positions in the bundle (Figure 4.3). As the mass flux increased the cross-correlation changed. At low mass fluxes the two measurements had no relation to each other probably due to noisy and random bubbly flow. At higher mass fluxes there was a weak time-lagged offset, probably related to general flow pattern similarity or stronger intermittent surges observed in the videos. Therefore, the conclusions reached about the flow pattern from the observations will be a function of the position in the bundle.

The flow patterns are presented on a vapour quality and mass flux plot (Figure 4.4). The transition lines indicate the transition zone between bubbly and annular flow to be:
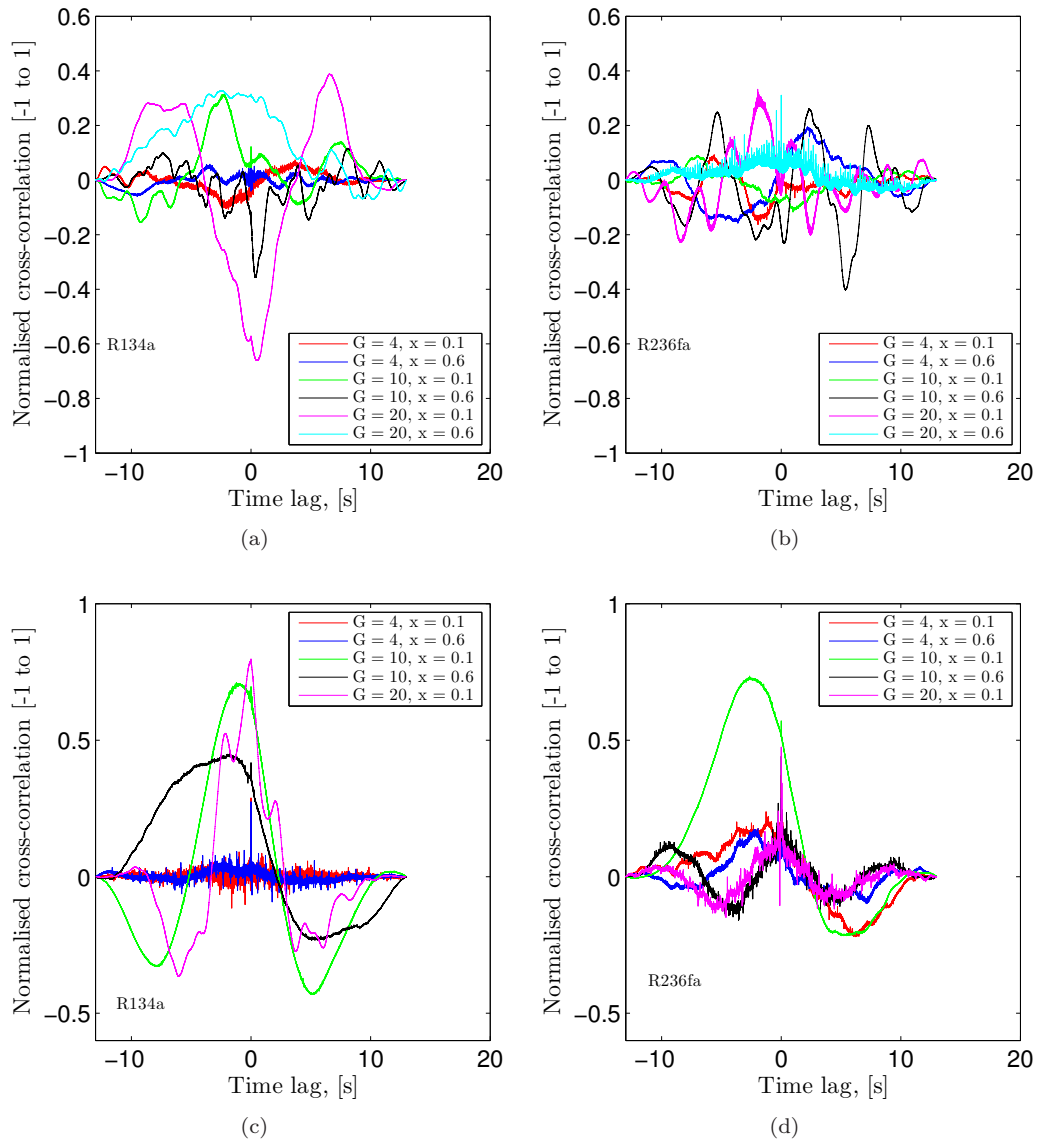
Figure 4.3: Sample cross correlation between pressure measurement points on two consecutive tube rows for representative mass fluxes at 5^oC saturation temperature
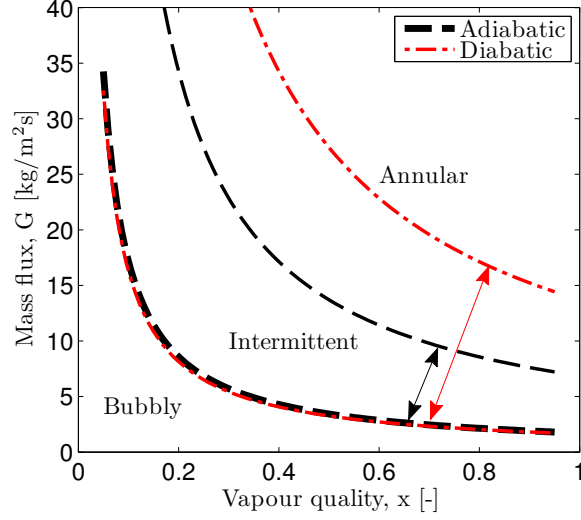
Figure 4.4: Flow pattern map for bundles with transition from bubbly to annular flow in adiabatic and diabatic conditions

$$G_{trans} = j_{g,trans} \frac{\rho_g}{x} \qquad (4.1)$$

where for adiabatic conditions, the transition zone could be given as $j_{g,trans} = 0.25 \pm 0.15$ m/s. For similar observations made during diabatic conditions, the transition zone was wider and a function of heat flux. For 20 kW/m^2 , $j_{g,trans}$ ranged from 0.1 to 0.8 m/s and for 60 kW/m^2 $j_{g,trans}$ was from 0.1 to 1 m/s. This was assumed to be the direct effect of additional vapour generation and bubble coalescence at higher heat fluxes. There are probably two bubble coalescence mechanisms: that of the narrow gap for the bubbles passing between the tubes and that of nucleation sites on the boiling tubes.

The local, external, macro-scale flow patterns had no strong impact on heat transfer (Chapter 6. This can be attributed to the mechanisms of heat transfer for enhanced tubes that were only slightly affected by the external flow (Kim *et al.*, 2002, Liu and Qiu, 2004) and were therefore likely dominated by the internal processes. The additional transition defined by the onset of dryout line was significant for tube bundles. The prediction method for the onset of dryout is given in Chapter 8. This onset of dryout prediction is indicated on the flow pattern map (Figure 4.2).

The pressure drop was a strong function of mass flux and vapour quality (Chapter 5). Both these parameters influenced the flow structure. The pressure drop increased as vapour quality and mass flux increased. For lower mass flux (bubbly flow) the pressure drop increased with
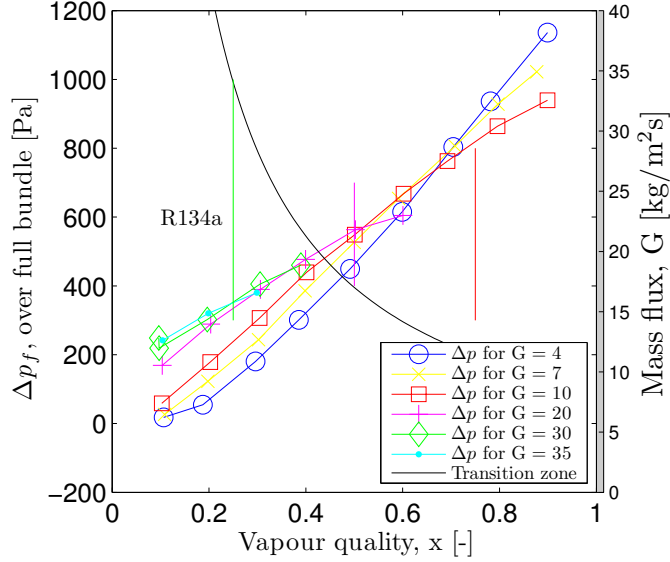
Figure 4.5: Adiabatic flow pattern map for bundles

vapour quality, but for higher mass flux there was a slight deviation in the pressure drop as it increased with a lower slope (Figure 4.5). This could be caused by the flow pattern changing to an annular structure with a vapour core moving up in-between the wetted tubes (Aprin *et al.*, 2007). The annular flow pattern could induce less frictional loss than a flow with bridging and colliding liquid slugs. The testing of higher mass flux and vapour quality combinations were limited by the power of the pre-heater. Flow development in the bundle also remained uncertain, since observations were difficult through the thin wavy film on the tube and only possible at one location. It appears as if the external, discontinuous nature of the flow dampens any strong direct effect of flow pattern and homogenizes the flow effects. No conclusive comments can be made on this trend and testing a wider vapour quality range at high mass flux is recommended.

4.2.1 Pool boiling

Pool boiling observations were conducted on a single tube without vapour bubbles from other tubes below the observation point. The two different tubes each had a unique vapour generation pattern. The *Wolverine Turbo-B5* tube produced more bubbles that were smaller in diameter, even at low heat flux (Figure 4.6) whereas the *Wieland Gewa-B5* tube had larger bubbles emerging from fewer pores at low heat fluxes (Figure 4.7). At higher heat fluxes vapour emerged from all over the tubes and the surface was generally not visible.

At low heat fluxes the tube surface was still visible and measurements of certain activities could be made of isolated bubbles. At high heat fluxes the vapour generation rate was too high and the image too obscure and chaotic for taking reliable measurements. It was found that the bubble departure process changed from isolated bubbles at the lowest heat fluxes to a prolific bubble releasing regime with bubble coalescence laterally and vertically and interactions that are difficult to quantify at higher heat fluxes. Larger bubbles were also observed intermittently as they passed from below the field of view (from the bottom of the tube) and moved upwards past the tube. These larger bubbles and the bubbles emerging from the surface interacted by convecting or coalescing together.

(a)

(b)

(c)
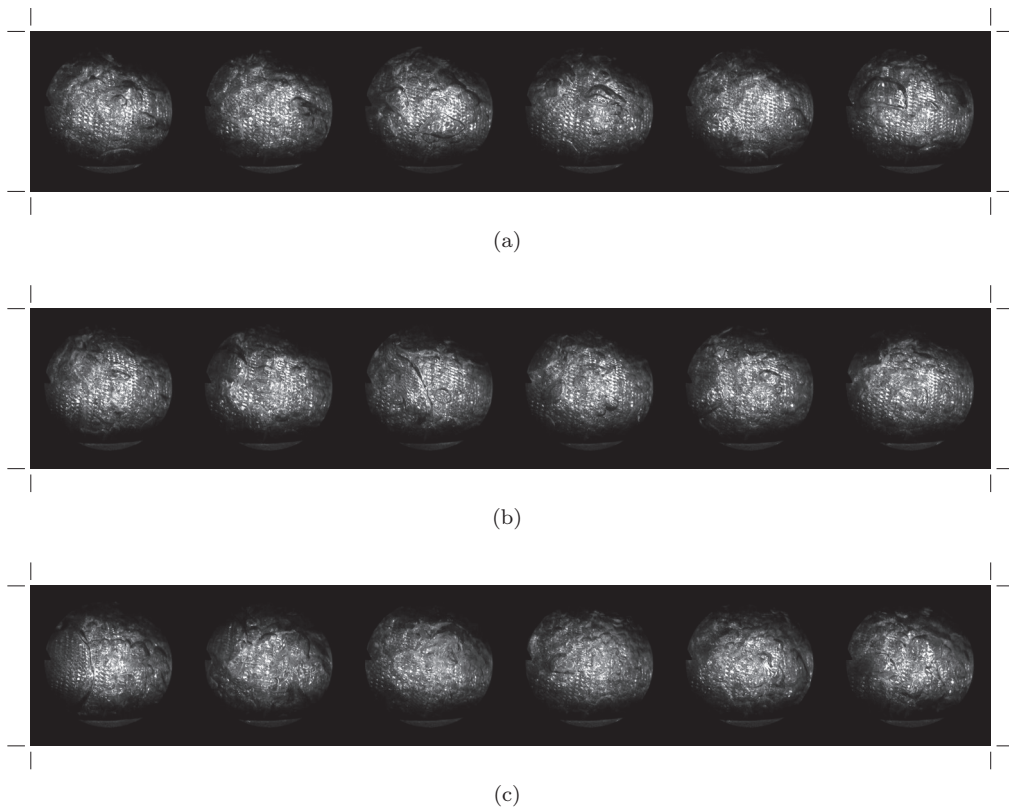
Figure 4.6: Pool boiling on a *Turbo-B5* tube at (a) low ($\approx 15\ kW/m^2$), (b) medium and (c) high ($\approx 55\ kW/m^2$) heat fluxes with R236fa at 5^oC

(a)

(b)

(c)
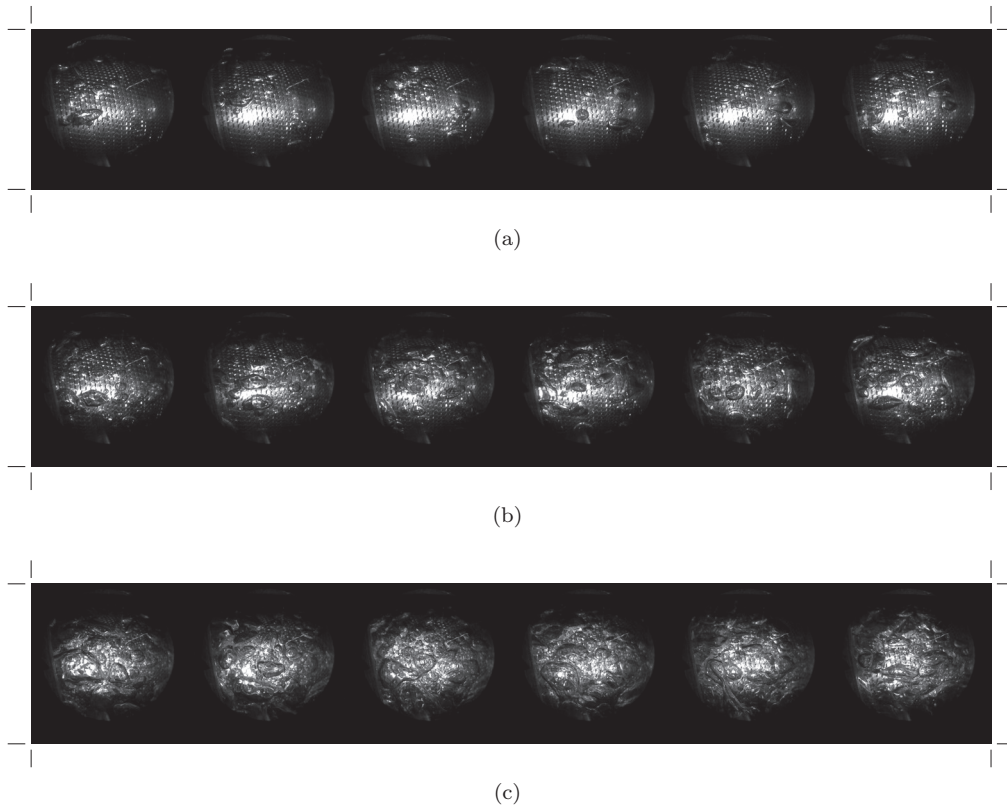
Figure 4.7: Pool boiling on a *Gewa-B5* tube at (a) low ($\approx 15 \ kW/m^2$), (b) medium and (c) high ($\approx 55 \ kW/m^2$) heat fluxes with R236fa at 5^oC

4.3 Pool boiling flow pattern measurement

4.3.1 Piezo-electric pressure transducer

Frequency measurements were carried out in the bundle and during pool boiling conditions. The experimental procedure and measurement frequencies were discussed in Chapter 3. Preparatory work done before testing included sampling data from the various measurements at the maximum frequency of 250000 Hz. All active components or sources of external noise were turned off and measurements were made as they were turned on, one at a time. Several experimental conditions were also tested and accelerometers were temporarily mounted to compare frequencies from moving components and natural excitations with the frequency spectra from the measurements. Based on these results no interference or influences from external elements were anticipated. The sampling frequency was reduced to more appropriate levels to allow longer samples, thereby increasing the accuracy.
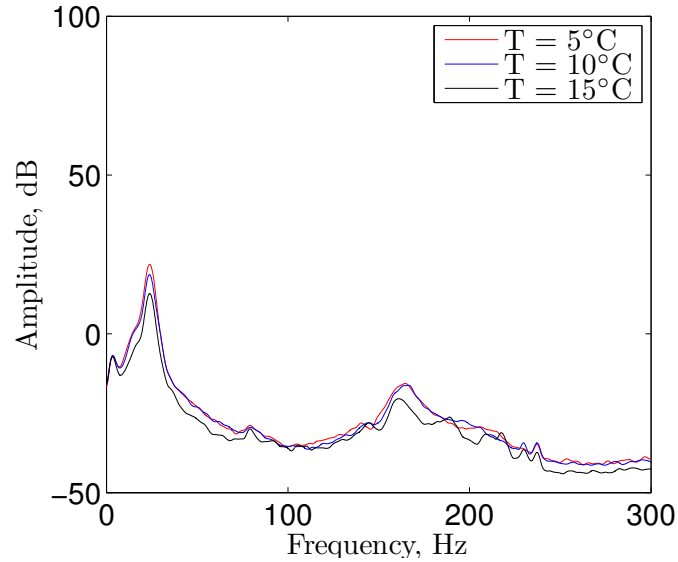
Figure 4.8: Frequency content of the piezo-electric pressure transducer next to a *Turbo-B5* tube in pool boiling with R236fa, averaged for all heat fluxes

During the pool boiling experimental phase a piezo-electric pressure transducer was mounted horizontally in the tube opposite the boiling tube. The high-speed camera was mounted in the same tube with a viewing port. The aim was to find a frequency related to the bubble departure from the enhanced surface from the piezo-pressure signal. The frequency response of tubes in pool boiling remain unchanged with heat flux (Figures 4.8-4.10). The figures represent the power spectral density of all heat fluxes averaged per temperature. The amplitude of pressure fluctuations were much lower for the *Turbo-B5* than the *Gewa-B5* tube. This could be attributed to the smaller bubbles emerging from more numerous pores in the *Turbo-B5* . The power of the signal spectra reduced with increasing saturation temperature. The video images were used to measure basic bubble dynamics and to associate the frequencies with occurrences on the tube.

4.3.2 Visual measurements

Individual bubble measurements were taken at low heat fluxes where bubble interaction was limited in the isolated bubble regime. The frequency of departure, approximate diameter of departure and bubble passage rate past a fixed point were measured. The standard image calibration process using a grid of points with known positions and spacing was used. The grid was printed and wrapped tightly around the tube for the calibration since measurements would be made of bubbles emerging from the tube surface. This resulted in a pixel to millimeter map
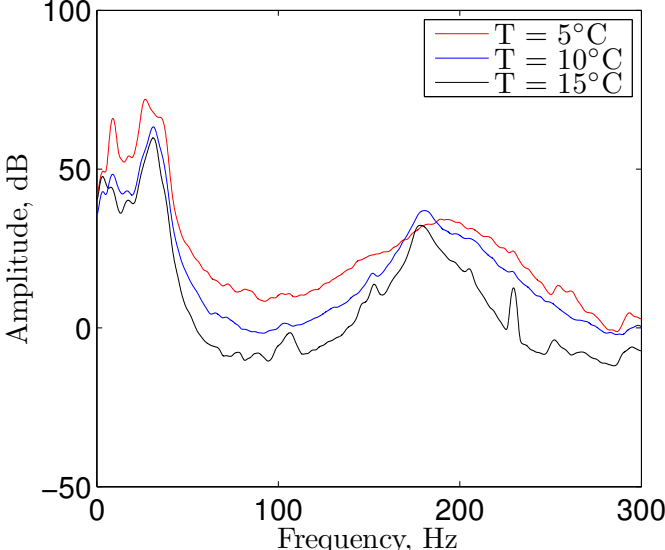
Figure 4.9: Frequency content of the piezo-electric pressure transducer next to a *Gewa-B5* tube in pool boiling with R134a, averaged for all heat fluxes
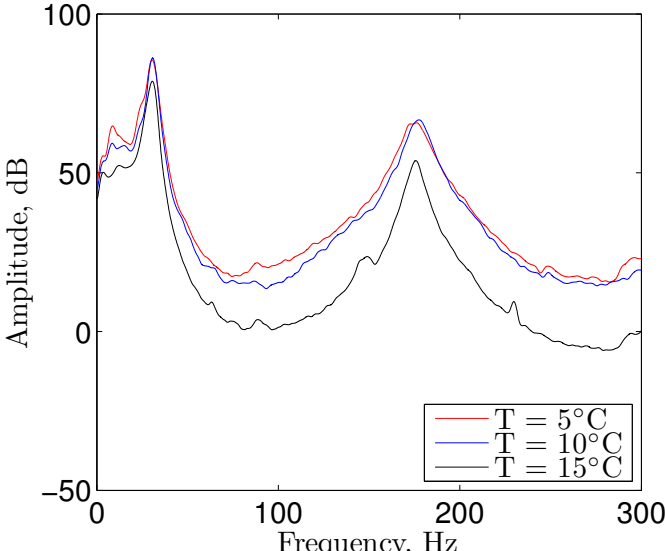
Figure 4.10: Frequency content of the piezo-electric pressure transducer next to a *Gewa-B5* tube in pool boiling with R236fa, averaged for all heat fluxes
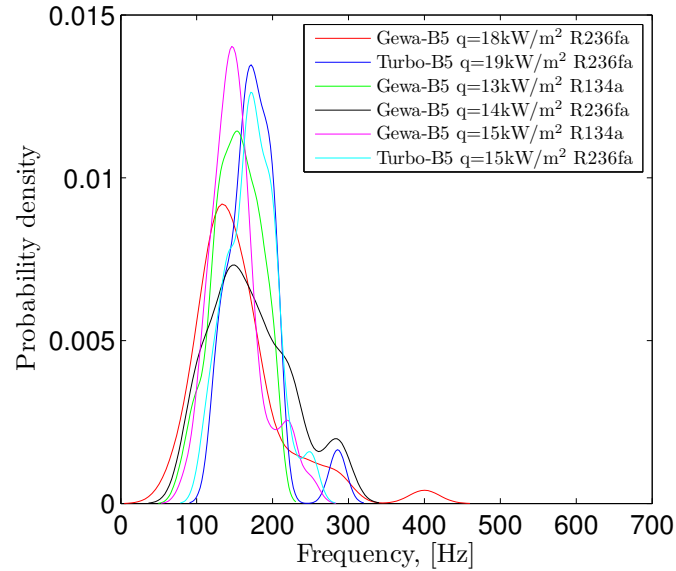
Figure 4.11: PDF of the frequency of consecutive departures from the same pore measured for visible active pores

of the tube surface. Constant lighting and position were used for the images to facilitate the measurements.

Consecutive bubbles emerging from the same active pore were measured to find the frequency often referred to as the departure frequency (Figure 4.11). The bubble dynamics models for enhanced tubes simplify bubble departure as a continuous process happening at active pores (Ramaswamy *et al.*, 2003). The video observations show some pores that were active and releasing consecutive bubbles (two to four bubbles) at intermittent intervals while other types of active pores released single bubbles randomly.

From the above measurements the consecutive bubble departure rates were found to occur over a wide range of frequencies with a peak probability in the 150-200 Hz range, corresponding to the pressure measurement peak in the same range. The peak in frequency found within this frequency range was present for both tubes with varying strength and was considered to present consecutive bubble departure. The *Wolverine Turbo-B5* tube had a much weaker amplitude at this frequency and from the observations the flow around this tube was more varied with fewer bubbles observed emerging consecutively due to the large amount of vapour passing around the tube, compared to *Wieland Gewa-B5* at similar heat flux.

A fixed point was selected, similar in size to the pressure tap, and bubble passages were counted. Bubble passage was considered as a bulk fluid activity, not a tube surface activity such
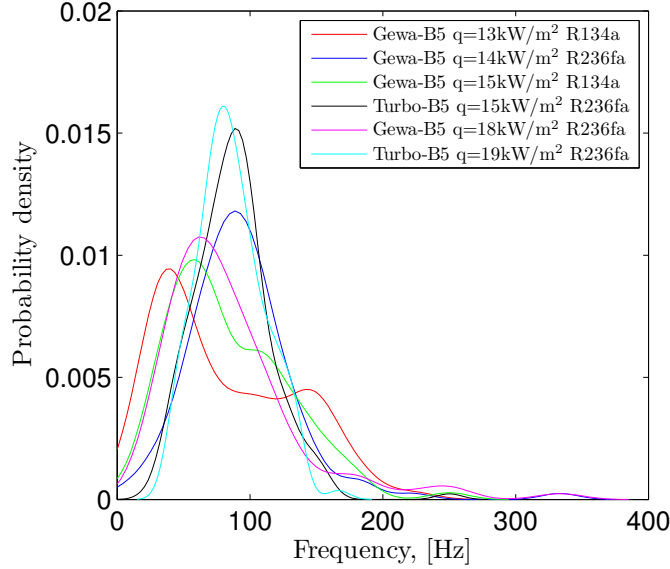
Figure 4.12: PDF of the frequency of interfaces passing a fixed point in the middle of the field of view

as bubble departure. The rate of events passing a fixed point was lower than the consecutive bubble departure. A manual count of the period between any activity passing a fixed point resulted in frequencies of around 70-110 Hz (Figure 4.12). There was little pressure activity at this frequency in pool boiling even though this method of visual observation corresponded closely with the actual pressure tap position. The pressure fluctuations caused by the departing bubbles were therefore assumed stronger than the passage of bubbles past the pressure tap in pool boiling.

The remaining measurement was that of bubble departure within a sample area on the surface of the boiling tube. The bubbles departing from pores in such a sample area was random and not necessarily consecutive. The sample area was similar in size to a projection of the pressure tap on the tube surface. The frequency of activity in an arbitrarily selected sample area ranged from 20-50 Hz (Figure 4.13). This corresponded to the highest amplitude frequency measured from the pressure signals.

The diameter of the departing bubbles was measured at random departure locations (Figure 4.14). The probability distribution indicated an average diameter around 0.6 mm for the *Turbo-B5* and a larger, wider bubble distribution for the *Gewa-B5* tube. Most bubbles on the tube had similar sizes at departure if no interaction occurred with other bubbles.

As part of a mechanistic model for enhanced boiling of a surface with pores and tunnels Ramaswamy *et al.* (2003) modelled pool boiling frequencies by using a force balance and empirically
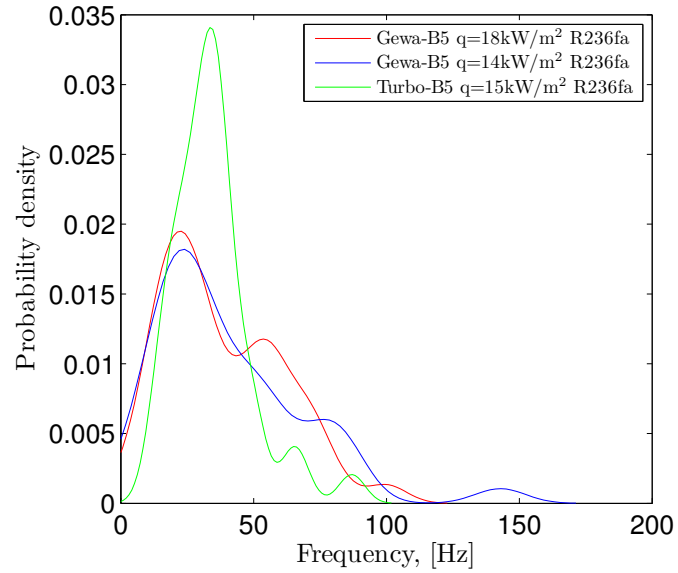
Figure 4.13: PDF of the frequency of bubbles leaving a pore from a fixed area of tube similar in size to the piezo-pressure tap
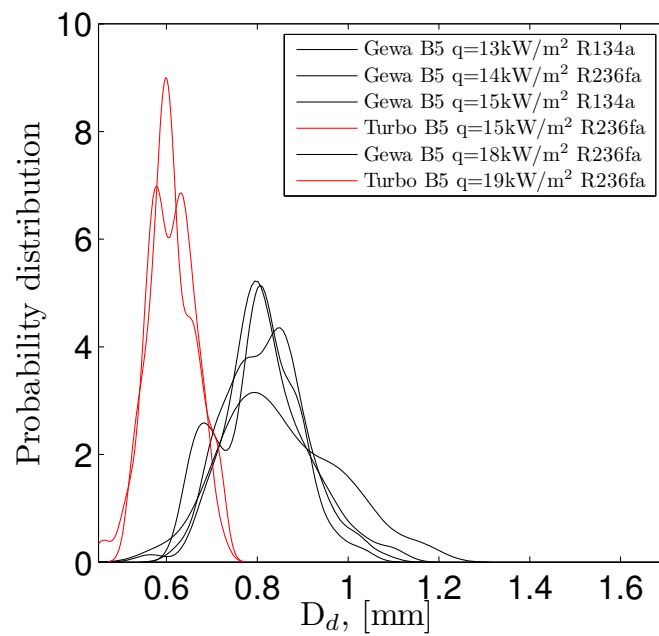
Figure 4.14: PDF of bubble departure diameters measured for active pores on the tube during the video sequence
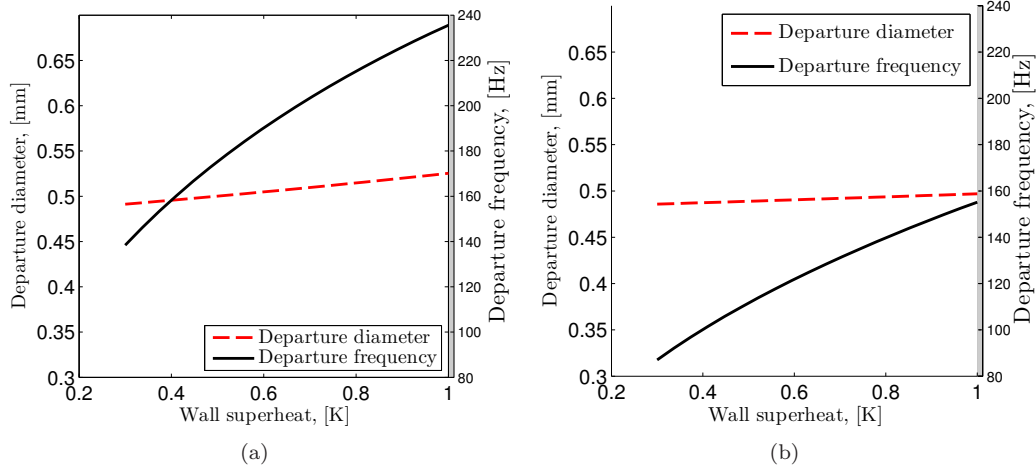
Figure 4.15: Departure diameter and frequency prediction for a 100μm pore in (a) R134a and (b) R236fa using the growth time predicted by Ramaswamy *et al.* (2003)

fitted growth rate originally proposed by Chien and Webb (1998b) and based on the bubble growth model of Mikic *et al.* (1970). The empirical coefficient C_{tg} was 0.0296 and originates from experimental data that were used to fit the correlation for enhanced surfaces. The prediction of bubble departure frequency and diameter for the two fluids used in this study is compared in Figure 4.15 (see equations in Appendix C). The model is proposed only for the isolated bubbles regime and does not deal with any form of coalescence. The predicted departure diameter was a function of pore diameter and wall superheat. The wall superheat is plotted up to a value of 1.0 K to avoid the region where bubble interaction takes place and its effect on departure frequency. The predicted departure diameter was slightly lower than that measured and the discrepancy can be attributed to the unknown pore diameter, completely different tube geometry and a different force balance for the horizontal tubes.

The bubble departure frequency predicted in Figure 4.15 was based on the growth time only and the true frequency would be lower. The departure frequency was a function of the wall superheat in the prediction, but the experimental data indicated a constant departure frequency. The true departure frequency as measured by the observations included the waiting time and growth time of a bubble. The waiting time (as discussed in Appendix C) is the time from bubble departure until the pressure inside the tube is sufficient to overcome the surface tension at the pore. It is a function of the internal geometry and fluid type. For enhanced tubes the waiting time is a small fraction of the growth time (Chien and Webb, 1998b).

4.3.3 Bundle boiling flow pattern measurements

The pressure fluctuation measurements in the adiabatic section of the bundle was synchronised with high-speed video recordings and the following section presents the frequency content of the adiabatic tests conducted (Figures 4.16-4.17). Each subplot represents a single mass flux with a series of vapour qualities on the x-axis and with the frequency of each individual measurement on the y-axis. A coloured contour map was fitted to show the amplitude of the signal over the frequency spectrum.
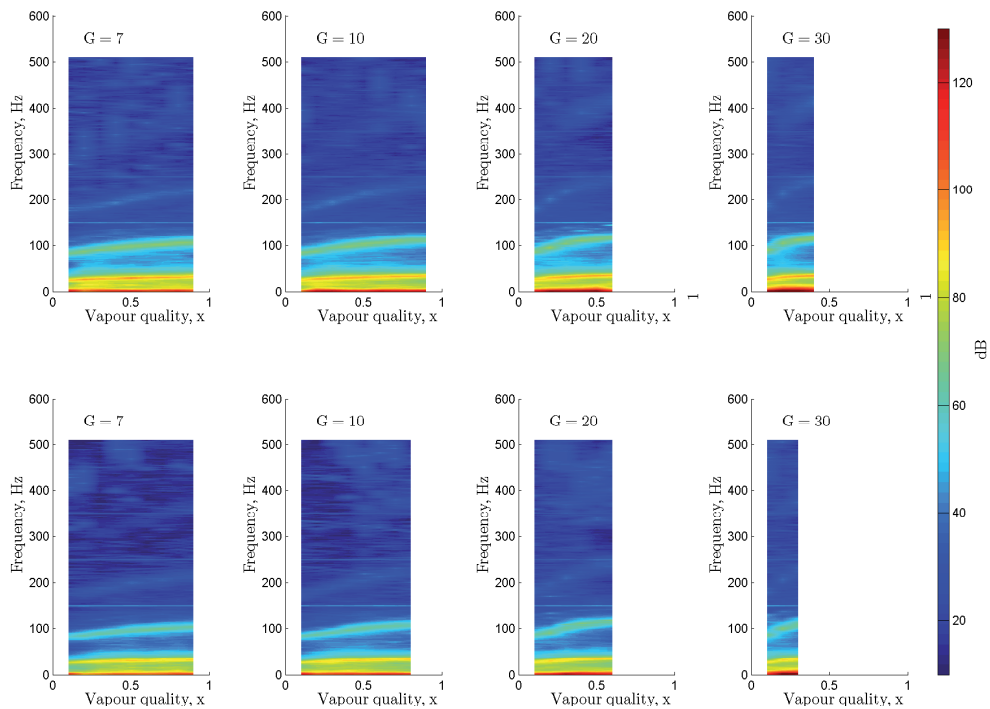
Figure 4.16: Frequency plot of 5^oC and 15^oC adiabatic tests over the mass flux and vapour quality range tested for *Wolverine Turbo-B5* with R134a

The plots indicated at least two strong, continuous frequency bands that were a function of vapour quality and mass flux. The low frequency peak was under 50 Hz and increased with vapour quality and slightly with mass flux. The second peak was at higher frequencies ranging from 90 Hz to 120 Hz and exhibited the same trend as the low frequency peak. There were no significant peaks measured with the present equipment at higher frequencies. When the signal had oscillations lower than the frequency resolution (2.5 Hz), it could be seen as a peak at 0 Hz.
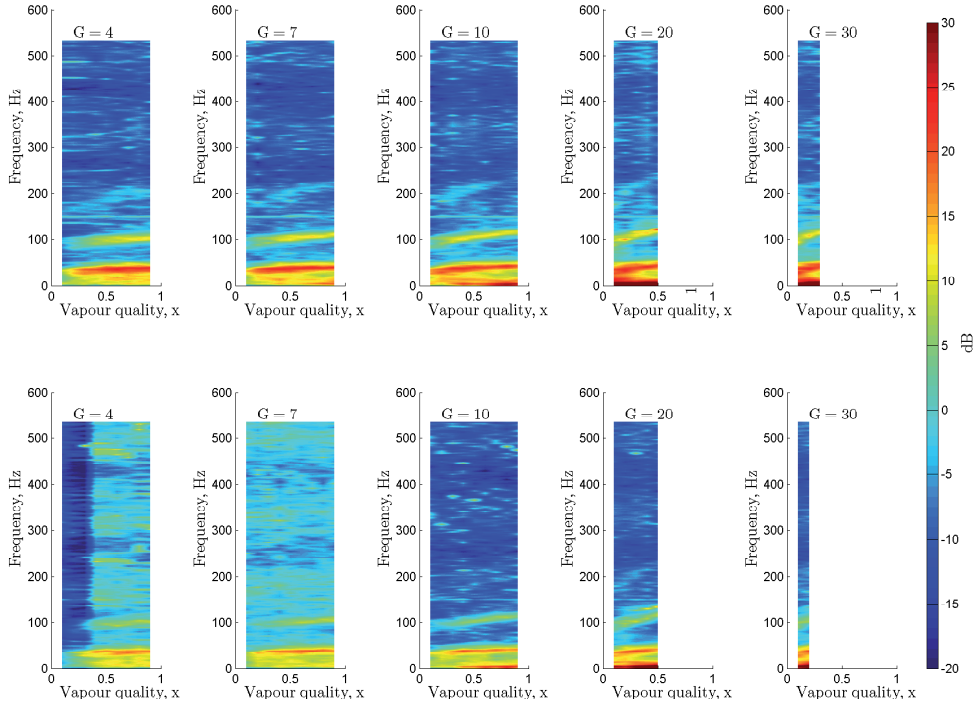
Figure 4.17: Frequency plot of 5°C and 15°C adiabatic tests over the mass flux and vapour quality range tested for *Wieland Gewa-B5* with R134a

The diabatic flow pattern should contain information related to the external flow pattern moving through the bundle as well as possible remnants of the boiling process on the tubes below the measurement point. Figures 4.18 and 4.19 present the diabatic conditions tested for the *Wolverine Turbo-B5* and Figures 4.20 and 4.21 is for *Gewa-B5* tubes.

The frequency peaks found could be attributed to specific phenomena through statistical analysis and video observations mentioned above. In adiabatic flow, the 40 Hz frequency was attributed to the stronger flux of coalesced bubbles that were generally larger in size than the intertube gap and can be measured by observing the flow and noting the time period between passes of bubbles in the bulk flow. The 110 Hz frequency was associated with the frequency of smaller interface related features moving past the measurement point. This frequency was close to the bubble passage rate found in the bulk flow of pool boiling. Thus the fluctuations measured in the adiabatic section were found to differ from those in the diabatic conditions like pool boiling. Diabatic measurements during pool boiling pick up the bubble dynamics and adiabatic measurements only detect the interface passage since no bubble departure was present
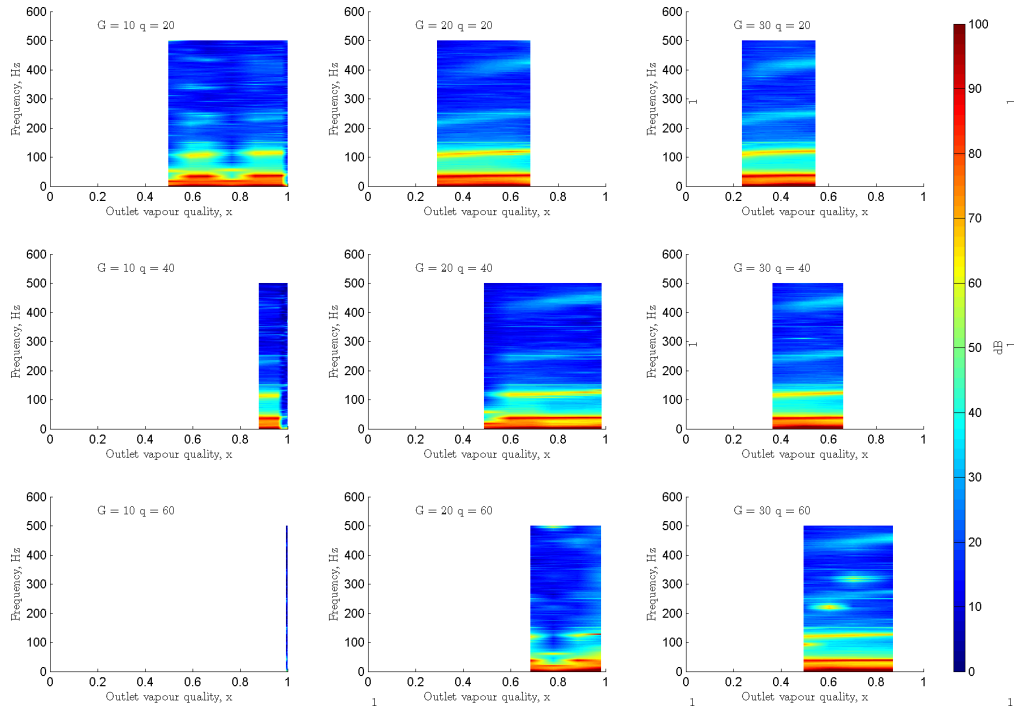
Figure 4.18: Frequency plot of 5°C, diabatic tests over the mass flux and vapour quality range tested for *Wolverine Turbo-B5* with R134a

in the vicinity. The 170 to 200 Hz frequency was unique to diabatic conditions.

No quantitative measurements of bubble dynamics could be made during bundle boiling due to poor visibility. If bubble dynamics are responsible for the pumping of liquid into the tunnels and external heat transfer enhancement, understanding the interaction will be important for mechanistic models. By performing more dedicated frequency measurements of low heat flux diabatic conditions in pool boiling and bundle boiling, the bubble dynamics may be characterised.

4.4 Conclusions

Flow patterns and bubble dynamics were investigated for conditions of pool boiling and convective bundle boiling. There was no flow pattern effect on heat transfer or pressure drop that caused any strong deviation in trends except the onset of dryout. The hypothesis regarding flow pattern effect is thus accepted. Agostini (2008) found no effect of flow pattern for smooth bundles at low mass fluxes and reported a smooth and gradual evolution of flow pattern with vapour quality and
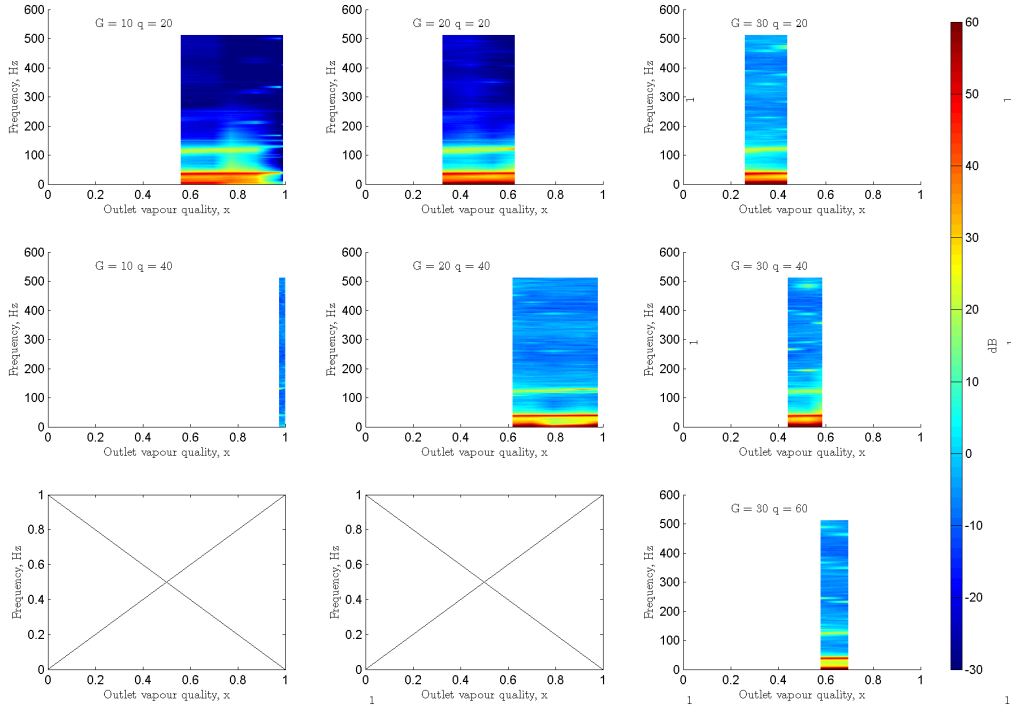
Figure 4.19: Frequency plot of 5°C, diabatic tests over the mass flux and vapour quality range tested for *Wolverine Turbo-B5* with R236fa

mass flux. There was however a certain development of the flow through the bundle that seems to maintain the tubes in a wetted state until onset of dryout.

Quantitative measurement on a single tube were made of bubbles and flow observations to clarify the frequency content. Bubbles did not depart continuously from active pores, but randomly from many pores and sometimes consecutively. Frequency activity remained constant with heat flux (Figures 4.6 and 4.6) unlike the predictions (Figure 4.15). Bubble departure diameters remained relatively constant for different heat fluxes and fluids leaving only the active sites N_a to increase. Bubble departure diameters differed for each tube.

No quantitative measurement of bubble dynamics was possible for convective bundle boiling and the effect of convection on heat transfer could therefore not be directly attributed to external convection or internal evaporation/convection effects. Mechanistic models should include the dynamics of convection over tubes on bubble dynamics and subsurface heat transfer to determine which is the dominant factor or if they have equal importance.
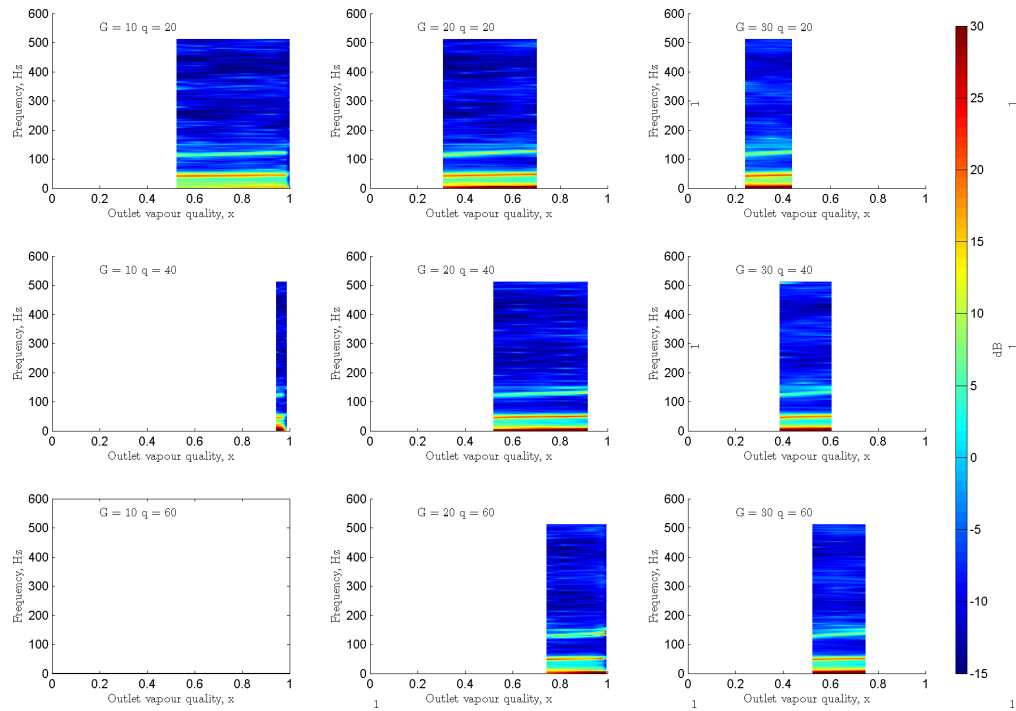
Figure 4.20: Frequency plot of 5°C, diabatic tests over the mass flux and vapour quality range tested for *Wieland Gewa-B5* with R134a
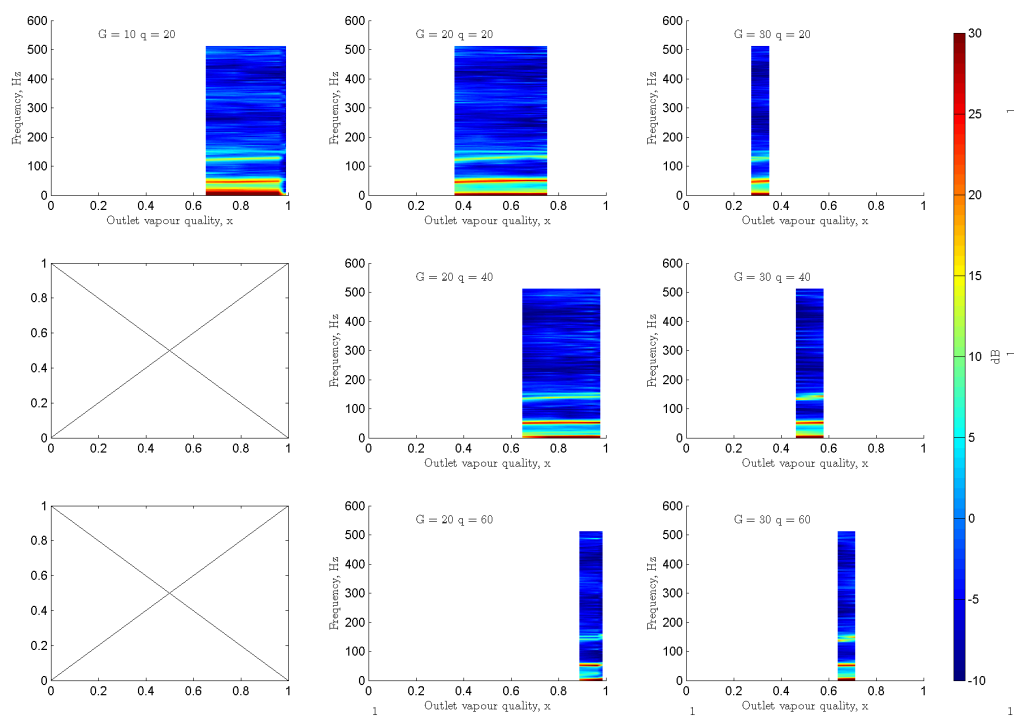
Figure 4.21: Frequency plot of 5ºC, diabatic tests over the mass flux and vapour quality range tested for *Wieland Gewa-B5* with R236fa

Chapter 5

Two-phase pressure drop results

For normal design purposes, the two-phase pressure drop is an important consideration in tube bundle evaporation due to the pumping power requirement and the close temperature approaches in certain large evaporators where the change in saturation temperature could have a significant effect on heat transfer. The two-phase pressure drop components in a vertical flow require a void fraction for their calculation and are therefore sensitive to modelling assumptions related to void fraction. Past studies of tube bundle pressure drop mentioned in Chapter 2 have remarked that the static component is generally the dominant component. The purpose of this study was to evaluate the assumptions related to the test section and evolve the pressure prediction from an empirical curve fit to an empirical, phenomenological relation. In this chapter all aspects of pressure drop in tube bundles are presented and frictional prediction methods are compared against experimental data.

5.1   Adiabatic results

The relative size of the static head has always been acknowledged as the main component of pressure drop in flooded evaporators. The data will show that for low vapour quality this is true but that higher mass flux and vapour quality conditions have a significant frictional pressure drop. The momentum component is relatively small, but still important in the data reduction process. The frictional component of the two-phase pressure drop is the major focus of the discussion that follows.

In order to quantify the relations and interactions between the independent variables (controlled by the experiment) and the dependent variables (measured or calculated), a factorial analysis was done. The results of the analysis tabulates the effects of the main variables and

interactions between each combination of the main variables. The effect of a main variable can be considered as the change in the measured quantity caused by the change in a single main variable while all other variables remain constant. When the interaction is large the main effects have little meaning. The variable response is assumed to be linear. The effect gives the response of a dependent variable to the change in the independent variable. This in itself has no meaning as the weight or importance is uncertain. The t-ratio gives the probability that a change in the variable is important. The significance is a report based on the experimental uncertainty of the variables giving an indication whether or not the probability is a significant one when compared against the distribution function. Lower values of significance indicate a higher likelihood that the probability given for a change in measured quantity is significant.

Since a five-variable factorial test results in unwieldy matrices, T_{sat} was not included as an independent variable. The saturation temperature was not found to influence the frictional pressure drop in this study. Each pair of conditions evaluated for the factorial analysis is presented below. For the adiabatic pressure drop the functional relation tested is as follows:

$$
\begin{aligned}
Measured \quad &= \quad f(Independent\ variables)\\
\Delta p_f \quad &= \quad f(x, G, Refrigerant, Tube, T_{sat})\\
\text{options:}\ x \quad &= \quad \begin{pmatrix} 0.1 \\ 0.5 \end{pmatrix} \quad G = \begin{pmatrix} 4 \\ 20 \end{pmatrix} \quad \text{Refrigerant} = \begin{pmatrix} R134a \\ R236fa \end{pmatrix} \quad \text{Tube} = \begin{pmatrix} Turbo\text{-}B5 \\ Gewa\text{-}B5 \end{pmatrix}
\end{aligned}
$$

The conditions selected for the test required two test cases for each main effect. Vapour qualities of 0.1 and 0.5, mass fluxes of 4 and 20, refrigerants R134a and R236fa and two tube types (*Wolverine Turbo-B5* and *Wieland Gewa-B5*) were selected. The effects of the main parameters and some significant interactions on the frictional pressure drop are reported in Table 5.1. The effects indicate a strong effect of vapour quality and mass flux. From the main effects, the pressure drop for *Wieland Gewa-B5* was slightly lower than *Wolverine Turbo-B5* and R236fa had a higher pressure drop than R134a. The latter two effects are not significant compared to the effect of vapour quality and mass flux. From the secondary effects or interactions (none were significant), it is possible to state that the frictional pressure drop is not likely to vary much as a function of vapour quality and mass flux for the different tubes (column ABD) and more likely to vary as a function of refrigerant (column ABC). From this analysis, it can already be concluded that the prediction method does not need to be a function of tube type or refrigerant type.

To investigate the actual data, a series of figures will illustrate the trends mentioned above. Static and frictional components are presented as a percentage of the total pressure drop in

Table 5.1: Factorial test results for frictional pressure drop with main effect and selected interactions

Effect	A[a]	B[b]	C[c]	D[d]	AB	AC	BC	AD	BD	CD	ABC	ABD
Factors	430.7	101.7	8.7	-12.2	-58.1	13.7	-23.4	-0.7	-6.6	6.1	-28.7	-9.9
t ratio	24.4	5.8	0.5	-0.7	-3.3	0.8	-1.3	-0.0	-0.4	0.3	-1.6	-0.6
Significance	0.00	0.00	0.35	0.31	0.01	0.29	0.16	0.39	0.36	0.37	0.11	0.33

[a] Vapour quality [b] Mass flux [c] Refrigerant [d] Tube type

Figure 5.1a and 5.1b respectively. The total pressure drop decreases as mass flux and vapour quality increase (Figure 5.2). As noted above, the static component (Figure 5.3) is mostly the dominant pressure drop component and the overall pressure drop will therefore follow the static pressure drop trend. The static pressure drop is mainly a function of void fraction and the Feenstra *et al.* (2000) model predicts an increase in void fraction with mass flux and vapour quality (Figure 5.4).
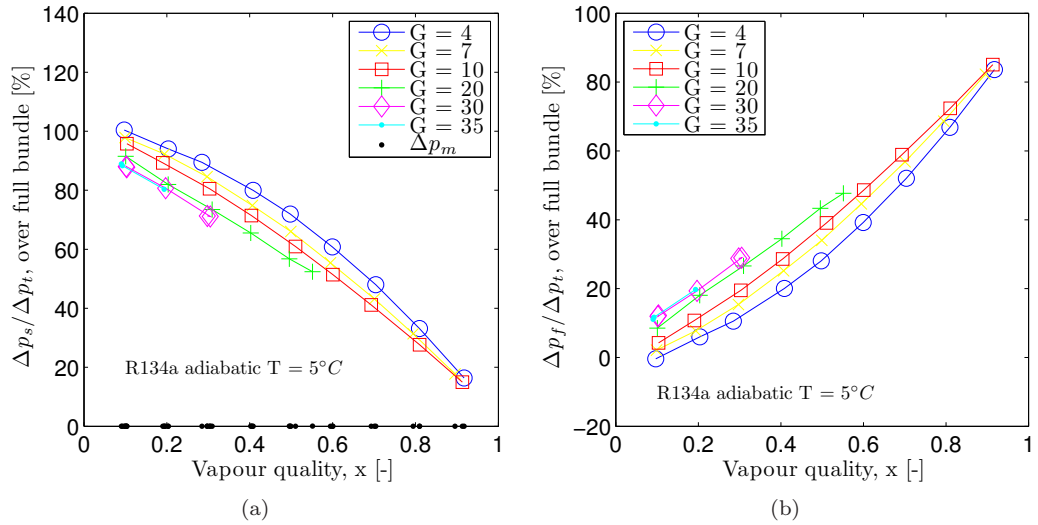
Figure 5.1: Percentages of (a) static and (b) frictional pressure drop with respect to the total pressure drop for sample cases with R134a at 5°C with *Gewa-B5* tubes

An important note is that the static component can exceed 100% at the lowest vapour qualities and mass fluxes. This is the result of all the errors compounded in the assumptions and models used to calculate this value and this matter is addressed in Appendix D. The errors include the heat flux prediction error, which affects the vapour quality prediction in diabatic cases. The void fraction is a model with a limited range and applicability and the lowest mass flux and vapour quality is clearly at the extreme limits of the method used.
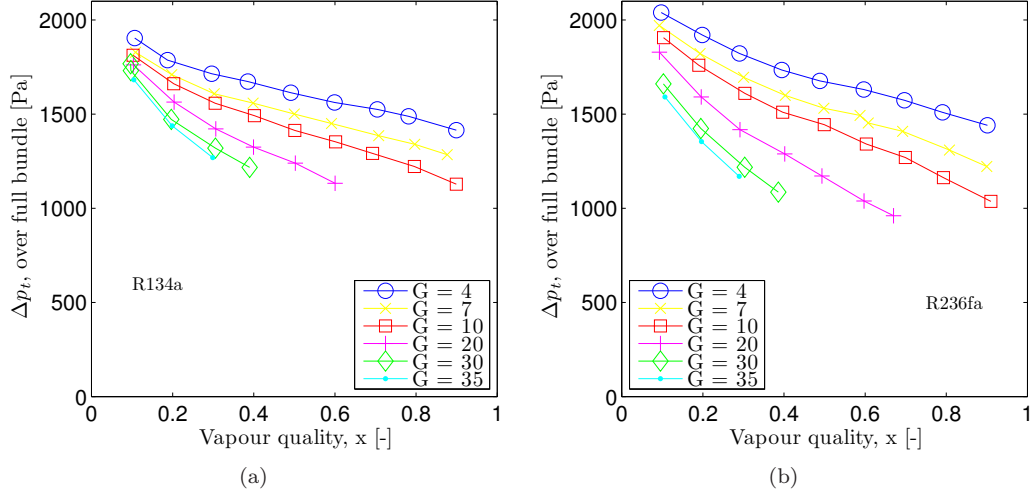
Figure 5.2: Δp_t for *Wolverine Turbo-B5* with (a) R134a and (b) R236fa at all mass fluxes and vapour qualities tested at 5°C
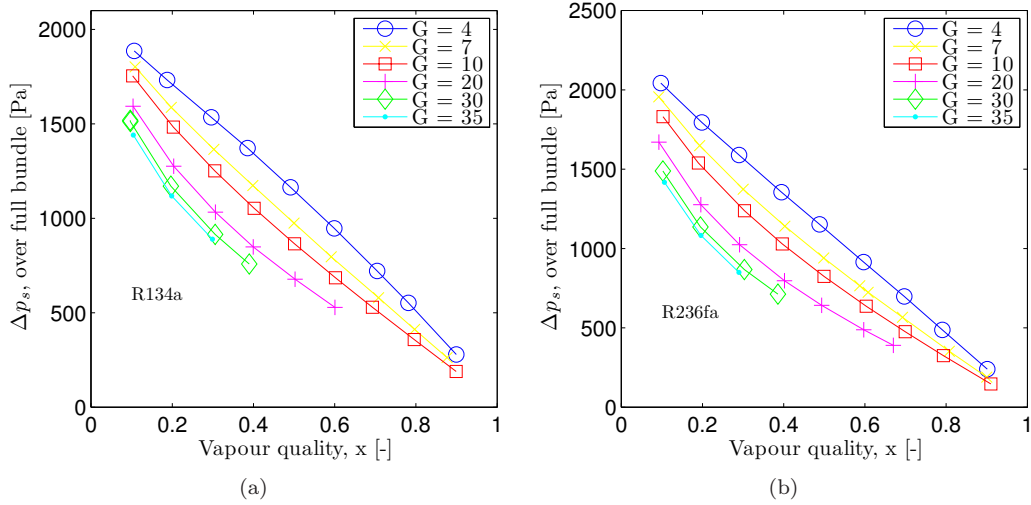
Figure 5.3: Δp_s for *Wolverine Turbo-B5* with (a) R134a and (b) R236fa at all mass fluxes and vapour qualities tested at 5°C

The frictional pressure drop is caused by the surface friction of the flowing fluid and other losses in the flow. These actual components are unknown and are commonly lumped into the frictional pressure drop. All other pressure drop components (static and momentum) are estimated from the experimental data using appropriate prediction methods and then the frictional component can then be calculated. Under most conditions it is a function of the fluid properties like viscosity, density and surface tension and of the physics in the flow *e.g.* phase velocity and
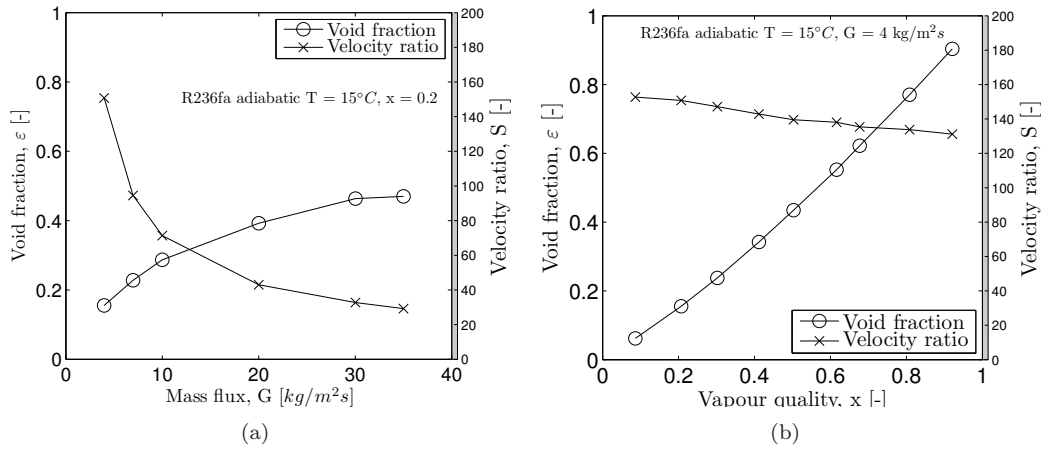
Figure 5.4: Comparisons for sample condition of the Feenstra *et al.* (2000) model with R134a for (a) x = 0.2 and (b) G = 4 $kg/m^2 s$

flow structure (flow pattern). The frictional pressure drop increases with mass flux and vapour quality (Figure 5.5). As noted in Figures 5.4a and 5.4b the relative velocity of vapour and liquid, which would influence frictional losses, is a function of the mass flux and vapour quality. The difference in frictional pressure drop between tube types is not large even though the surface structure is very different. The liquid, which clings to the tubes, probably forms a boundary layer with fairly constant losses and the rest of the frictional component can be attributed to the shear at the interface and other interactions between the fluid and the tubes.

The testing included saturation temperatures of 5^oC and 15^oC. No strong dependence on saturation temperature can be seen for either refrigerant (Figure 5.6). The uncertainty propagation presented here is a function of the error in the calculated variables. It does not include the error in the actual models such as void fraction, since the model is only a hypothesis which attempts to predict void fraction and the true void fraction is unknown.

The two-phase friction factor indicated clear mass flux and vapour quality trends (Figure 5.7). The different fluids and tubes all behave similarly. The low mass fluxes have increasingly higher friction factors and there is a peak friction factor for vapour qualities slightly higher than 50% after which it drops down towards a single phase value. The friction factor spread is wider for the lower vapour quality and mass fluxes and this is likely due to increased uncertainty or secondary effects, such as flow pattern and inlet effects. The shape of the friction factor curve is related to the use of a two-phase density in its definition. As the vapour quality increases the density drops and thus also the friction factor. The frictional pressure drop continues to rise with quality
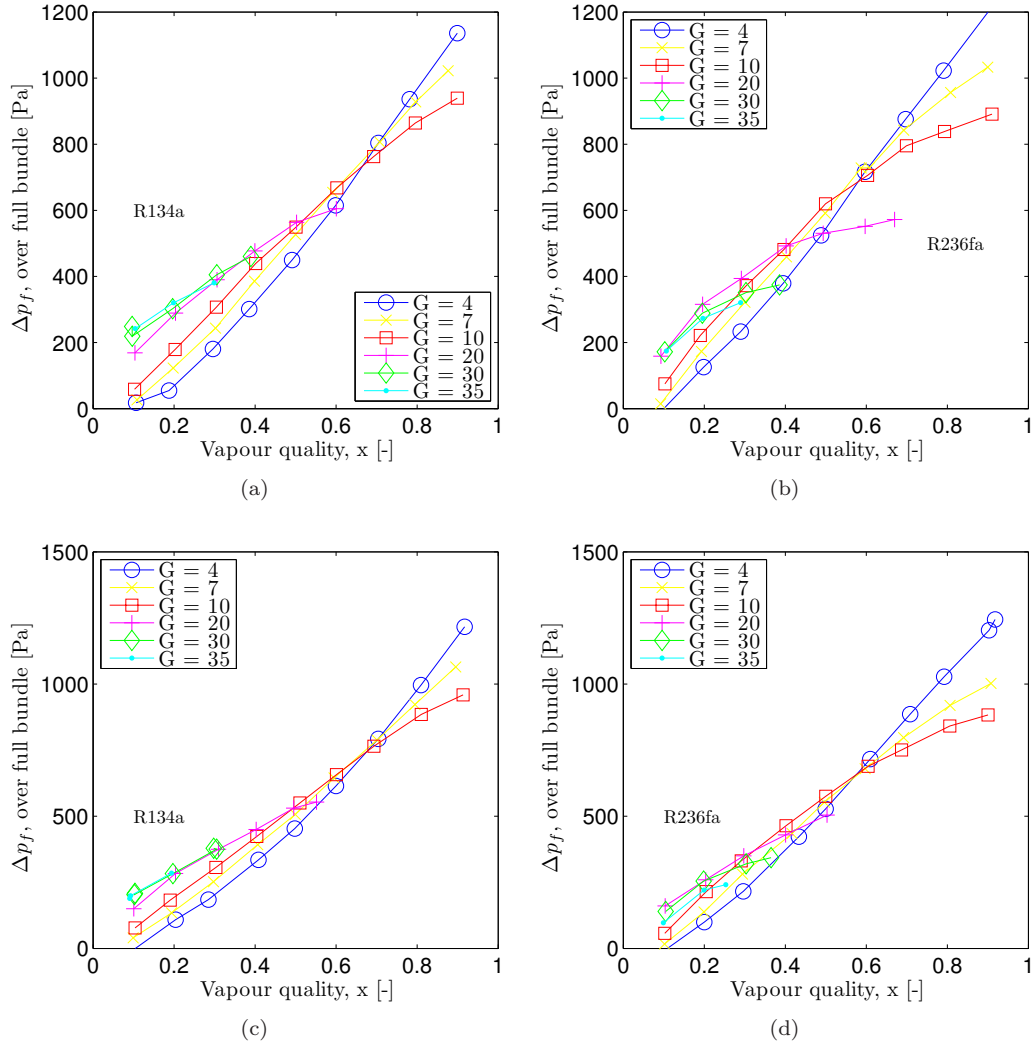
Figure 5.5: Δp_f for *Wolverine Turbo-B5* with (a) R134a and (b) R236fa and (c-d) *Wieland Gewa-B5* at all mass fluxes and vapour qualities tested at 5^oC

(Figure 5.5).

The single phase friction factor can be defined for the two-phase region by using the two-phase definitions of density and viscosity with void fraction as described in Chapter 2. The ratio of the two-phase friction factor over the single phase friction factor gives a type of two-phase multiplier and collapses the data for all tube, refrigerant and temperature data with reasonable success (Figure 5.8). From this single figure it is clear that the tube type, refrigerant and temperature do not have a strong effect on the frictional pressure drop beyond that in the underlying single phase friction factor and that the major variables are mass flux, vapour quality and heat flux

(a) Δp_f for different saturation temperatures with *Wolverine Turbo-B5* and R134a at G = 10 kg/m^2s

(b) Δp_f for different saturation temperatures with *Wolverine Turbo-B5* and R236fa at G = 10 kg/m^2s

(c) Δp_f for different saturation temperatures with *Wolverine Turbo-B5* and R134a at G = 20 kg/m^2s

(d) Δp_f for different saturation temperatures with *Wolverine Turbo-B5* and R236fa at G = 20 kg/m^2s

Figure 5.6: Samples of frictional pressure drop at different saturation temperatures for combinations of refrigerants and mass fluxes indicating the relatively weak dependence on temperature

(the latter is provided in the next section on diabatic flow). Similar results can be found for the pressure drop measured over the diabatic section of the bundle.

The demand curve gives an indication of how the frictional pressure drop behaves as a function of mass flux. For tube bundles the lower mass fluxes have a wide range of frictional pressure drop and these are related to the refrigerant type, vapour quality and other parameters (Figure 5.9).
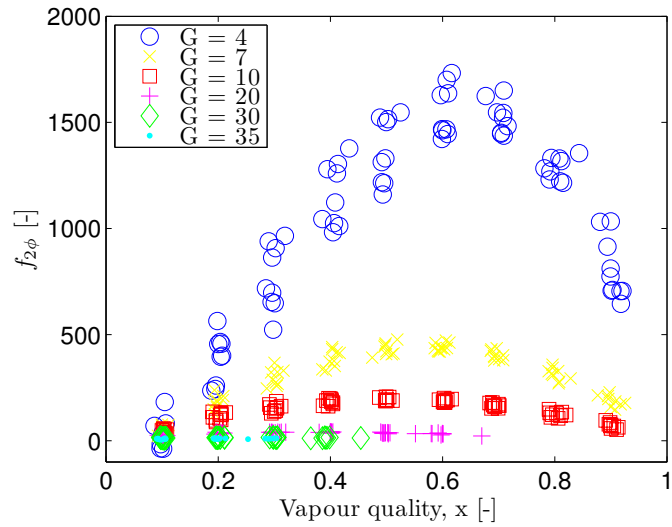
Figure 5.7: Two-phase friction factor ($f_{2\phi}$) for all tube, refrigerant and temperature combinations tested in adiabatic mode over the full bundle
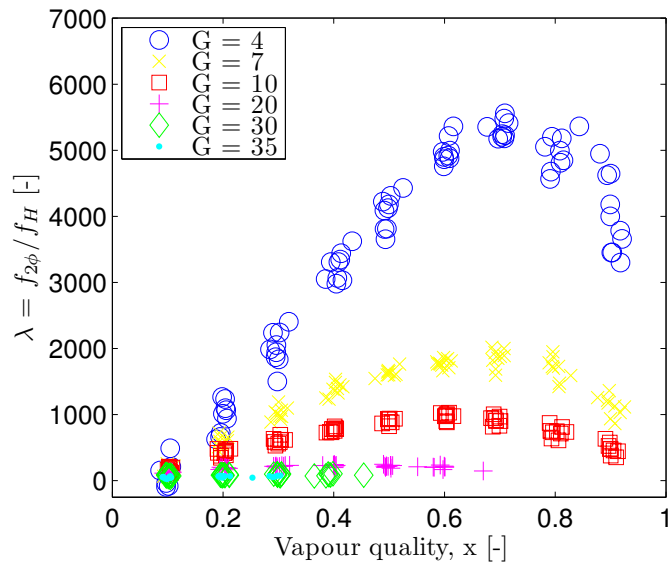
Figure 5.8: Friction factor ratio ($f_{2\phi}/f_H$) for all adiabatic tube, refrigerant and temperature combinations tested in this study and measured over the full bundle
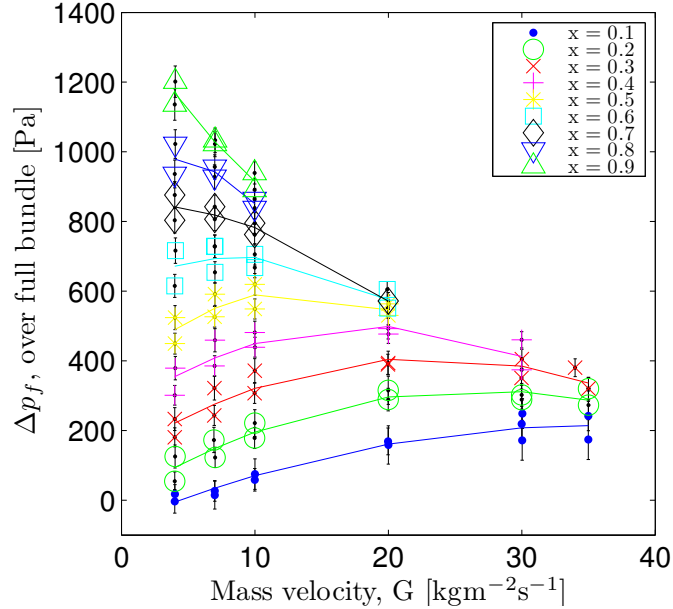
Figure 5.9: Demand curve for the bundle indicating the difference in frictional pressure drop with mass flux for R134a data sampled at 5^oC

As the mass flux increases the frictional pressure drop appears to converge. From the friction factor ratio in Figure 5.8, the drop in ratio as the mass flux increases indicated an increase in the homogeneity of the flow. This happens as the slip ratio decreases and the flow assumes a continuous structure throughout the bundle.

5.2 Diabatic results

During diabatic experiments the vapour quality and therefore the void fraction increased during the evaporation process. This poses a problem in determining the local values of these variables that are required to evaluate the pressure drop components. The uncertainty in the heat flux also introduces added uncertainty in the calculated variables, in particular the local vapour quality. For certain high heat flux and low mass flux conditions the change in vapour quality can be large. A finer discretisation scheme in the bundle during data reduction mitigates this effect as much as possible. The onset of dryout and dryout conditions was considered important for this study and special attention was devoted in the control system improvements to reduce unstable conditions and to maximize the possible data gathered near onset of dryout. As a result, a good number of dryout data points are available.
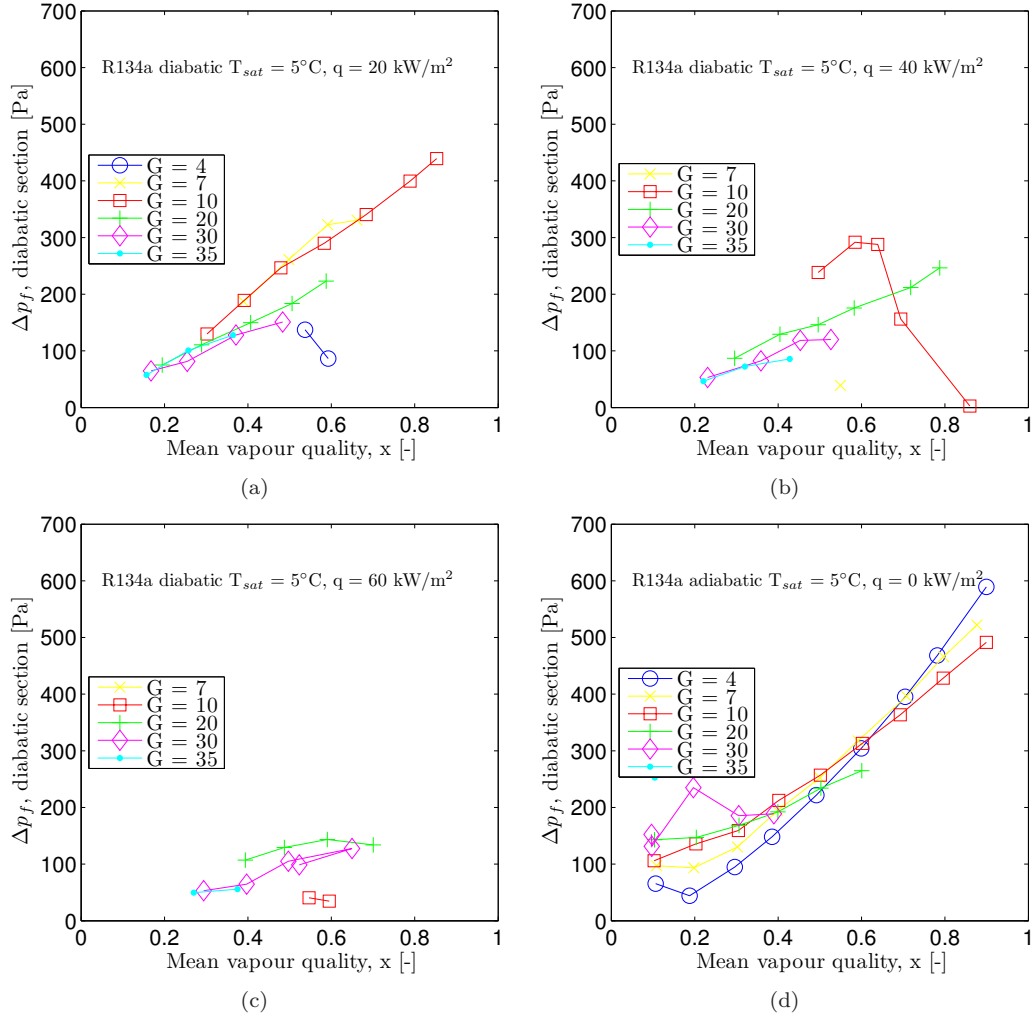
Figure 5.10: R134a frictional pressure drop in diabatic conditions for a range of heat fluxes on the *Turbo-B5* tube [(a) q = 20 kW/m² (b) q = 40 kW/m² (c) q = 60 kW/m² (d) q = 0 kW/m²]

These points can be classified by several methods. The easiest and most certain is by visual inspection with the borescope. Another option available is to monitor the refrigerant enthalpy and heat flux to see whether superheated conditions exist at the exit. The water temperature profile will reflect the sudden reduction in heat transfer coefficient after onset of dryout. The laser light attenuation measurement has a unique signal pattern that can be associated with dryout (Agostini, 2008). All these methods were used to identify the onset of dryout in the bundle and thereby to develop a prediction method specific to the tubes tested.

Some of the diabatic data are presented here to explain the main differences with adiabatic conditions (Figures 5.10 and 5.11). The series of figures indicate the frictional pressure drop for a
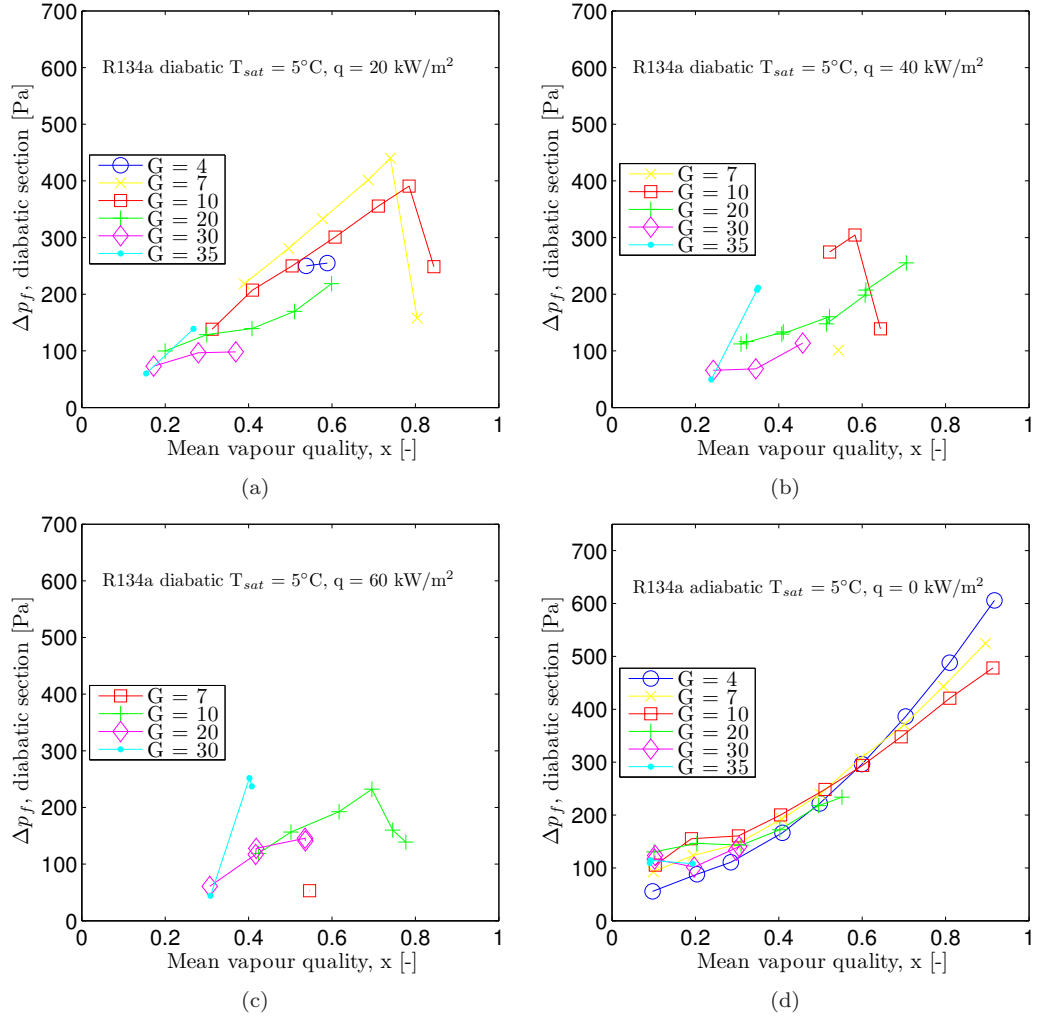
Figure 5.11: R134a frictional pressure drop in diabatic conditions for a range of heat fluxes on the *Gewa-B5* tube [(a) q = 20 kW/m² (b) q = 40 kW/m² (c) q = 60 kW/m² (d) q = 0 kW/m²]

variety of mass fluxes and heat fluxes. Figure 5.10 represents R134a flow over the *Turbo-B5* tube at several heat fluxes and Figure 5.11 represents R134a flow over the *Gewa-B5* tube at several heat fluxes. The 20 kW/m² data for R236fa with both tubes are illustrated in Figure 5.12. As the latent heat of evaporation for R236fa is lower than for R134a, dryout occurs sooner for a given mass flux and less data are available for higher heat fluxes.

As the heat flux increases the difference between the local quality in the bundle and that represented by the mean vapour quality increases. The heat input from a given heat flux has less effect on vapour quality as the mass flux increases. Thus a prediction using only mean conditions does not include these interacting effects which occur for diabatic cases because of the vapour

91

quality, void fraction and mass flux interaction.
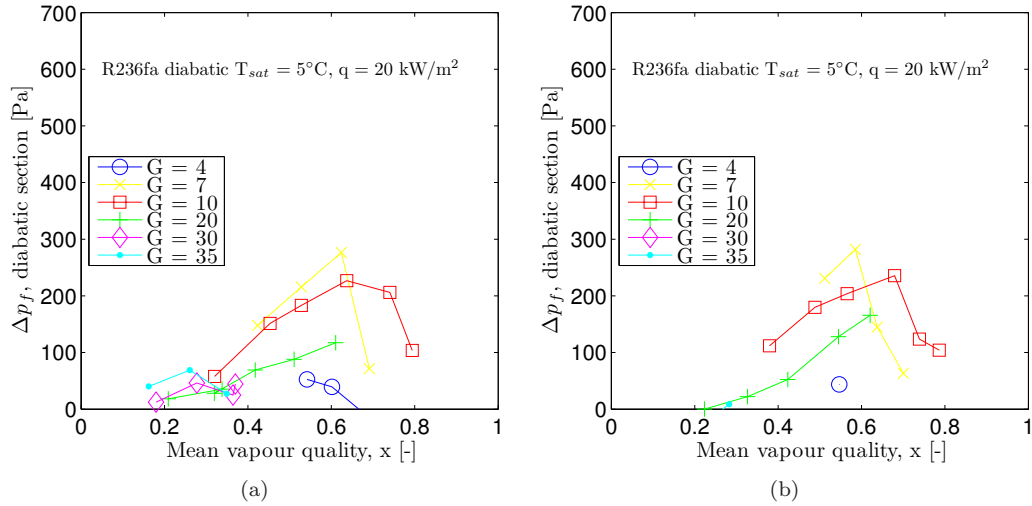
Figure 5.12: R236fa frictional pressure drop in diabatic conditions for a range of heat fluxes on the *Turbo-B5* and *Gewa-B5* tubes [(a) q = 20 kW/m^2 (b) q = 20 kW/m^2]

When plotting the same pressure drop data for some representative cases against the outlet vapour quality, the correspondence of onset of dryout with the sudden reduction in pressure drop at high vapour quality is clear (Figure 5.13). In general, for G = 4 and 7 kg/m^{2}s there are not many data points of dryout because of the very rapid onset of dryout and subsequent unstable operating conditions. The higher mass fluxes show an increase in outlet vapour quality and then onset of dryout. At the highest mass fluxes the heating power available is not enough to reach onset of dryout in the present facility.
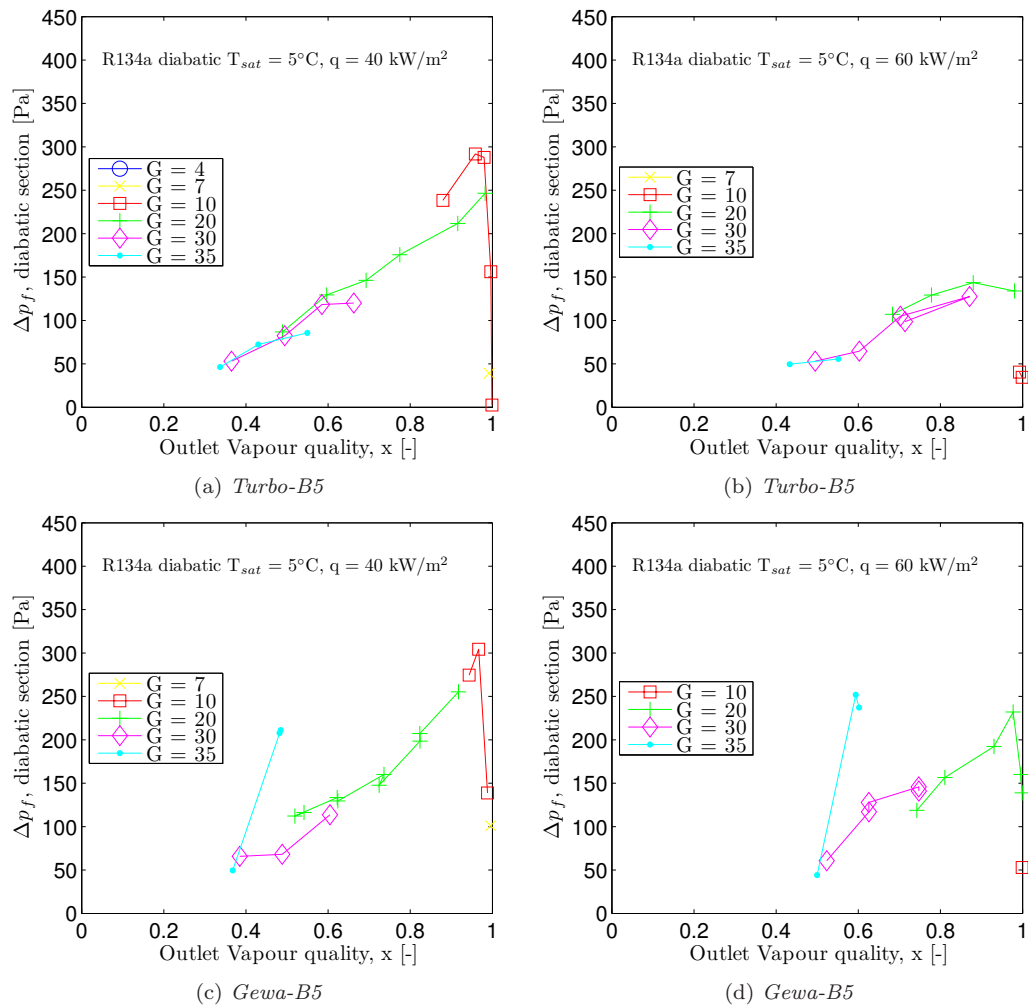
Figure 5.13: R134a frictional pressure drop in diabatic conditions for a range of heat fluxes on the *Turbo-B5* and *Gewa-B5* tubes plotted with outlet vapour quality to inspect the onset of dryout

5.3 Existing prediction methods

The two-phase, tube bundle pressure drop prediction methods described in Chapter 2 are compared with measurements of adiabatic and diabatic data taken during this study.

5.3.1 Adiabatic results comparison

The methods of Ishihara *et al.* (1980) and Xu *et al.* (1998b) are implemented as described earlier and both methods underpredict the present data (Figure 5.14). All data are presented together in one single figure per method. The full bundle and diabatic section pressure drop is used for

this comparison with all sections of the bundle operating adiabatically. The underprediction of these methods could be the result of poor comparative conditions (extrapolation) between the intended use of these methods and the present bundle configuration (fluids, geometry, tubes and sizes).
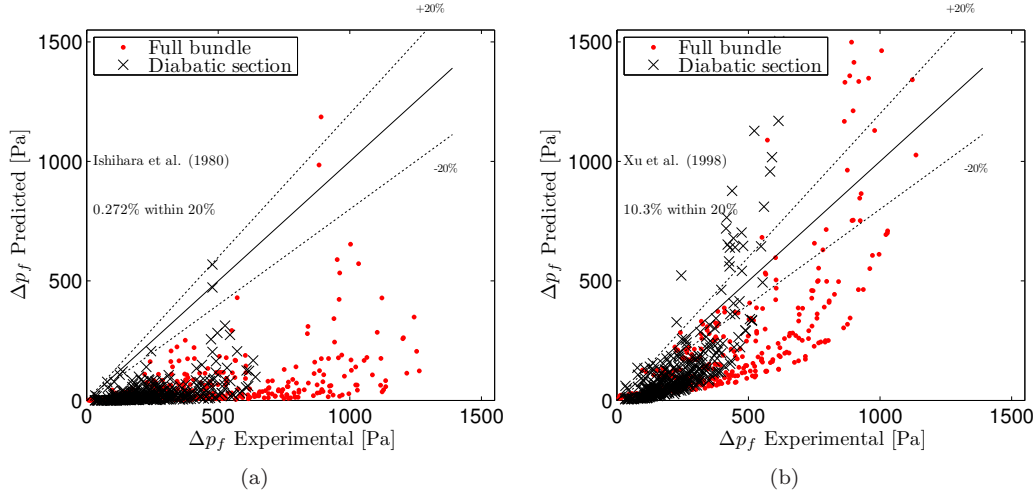
Figure 5.14: Comparison of (a) Ishihara *et al.* (1980) and (b) Xu *et al.* (1998b) with experimental data from this study measured over the full bundle and diabatic section

The method of Consolini *et al.* (2008) was based on diabatic data for smooth and enhanced tubes and compared against the adiabatic dataset (Figure 5.15). The diabatic nature of the prediction method means the vapour quality and void fraction were difficult to determine locally and averages had to be used as input for the method. Since the full bundle was diabatic when they conducted their experiment a large quality difference was present between inlet and outlet conditions and therefore the method was not local.

The method developed by Van Rooyen *et al.* (2011a) from the data in Agostini (2008) for adiabatic plain tubes in the bundle is based on local vapour qualities and void fractions. The method compares favorably with the data from the present study with only minor differences between the smooth tubes and enhanced tubes (Figure 5.16). In most cases around 60% of the data fall within ±20% of the prediction method and 80% fall within ±30%. The method has a slight bias to overpredict the enhanced tube pressure drop.

The comparisons made with prediction methods from other studies and the new method proposed in Chapter 8 are summarised in Table 5.2.
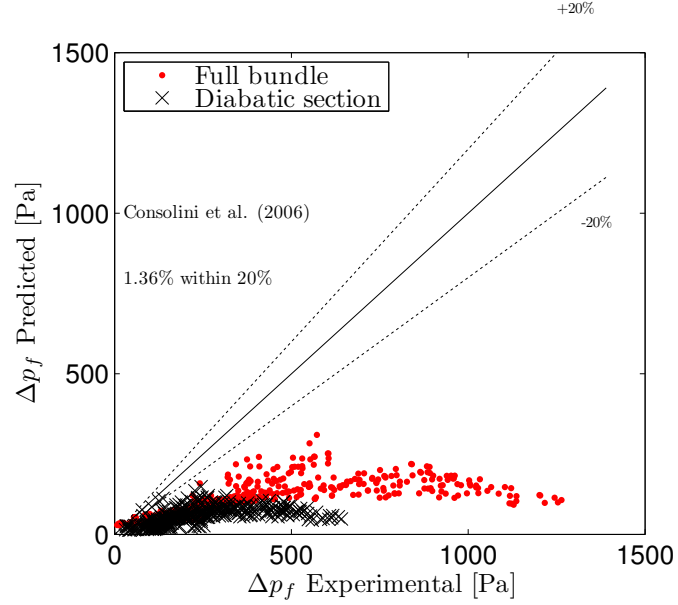
Figure 5.15: Comparison of the Consolini *et al.* (2008) method for the full bundle and diabatic section with experimental data from this study

Table 5.2: Prediction limits for the various prediction methods for frictional pressure drop

Test	Adiabatic data		Diabatic data	
Range	20%	30%	20%	30%
Ishihara *et al.* (1980)	1	1	7.2	10
Xu *et al.* (1998b)	10.3	16	18.2	28
Consolini *et al.* (2008)	1.4	2.5	9	16
Van Rooyen *et al.* (2011a)	67	79	29	36
Present method	88	93.5	37	53.4

5.3.2 Diabatic results comparison

The only method explicitly based on diabatic data is that of Consolini *et al.* (2008) and when compared against the present diabatic database (Figure 5.17) the method also generally underpredicts with only 12% of the data within the ±20% limit.

Applying the method of Van Rooyen *et al.* (2011a) to predict the diabatic data provides a fair comparison with general overprediction (Figure 5.18) but only 35% of the prediction falling within ±20% of the data. The experimental diabatic pressure drop is generally lower than predicted.
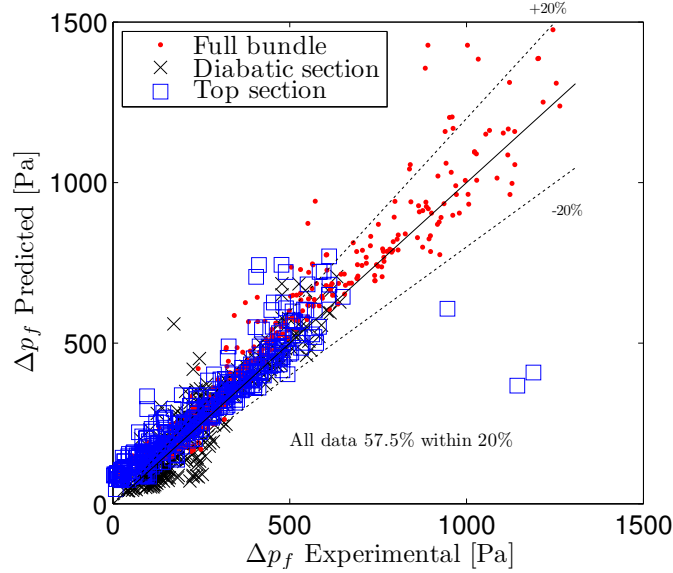
Figure 5.16: Comparison of the Van Rooyen *et al.* (2011a) method for the diabatic section, adiabatic section and full bundle with adiabatic experimental data from this study

5.4 Conclusion

Prediction of pressure drops for flow over tube bundles is required during the thermal design, yet they are still difficult to predict. The inability of methods to cater to local conditions in diabatic testing is one aspect that needs to be addressed by getting local data of all flow parameters. Most methods are empirical and therefore limited in application. The difference between conditions of adiabatic and diabatic flow and the possibility of inlet effects during flow development are not easily included in a model. The adiabatic data are measured at uniform vapour quality with only the flow structure changing as the flow passes over the bundle. These flow-induced effects are not included in the void fraction or pressure drop model and for the time being remain beyond reach. The proposed prediction method is based on the hypothesis that the adiabatic pressure drop will be able to predict the diabatic pressure drop as the increment of evaluation becomes ever smaller and therefore more local. As the more complex nature of external flows over tubes with and without heat transfer becomes better understood, proper models of physical behaviour can replace these empirical approaches. The bundle geometry was not investigated during this study, however this geometry adds factors *e.g.* tube layout, tube pitch and tube diameters to the effects that must be investigated.
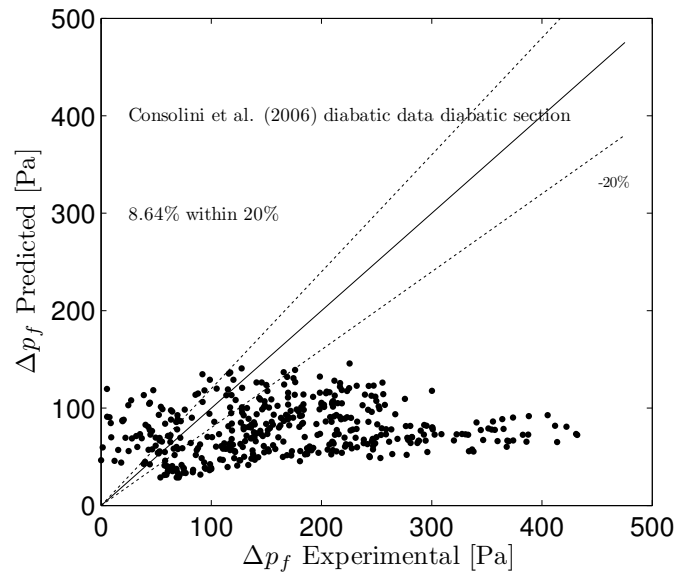
Figure 5.17: Diabatic pressure drop over diabatic bundle section compared with Consolini *et al.* (2008)
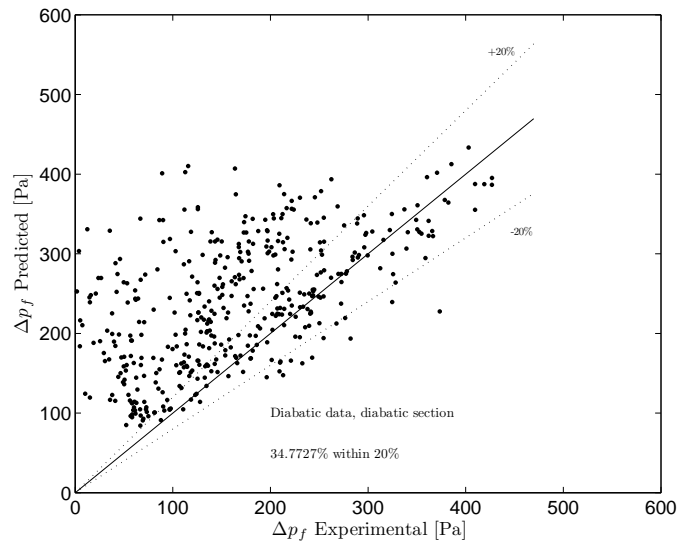
Figure 5.18: Diabatic pressure drop over diabatic bundle section compared with Van Rooyen *et al.* (2011a)

Chapter 6

Heat transfer results

Bundle effects previously investigated in the literature and described in previous chapters include: flow induced convection, tube row effect, onset of dryout and flow patterns (bubbly, dispersed, annular and mist flow), heat flux effect in a bundle, vapour quality, mass flux, tube type, tube layout, refrigerant type and the effects of oil. The main objective of the current heat transfer study was to investigate bundle boiling and possible bundle effects.

In this chapter the heat transfer results of all the tests done with the tubes are given. These encompass Wilson plot and pool boiling type tests to characterise the tubes inside and outside heat transfer coefficients and bundle boiling tests with convection. Water-water test results of the inside heat transfer coefficient are given as validation of the Wilson plot method results (Appendix B.5). The methods for determining the heat flux and outside heat transfer coefficient were described in Chapter 3.

6.1   Wilson plot

A modified Wilson plot method was implemented to characterise the heat transfer coefficient on the inside of the enhanced tubes. Two tubes were tested in this experimental phase, namely the *Wolverine Turbo-B5* and the *Wieland Gewa-B5*.

6.1.1   Experimental matrix

The modified Wilson plot tests were conducted over a water-side Reynolds number range of 8000 to 18000. Three saturation temperatures were tested, namely 5, 10 and 15°C. Finally, tests were performed at heat fluxes ranging from 15 to 60 kW/m^2. These conditions mimic the conditions that will be present during pool boiling and bundle boiling and consequently the Wilson plot

will be valid exclusively for the conditions that were used within the experimental range. The
experimental conditions achieved during testing are summarised in Table 6.1.

Table 6.1: Nominal experimental conditions for Wilson plot experiments

	Wolverine Turbo-B5	*Wieland Gewa-B5*
T_{sat} [^{o}C]	5,10,15	5,10,15
$\dot{q}$ [kW/m^2]	15–60	15–60
Re_{wat}	8–18·10^3	8–18·10^3
Refrigerant	R134a	R134a

6.1.1.1 Modified Wilson plot results

The data gathered in the experimental phase were used as input for the LTCM modified Wilson
plot method. For the *Wolverine Turbo-B5*, the tube-side Wilson plot for these data is presented in
Figure 6.1a, while for the *Wieland Gewa-B5*, the tube-side Wilson plot is shown in Figure 6.1b.
The coefficient of determination for the *Turbo-B5* data was $R^2 = 0.98$, while for the *Gewa-B5* it was $R^2 = 0.89$. The data at the lowest heat fluxes (< 30 kW/m^2) showed a larger
experimental uncertainty due to the smaller temperature difference between the water-side and
the high refrigerant-side heat transfer coefficients ($\Delta T < 0.5\,K$). This influenced the calculated
values of the uncertainty in x and y. The values of C_i, C_o and n derived from the successive
linear regressions are tabulated in Table 6.2.
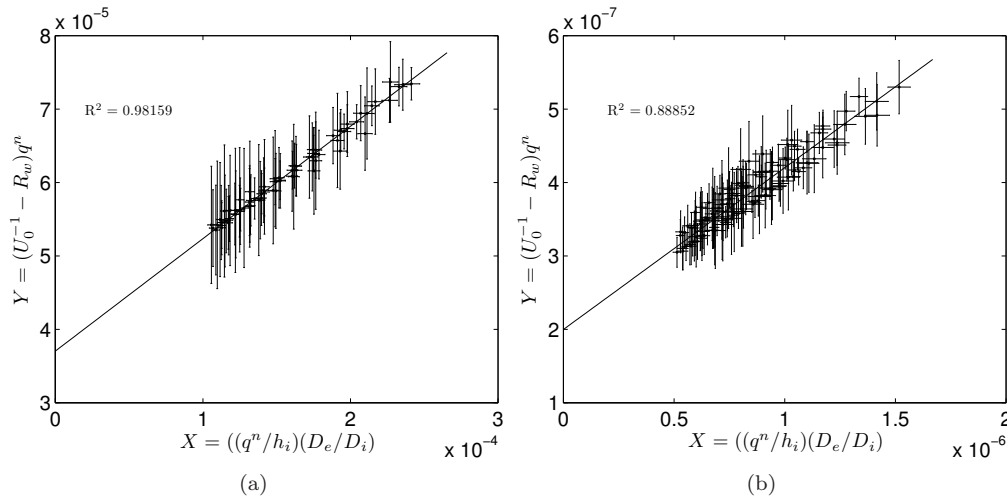
Figure 6.1: Tube-side Wilson plot for the (a) *Wolverine Turbo-B5* and (b) *Wieland Gewa-B5*
tubes

Table 6.2: Wilson plot coefficients for the *Turbo-B5* and the *Gewa-B5* tubes from the bundle boiling facility

	Turbo-B5	Gewa-B5
C_i	6.7279 ± 0.501	4.49 ± 0.301
C_o	20700	$1.35 \cdot 10^6$
n	0.029	-0.367

6.1.1.2 Optimisation algorithm results

The solution with the data were also minimized using the method described in Appendix B.4.4. The results from this analysis are shown in Table 6.3. In this method, no uncertainties can be determined. The results from the optimisation are within the quoted uncertainty range for the LTCM modified Wilson plot method, shown in Table 6.2.

Table 6.3: Wilson plot coefficients using the nonlinear least-squares method for the *Wolverine Turbo-B5* and the *Wieland Gewa-B5* tubes

	Turbo-B5	Gewa-B5
C_i	6.6552	4.52
C_o	25000	$4.28 \cdot 10^6$
n	0.018	-0.472

6.2 Measurement system validation

To ensure accuracy and to substantiate the results found, the measurement and reduction methods had to be validated. Since all heat transfer results would be dependent on the Wilson Plot, considerable effort was spent on the validation. This includes: comparison between two LTCM test facilities; independent programming of multiple data reduction methods; and direct wall temperature measurements. More details concerning the Wilson plot method and its implementation during this study is provided by Christians (2010) and Van Rooyen *et al.* (2011b).

6.2.1 Comparison against the falling film facility's results

Christians (2010) performed the same tests using the same tubes and the same method in the LTCM falling film facility. The main difference between the facilities was the heated length of the tube, *i.e.* 1.027 m in the bundle and 0.554 m in the falling film facility. The falling film facility's values for the internal enhancement coefficient were within the uncertainty range of the

two measurements (Table 6.4). Overall, the uncertainty in the bundle boiling facility is lower, primarily as a result of the larger temperature difference of the water-side of the longer tube. The external enhancement coefficients differ, but if the two correlations are plotted for the range of test heat fluxes, there is adequate agreement between the two plots indicating a weak local minimum and several possible good solutions.

Christians (2010) also utilised the minimisation method described previously and found that the values for the internal enhancement between the two facilities were essentially identical for the Wolverine tube (Table 6.4). A larger difference was found for the Wieland tube. The results remain within the range of uncertainty. It should be noted that the Wieland tubes used in the two facilities were not from the same manufacturing batch.

Table 6.4: Wilson plot coefficients for the *Turbo-B5* and the *Gewa-B5* tubes in the falling film facility (Christians, 2010)

	Turbo-B5	Gewa-B5
LTCM method		
C_i	6.2158 ± 0.8	4.1708 ± 0.5398
C_o	10600	$5.72 \cdot 10^6$
n	-0.113	-0.479
Minimisation		
C_i	6.6557	4.2454
C_o	25000	$5.02 \cdot 10^6$
n	-0.112	-0.469

The Wilson plot measurements were compared against direct heat transfer coefficient measurements performed on a simple tube-in-tube water-to-water test section. The detail of this validation experiment and the results are presented in Appendix B.5. The conclusion of the direct wall temperature measurement was that the heat transfer coefficients predicted by the Wilson plot method used in this study are within 5% of the direct measurements.

6.2.2   Summary of modified Wilson plot method

The modified LTCM method was applied to experimental data obtained with the two tubes tested in this experimental phase. An optimisation method was developed and implemented, and shown to give similar results to the modified Briggs and Young methodology. The results compared favourably with independent Wilson Plot experiments and direct water-to-water measurements. Results were shown to be repeatable as well as reproducible on two installations. The successful

comparison against data gathered using a direct method confirms the reliability of the modified Wilson plot method and the minimisation method used here.

6.3 Pool boiling results

The pool boiling curve of a tube constitutes an important measure of performance. These pool boiling curves are later used as benchmark for boiling when convection is present by means of the ratio between the convective heat transfer coefficient and the pool boiling coefficient (bundle factor). From this point on, the Wilson plot result is implemented for the inside heat transfer coefficient and the external heat transfer coefficient result is considered the final result of interest.

The experimental ranges used for measuring the nucleate pool boiling curves are stated in Table 6.5. At low saturation temperatures the maximum power available from the cold source was limited. A larger temperature difference between the cold source and the saturation temperature allowed higher heat fluxes to be achieved.

Table 6.5: Pool boiling experimental test conditions for *Turbo-B5* and *Gewa-B5* tubes

	Turbo-B5	*Gewa-B5*
Test fluids	R134a, R236fa	R134a, R236fa
Tube layout	1 tube	1 tube
Saturation temperature	5, 10 and 15°C	5, 10 and 15°C
Reduced pressure range	$0.04 - 0.12$	$0.04 - 0.08$
Local heat flux	15-80 kW/m^2	15-60 kW/m^2
Water Reynolds number	~ 11000	~ 11000

6.3.1 *Wolverine Turbo-B5*

The results are grouped by refrigerant in Figures 6.2a and 6.2b. Each figure contains all the temperatures investigated and there was no large dependence on saturation temperature for either refrigerant in the present range. The heat transfer coefficient was either constant over the heat flux range tested or there was a decrease in heat transfer coefficient as the heat flux increased. The R236fa results were lower than R134a for all temperatures and heat fluxes. There are presently no independent data available for comparison. A discussion of tube performance in relation to the previous tube types tested at the LTCM is presented in Christians (2010).

The pool boiling curve experiments done on the falling film facility for exactly the same conditions are presented as comparison in Figure 6.3. For both refrigerants the results of the
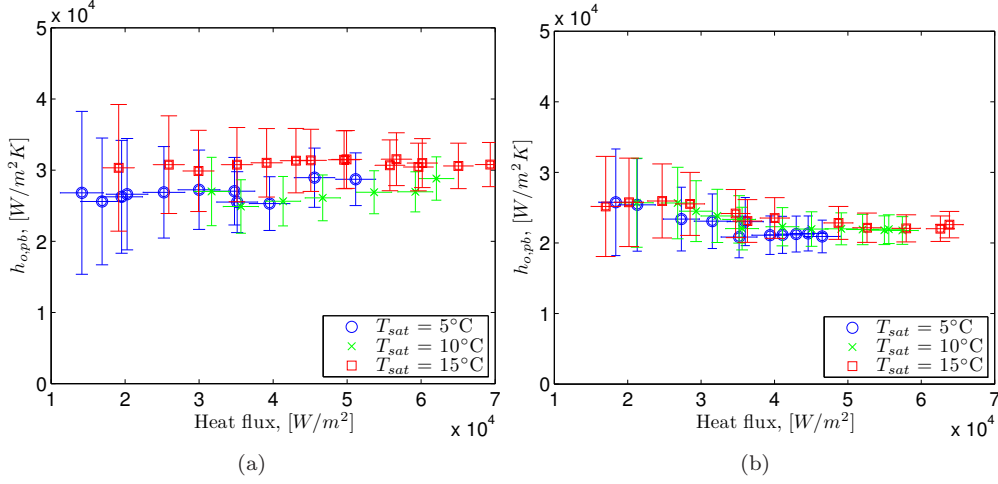
Figure 6.2: Pool boiling measurements on the *Turbo-B5* tube at all temperatures with (a) R134a and (b) R236fa

bundle boiling facility and the falling film facility were similar and always within the experimental uncertainty of either experiment. Due to the lower uncertainty of the heat flux measured in the bundle boiling facility and the fact that the refrigerant temperature was not inferred from pressure measurements, but directly measured by three arrays of seven thermocouples, there is more confidence in measurements from the bundle. The data compare very well over the entire range of heat flux except for the lower heat fluxes, where the bundle boiling facility has lower values. The strong increase in heat transfer coefficient in the falling film facility was attributed to the deduction of temperature from the refrigerant pressure (Christians, 2010). Detailed comparisons between the two facilities are presented in Christians (2010). Both tubes compared well in the two facilities and no further comparisons are presented here.

6.3.2 *Wieland Gewa-B5*

The results for the *Wieland Gewa-B5* tube are sorted by refrigerant in Figures 6.4a and 6.4b. All the temperatures investigated are presented together. No strong dependence on saturation temperature was noted. At lower heat fluxes the heat transfer coefficient of different saturation temperatures were not significantly different when compared to the uncertainty. There was a general decrease in heat transfer performance with an increase in heat flux in this tube for both refrigerants. The R236fa results were lower than R134a for all temperatures and heat fluxes. There are presently no external databases available for comparison.
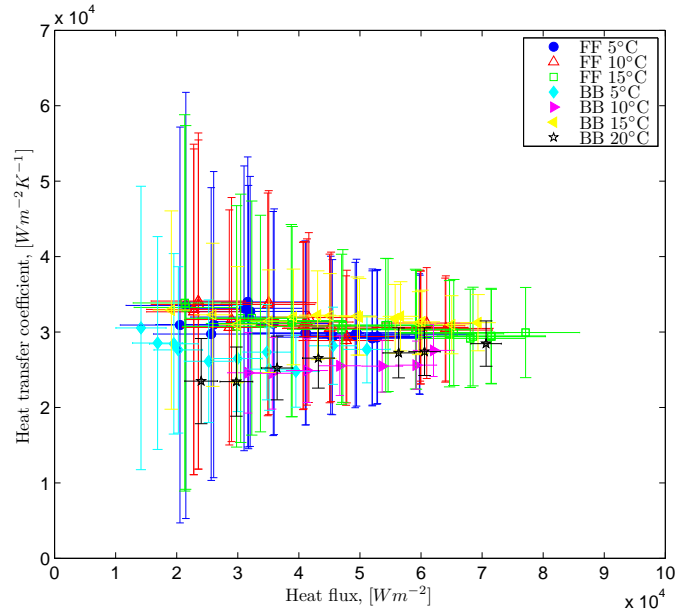
Figure 6.3: Comparison of R134a pool boiling measurements on the *Turbo-B5* tube performed on the LTCM's falling film (FF) and bundle boiling (BB) facilities
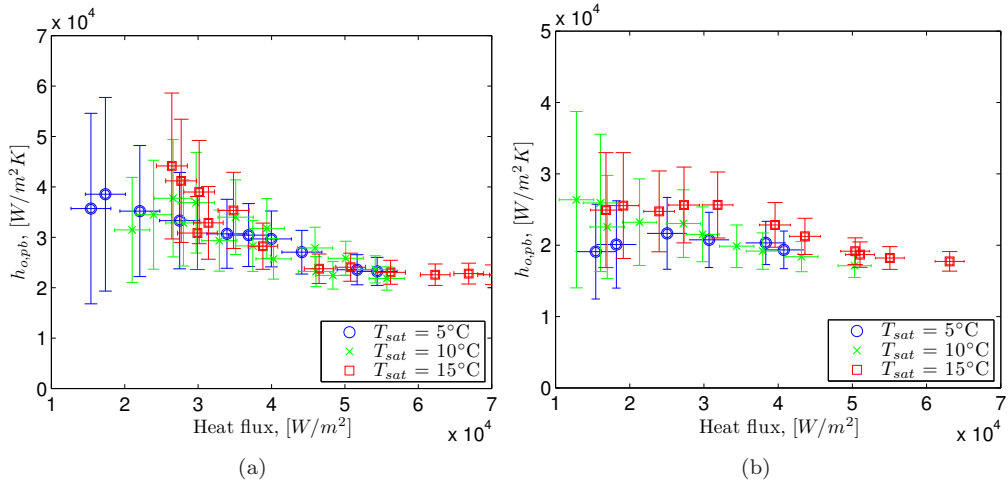
Figure 6.4: Pool boiling measurements on the *Gewa-B5* tube at all temperatures with (a) R134a and (b) R236fa

6.3.3 Discussion and comparison

Factorial testing of the pool boiling data revealed that the refrigerant had the strongest effect on the heat transfer coefficient (Table 6.6). The heat flux had a relatively large impact and the

Table 6.6: Factorial test results for pool boiling with main effects and selected interactions

Effect	A[a]	B[b]	C[c]	D[d]	AB	AC	BC	BD	CD
Factors	2469.8	-5766.9	-8157.7	-526.5	-1994.8	-1154.4	1871.3	-4501.5	-2705.8
t ratio	0.7	-1.7	-2.4	-0.2	-0.6	-0.3	0.6	-1.3	-0.8
Significance	0.29	0.09	0.03	0.39	0.33	0.37	0.33	0.16	0.28

[a] Temperature [b] Heat flux [c] Refrigerant [d] Tube type

tube type did not affect the heat transfer significantly. The saturation temperature had a larger effect than tube type, but neither was significant. As a result, any empirical correlation that can capture the effect of refrigerant and heat flux should be successful. For the two tubes in question the performance is similar, however the tube type and geometry is of major importance in understanding the process during boiling and for a mechanistic model.

The factorial test only compared two data points per main variable. The conditions selected were as close as possible to the extremities of the experimental ranges and the method assumed linear interactions, as follows:

$$
\begin{aligned}
h_o &= f(T_{sat}, q, \text{Refrigerant}, \text{Tube}) \\
\text{options:} \, T_{sat} &= \begin{pmatrix} 5 \\ 15 \end{pmatrix} \quad q = \begin{pmatrix} 20 \\ 60 \end{pmatrix} \quad \text{Refrigerant} = \begin{pmatrix} 1 \\ 2 \end{pmatrix} \quad \text{Tube} = \begin{pmatrix} \textit{Turbo-B5} \\ \textit{Gewa-B5} \end{pmatrix}
\end{aligned}
$$

A tube-specific heat transfer prediction can be made in its simplest form by grouping the data per tube, per refrigerant and per temperature. This allows an accurate fit with a simple Cooper type nucleate pool boiling relation ($C_o q^n$) that groups all the factors, such as roughness, molar mass, reduced pressure and tube material, into a single leading coefficient (C_o). For a tube-specific comparison the curve fits for data from this study are presented in Table 6.7. The problem becomes awkward to manage when a multitude of tube and refrigerant combinations need to be accounted for. This problem was addressed by Christians (2010) by using dimensional analysis to isolate a π-group with strong correlating characteristics over wide-ranging conditions for enhanced tubes. The Christians (2010) approach was similar to that followed in the past by Stephan and Abdelsalam (1980) and Jabardo *et al.* (2004) but the primary objective was to develop a method specific for enhanced tubes. The issue of different enhanced tube geometries was addressed by a tube-specific factor. This factor was not characterised by the geometry of the tubes because each enhanced tube functions differently and has unique geometrical attributes. This means that the same metric can not be used for different tubes. Therefore, a general method for enhanced tubes

is still elusive and will probably remain so until a complete and accurate mechanistic model can be applied to the myriad of enhanced geometries available.

Table 6.7: Empirical coefficients for pool boiling on the *Wolverine Turbo-B5* and *Wieland Gewa-B5* tube per refrigerant in the form: $h_{pb}=C_o q^n$

	Wolverine Turbo-B5		*Wieland Gewa-B5*	
	C_o	n	C_o	n
R134a	12026	-0.082	2503123	-0.4221
R236fa	103482	-0.143	164837	-0.1978

The present pool boiling data for both refrigerants and tubes were compared against the prediction method proposed in Christians (2010) (Figure 6.5) where a combination of symbols is used to represent the tube/fluid combination. This method was created by using a database of seven enhanced tubes and two refrigerants. Direct application of the method predicted 76% of the data within $\pm 20\%$.
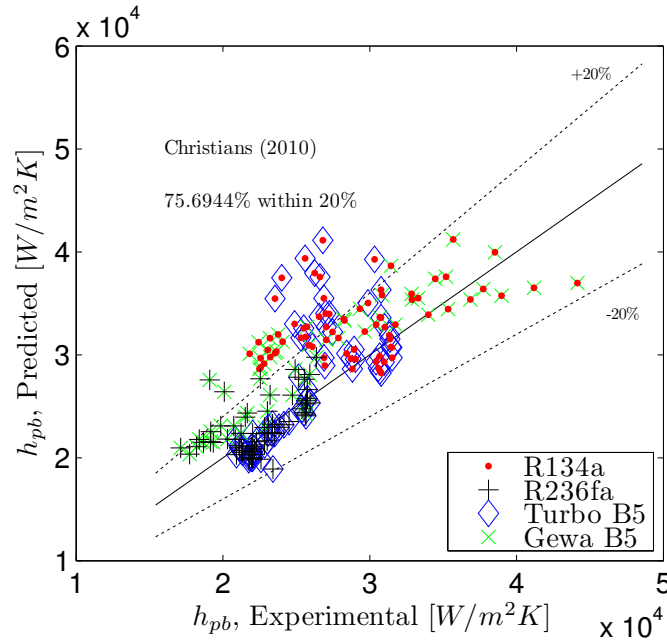
Figure 6.5: Comparison of all experimental pool boiling measurements of the current study and the prediction method presented by Christians (2010)

The lower uncertainty of the bundle boiling facility enabled experiments to be run with heat fluxes lower than 20 kW without causing an unrealistic error. The error bars indicate that, for the present instrumentation, the error increased exponentially as the heat flux decreased. The

uncertainty was related to the measured quantities. The mass flow measurements made with Coriolis flow meters did not add significantly to the uncertainty of the heat flux. The dominant contributor to uncertainty was temperature difference, which was related directly to the heat flux calculation. Also the temperature difference through the tube wall between the refrigerant and the water, is directly related to the heat transfer coefficient. These two components interact as the heat flux, water mass flux and heat transfer coefficient vary. The uncertainties in both the heat flux and the heat transfer coefficient were lowest at the higher heat fluxes tested, due to the increased temperature gradient in the water, and the increased difference in temperature between the water and the saturated refrigerant. A higher heat transfer coefficient at a given heat flux will result in a higher uncertainty because the temperature difference across the wall would be lower. The experimental uncertainties in the heat flux and the measured pool boiling heat transfer coefficients are tabulated in Table 6.8 for both tubes.

Table 6.8: Experimental uncertainties of the measured heat fluxes and pool boiling heat transfer coefficients using the *Turbo-B5* and *Gewa-B5* tubes at all saturation temperatures tested

	Wolverine Turbo-B5					
	R134a			R236fa		
	δ_{min}	δ_{max}	δ_{avg}	δ_{min}	δ_{max}	δ_{avg}
q	1.83%	20.54%	5.8%	2.17%	12.54%	5.35%
h_{pb}	6.5%	42.7%	14.7%	6.04%	29.34%	12.19%
	Wieland Gewa-B5					
	δ_{min}	δ_{max}	δ_{avg}	δ_{min}	δ_{max}	δ_{avg}
q	2.81%	17.64%	6.93%	3.11%	18.07%	8.51%
h_{pb}	8.52%	52.93%	20.75%	7.75%	46.85%	20.37%

The tubes are designed for operating with R134a. It appears that the tubes are designed to perform at or near a maximum for the higher temperatures and the lower range of heat fluxes tested. That indicates a pore diameter that allows sufficient exchange of liquid and vapour over this range without flooding or drying out the "tunnels" in the enhancement geometry.

The reduced pressure is a powerful correlating parameter, but merely as a surrogate for the dynamics controlling the mechanisms of boiling at different temperatures and fluids. The fluid properties, such as viscosity, surface tension and latent heat of vaporisation are temperature-dependent and they have a direct impact on the liquid intake and evaporation processes. Thome (1990) showed that at high reduced pressures, the advantage of using enhanced surfaces is diminished, because nucleation sites on plain tubes are already activated due to a decrease in the required activation superheat. The mechanisms of heat transfer at nucleation sites of bubbles are

near-wall evaporation, interface evaporation and transient sensible heating with associated fluid property dependencies. If the dominant heat transfer mechanism is thin film evaporation at high reduced pressures when nucleation sites are active all over the surface, this mechanism would be similar to that expected inside enhanced surfaces.

Habert (2009) stated that the very high enhanced surface heat transfer coefficients that decreased with increasing heat flux were attributed to 'a throttling effect of the pore opening on the inflow of liquid and the escape of liquid'. The decreasing trend reported might correspond to a progressive, partial dryout of the channels within the enhancement structure. This was observed by Arshad and Thome (1983). If the film inside a tunnel was thick, a lower liquid supply and thus thinner film would improve the meniscus heat transfer unless the wall material or local liquid distribution are limiting factors. The cross-sectional distribution and circumferential distribution of phases in the tunnels remain unknown. If flooding increases locally due to a change in liquid intake with heat flux, the heat transfer would be affected. The fact that R236fa performs poorly compared to R134a is testament to the fact that these tubes were probably not designed for this fluid and therefore the performance drop is also more severe as heat flux increases.

Isolating any single physical property and attributing lower or higher heat transfer to it is unlikely, because of the many mechanisms interacting to produce the final result. If one fluid had a 20% lower latent heat this could reduce the heat transfer, but if the surface tension of this fluid was high enough to ensure a thin film in most tunnels rather than a flooded state, the 20% reduction in latent heat could easily be compensated without considering the external heat flux. A simple one-size-fits-all explanation is unlikely. The mechanisms of boiling in and on enhanced tubes are discussed and analysed in Chapter 7 and Appendix C in an attempt to find a phenomenological correlation with a strong relation to the fluid properties that control these mechanisms.

A final comparison of the two tubes was done by comparing the overall thermal resistance (Figure 6.6). The *Wolverine Turbo-B5* tube performed slightly better and more consistently in terms of overall resistance. The *Wieland Gewa-B5* tube performed equally well at low heat fluxes, but its performance decreased slightly at higher heat fluxes.
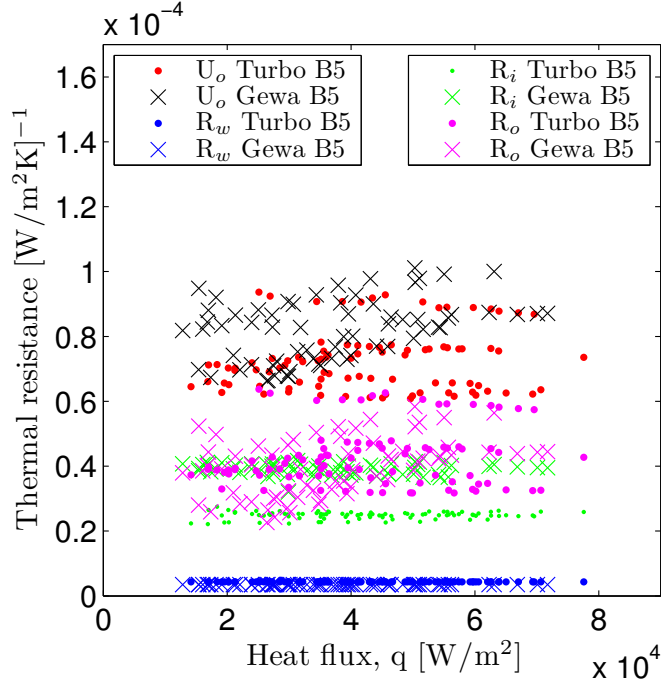
Figure 6.6: Overall thermal resistance for both tubes with the components for inside, wall and outside thermal resistances indicated

6.4 Convective boiling

Factorial analysis of the bundle boiling data revealed that the refrigerant had the largest effect (Table 6.9). Each pair of conditions evaluated for the factorial analysis is presented below:

$$h_o = f(G, q, Refrigerant, Tube)$$
$$\text{options:} G = \begin{pmatrix} 7 \\ 30 \end{pmatrix} \quad q = \begin{pmatrix} 20 \\ 60 \end{pmatrix} \quad \text{Refrigerant} = \begin{pmatrix} 1 \\ 2 \end{pmatrix} \quad \text{Tube} = \begin{pmatrix} \textit{Turbo-B5} \\ \textit{Gewa-B5} \end{pmatrix}$$

The heat flux was the second largest effect, which was still relatively significant. The mass flux effect was negligible and each tube had a different heat transfer coefficient although the difference was not significant. Interactions were not significant. The vapour quality was tested separately and found to have a minor impact on the heat transfer coefficient. For a similar analysis including vapour quality the factor was 1514 with a t-ratio of 0.3 and significance of 0.38. Similar conclusions were reported by Jensen *et al.* (1992) and Kim *et al.* (2002).

Below, some representative data are first presented in the classical heat transfer coefficient against vapour quality type of plot. The most notable characteristic of the data was that a large

Table 6.9: Factorial test results for bundle boiling with main effects and selected interactions

Effect	A[a]	B[b]	C[c]	D[d]	AB	AC	BC	AD	CD
Factors	691.5	-6193.6	-7825.5	-4902.1	-772.3	977.0	-524.6	-1148.4	-961.5
t ratio	0.2	-1.7	-2.2	-1.4	-0.2	0.3	-0.1	-0.3	-0.3
Significance	0.38	0.09	0.05	0.16	0.38	0.38	0.39	0.37	0.38

[a] Mass flux [b] Heat flux [c] Refrigerant [d] Tube type

Table 6.10: Experimental conditions for enhanced tube bundle boiling tests

Experimental test conditions	
Test fluid	$R134a$, $R236fa$
Saturation temperature	T_{sat}=5, 15 [°C]
Wolverine Turbo-B5	D_o=18.95 [mm], D_i=15.75 [mm]
Wieland Gewa-B5	D_o=19.05 [mm], D_i=15.30 [mm]
Tube pitch	P=22.22 [mm]
Tube layout	Staggered equilateral
Vapour quality	x=0.1-0.9 [$-$]
Mass velocity	G=4, G=7, 10, 20, 30, 36 [kg/m^2s]
Heat flux	q_o=0, 20, 40, 60 [kW/m^2]

number of points had essentially the same heat transfer coefficient. Therefore, plotting them together was not ideal. Secondly, a new method of presenting the data, where mass flux and vapour quality (both of minor significance) are combined into a liquid film Reynolds number for bundle flow, is introduced (discussed below).

In Figure 6.7, the 5°C data for R134a with Turbo-B5 at all heat fluxes are presented. The heat fluxes were grouped into nominal groups around 20, 40 and 60 kW/m^2 with some experiments also done at 15 kW/m^2. The slight decrease normally seen in the second pass (r2) can be attributed to the lower local heat flux from the water when compared with the first pass (r1). In this figure the heat flux difference was most important. The saturation temperature did not influence the heat transfer significantly and trends were similar for other parameters. The Gewa-B5 results showed a larger impact of heat flux similar to the pool boiling results (Figure 6.8). The performance of both tubes remained constant with mass flux and vapour quality as indicated by the statistical analysis. Data that deviated sharply from the normal heat flux dependent plateau behaviour can be attributed to the onset of dryout conditions.

To consolidate these plots, a different method of presentation was required to reduce the
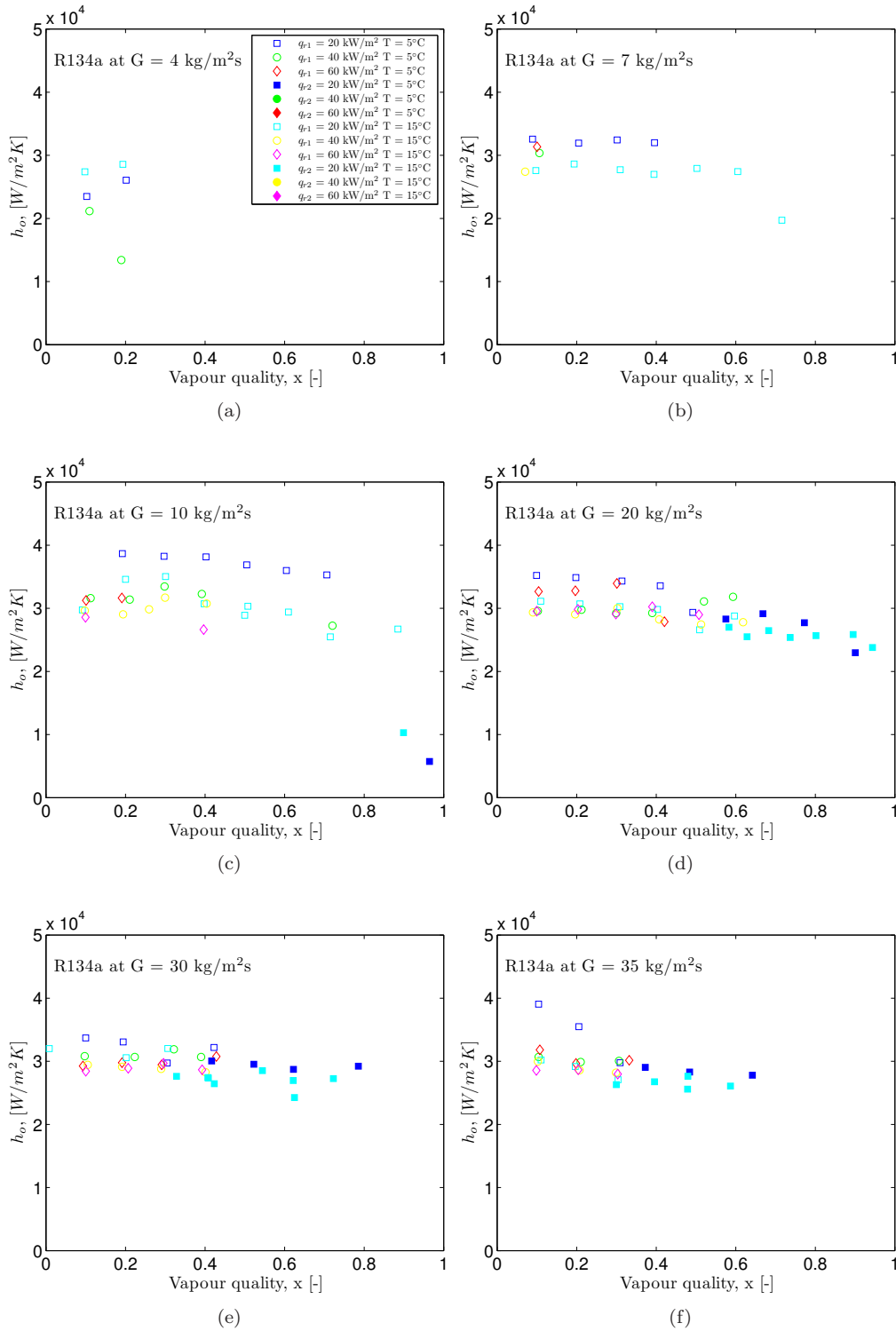
Figure 6.7: Heat transfer coefficient for all heat fluxes at 5°C and 15°C on the *Turbo-B5* tube with R134a and separated by mass flux per subfigure
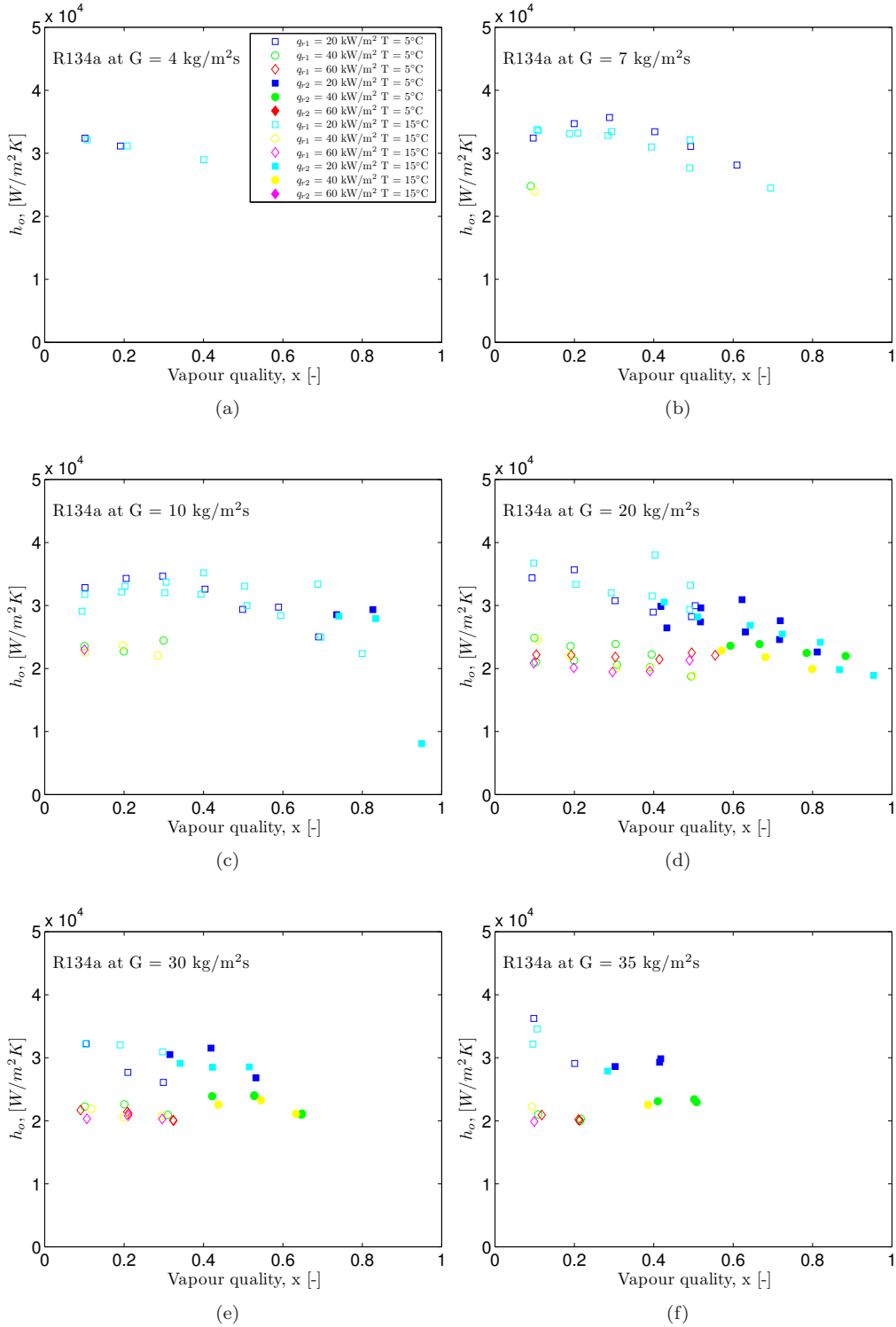
Figure 6.8: Heat transfer coefficient for all heat fluxes at 5°C and 15°C on the *Gewa-B5* tube with R134a and separated by mass flux per subfigure

control variables. The mass flux and vapour quality can be combined by obtaining a liquid only mass flow rate. Rather than using a dimensional value such as the liquid mass flow rate a liquid film Reynolds number is more appropriate. This can be used as a single variable to present all the mass fluxes and vapour qualities (Figure 6.9).
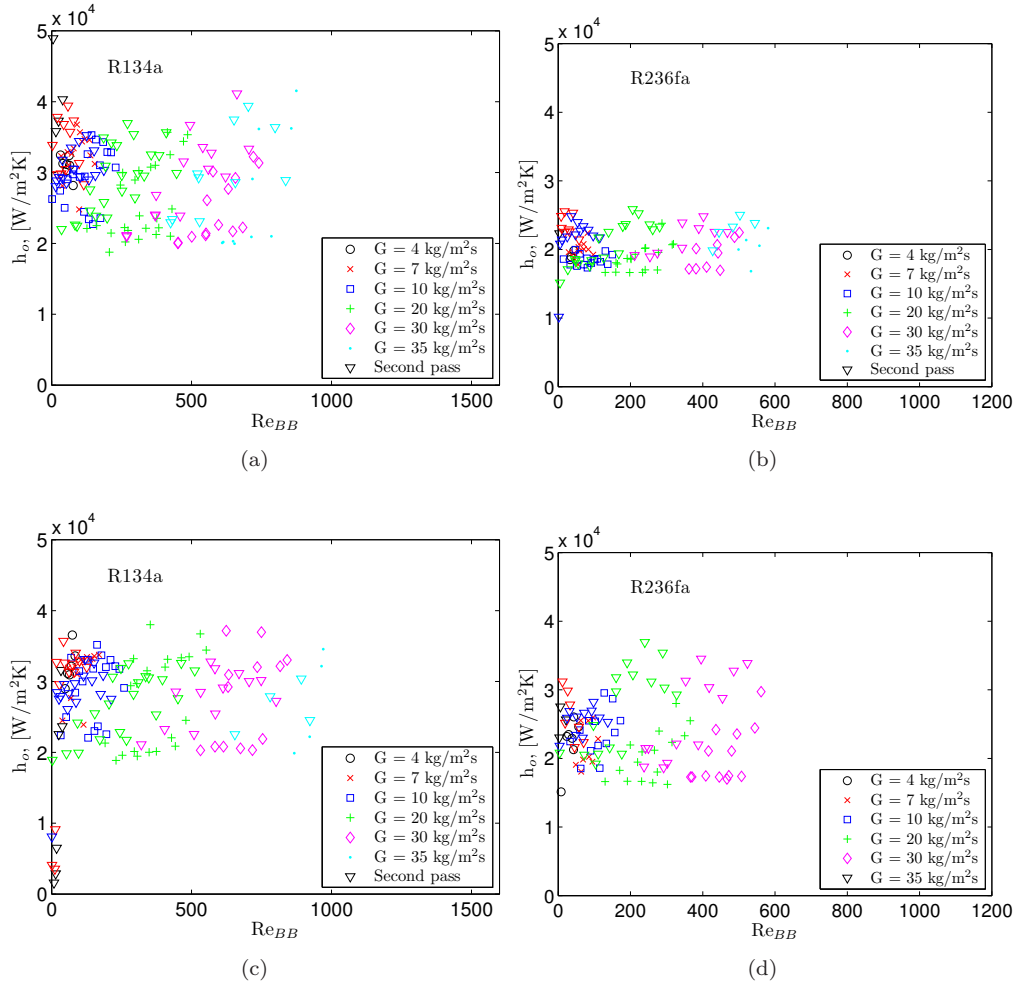
Figure 6.9: The Reynolds number presentation sorted by mass fluxes for each refrigerant, for the *Gewa-B5* tube at (a,b) 5°C and (c,d) 15°C

The present Reynolds number is defined in the same manner as that of a falling film experiment, thus a direct parallel between the two bundle heat transfer modes can be drawn. The liquid only mass flow rate, as the flow leaves the tube, was used to define a Γ for a single tube and this local Γ (flow rate in kg/s per unit length on one side of the tube) was used to define a local film Reynolds number. The set of equations to derive the Reynolds number from the measured

mass flow rate is described below for the test bundle (equation 6.1). The assumption is similar to the redistribution of the liquid film around the tube, but void fraction is not required. Since the flow is well distributed and in almost all the flow patterns observed during the experiments the liquid tended to remain attached to the tubes, the assumption is acceptable, if not always exact.

$$
\begin{aligned}
\dot{m}_l &= \dot{m}_t(1-x) \\
\dot{m}_{tube} &= \frac{\dot{m}_l}{number\ of\ tubes} = \frac{\dot{m}_t(1-x)}{3} \\
\dot{m}_{one\ side} &= \frac{\dot{m}_{tube}}{2} \\
\Gamma &= \frac{\dot{m}_{one\ side}}{L} \\
Re &= \frac{4\Gamma}{\mu_l}
\end{aligned}
\tag{6.1}
$$

6.4.1 Discussion for *Wolverine Turbo-B5* and *Wieland Gewa-B5* with convection

The Reynolds number presentation of data indicated a plateau of heat transfer that was maintained as long as the onset of dryout was avoided. Jensen *et al.* (1992) and Kim *et al.* (2002) found a lack of dependency of heat transfer on mass flux for their high performance enhanced tubes. There was almost no Reynolds number effect, indicating that convection had little impact on the heat transfer coefficient. Any convection effects could be through the external component of the heat transfer or due to the convection affecting the bubble cycle and thereby the liquid intake. The fact that the performance was similar to pool boiling indicate that these convective effects were limited or that they are not the dominant heat transfer mechanisms.

A change in vapour quality in bundle boiling had little impact on heat transfer. This is noteworthy because the vapour quality range represented a significant change in conditions on the outside of a tube from a discrete bubbly type flow to an annular liquid film with a fast moving vapour phase. The increase in saturation temperature decreased the heat transfer coefficient slightly. The refrigerant type had similar effects on the bundle heat transfer compared to pool boiling. The R134a refrigerant performed better then R236fa for all conditions.

The onset of dryout occurred as the Reynolds number reduced to zero. The onset of dryout was found at very low Reynolds numbers and this was thought to be due to the vertical upward flow through the bundle that keeps the liquid phase together and mixed between tube rows until close to the superheated transition. The partial dryout zone of heat transfer is very limited in
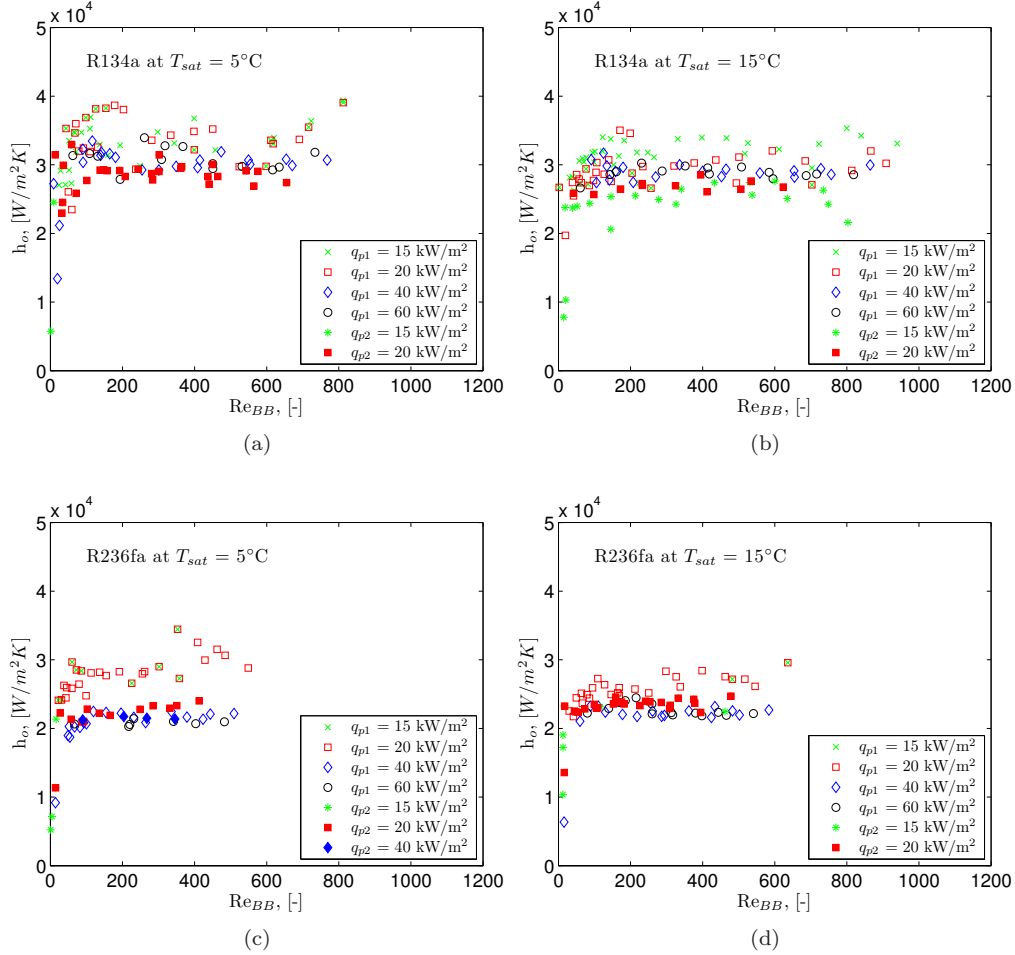
Figure 6.10: The *Turbo-B5* tube at saturation temperatures of 5°C with (a) R134a and (b) R236fa and at 15°C with (c) R134a and (d) R236fa at different heat fluxes for the first and second pass

bundle boiling compared to falling film where the vertical downward flow falls from tube to tube. The higher film velocity in falling film means the films are much thinner and thus prone to local dryout and subsequent lower performance. In falling film partial dryout can be induced on a tube at significantly higher Reynolds numbers than in bundle boiling. Furthermore, the column and drop flow regimes of a falling film also tend to promote local dry patches along the lower tubes.

The Reynolds numbers tested in the bundle were limited to less than 1000. The falling film study of Christians (2010) tested Reynolds numbers up to 2500 but found that the heat transfer reached a plateau as long as the onset of dryout was avoided. The absolute plateau behaviour of falling film could be due to the gravity-driven falling film which performs constantly compared
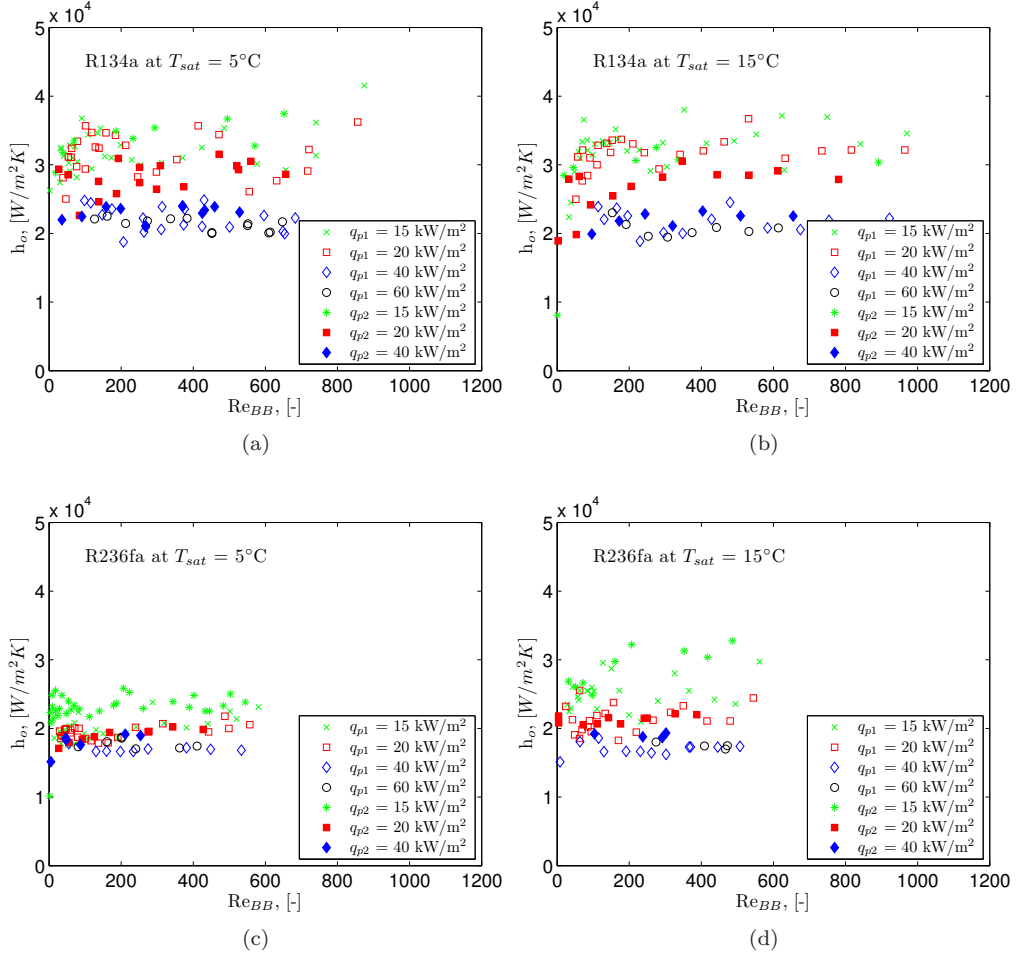
Figure 6.11: The *Gewa-B5* tube at saturation temperatures of 5°C with (a) R134a and (b) R236fa and at 15°C with (c) R134a and (d) R236fa at different heat fluxes for the first and second pass

to the pump-driven and vapour buoyancy affected flooded evaporator conditions tested in this study.

The *Wolverine Turbo-B5* tube showed less heat flux dependence for both fluids with a fairly constant performance around 30 kW/m^2K for R134a and 23 kW/m^2K for R236fa (Figure 6.10). The *Wieland Gewa-B5* tube had a dependance on heat flux for both fluids with a particularly high peak for R134a at lower heat fluxes around 35 kW/m^2K (Figure 6.11). The *Gewa-B5* had a more consistent performance with R236fa around 20 kW/m^2K. The probable causes are the fluid properties, liquid intake process and tube external geometry affecting internal and external heat transfer. The lower latent heat of vaporisation for R236fa has an effect on the evaporation

117

component.

Heat flux had the dominant impact on heat transfer but the trends were similar to that of pool boiling. A comparison with pool boiling is provided through bundle factors k_{BB} (Figure 6.12).

The bundle factors are presented by means of probability density plots (Figure 6.12). Most data indicate a similar performance to pool boiling with $k_{BB} \approx 1$. Extreme values ranged from 0.6 to 1.5 indicating some degradation and some enhancement of heat transfer. The multiple peaks are groupings of heat flux. The *Wieland Gewa-B5* tube has a higher probability of bundle factors less than one, while the *Wolverine Turbo-B5* has a spread around 1 to 1.2 when both fluids are taken into account.
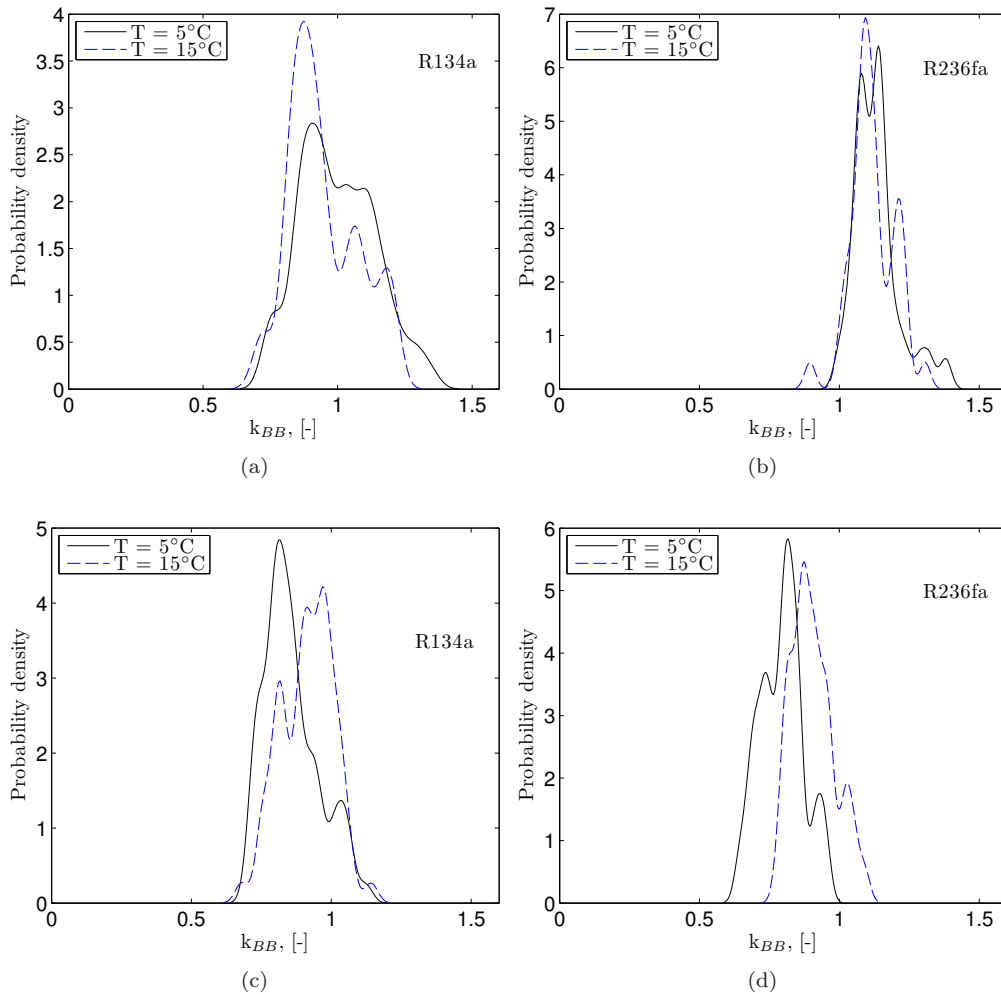
Figure 6.12: Bundle factors of all data presented as probability density functions for the *Turbo-B5* tube with (a) R134a and (b) R236fa and the *Gewa-B5* tube with (c) R134a and (d) R236fa

6.5 Comparison with prediction methods

The method of Christians (2010) assumes a heat flux, saturation temperature dependent plateau for non-dryout conditions. The heat transfer prediction is constant without relation to convection. Upon examining the correlation (equation 2.26) it is clear that the π-group is taken largely out of play by the low value of the exponent, thus leaving the tube-specific factor and leading coefficient to determine the heat transfer coefficient. The correlation does trend correctly with temperature but was only defined for 5^oC data (Figure 6.13).
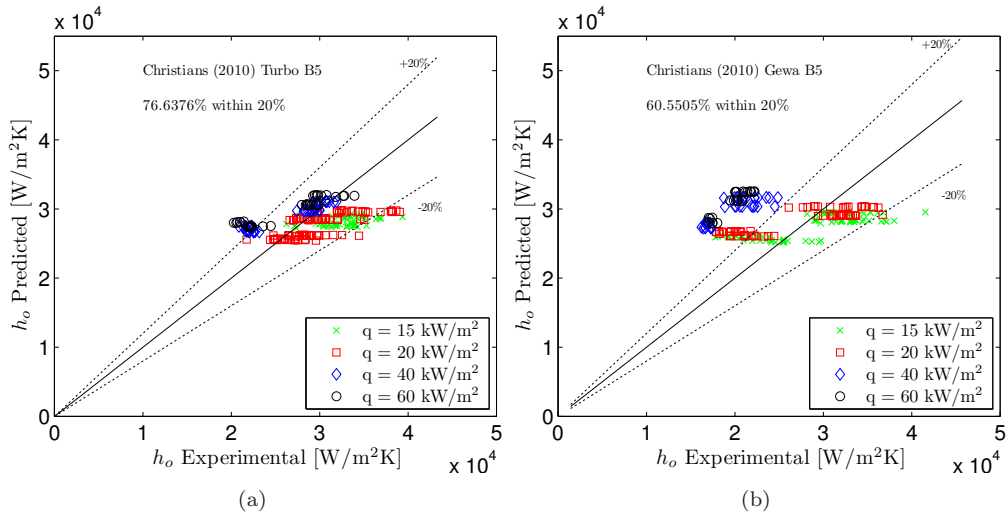
Figure 6.13: Comparison of experimental data with Christians (2010) separated by (a) *Turbo-B5* and (b) *Gewa-B5* and marked by heat flux

The prediction of Robinson and Thome (2003) was based on an older enhanced tube (Turbo-Bii) and defines two multipliers related to the reduced pressure and local void fraction around a tube to adjust the pool boiling prediction. This method was applied by using the pool boiling prediction method defined for the present tubes with the multipliers from Robinson and Thome (2003) (Figure 6.14). Since the method is based on the current pool boiling prediction, the error is due to an overprediction in the bundle factor by the multipliers. If the convective contribution for older generation tubes is larger than that of new tubes, it can explain the over prediction obtained when using the Robinson and Thome (2003) method on the new tubes.
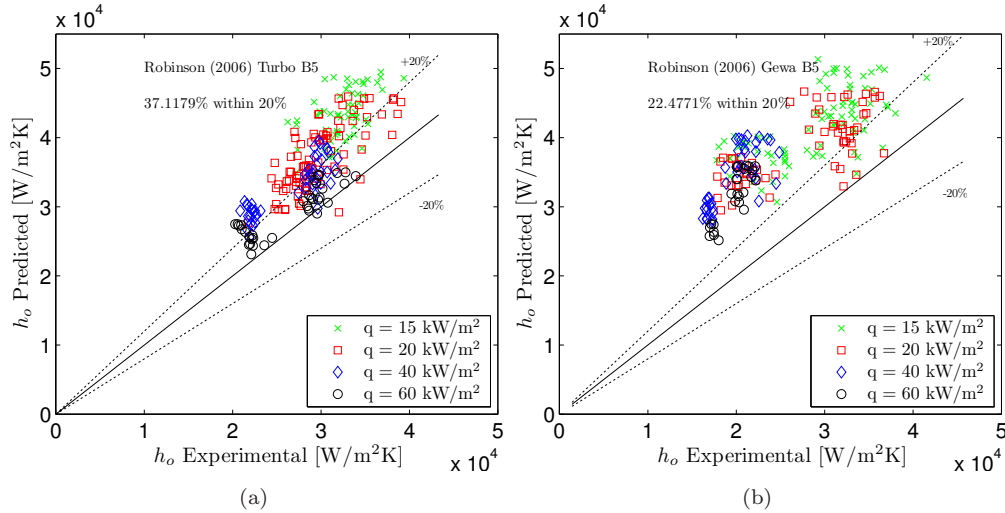
Figure 6.14: Comparison of experimental data with Robinson and Thome (2003) separated by (a) *Turbo-B5* and (b) *Gewa-B5* and marked by heat flux

6.6 Conclusion

A test matrix for two new enhanced tubes was completed in pool boiling and convective boiling with two refrigerants for a range of temperatures, heat fluxes, inlet vapour qualities and mass fluxes. A thorough Wilson plot method implementation and validation was done. A statistical and full uncertainty analysis was conducted on the data to quantify trends and errors. Comparisons with tests of similar tubes and prediction methods are presented. Findings are consistent with previous enhanced tube investigations. Previous prediction methods for other enhanced tubes do not predict the present heat transfer coefficients well and falling film prediction methods do not capture the trends present in bundle boiling.

The hypothesis that heat transfer of enhanced tubes was unaffected by position and flow pattern in the bundle can be accepted after evaluation of the heat transfer data. Thus, any new prediction method resulting from this study is expected to be applicable locally and no row effect or other flow pattern related effects need to be taken into account for a non-mechanistic prediction method.

Chapter 7

Analysis of enhanced tube evaporation

The effects of a range of heat flux on enhanced tubes were investigated during this study. It was found that the bubble departure process changed from isolated bubbles at the lowest heat fluxes to a prolific bubble releasing regime with bubble coalescence laterally and vertically and interactions that are difficult to quantify at higher heat fluxes. It can be assumed that the amount of flooding in the substructure varied significantly over the range of heat flux. At lower heat fluxes more flooding was present, *i.e.* individual bubbles were sometimes seen rising inside the channels of *Gewa-B5* tubes. At higher heat fluxes the substructure was mostly filled with vapour and suction-evaporation was considered the most probable mode of boiling. The amount of flooding in the substrate changes with heat flux and thereby the boiling mode (Chien and Webb, 1998d). The intake mechanisms are not well understood and might be influenced by external flow. A short analytical investigation is now pursued to elaborate on these evaporation mechanisms.

7.1   Models of near-wall evaporation

Some of the existing models for evaporation inside enhanced tubes are mentioned in Appendix C. These methods include the surface tension and Hamaker constant (order of magnitude 10^{-20} to 10^{-21} kgm^2/s^2) in a formulation of the pressure difference over the liquid-vapour interface. The pressure difference is then related to a temperature difference through the Clausius-Claperon equation for steady state conditions by these models. This method approximates the interface temperature rather than modelling it.

7. ANALYSIS OF ENHANCED TUBE EVAPORATION

The nature of the interface shape and mass transfer is important in studies of heat pipes and capillary pump loops and therefore models of interface mass flux or heat transfer have been implemented by this community (Longtin *et al.*, 1994, Lips *et al.*, 2011). The mass flux across an evaporating interface is described by Wayner Jr. *et al.* (1976) through application of kinetic theory. The expression takes into account the pressure and temperature of each phase and an evaporation coefficient (ν). The evaporation coefficient represents the intrinsic characteristic of the molecular interaction during the phase transfer and is a complex function of reflection, replacement and molecular transfer across the interface. The net mass flux across the interface is then determined as J (kg/m²s):

$$J = \frac{\nu}{2 - \nu} \sqrt{\frac{M}{2\pi\Re}} \left(\frac{\rho_{lv,i}}{\sqrt{T_{lv,i}}} - \frac{\rho_v}{\sqrt{T_v}} \right) \tag{7.1}$$

where lv, i represents the liquid-vapour interface condition. For evaporation the value of ν is often assumed to be unity (Ajaev and Homsy, 2001, Ajaev, 2005, Wang *et al.*, 2007). A linearised version of the interface mass transfer equation was assumed by Ajaev (2005) and Hristov *et al.* (2009). Wang *et al.* (2007) stated that there is much debate around the evaporation coefficient for polar fluids like water and methanol while non-polar fluids like benzene and hexadecane have been found to have evaporation coefficients of unity. Wang *et al.* (2007) compared the complete version with the linear approximation and concluded that the approximation is sufficient for values of wall superheat less than 5 K:

$$
\begin{aligned}
J_e &= \left(\frac{2\rho_v h_{lv}}{T_{sat}\sqrt{2\pi\Re T_{sat}}} \right) (T_{sat} - T_i) + \left(\frac{2\rho_v}{\rho_l\sqrt{2\pi\Re T_{sat}}} \right) (\Delta p_i) \\
\text{or } J_e &= J_T(T_{sat} - T_i) + J_P(\Delta p_i)
\end{aligned} \tag{7.2}
$$

By neglecting the sensible heating of the liquid, assuming the interface temperature is close to the saturation temperature and the interfaces are flat and parallel to each other, the problem can be solved by equating the evaporative heat flux to thermal conduction over the film thickness (δ):

$$k_l\frac{T_i - T_w}{\delta} = J_e h_{lv} \tag{7.3}$$

By substituting J_e into the above equation and defining ϕ, the interface temperature can be solved:

$$T_i \quad = \quad \frac{\phi T_w + J_T T_{sat} + J_P \Delta p_i}{\phi + J_T} \tag{7.4}$$

$$\text{where } \phi \quad = \quad \frac{k_l}{\delta h_{lv}}$$

Substituting this equation for T_i into equation 7.2 gives a relation of interface mass flux as a function of the wall superheat:

$$J_e = \frac{\phi J_T}{\phi + J_T}(T_w - T_{sat}) + \frac{\phi J_P}{\phi + J_T}(\Delta p_i) \tag{7.5}$$

The pressure term is usually small compared to the temperature term, but when the film becomes thin or the curvature high, the pressure jump is appreciable and influences the local evaporative mass flux. The pressure jump across the interface is given as a function of surface tension, the Hamaker constant and the evaporative mass flux where the disjoining pressure is given as an approximation for wetting fluids in one dimension:

$$-\Delta p_i = \underbrace{\sigma K}_{Curvature} + \underbrace{\frac{A}{\delta^3}}_{Disjoining} + \underbrace{\left(\frac{1}{\rho_v} - \frac{1}{\rho_l}\right) J_e^2}_{Momentum flux} \tag{7.6}$$
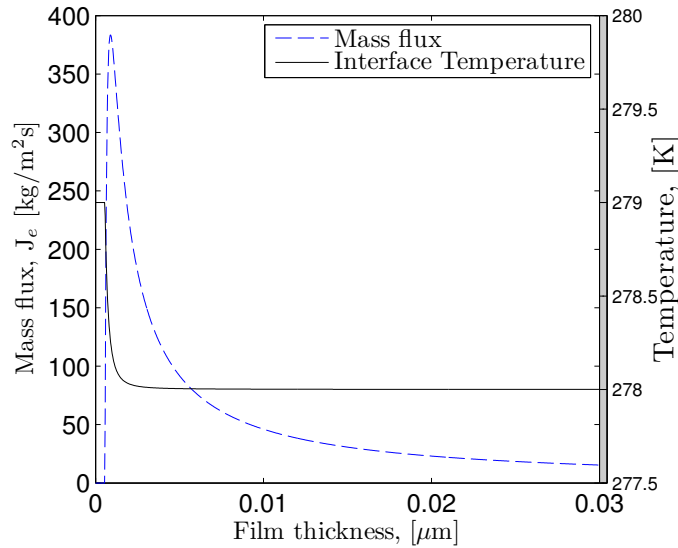
Figure 7.1: Interaction of the interface heat flux with film thickness for R134a at a wall superheat of 1 K and saturation temperature of 278 K

Using this relation and imposing a film thickness and superheat with a constant wall temperature to solve for J_e, the interaction of the terms can be inspected. The mass flux is expected

to peak in the near wall region before the disjoining pressure becomes strong enough to stop evaporation (Stephan and Wondra, 2008). The disjoining pressure peaks as the film thickness decreases. The interfacial temperature is almost equal to the saturation temperature and increases to the wall temperature due to the pressure jump caused by the mass flux and disjoining pressure as the film reduces (Figure 7.1). The film thickness when evaporation is no longer possible due to the high disjoining pressure is the absorbed film thickness (δ_a). This represents the minimum film thickness possible.

7.1.1 Solution of near-wall model

In order to predict the film thickness in a corner of a microchannel during evaporation, several assumptions can be made to simplify the problem.

The problem can be divided into several scales (Figure 7.2). The macro-scale makes up the larger part of the liquid and the interface shape is determined by surface tension force. The surface tension force dominates other body forces when the capillary length ($\sqrt{\frac{\sigma}{\rho g}}$) is shorter than the physical dimensions involved. Heat flux to the evaporating surface takes place through heat conduction by Fourier's law. The rate of evaporation is relatively slow and curvature and disjoining pressure have little effect.

As the film thins out towards the micro-scale region, surface tension becomes dominant if the curvature increases. In this second region the curvature might be significant and the film thin enough to re-balance the interface temperature and heat flux, respectively.
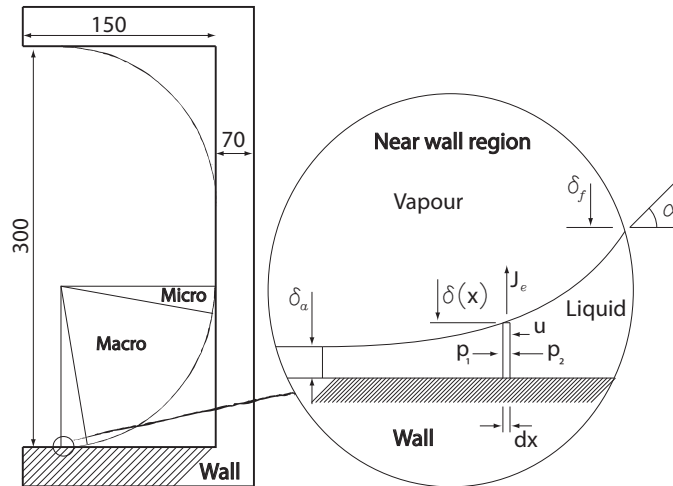
Figure 7.2: A corner in a square subsurface microchannel with length scales indicated (μm). The enlarged near-wall region indicates the liquid interface

A third region, dominated by the disjoining pressure, exists. In this region the evaporation rate is very high but the interface resistance also increases rapidly as the film becomes thinner. There is an interrelation between the disjoining pressure, pressure jump due to the mass flux via phase change, heat conduction over the very thin film and the interface temperature. Eventually the interface temperature surpasses the wall temperature as the disjoining pressure dominated interface resistance balances the evaporation and the process stops. This corresponds to a liquid film of several nanometers for the case of R134a on copper. Essentially only a few molecules of 'liquid' phase perpetually wet the wall because the attractive force of the wall is so high that evaporation (escape into the vapour phase) is unlikely. This is called the absorbed film region and in an evaporating tunnel with surface tension pulling liquid into the corners this is a region further away from the corner where the film is not evaporating.

Now consider the near-wall region where the film thickness is equal to the absorbed film thickness up to a thickness where the disjoining pressure has no more influence (enlarged area in Figure 7.2). The purpose is to set up a force balance between the dominant forces and the evaporation process to determine the shape of the liquid interface at the near-wall zone. The assumptions for the model include:

- A two-dimensional domain is used

- The wall temperature is constant in the small part of the wall

- Fluid properties are evaluated at T_{sat}

- There is no inertia in the liquid (compared to disjoining forces)

- There is no surface tension in this region (compared to disjoining forces)

- All previous assumptions regarding interface evaporation are used.

A momentum balance on an element, dx, (Figure 7.2) results in:

$$-\frac{\partial p}{\partial x} + \frac{\overline{\tau_w}}{\delta} = 0 \tag{7.7}$$

where the mean wall shear is $\overline{\tau_w} = -3\mu_l \frac{\overline{u}}{\delta}$ for a parabolic profile and the pressure is due to the disjoining pressure $p = -\frac{|A|}{\delta^3}$ for this model. Introducing these terms into the momentum balance gives:

$$\frac{\partial |A|}{\partial x} \frac{1}{\delta^3} - 3\mu_l \frac{\overline{u}}{\delta^2} = 0 \tag{7.8}$$

7. ANALYSIS OF ENHANCED TUBE EVAPORATION

A relation for velocity can then be deduced:

$$\bar{u} = -\frac{|A|}{\mu_l}\frac{1}{\delta^2}\frac{\partial\delta}{\partial x} \tag{7.9}$$

The mass balance for the element dx states that the evaporating mass flux is equal to the incoming liquid:

$$\frac{\partial}{\partial x}u\delta = -\frac{J_e}{\rho_l} \tag{7.10}$$

where J_e is the evaporative mass flux given by equation 7.5 as a function of the wall superheat with the only dominant term in the pressure jump being disjoining pressure. For a flat surface, the equations for ϕ (equation 7.4) and I_R can be introduced into equation 7.5 to produce:

$$J_e = \frac{k_l\Delta T}{\delta h_{lv}}\frac{1}{1+I_R}\left[1 + \frac{J_P A}{J_T\delta^3\Delta T}\right] \tag{7.11}$$

$$\text{where } I_R = \frac{k_l}{J_T h_{lv}\delta}$$

To solve for the absorbed film thickness, the boundary condition is set to zero, $J_e(\delta = \delta_a) = 0$, and then δ_a can be solved for a no-evaporation condition:

$$\delta_a = \left(\frac{J_P}{J_T}\right)^{\frac{1}{3}}\left(\frac{|A|}{\Delta T}\right)^{\frac{1}{3}} \tag{7.12}$$

Accordingly, the film thickness is non-dimensionalised by the ratio y $= \frac{\delta}{\delta_a}$. Substituting $\delta = y\delta_a$ into equation 7.11 gives:

$$J_e = \frac{1}{y}\frac{k_l\Delta T}{\delta_a h_{lv}}\left[\frac{y^3-1}{y^3+y^2 I_R}\right] \tag{7.13}$$

$$\bar{u}(x) = -\frac{|A|}{\mu_l}\frac{1}{\delta_a}\frac{y'}{y^2}$$

Here y' denotes the first derivative with respect to x. By substituting $\bar{u}$(x) and J_e into the mass balance relation, identifying l_H as a length dimension and simplifying, this yields:

$$l_H = \left(\frac{\rho_l h_{lv}\delta_a|A|}{\mu_l k_l\Delta T}\right)^{\frac{1}{2}}$$

$$\frac{\partial^2 y}{\partial x^2} - \frac{1}{y}\left(\frac{\partial y}{\partial x}\right)^2 = \frac{1}{l_H^2}\left[\frac{y^3-1}{y^3+y^2 I_R}\right] \tag{7.14}$$

This result is the governing equation for the film thickness y = f(x,l_H,I$_R$), although not yet dimensionless. The boundary conditions state that y(x = 0) = 1 (which is the absorbed film

thickness) and that y(x=l) = y_f where l is the, still unknown, total length of the near-wall region involved and y_f is the film thickness where the near-wall region ends and the assumptions regarding disjoining pressure are no longer valid. By non-dimensionalising x by $x^* = \frac{x}{l}$, the final non-dimensional governing equations become:

$$\frac{\partial^2 y}{\partial x^{*2}} - \frac{1}{y}\left(\frac{\partial y}{\partial x^*}\right)^2 = \frac{l^2}{l_H^2}\left[\frac{y^3 - 1}{y^3 + y^2 I_R}\right] \tag{7.15}$$

or

$$y'' - \frac{1}{y}(y')^2 = \frac{l^2}{l_H^2}\left[\frac{y^3 - 1}{y^3 + y^2 I_R}\right]$$

Here y_f is chosen by recalling that the disjoining pressure drops in magnitude by the relation $1/y_f^3$. The domain is limited to where the disjoining pressure is 1% of its maximum. When $1/y_f^3$ = 1/100 then $y_f \approx 4.64$. The governing equation can now be solved numerically or the first order approximation solution can be expressed as:

$$
\begin{aligned}
y(x) &= 1 + \epsilon\frac{e^{x\sqrt{\pi}} - e^{x\sqrt{\pi}}}{e^{\sqrt{\pi}} - e^{\sqrt{\pi}}} \\
\pi &= \frac{3\left(\frac{l}{l_H}\right)^2}{1 + I_R} \\
\epsilon &= y_f - 1
\end{aligned}
\tag{7.16}
$$

The numerical solution proceeds by discretising the governing equation with a central difference scheme for the domain described by the boundary conditions. The initial guess is a linear film thickness profile from y = 1 ($\delta = \delta_a$) to y_f and the solution is iterated until the profile converges on a solution. The ratio l/l_H is set to around 15 and y_f = 5. Comparing the numerical solution to the first order approximation there are some slight differences, but the solutions match well within the constraints of the assumptions (Figure 7.3). The non-dimensional solution can then be transformed back into dimensional form for use in a model.

From the dimensional solution it is possible to determine the apparent contact angle at the point where the near-wall region ends (x = 1). From the film thickness it is also possible to determine the evaporative mass flux from the liquid interface. The mass flux can be converted to a heat flux through the relation q = J_e h_{lv}.

Finally, it is important to note that the heat transfer in the near-wall region is exceptionally high (Ibrahem *et al.*, 2010, Heng *et al.*, 2010). Therefore, even if it is a very small region and seems
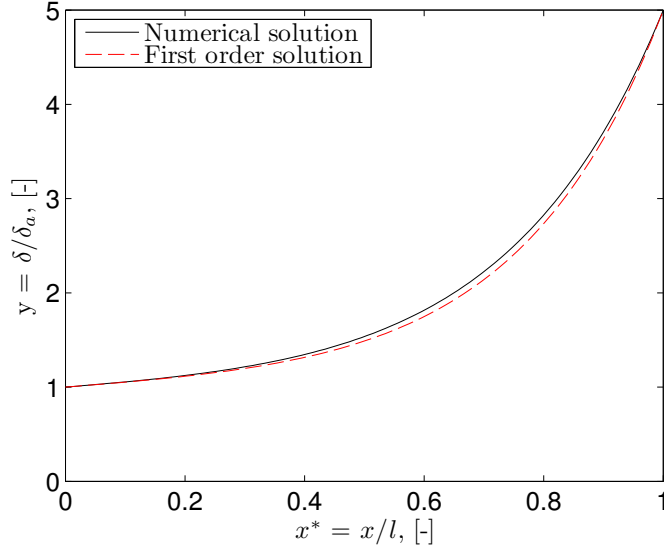
Figure 7.3: Numerical and first order solution to the film thickness for the near-wall region

insignificant the heat flux can be several orders higher than the average in the macro region and thereby make a significant contribution. The parameters determining how this one mechanism of evaporation operates might therefore be important if this mechanism is responsible for a large fraction of the heat flux. From the governing equation several parameters can be identified: δ_a, l_H and I_R. The length parameter (l_H) is proportional to the amount of energy that can be evaporated from a film in relation to the temperature difference. As a ratio of lengths $(\frac{l_H}{\delta_a})$ this parameter provides a possible dimensionless parameter that could prove significant if the type of evaporation present on or in a tube is dominated by thin films evaporating and drying out.

Because the region is very small, the wall material plays an important part in determining the final heat flux. The wall material thermal diffusion limit might not be able to provide the heat at a constant temperature. It would thus be necessary to include the wall conduction and transient effects into any model attempting to solve evaporation of this nature (Mitrovic, 2006, Stephan and Kern, 2004, Stephan and Wondra, 2008).

7.2 Conclusion

The processes governing thin film evaporation and near-wall evaporation of the menisci are considered important components of heat transfer. The overall heat transfer is a combination of internal processes and external heat transfer with notable interactions that remain difficult to

model. The dominant mechanism in enhanced boiling is not only a function of reduced pressure or latent heat, but rather a complex set of fluid and wall properties (including disjoining pressure, surface tension, thermal conductivities, specific heat capacities and densities).

On plain surfaces the open structure is affected by convection and the less powerful mechanisms of convection and conduction play important parts in the total heat transfer. On and in enhanced surfaces the wall superheat is preserved during the boiling cycle, thin films and menisci are more prevalent and the heat transfer associated with phase change is therefore more efficiently utilised. Ultimately, a model of heat transfer for each mechanism present and fluid mechanics relating the liquid pumping and phase distributions in different geometries in and on enhanced tubes would be needed to provide the overall model of this evaporation process.

Chapter 8

Prediction methods

8.1 Two-phase pressure drop prediction methods

The dynamics of pressure drop were reported on in Chapter 5. The database was made up of adiabatic and diabatic data and the prediction method was based only on adiabatic data. The previous predictions of bundle pressure drop were empirical. For a more fundamental approach to the data the flow patterns need to be considered. For the range of mass flux and vapour quality tested, a bubbly type flow was observed at the lowest vapour qualities. As the mass flux increased, the flow transitioned into an intermittent type flow and eventually a "inter-tubular" annular flow dominated. For external flow the flow pattern changed with vertical position in the bundle. It was assumed that the observation position was representative of the general bundle condition even though a certain degree of flow development was present through the bundle.

For in-tube flow, annular flow is generally modelled with a friction factor representing the interface shear. For the range of flow patterns present in bundles, an annular model would not be correct. The film thickness of a redistributed annular liquid film is not always negligible in the bundle. For flow over complex external structures, a type of homogenization is proposed. The approach proposed is to fit the data to a prediction method by assuming wall shear stress in a homogeneous bundle, while maintaining the concept of a redistributed film as a physical-dimensional factor. This is accomplished by assuming the liquid is redistributed around the tubes within a hexagonal unit element as done by Robinson and Thome (2003) for heat transfer. This assumption is not always valid but provides a reasonable and simple flow distribution.

From a force balance for the intertube flow in a vertical flow (Figure 8.1) the shear force can be represented as:
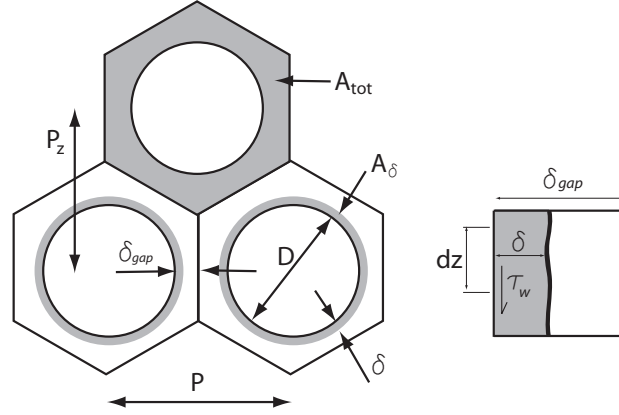
Figure 8.1: The simplified flow distribution and an element of flow in between two tubes at the narrowest point where the flow is parallel

$$
\begin{aligned}
\frac{dp}{dz} &= \frac{\tau_w}{\delta_{gap}} - \rho_H g \\
\tau_w &= f\frac{1}{2}\rho_H (u)^2
\end{aligned}
\tag{8.1}
$$

The classical definition of friction factor for bundle flow was used. The homogeneous two-phase density (equation 2.8) and a geometric ratio $\left(\frac{\delta_{gap}\delta - \delta^2}{\delta_{gap}^2}\right)$ were used in the correlation's definition for pressure drop. A phenomenological (mechanistic) relation can then be defined for the friction factor to correlate the database:

$$
\begin{aligned}
f_{2\phi} &= a\left[\frac{\delta_{gap}\delta - \delta^2}{\delta_{gap}^2}\right]^b \left[\frac{(\rho_l - \rho_v)g\delta^2}{\sigma}\right]^c [We_l]^d \left[\frac{\mu_v}{\mu_l}\right]^e \\
We_l &= \frac{\rho_l u_l^2 D_o}{\sigma} \quad \text{and} \quad u_l = \frac{\dot{m}(1-x)}{\rho_l A(1-\varepsilon)}
\end{aligned}
\tag{8.2}
$$

The terms in this relation are adaptations of those in annular flow correlations of Quiben and Thome (2007) to a tube bundle. The first term after the leading coefficient is the geometric term. The geometric term is defined in such a way as to respect the trend in friction factor and to approach the boundary conditions of liquid or vapour only flow, but does not explicitly satisfy these boundary conditions, since the rest of the correlation has no relation to the single phase pressure drop.

The redistributed film thickness δ is used for the geometric factor and the second term (a modified Helmholts instability term) represents the unstable film thickness. The liquid Weber

number is defined with the liquid velocity and the last term is a ratio of vapour and liquid viscosity to represent interfacial shear.

The equations relating the hexagonal unit element of Figure 8.1, void fraction and film thickness are given by:

$$
\begin{aligned}
A_{hex} &= \frac{6P_z}{3}\frac{P}{2} \\
A_t &= A_{hex} - \frac{\pi}{4}D_o^2 \\
A_\delta &= A_t(1 - \varepsilon) \\
D_\delta &= \sqrt{4\frac{A_\delta}{\pi} + D_o^2} \\
\delta &= \frac{D_\delta - D_o}{2}
\end{aligned}
$$

The empirical correlation is also proposed here, given by the form in equation 8.3 and the single phase component of the two-phase multiplier was found by using the Žukauskas and Ulinskas (1983) correlation with a homogeneous density and viscosity (Chapter 2).

$$
\begin{aligned}
\lambda = \frac{f_{2\phi}}{f_H} &= e\left[-\left(\frac{(x - C_2)}{0.392}\right)^2 + C_1\right] \\
\text{with:} \quad C_1 &= a\Lambda + b \\
C_2 &= c\Lambda + d \\
\Lambda &= \left(\frac{G}{469}\right)^e
\end{aligned}
\tag{8.3}
$$

where G is in kg/m^2s and 469 has the same units.

8.1.1 Adiabatic pressure drop

A nonlinear least-squares fitting procedure was used to fit the data and determine the empirical coefficients. The entire adiabatic database was used for the fit and it included data for R134a and R236fa at 5, 10 and 15°C for both tubes. As illustrated by the results in Chapter 5, the tube type did not have a strong influence. The results of the fitting procedure are summarised in Table 8.1 and graphically presented in Figures 8.2 and 8.3.

The empirical prediction was the most accurate and follows the trends for both measurements (Figure 8.2). There was more scatter in the shorter diabatic section data and this was probably due to the difficulty in measuring small pressure drops and sensitivity to the data reduction assumptions. The data in Figure 8.3 were grouped per tube and showed no particular difference

in the prediction for the different tubes. Overall, the empirical method predicted 94% of the data within ±20% whereas the phenomenological method predicted 88% within ±20%. In the diabatic section the phenomenological method improved the data prediction with 75% of the data within ±20% compared to 64% for the empirical method. This indicated a greater potential for scaling the implementation of the phenomenological model to local conditions as will be recommended for diabatic cases.

Table 8.1: Coefficients for the various new prediction methods of adiabatic frictional pressure drop

Method	Empirical (eq. 8.3)	Phenomenological (eq. 8.2)
a	-22.89	165
b	19.51	1.2844
c	-1.905	-0.15921
d	1.6131	-0.84625
e	0.15468	-0.14487
% in ±20%	94%	88%
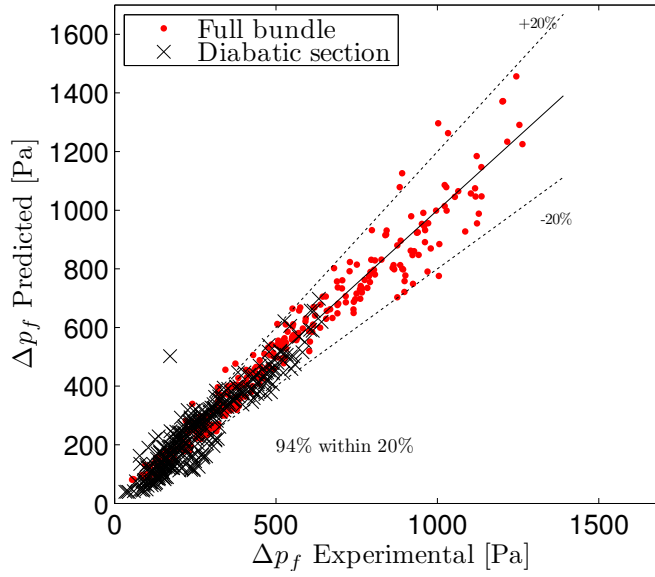
Figure 8.2: Comparison of the empirical prediction method against experimental data over the full bundle and diabatic section for both tubes during adiabatic tests

For select cases the phenomenological prediction method was directly compared against the frictional pressure drop data to observe the trends (Figure 8.4). The friction increases with mass flux and vapour quality and the prediction method followed most trends closely. Notably the
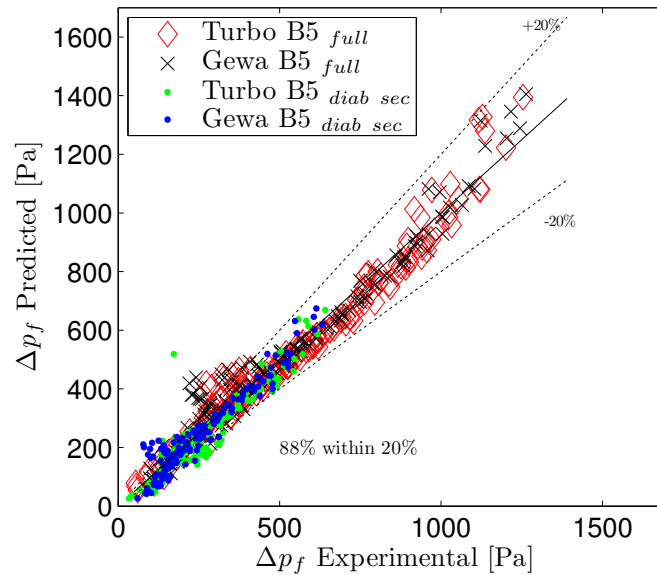
Figure 8.3: Comparison of the phenomenological prediction method with experimental data over the full bundle and diabatic section for both tubes during adiabatic conditions

slope increased or decreased depending on the mass flux. The limited data available at vapour qualities higher than 30% at the highest mass fluxes means that the extension of the trends are extrapolated. The range of physical properties in the database and the trends of the prediction method provides an indication of the applicability (Figure 8.5). The lower vapour quality data were poorly predicted and some of the worst predictions were also at the maximum mass flux. At these conditions certain assumptions regarding the calculation of the void fraction to back out the frictional pressure drop and other data reduction procedures were not ideal and the system itself was less stable at the maximum mass flux.

8.1.2   Diabatic pressure drop

The pressure drop method defined in the previous section can now be implemented to predict the diabatic data and different options are evaluated. The first option is a direct implementation of the method by using the mean values of vapour quality and void fraction (Figure 8.6).

An alternative approach is to evaluate the pressure drop in increments and sum the increments to obtain the total. This means that a vapour quality and void fraction distribution must be known or assumed. The local conditions were evaluated at steps equivalent to the tube pitch (Figure 8.7b). This solution is probably a good one in larger bundles, but in the present test section the tube rows are made of either two or three tubes. Thus the amount of evaporation

135
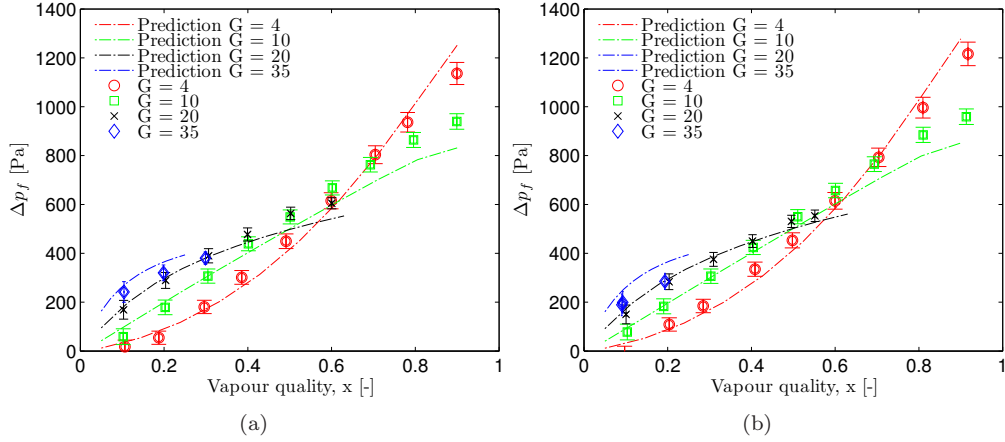
Figure 8.4: Sample calculations of the phenomenological frictional pressure drop for (a) *Wolverine Turbo-B5* and (b) *Wieland Gewa-B5* for two mass fluxes with R134a

varies by 30% at each level and the void fraction profile is not linear. Using the local vapour quality at each tube row a more accurate prediction can be made (Figure 8.7b). For predicting the full bundle, the local values change in the diabatic section and then remain constant in the adiabatic section (Figure 8.7a). When using the prediction method per row ($N_R = 1$) an adjustment factor which relates the vertical pitch to the center-to-center pitch, is recommended ($\frac{P_z}{P} = \sin 60° = \frac{\sqrt{3}}{2}$). Further refinement of this method requires larger bundles to be tested with many more tube rows.
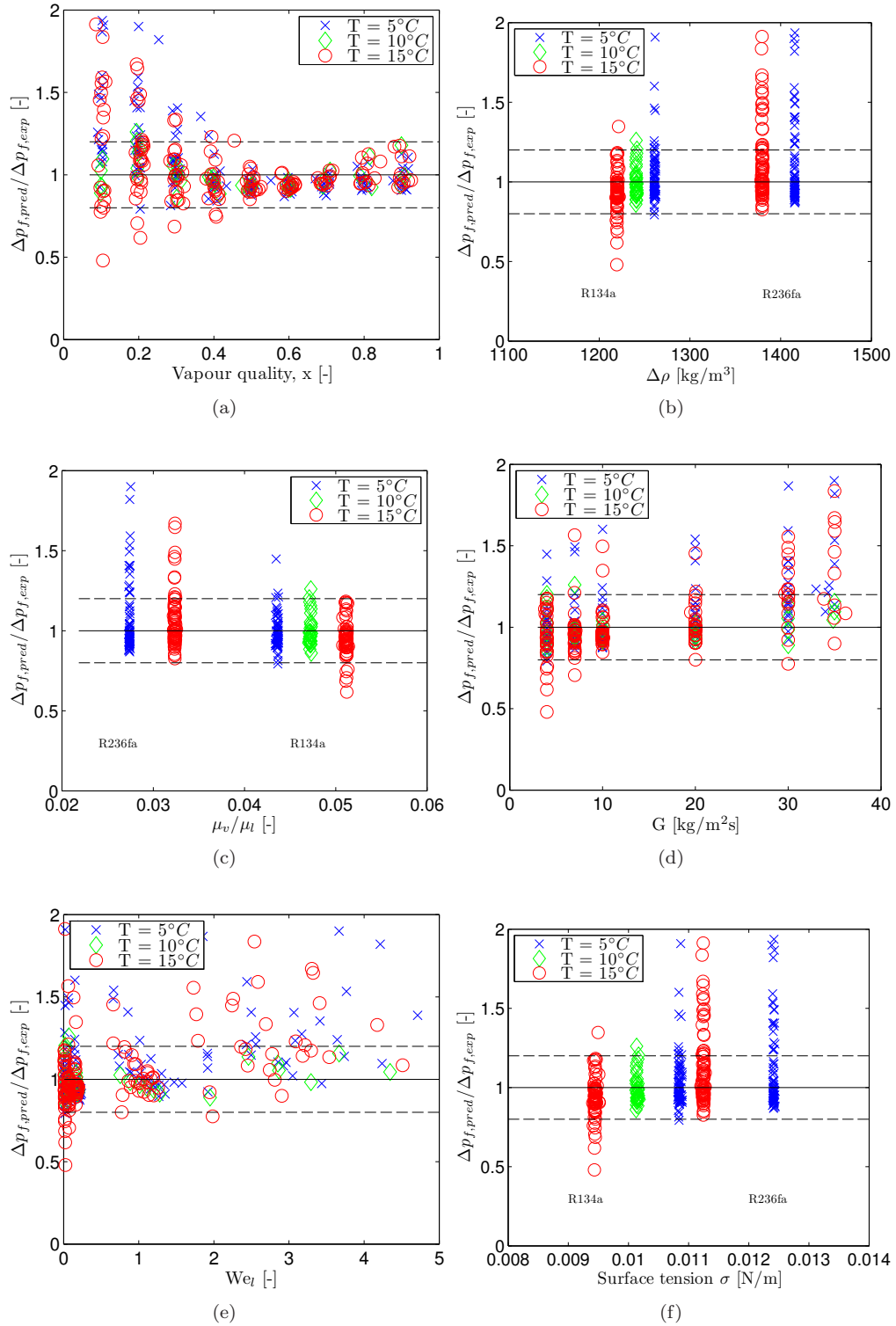
Figure 8.5: Trends in the variables making up the phenomenological prediction method for pressure drop (a) x, (b) $\Delta\rho_l$, (c) μ_v/μ_l, (d) G, (e) We$_l$ and (f) σ
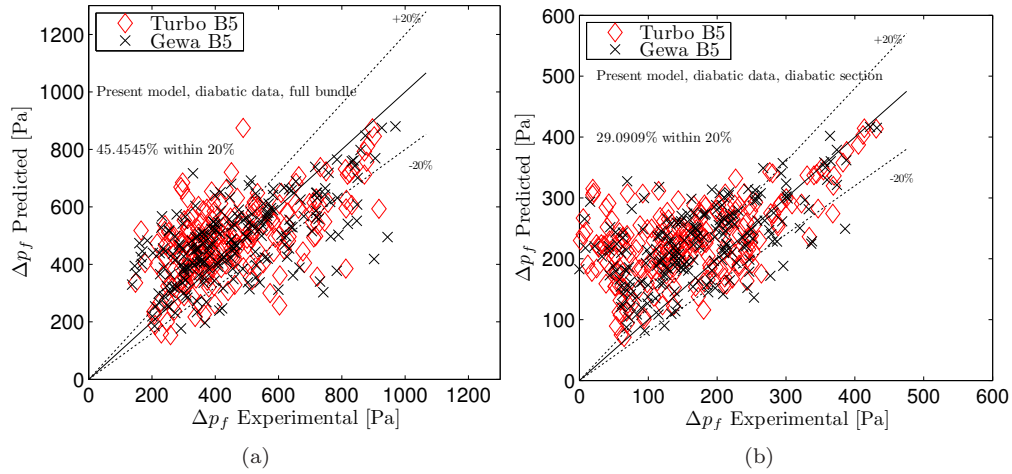
Figure 8.6: Comparison of the phenomenological prediction method with experimental data over the (a) full bundle and (b) diabatic section for diabatic data using mean bundle conditions
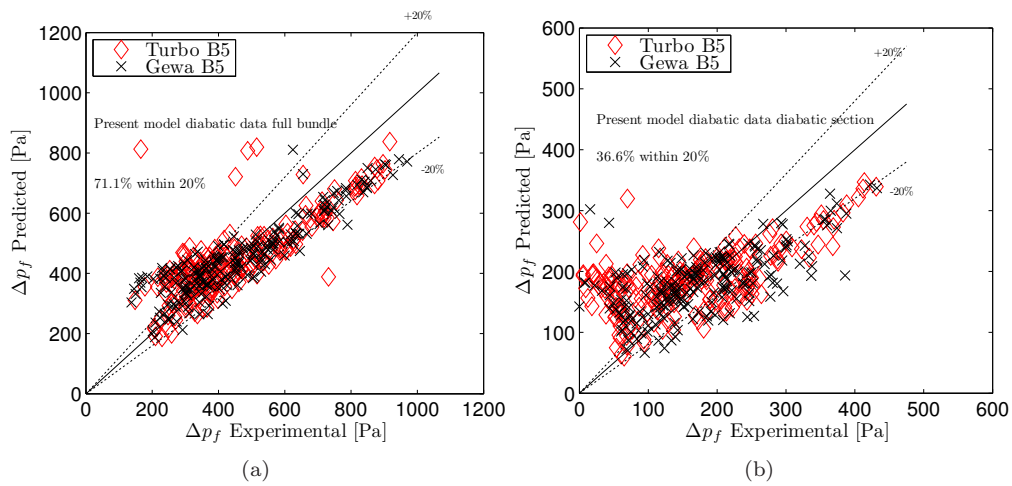
Figure 8.7: Comparison of the phenomenological prediction method for diabatic data on (a) full bundle and (b) diabatic section using local conditions in increments of one tube row

8.2 Heat transfer prediction methods

From the heat transfer investigation it was clear that heat flux was one of the dominant factors influencing heat transfer performance. The fluid type also changed the heat transfer performance significantly. From the mechanistic investigations, the fluid type determined how most of the complex phenomena interacted. The liquid viscosity, surface tension and wall material all played an important role. The evaporation process was influenced by all these factors and the heat flux determined the rate at which the mechanisms occurred and interacted.

Evaporation was an important process and the analysis of the film evaporation identified a simple set of parameters with a strong relation to the evaporation process. The dimensionless parameter $\frac{l_H}{\delta_a}$ relates the fluid properties and the temperature difference to the heat transfer process of evaporation.

The current objective was to investigate the tube geometry and the impact of different enhanced tube types on the heat transfer. The previous correlation by Christians (2010) used a tube specific variable with great success in correlating different tubes. The Christians (2010) correlation used dimensional analysis to define the dimensionless number. This number used heat flux, latent heat of evaporation and saturation pressure, but it was not explained why this correlation group worked well with enhanced tubes, although an analogy was drawn between the dimensionless number and heat flux from the latent heat of evaporation and the pumping action of the liquid phase through the tunnels by the bubbles.

In the present study a more fundamental approach was used by investigating the mechanisms of boiling, characterising the specific nature of evaporation inside the subsurface tunnels and then using this to define the correlation. The secondary result of this investigation was the identification of specific aspects that need to be addressed in order to understand the role of the tube geometry such as: liquid intake, liquid distribution, subsurface tunnel pressure fluctuations, active pore distribution and bubble dynamics. Since the tube geometry was not disclosed by the tube manufacturers and the modelling of certain physical mechanisms remains complex, this issue will have to be addressed in future work.

8.2.1 Pool boiling heat transfer

The prediction method is based on the ratio of lengths identified by the near-wall region analysis. This ratio correlates the heat transfer coefficient data in a linear manner with values from two to ten in the present study. The Hamaker constant can be calculated from Lifshitz theory (Israelachvili, 1985). A Hamaker constant of $8.6 \cdot 10^{-21}$ was used for refrigerant on copper. To

Table 8.2: Coefficients for each tube for the new pool boiling prediction method

Coefficient	Value
a	1400
TSF_a (Turbo-B5)	0.9323
TSF_a (Gewa-B5)	0.8224
TSF_b (Turbo-B5)	2.141
TSF_b (Gewa-B5)	9.585

accommodate the fit, a leading coefficient and an exponent were applied. The leading coefficient was a constant and the exponent was a tube specific factor. The exponent was chosen as the tube specific factor to allow for the different slopes noticed in the heat transfer coefficients as a function of heat flux for the different tubes. This trend was assumed to be a function of the tube geometry that allows varying amounts of liquid and vapour exchange and external convection at certain heat fluxes. The heat transfer was assumed to be dominated by the evaporation component as long as optimal conditions exist. This heat transfer component was fairly constant with heat flux, thus the tube geometry determined how much liquid entered and whether the tube performed well or not, based on the flow distribution in the tunnels. Studies of pore size and distribution confirmed that flooding occurs in cases when pore area is too large and dryout of tubes occurs with too small a pore area (Chien and Webb, 1998a). The resulting mechanistic correlation is:

$$
\begin{aligned}
\frac{h_{o,pb}D_o}{k_l} &= a\left(\frac{l_H}{\delta_a}\right)^{TSF_a}\left(1 - \frac{1}{(\Delta T + 1)^{TSF_b}}\right) \\
\text{with } \frac{l_h}{\delta_a} &= \left(\frac{|A|}{\Delta T}\right)^{\frac{1}{3}}\frac{(\rho_l h_{lv})^{\frac{2}{3}}}{(k_l\mu_l)^{\frac{1}{2}}T_{sat}^{\frac{1}{6}}}
\end{aligned}
\tag{8.4}
$$

The second term in the correlation is a relation that is a function of the temperature difference. The trend expected in the method, when only the first term is used, is to increase h_o as ΔT decreases. This is not the case, and even if this study did not investigate such low heat fluxes, the second term is included as a balance in order to respect the minimum limit. The proposed mathematical term is a substitute for a possible temperature-dependent term that would represent the change in mechanisms at lower heat flux. Ideally, this second term represents the partial flooding of tunnels at low heat fluxes or a shift in mechanism from menisci to thin film evaporation and even single phase or sensible heat transfer as liquid pumping slows down. The second term should allow a peak (depending on the tube and fluid) in heat transfer coefficient as the wall
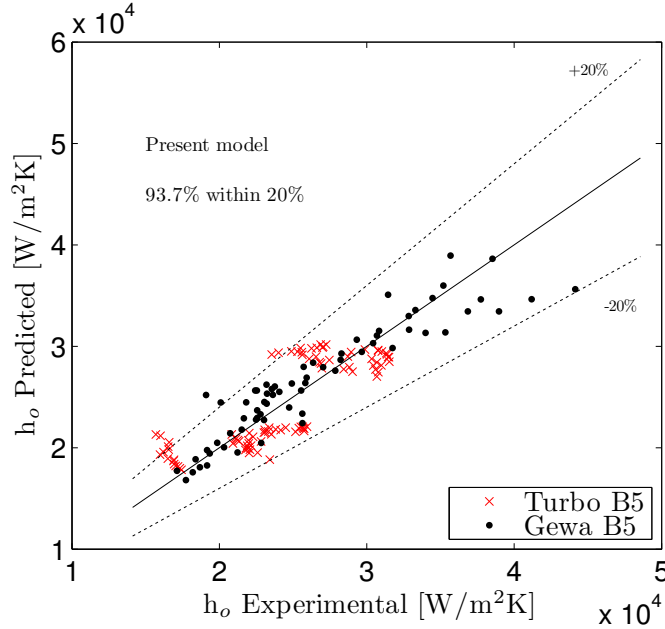
Figure 8.8: A comparison of the pool boiling data with the proposed prediction method

superheat decreases. For wall superheats lower than the peak the heat transfer coefficient drops proportionally with the temperature difference.

A nonlinear optimisation procedure was used to fit the unknown coefficients to the data set so that the prediction of heat transfer coefficient matches the experimental data. The results are summarised in Table 8.2. The trends in the prediction method with heat flux and $\frac{l_H}{\delta_a}$ indicated little variation over the intended range (Figure 8.9). The relationship represents the amount of energy that can be evaporated from a film in relation to the limit that stops evaporation as a function of temperature difference. It is inherently a function of complex interacting fluid properties that determine how evaporation will take place. The correlation predicted 94% of the data for both fluids within $\pm 20\%$.

No low heat flux measurements were possible in order to validate the trend for heat fluxes lower than 15 kW/m^2. The temperature reduction term was nevertheless included in the correlation. Once low heat flux measurements are made the method can be re-evaluated and updated. The mechanisms of low heat flux conditions could also be investigated to eventually replace the second term with a phenomenological relationship.

The outside surface of the *Wolverine Turbo-B5* tube was similar to the *Wolverine Turbo-EDE2* tube. The *Turbo-EDE2* tube was tested by Habert (2009) and its prediction method was
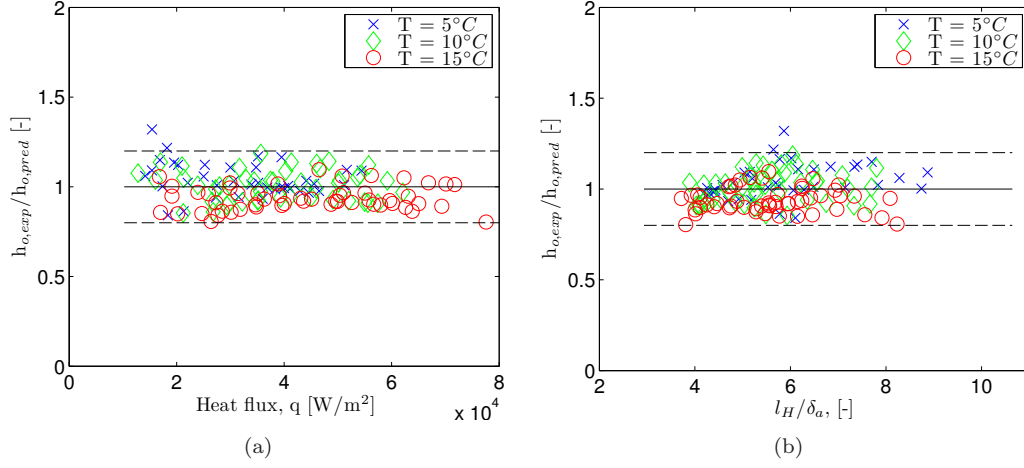
Figure 8.9: Trends in the pool boiling prediction method for both tubes with (a) heat flux and (b) $\frac{l_H}{\delta_a}$

compared with the present method for *Turbo-B5* (Figure 8.10). The predictions were extrapolated to 5 kW/m^2 to indicate the effect of the temperature term on the heat transfer coefficient. Over the range of validity of the two methods ($> 20\ kW/m^2$), it can be seen that the trends and magnitude are for the most part similar. As there are no other data available for these tubes, it was not possible to make any further comparisons.

8.2.2 Bundle boiling heat transfer

As hypothesized in Chapters 2 and 6 the prediction method for enhanced tubes does not depend strongly on bundle convection effects or row effects, but mostly on the local heat flux, fluid choice and any other secondary effects that would have an impact on pool boiling performance. These secondary effects, however slight, can be attributed to the convection in the bundle causing bubble dynamics or external heat transfer to change. Presently these additional effects are correlated by introducing a Reynolds number factor to the pool boiling prediction method. This is a function of the tube surface topography and its influence on the mechanisms of convective heat transfer. Therefore, the factor (TSF) is a function of tube type, since each tube is affected by convection differently. The bundle correlation is:

$$\frac{h_{o,BB}D_o}{k_l} = \frac{h_{o,pb}D_o}{k_l}\,TSF\left(\frac{Re_{BB}}{a}\right)^b \tag{8.5}$$

The value of TSF and the two new empirical coefficients were determined by a nonlinear optimisation procedure (Table 8.3) and the prediction is compared with the data in Figure 8.11.

Table 8.3: Coefficients for each tube in the new bundle boiling prediction method

Coefficient	Value
TSF (Turbo-B5)	1.164
TSF (Gewa-B5)	0.835
a	522
b	-0.0059

The trends in the prediction method with vapour quality, mass flux, heat flux and refrigerant indicated that lower heat flux data were poorly predicted but with the majority of the data corresponding within the limits (Figure 8.12).

On the other hand, for simplicity sake, the Reynolds number term can be excluded from the prediction method leaving only the tube specific coefficient as a multiplier on the pool boiling heat transfer coefficient $h_{o,pb}$. This correlation predicted 94% of the data within $\pm20\%$. The multiplying factor assumed values around 1.16 for *Turbo-B5* and 0.84 for *Gewa-B5* in the Reynolds number range from 50 to 1000. From the trends in Figure 8.12 and the probability density in Figure 8.13 the remaining variation in heat transfer performance could not be uniquely attributed to any of the test variables and the prediction was centered on the mean of all variations.
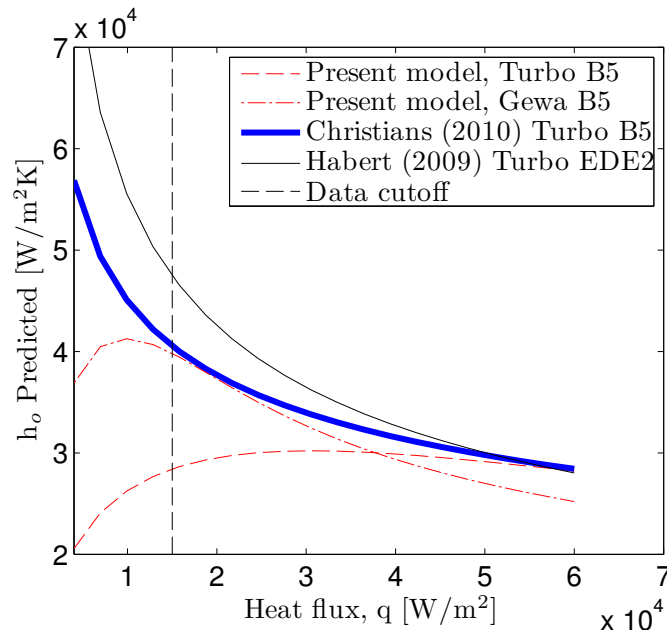
Figure 8.10: Comparison of the *Turbo-B5* data with the prediction method for Turbo-EDE2
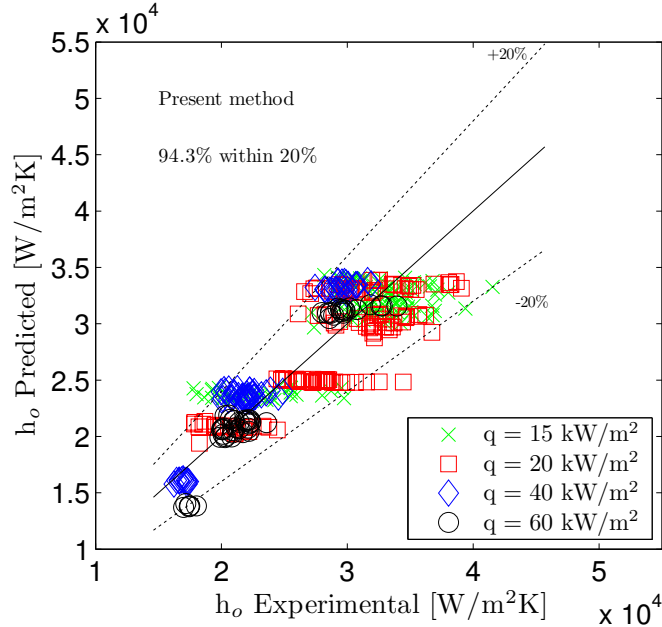
Figure 8.11: The comparison of the prediction method for both tubes and sorted according to nominal heat flux

The use of a void fraction factor similar to that used in Robinson and Thome (2003) was not needed since the bundle Reynolds number had a good relation to the conditions expected outside the tubes. The fluid properties were directly included in the pool boiling method and did not use the reduced pressure often used in boiling correlations.

The prediction method is presented with data for several sample conditions (Figures 8.14 and 8.15). The trends with Reynolds number are indicated opposite the pool boiling data and prediction method. Heat fluxes of 20 kW/m^2 (red) and 60 kW/m^2 (black) were simulated using both convective bundle boiling (equation 8.5) and falling film (Christians, 2010) methods. In general, the pool boiling performance was constant for *Turbo-B5* and the bundle factor slightly larger than one. *Gewa-B5* heat transfer coefficients decreased for bundle boiling conditions (*i.e.* with convection), but still followed the same trends as pool boiling with heat flux. The onset of dryout (discussed in the next section) was indicated for the simulated conditions.

8.2.3 Onset of dryout

The onset of dryout was identified in the bundle by using all the methods described in Chapter 4. The relation used for bundle boiling was similar to the one defined for smooth tubes (Van Rooyen *et al.*, 2011a). This relation was accurate for the available data, but can be improved if onset
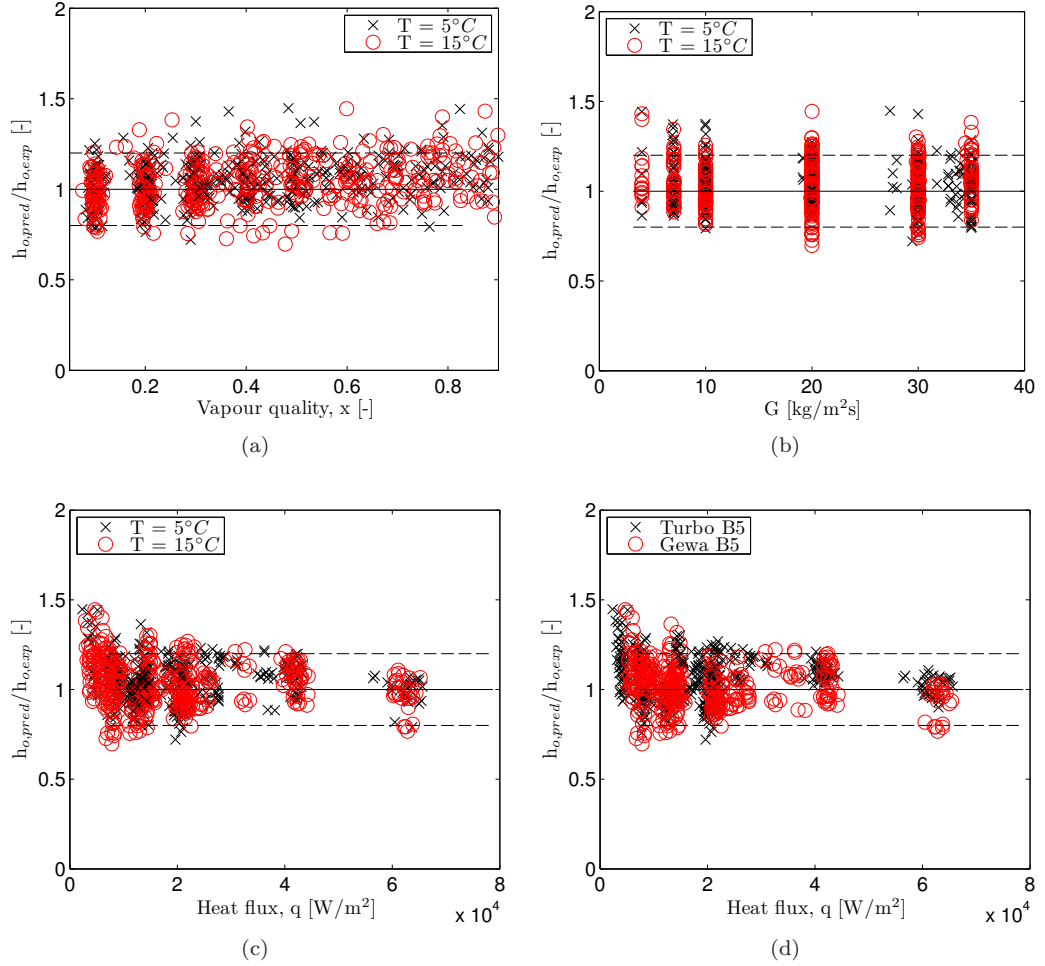
Figure 8.12: Trends in the error ratio of the bundle boiling heat transfer coefficient for (a) vapour quality (b) mass flux (c) heat flux and (d) heat flux sorted by tube type

of dryout testing on a wider range of mass flux and heat flux conditions were possible. The dependence of onset of dryout on heat flux and mass flux in tube bundles is important for thermal designers, since low performance conditions can be avoided or minimized. By using the same relation as smooth tubes, a comparison can be made with enhanced tubes.

The onset of dryout transition line is defined for superficial velocities in relation to a critical vapour quality by:

$$j_l = j_v \left(\frac{\rho_l}{\rho_v} \frac{x_{dry}}{(1 - x_{dry})} \right)^{-1} \tag{8.6}$$

Onset of dryout occurred at a vapour quality of 98% ($x_{dry} = 0.98$) for both tube types
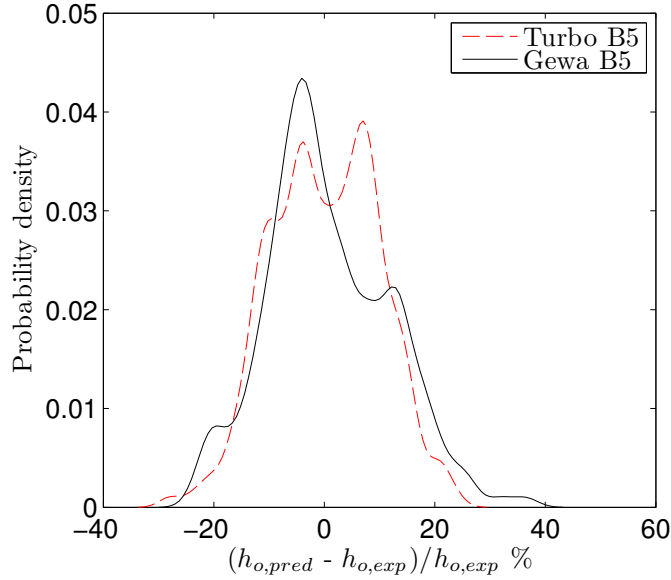
Figure 8.13: Probability density estimate based on the difference between the prediction method and the experimental data for both tube types
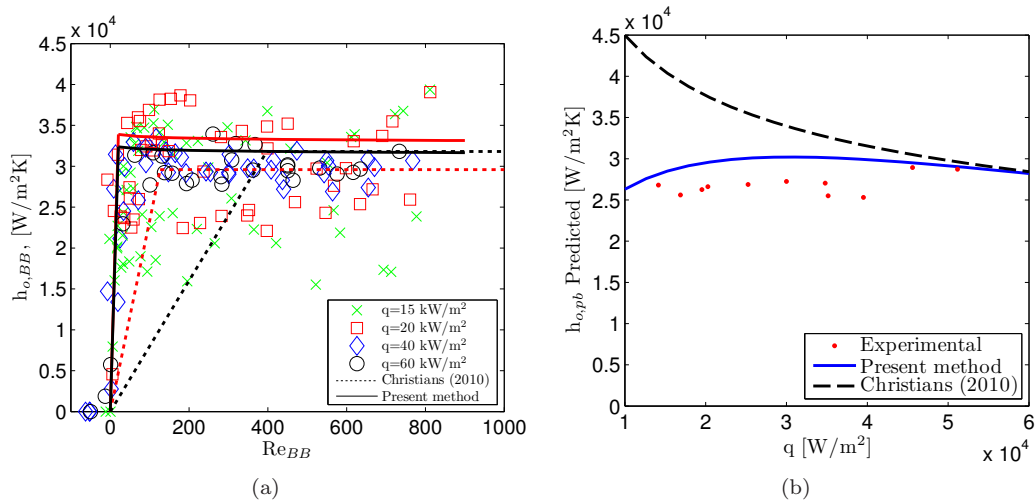
Figure 8.14: Comparison of sample data and prediction methods for (a) bundle boiling and (b) pool boiling with *Turbo-B5* at 5^oC with R134a

(Figure 8.16). This compares to 90% ($x_{dry} = 0.9$) for smooth tubes, meaning that enhanced tubes, with their re-entrant enhanced structure, maintained good performance until much closer to the complete vapour (x = 1.0) condition in bundle boiling. This was attributed to the nature of the vertical upward flow in bundles and the enhanced surface. For the flow rates in this study
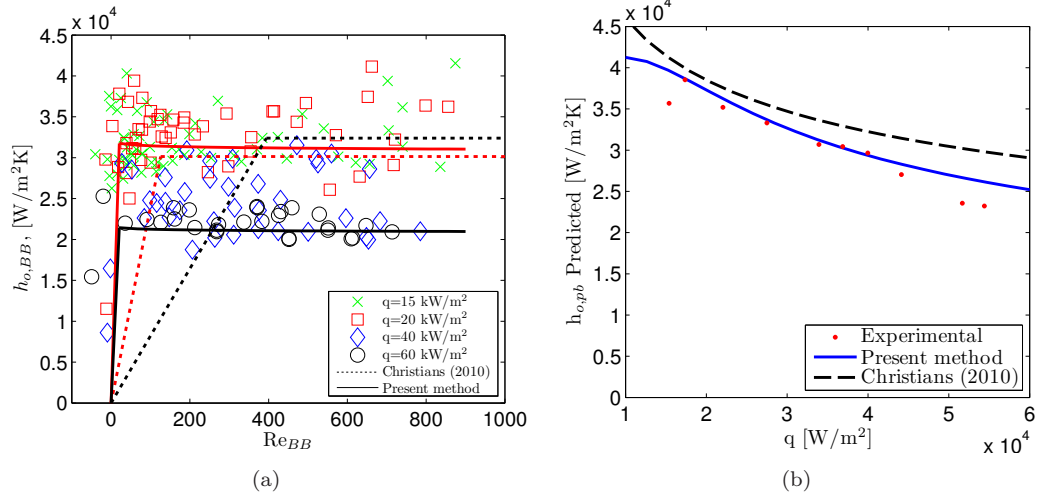
Figure 8.15: Comparison of sample data and prediction methods for (a) bundle boiling and (b) pool boiling with *Gewa-B5* at 5°C with R134a

the liquid is "absorbed" by the enhanced structure and evaporated from the tunnels. Thus, onset of dryout occurred suddenly and, for all purposes, near the thermodynamic limiting condition of x = 1.0.

By converting the equation above to a film Reynolds number, a comparison with falling film can also be made:

$$Re_{onset} = \frac{4\dot{m}_t(1 - x_{dry})}{2N_{tubes}L\mu_l} \tag{8.7}$$

Falling films are more likely to experience onset of dryout since the liquid flow velocity is high and therefore the film is thinner. The impinging flow, thin film and higher velocity allow slightly higher and constant heat transfer coefficients over a wide range of conditions in falling film. The thin falling films are not sufficient to wet the tubes at higher heat fluxes and the tube-to-tube flow pattern passes from sheet mode to column mode, increasing the propensity of dry patches to form between the columns. As the heat flux increases so does the limiting film Reynolds number at which partial dryout occurs on the tube. The onset of dryout can occur at Reynolds numbers as high as 500 in falling film applications and is a function of heat flux. In bundle boiling, the onset of dryout is delayed to Reynolds numbers as low as 30 and no heat flux effect has been found. The onset of dryout prediction for bundle boiling is a weak function of mass flux. The earliest dryout will occur for the highest mass flux in bundle boiling. This could be due to the higher velocities in the bundle for the high mass fluxes and the thinner film is susceptible to partial dryout similar
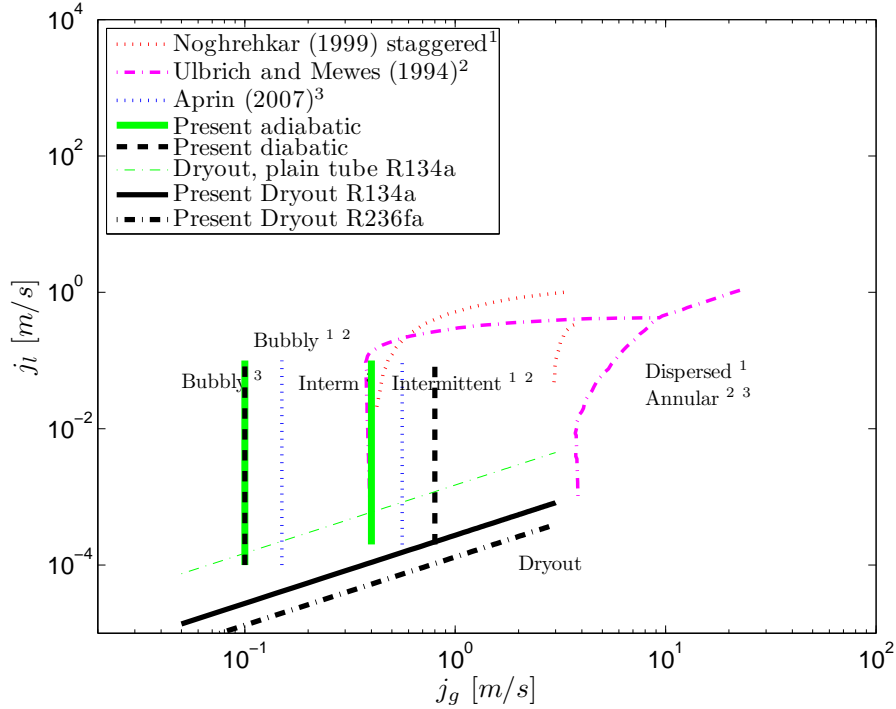
Figure 8.16: Onset of dryout function on a superficial velocity flow pattern map including the smooth tube dryout for comparison

to falling film. At lower mass fluxes the tubes remain wet and partial dryout happens at very low Reynolds numbers.

No prediction method was proposed for heat transfer during partial dryout in bundle boiling for the present enhanced tubes since it occurs only from x = 0.98 to x =1.0. The dryout condition was expected as the saturated vapour condition was approached and the drop in heat transfer coefficient was extremely sharp due to the sudden onset of dryout. Predicting the steep slope accurately as a function of Reynolds number would produce large errors.

8.3   Conclusions

The existing frictional pressure drop prediction methods were found to be inconsistent and inaccurate for the two-phase flow data for tube bundles gathered here. Thus a new method based on accurate data for a variety of conditions and tubes was developed. A new prediction method was thus proposed, based on a phenomenological empirical approach, and it predicted the present adiabatic dataset well. The method can be implemented on a local scale to predict diabatic data

with reasonable success. The model captures the variations in vapour quality and mass flux well.

The heat transfer data presented in Chapter 6 were utilised to generate new prediction methods for the single-tube pool boiling heat transfer coefficient, the bundle boiling heat transfer coefficient and the onset of dryout for bundle boiling. Analysis of evaporation lead to a correlation parameter that related the length scale of intense fluid evaporation to the absorbed film thickness, then utilised in the prediction methods. The pool boiling correlation was then adjusted by a single tube specific constant, ignoring the weak effect of Reynolds number for the prediction of the bundle boiling heat transfer database.

The purpose of the analysis and extensive discussion of mechanisms on 3D-enhanced tubes was to gain insight into the heat transfer components responsible for the final result. When a complete model is proposed, based on accurate mechanisms, such as the one described for boiling in this study, a powerful design tool will be available. With such a prediction method the tube geometry, material and fluid combination can be analysed and optimized without expensive trial and error design procedures. This objective still remains as a long term objective that require better understanding of the liquid and vapour flow into and out of the pores of the enhancement and the distribution of the liquid film within its complex tunnels.

Chapter 9

Conclusions

In the present study an experimental investigation of two-phase flow and evaporation was performed for two enhanced boiling tubes using two refrigerants. A large heat transfer and pressure drop database for enhanced tubes in various operating conditions was added to the existing LTCM database. The study achieved the following goals:

- An investigation into the use and improvement of the Wilson plot method as a means to accurately estimate the internal heat transfer coefficient of the water-side heating fluid, required for backing out the boiling-side heat transfer coefficients.

- The pool boiling performance of a single tube in a stagnant pool of liquid refrigerant. The mechanisms of boiling were elaborated theoretically as basis for developing a prediction method and explaining the different performance obtained by different refrigerants.

- Local heat transfer on the enhanced tubes under bundle boiling conditions were obtained and the effect of convection on enhancement relative to pool boiling established.

- Pressure drops over the tube bundle under adiabatic and diabatic conditions with various flow rates and vapour qualities were obtained.

- The development of new prediction methods for heat transfer and pressure drop with a phenomenological representation of underlying mechanisms were proposed.

- Novel inspection of the two-phase flow patterns through visual observations in pool boiling and bundle boiling conditions was implemented. This aspect focused on obtaining quantitative bubble dynamics data where possible to substantiate theories related to flow patterns and boiling.

- A thorough uncertainty analysis of the propagation in experimental errors was carried out for heat transfer and all pressure drop components.

9.1 Main findings of the present study

Wilson Plot: The internal heat transfer coefficient correlation of Gnielinski (1976) with a leading coefficient variable was used and validated. The three-variable iterative Briggs and Young (1969) method was improved by using the linear regression method of York *et al.* (2004) to propagate the experimental uncertainties throughout the process into the estimation of the empirical fitting parameter C_i. The new minimisation method is not limited by the linear regression used to solve the Briggs and Young method. The validation procedure involved comparison between independent data sets for the enhanced tubes from different facilities and a further direct wall temperature measurement experiment to confirm the internal heat transfer prediction.

Pool boiling: Pool boiling performance was measured on a single tube at different saturation temperatures and heat fluxes with two refrigerants. Both tubes performed better with R134a than R236fa. The effect of the heat flux was stronger for the *Wieland Gewa-B5* than the *Wolverine Turbo-B5* tube using both refrigerants, depicting higher heat transfer coefficients at lower heat fluxes. A thorough investigation of boiling mechanisms was undertaken and a theoretical approach was used to characterise the evaporation process in the near-wall region. One of the stronger mechanisms in pool boiling was latent heat transfer. This lead to a new simple dimensionless ratio of two lengths (l_H and δ_a) that proved to have a good thermal correlating potential.

Bundle boiling: Convective bundle boiling experiments were carried out at various mass flux and vapour quality combinations with the two refrigerants. The induced convection did not have a strong influence on the performance of the tubes and a simple multiplier was able to predict the heat transfer in bundle conditions with the newly defined prediction method. The first ever direct comparison between falling film and bundle boiling data using a film Reynolds number definition for convective bundle boiling was presented. Contrary to falling film, where the heat flux dependence of the pool boiling condition was no longer present (constant plateau), bundle boiling maintained a heat flux dependence (heat flux dependent plateau). In general falling film thermal performance will be equal or higher than bundle boiling, but bundle boiling suffered less from dryout effects.

Onset of dryout: Onset of dryout was observed visually and from the laser light measurements. A transition line was defined on the bundle's flow pattern map. The enhanced tubes did not experience any substantial partial dryout conditions in convective bundle boiling. Smooth tubes experienced an earlier onset of dryout than the enhanced tubes. Convective bundle boiling did not have a large region of partial dryout with reduced heat transfer performance compared with falling film where higher film velocities and liquid column flow from tube to tube has more proclivity to local dryout.

Pressure drop: Pressure drops were measured for adiabatic and diabatic conditions. The conditions during diabatic testing were repeated for adiabatic tests. More adiabatic conditions were possible since dryout limit the conditions under diabatic testing. A new adiabatic pressure drop prediction method was proposed and applied for the diabatic conditions. In the past, mean values of vapour quality and void fraction were used for diabatic prediction. In a relatively small bundle this works fine, but it is proposed that the prediction method is implemented in smaller increments with local conditions.

Visual observation: A new flow pattern observation method using a borescope was developed. Flow pattern observations can be divided into several aspects:

- Visual observations of pool boiling with a focus on observing and quantifying bubble dynamics.

- Visual observations of bundle boiling performed in the adiabatic section of the bundle with the aim to classify the intertube flow patterns in tube bundles.

- Measurements of two-phase flow with piezo-electric pressure transducers and detection of dryout with the laser-light attenuation method.

Local flow measurements were taken to characterise the two-phase flow structure and improve the understanding of physical phenomena taking place. From the bundle observations it was found that changes in experimental conditions lead to a gradual change in the relative distribution of gas and liquid phases. Furthermore, no distinct effects were observed on the heat transfer and pressure drop.

The analysis of the pressure fluctuation power spectrum and the flow visualisation results improved the view of the two-phase flow on enhanced tubes. Some bubble dynamics data could be gathered, but were limited to conditions at low heat fluxes since the vapour generation obscured

the view. The flow frequencies could be identified with visual measurements and correlated to the measured frequencies from the piezo-electric pressure measurements. The pressure measurements were then used to show the continuous nature of the flow pattern transition from bubbly to "inter-tubular" annular flow.

9.2 Recommendations for future research

Within the scope of this study, many objectives were fulfilled and questions answered. However, the study generated new research questions that require additional research to be done. These topics are briefly mentioned below.

- An improvement of the instrumentation to allow accurate lower heat flux experiments to be made, down to a nominal heat flux of around 3 kW/m^2, are needed to track the trend in heat transfer coefficient as a function of heat flux. Applications often operate with small temperature differences and designers require reliable data for such conditions. Testing methods must be improved to allow low heat flux experiments with acceptable uncertainty.

- The prediction of pool boiling heat transfer through mechanistic models that are based on the physics involved require a fundamental approach with careful investigation. Isolating and quantifying each mechanism and the interactions of all the tube geometry, heat transfer and flow related phenomena would be invaluable to enhanced boiling tube designers. An accurate physical model of heat transfer, including as much physics as possible without using empirical stop-gaps, should be attempted.

- A comparison between pool boiling, falling film evaporation and convective bundle boiling could illuminate the convective mechanisms on enhanced tubes.

- The diabatic pressure drop in a bundle is not satisfactorily addressed by the adiabatic based methods. A larger diabatic test bundle and a diabatic void fraction model with additional local measurements could improve the understanding and prediction of diabatic pressure drops.

- Using the visualisation approach and improving the capability to extract accurate quantitative data representative of the flow phenomena will give further valuable insight into the understanding of the boiling mechanisms observed.

Appendix A

Uncertainty analysis

A.1 Introduction

The measuring equipment in experimental facilities provides information describing the system. If there is any error in an original measurement this error is carried forward into the calculations, and this introduces error into an otherwise exact equation. The test data comprising a single data point in this study is the average of values measured during a phase of steady operation. All recorded measurements are calibrated and have known uncertainty. Thus the uncertainties derived in this section are all for single-sample data and are based on data measured at the sampling rates and conditions stated previously.

A rigorous uncertainty analysis based on the approach proposed in Kline and McClintock (1953) has been applied in this study. The experiment-specific uncertainties are derived and calculated in the rest of this appendix. For each variable the terms that make up the uncertainty will be given explicitly.

A.1.1 Generalised uncertainty analysis methods

The term *uncertainty* refers to a possible error that an value may have (Kline and McClintock, 1953). The terms *uncertainty* and *uncertainty interval* both refer to the interval around a measured value, within which the true value is expected to lie.

The uncertainty of a measurement is typically given in terms of percentages, and is shown as δ(measurand). If we consider a variable X_i, its uncertainty would be represented as δX_i.

A. UNCERTAINTY ANALYSIS

Uncertainties are usually indicated with a confidence level. This value, in terms of percentage, refers to a confidence that X_i will not deviate by more than δX_i. The uncertainty is made up of the bias, which is a fixed error (B_i), and the precision (P_i), which can be a random error in the measurement. The uncertainty is calculated as the Euclidian norm of the two:

$$\delta X_i = \left\{ (B_i)^2 + (P_i)^2 \right\}^{\frac{1}{2}}$$

While some researchers deal with bias and precision separately (as was done in Coetzee (2000)), others deal with the overall uncertainty directly. In this study, overall uncertainty will be dealt with directly, except in the rare instances where assumptions were made which necessitate the use of both bias and precision.

Consider a quantity R, function of n variables, X_0 through X_n, each with uncertainty δX_i:

$$R = f(X_0, X_1...X_n)$$

The effect of the uncertainty of a single variable on quantity R is the partial derivative of R with respect to that single variable (*i.e.* X_i), times that variable's uncertainty (δX_i). Thus:

$$\delta R_{X_i} = \frac{\partial(R)}{\partial X_i} \delta X_i$$

By summing the uncertainties of R in terms of its variables, the maximum uncertainty is found. It is however, unlikely that such a value can be obtained, and thus the Euclidian norm of the individual uncertainties is taken, (Taylor, 1997):

$$\delta R = \left\{ \sum_{i=1}^{n} \left(\frac{\partial}{\partial X_i}(R)\delta X_i \right)^2 \right\}^{\frac{1}{2}} \tag{A.1}$$

This equation is valid only when:

- The errors and uncertainties of each variable are independent of one another

- The distribution of errors or uncertainties is Gaussian, for all X_i

- All the X_is are provided at the same confidence level. In this study the 95% confidence level (2σ) was used.

It is customary to normalize equation A.1 with respect to the full value of R, with percentage units.

A.2   Measurements

A.2.1   Uncertainty in temperature measurements

Temperatures in the current experimental system were measured using type-K thermocouples from Thermocoax. The cold junction temperature utilised was built into the *National Instruments* SCXI-1095 card. The thermocouples were calibrated in a temperature bath, against two Pt-100 resistance temperature detectors (RTD), over the applicable range.

   The temperatures were calibrated using a second order function. As they were calibrated using a precise RTD, the thermocouples' bias was taken to be that of the Pt-100 RTD used. The uncertainty of the cold junction was not accounted for. Furthermore, the precision (P) of each thermocouple measurement was known to be the twice standard deviation from the steady-state value it measures repeatedly. An example of thermocouple measurements taken over a period of eight minutes under isothermal conditions and compared against the uncalibrated and RTD measurements is given in Figure A.1.
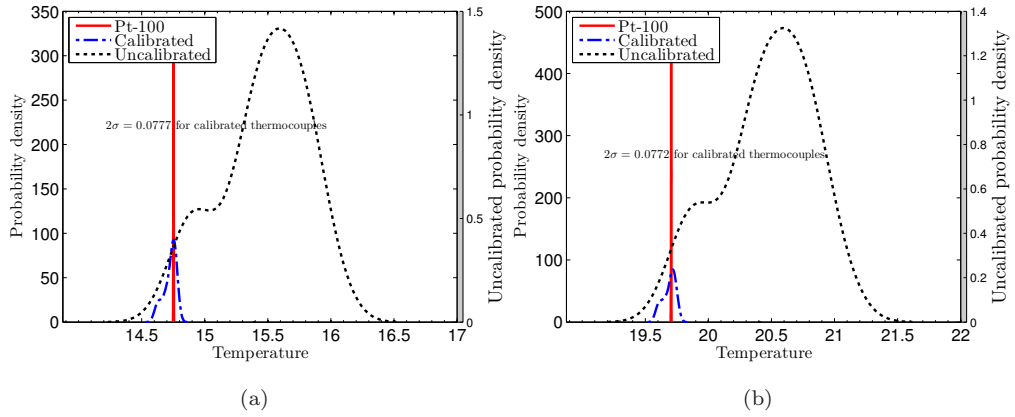
Figure A.1: Comparison of thermocouple measurements at isothermal conditions of (a) 15°C and (b) 20°C indicating the difference between uncalibrated, calibrated and RTD measurements

   Thus, the uncertainty in each thermocouple's reading was taken as:

$$\delta T_i = \sqrt{B^2 + P^2} = 0.1^oC$$

   There were several sections of the experimental set-up that utilised the average of several thermocouples. It follows that the mean temperature can be derived as:

$$T_{mean} = \frac{T_1 + T_2 + ... + T_n}{n}$$

and, that the partial differential of this mean temperature per measured temperature was:

$$\frac{\partial T_{mean}}{\partial T_i} = \frac{1}{n}$$

Taking the Euclidian norm, and assuming that the thermocouples have the same uncertainty, then:

$$\begin{aligned}
\delta T_{mean} &= \left\{ \sum_{i=1}^{n} \left(\frac{1}{n} \delta T_i \right)^2 \right\}^{\frac{1}{2}} = \left(\frac{n}{n^2} \delta T_i^2 \right)^{\frac{1}{2}} \\
&= \frac{\delta T_i}{\sqrt{n}}
\end{aligned}$$

A.2.2 Mass flow rate uncertainty

The refrigerant and water mass flow rates were measured with the same model Coriolis mass flow meter. The Krohne G100+ Coriolis flow meters have an accuracy of:

$$\delta \dot{m} = \pm \left(0.15 + \frac{S}{\dot{m}} \right) \dot{m}$$

where $S = 8.3\,10^{-3}$ kg/s is a constant for the Krohne G100+ mass flow meter.

A.2.3 Pressure measurement uncertainty

A.2.3.1 Absolute pressure measurement

The pressure transducers, Keller Series 23/25, with a full-scale (FS) reading of 10 and 20 bar ($\pm$ 1000 and 2000 kPa) had an uncertainty of 0.1% of full-scale. Thus:

$$\begin{aligned}
\delta P_j &= \pm \frac{0.1}{100} 2000 \\
&= \pm 2\,kPa
\end{aligned}$$

A.2.3.2 Differential pressure measurement

There were three Endress and Huaser pressure taps between the inlet and outlet of the test section (Chapter 3). As such, the measured pressures at the inlet and outlet were the mathematical average of three individual differential transducers, each with the same uncertainty δp (0.1% FS). The pressure transducers were all calibrated over the same range, and were found to be within the factory uncertainty specifications. Thus, it follows that:

$$\Delta p_{ave,measured} = \frac{1}{3} \sum_{j=1}^{3} \Delta p_{measured,j}$$

$$\delta \Delta p_{ave,measured} = \left\{ \sum_{j=1}^{3} \left(\frac{\partial}{\partial \Delta p_j} (\Delta p_{ave,measured}) \delta \Delta p_j \right)^2 \right\}^{\frac{1}{2}}$$

Since the pressure transducers' uncertainties were the same, it translated into:

$$\delta \Delta p_{ave,measured} = \left(\frac{1}{3} \right)^{\frac{1}{2}} \delta \Delta p_j$$

A fourth Endress and Hauser differential pressure transducer was added over the diabatic zone of the test section. This measurement was not averaged yet calibrated in the same manner as the preceding transducers and the manufacturer's specification of 0.075% FS was used.

A.2.4 Uncertainty in measurement of length

The precision limit was taken as twice the smallest increment of the tape measure, *i.e.* 0.5 mm, and a bias limit of 1 mm was assumed. Thus, the uncertainty in the measurement of length was:

$$\delta L = \sqrt{1^2 + 0.5^2} = 1.11 \ mm$$

For measurements made with calipers the precision limit was taken as twice the smallest displayed increment,*i.e.* 0.005 mm, and a bias limit of 0.01 mm was assumed, giving:

$$\delta L = \sqrt{0.01^2 + 0.005^2} = 0.0111 \ mm$$

A.2.5 Heat balance, pre-heater

The uncertainty in the heat load measured in the pre-heater was established by experiments with water prior to final installation. It was found that the measurement had a 3% error on the nominal measured value.

A.3 Physical properties

A.3.1 REFPROP uncertainty analysis

NIST (2007) REFPROP uses user inputs of pressure and temperature to calculate the correct property. The main thermo-physical properties of the fluid in question and the average uncertainties in terms of percentages are available in the *.fld* fluid files in the REFPROP directory. In a private e-mail communication Lemmon (2006) stated that the accepted practice is to take the uncertainty of the enthalpy as half of that of the isobaric specific heat. The water-side uncertainties are found in the water fluid file from REFPROP and the IAPWS Advisory Note (Watanabe, 2003) regarding uncertainties of enthalpy, thermal conductivity and surface tension.

The following typical uncertainties are reported in REFPROP, (Table A.1).

Table A.1: Uncertainties of properties determined by REFPROP

Property	Refrigerant	Water
$\delta h\%$	0.375	0.05
$\delta k_{l,v}\%$	5	0.001
$\delta \mu_l\%$	3	0.5
$\delta \mu_v\%$	4	0.5
$\delta \rho_l\%$	0.05	0.001
$\delta \rho_v\%$	0.05	0.001
$\delta \sigma\%$	0.05	0.1
$\delta c_p\%$	0.75	0.1

A.3.2 Uncertainty in the thermal conductivity value of copper tubing

Abu-Eishah (2001) performed a detailed analysis of the uncertainty of the copper tube thermal conductivity. He found that the total uncertainty in the conductivity in the temperature region of this study (*i.e.* $0 - 100^oC$) was:

$$\frac{\delta k_{Cu}}{k_{Cu}} \cdot 100 = \frac{4}{400} \cdot 100 = 0.01\%$$

It should be noted that the tubes in the current study were not pure copper $k = 340\ W/mK$. Determining the uncertainty of the thermal conductivity of these tubes was however subject to the same amount of error.

A.4   Propagation of uncertainty

A.4.1   Temperature difference uncertainty

Each temperature has its own uncertainty and using a temperature difference will only increase the uncertainty. Thus, for a generic temperature difference, the uncertainty was:

$$\delta \Delta T = \left(\delta T_1^2 + \delta T_2^2 \right)^{\frac{1}{2}}$$

A.4.2   Uncertainty in measurement of surface area

The tube surface area was calculated from:

$$A_i = \pi D_i L \qquad and \qquad A_o = \pi D_o L$$

Thus, the uncertainty in A was:

$$\delta A = \left\{ \left(\frac{\partial A}{\partial L} \delta L \right)^2 + \left(\frac{\partial A}{\partial D_i} \delta D_i \right)^2 \right\}^{\frac{1}{2}}$$

The partial differentials were:

$$\frac{\partial A}{\partial L} = \pi D$$
$$\frac{\partial A}{\partial D} = \pi L$$

The minimum flow area used for the mass flux was:

$$A_{gap} = (W_{bundle} - 3D_o)L$$

Then, the uncertainty in A_{gap} was:

$$\delta A_{gap} = \left\{ \left(\frac{\partial A_{gap}}{\partial W_{bundle}} \delta W_{bundle} \right)^2 + \left(\frac{\partial A_{gap}}{\partial D_o} \delta D_o \right)^2 + \left(\frac{\partial A_{gap}}{\partial L} \delta L \right)^2 \right\}^{\frac{1}{2}}$$

A.4.3   Mass flux uncertainty

The mass flux was defined as:

$$G = \frac{\dot{m}}{A_{gap}}$$

From the uncertainty of cross-sectional area, and that of the flow rate, the uncertainty in mass flux was:

$$\delta G = \left\{ \left(\frac{\partial G}{\partial \dot{m}} \delta \dot{m} \right)^2 + \left(\frac{\partial G}{\partial A_{gap}} \delta A_{gap} \right)^2 \right\}^{\frac{1}{2}}$$

where the partial differentials were:

$$\frac{\partial G}{\partial \dot{m}} = \frac{1}{A_{gap}}$$
$$\frac{\partial G}{\partial A_{gap}} = -\frac{\dot{m}}{A_{gap}^2}$$

A.4.4   Heat load uncertainty, water-side

The test section water-side heat load uncertainty can be calculated using:

$$\dot{Q}_i = \dot{m}_{water} c_p \Delta T_i$$

Thus, the uncertainty in the water-side energy transfer, knowing the uncertainties in the water mass flow rate, isobaric specific heat and temperature difference, were:

$$\delta \dot{Q}_i = \left\{ \left(\frac{\partial \dot{Q}_i}{\partial \dot{m}} \delta \dot{m} \right)^2 + \left(\frac{\partial \dot{Q}_i}{\partial c_p} \delta c_p \right)^2 + \left(\frac{\partial \dot{Q}_i}{\partial \Delta T_i} \delta \Delta T_i \right)^2 \right\}^{\frac{1}{2}}$$

A.4.5   Test section vapour quality uncertainty analysis

A.4.5.1   Inlet vapour quality uncertainty

The vapour quality at the inlet and outlet of the test section was calculated using measured data, including temperature, pressure, water-side heat transferred and pre-heater heat transferred. This means that the inlet and outlet enthalpies were calculated based on the initial measured conditions at the inlet of the pre-heater in the single-phase region. Thus, the uncertainty in test inlet enthalpy was:

$$h_{in,test} = h_{in,pre} + \left| \frac{\dot{Q}_{pre,H_2O}}{\dot{m}_{ref}} \right|$$

$$\delta h_{in,test} = \left\{ \underbrace{\left(\frac{\partial}{\partial h_{in,pre}}(h_{in,test})\delta h_{in,pre} \right)^2}_{A} + \underbrace{\left(\frac{\partial}{\partial \dot{Q}_{pre,H_2O}}(h_{in,test})\delta \dot{Q}_{pre,H_2O} \right)^2}_{B} + \underbrace{\left(\frac{\partial}{\partial \dot{m}_{ref}}(h_{in,test})\delta \dot{m}_{ref} \right)^2}_{C} \right\}^{\frac{1}{2}}$$

where the partial differentials above were:

Term A $\qquad \dfrac{\partial h_{in,test}}{\partial h_{in,pre}} = 1 \qquad$ Term B $\qquad \dfrac{\partial h_{in,test}}{\partial \dot{Q}_{pre,H_2O}} = -\dfrac{1}{\dot{m}_{ref}}$

Term C $\qquad \dfrac{\partial h_{in,test}}{\partial \dot{m}_{ref}} = \dfrac{\dot{Q}_{H_2O}}{\dot{m}_{ref}^2}$

Knowing what the enthalpy at the inlet was, the quality could be calculated as:

$$x_{in} = \frac{h_{in,test} - h_l}{h_v - h_l}$$

From the above, the uncertainty in x_{in} was:

$$\delta x_{in} = \left\{ \underbrace{\left(\frac{\partial}{\partial h_{in,test}}(x_{in})\delta h_{in,test} \right)^2}_{A} + \underbrace{\left(\frac{\partial}{\partial h_{l,test}}(x_{in})\delta h_{f,test} \right)^2}_{B} + \underbrace{\left(\frac{\partial}{\partial h_{v,test}}(x_{in})\delta h_{v,test} \right)^2}_{C} \right\}^{\frac{1}{2}}$$

The partial differentials were:

Term A $\qquad \dfrac{\partial x_{in}}{\partial h_{in,test}} = \dfrac{1}{h_{v,test} - h_{l,test}}$

Term B $\qquad \dfrac{\partial x_{in}}{\partial h_{v,test}} = \dfrac{h_l - h_{in,test}}{(h_v - h_l)^2}$

Term C $\qquad \dfrac{\partial x_{in}}{\partial h_{l,test}} = -\dfrac{1}{h_{v,test} - h_{l,test}} - \dfrac{h_{in,test} - h_{l,test}}{(h_{v,test} - h_{l,test})^2}$

Where h_l and h_v were evaluated at the saturation pressure and temperature measured at the inlet of the test section, and were functions of REFPROP.

A.4.5.2   Outlet vapour quality uncertainty

The outlet vapour quality, much like the inlet quality, was dependent on the quantity of heat extracted out of the test section, and was calculated from:

$$h_{out,test} = h_{in,test} + \left| \frac{\dot{Q}_{test,H_2O}}{\dot{m}_{ref}} \right|$$

Similar to the previous section, the uncertainty of this enthalpy was:

$$\delta h_{out,test} = \left\{ \underbrace{\left(\frac{\partial}{\partial h_{in,test}}(h_{out,test}) \delta h_{in,test} \right)^2}_{A} + \underbrace{\left(\frac{\partial}{\partial \dot{Q}_{test,H_2O}}(h_{out,test}) \delta \dot{Q}_{test,H_2O} \right)^2}_{B} + \underbrace{\left(\frac{\partial}{\partial \dot{m}_{ref}}(h_{out,test}) \delta \dot{m}_{ref} \right)^2}_{C} \right\}^{\frac{1}{2}}$$

Where the partial differentials were:

Term A $\dfrac{\partial h_{out,test}}{\partial h_{in,pre}} = 1$ Term B $\dfrac{\partial h_{out,test}}{\partial \dot{Q}_{pre,H_2O}} = \dfrac{1}{\dot{m}_{ref}}$

Term C $\dfrac{\partial h_{in,test}}{\partial \dot{m}_{ref}} = \dfrac{\dot{Q}_{H_2O}}{\dot{m}_{ref}^2}$

and the uncertainty in quality was:

$$\delta x_{out} = \left\{ \underbrace{\left(\frac{\partial}{\partial h_{out,test}}(x_{out}) \delta h_{out,test} \right)^2}_{A} + \underbrace{\left(\frac{\partial}{\partial h_{l,test,out}}(x_{out}) \delta h_{l,test,out} \right)^2}_{B} + \underbrace{\left(\frac{\partial}{\partial h_{v,test,out}}(x_{out}) \delta h_{v,test,out} \right)^2}_{C} \right\}^{\frac{1}{2}}$$

The partial differentials were:

Term A $\dfrac{\partial x_{out}}{\partial h_{out,test}} = \dfrac{1}{h_{v,test,out} - h_{l,test,out}}$

Term B $\dfrac{\partial x_{out}}{\partial h_{v,test,out}} = \dfrac{h_l - h_{out,test}}{(h_{v,out} - h_{l,out})^2}$

Term C $\dfrac{\partial x_{out}}{\partial h_{l,test,out}} = -\dfrac{1}{h_{v,test,out} - h_{l,test,out}} - \dfrac{h_{out,test} - h_{l,test,out}}{(h_{v,test,out} - h_{l,test,out})^2}$

A.4.6 Void fraction uncertainty

The basic equations of the Feenstra *et al.* (2000) method were applied and elaborated on to estimate the propagation of error through the model. The void fraction was given by equation A.2 which used the correlation in equation A.3 for the slip ratio. The capillary number was a function of u_g; a variable that was iterated during the solution procedure of the void fraction. To calculate the propagation of error for a data point the error in all these terms was needed. During the data reduction the final solution of all the variables was stored in the database for use in the propagation of error evaluation.

$$\varepsilon = \left[1 + S \frac{\rho_g}{\rho_l} \left(\frac{1-x}{x} \right) \right]^{-1} \tag{A.2}$$

$$S = 1 + 25.7 (Ri\, Cap)^{1/2} \left(\frac{P}{D} \right)^{-1} \tag{A.3}$$

$$Ri = \frac{(\rho_l - \rho_g)^2 g\, a}{G^2} \qquad Cap = \frac{\mu_l u_g}{\sigma}$$

The following discussion proceeds, in reverse order, with the derivative equations for the calculation of uncertainty in the capillary and Richardson numbers. These results were then used in the slip ratio and finally the void fraction.

A.4.6.1 Capillary number

By substituting $u_g = \frac{xG}{\varepsilon \rho_v}$ it follows that:

$$Cap = f(\mu_l, x, G, \sigma, \varepsilon, \rho_v)$$

$$\delta Cap = \left\{ \underbrace{\left(\frac{\partial Cap}{\partial \mu_l} \delta \mu_l \right)^2}_{A} + \underbrace{\left(\frac{\partial Cap}{\partial x} \delta x \right)^2}_{B} + \underbrace{\left(\frac{\partial Cap}{\partial G} \delta G \right)^2}_{C} + \underbrace{\left(\frac{\partial Cap}{\partial \sigma} \delta \sigma \right)^2}_{D} \underbrace{\left(\frac{\partial Cap}{\partial \varepsilon} \delta \varepsilon \right)^2}_{E} \underbrace{\left(\frac{\partial Cap}{\partial \rho_v} \delta \rho_v \right)^2}_{F} \right\}^{\frac{1}{2}}$$

Term A	$\dfrac{\partial Cap}{\partial \mu_l} = \dfrac{xG}{\sigma \varepsilon \rho_v}$	Term B	$\dfrac{\partial Cap}{\partial x}$	$= \dfrac{\mu_l G}{\sigma \varepsilon \rho_v}$
Term C	$\dfrac{\partial Cap}{\partial G} = \dfrac{\mu_l x}{\sigma \varepsilon \rho_v}$	Term D	$\dfrac{\partial Cap}{\partial \sigma}$	$= -\dfrac{\mu_l x G}{\sigma^2 \varepsilon \rho_v}$
Term E	$\dfrac{\partial Cap}{\partial \varepsilon} = -\dfrac{\mu_l x G}{\sigma \varepsilon^2 \rho_v}$	Term F	$\dfrac{\partial Cap}{\partial \rho_v}$	$= -\dfrac{\mu_l x G}{\sigma \varepsilon \rho_v^2}$

A.4.6.2 Richardson number

$$Ri = f(\rho_l, \rho_v, a, G)$$

$$\delta Ri = \left\{ \underbrace{\left(\frac{\partial Ri}{\partial \rho_l} \delta \rho_l \right)^2}_{A} + \underbrace{\left(\frac{\partial Ri}{\partial \rho_v} \delta \rho_v \right)^2}_{B} + \underbrace{\left(\frac{\partial Ri}{\partial a} \delta a \right)^2}_{C} + \underbrace{\left(\frac{\partial Ri}{\partial G} \delta G \right)^2}_{D} + \right\}^{\frac{1}{2}}$$

Term A	$\dfrac{\partial Ri}{\partial \rho_l} = \dfrac{2\Delta p a g}{G^2}$	Term B	$\dfrac{\partial Ri}{\partial \rho_v}$	$= \dfrac{-2\Delta p a g}{G^2}$
Term C	$\dfrac{\partial Ri}{\partial a} = \dfrac{\Delta p^2 g}{G^2}$	Term D	$\dfrac{\partial Ri}{\partial G}$	$= \dfrac{-2\Delta p^2 a g}{G^3}$

A.4.6.3 Slip ratio

$$S = f(Ri, Cap, P, D)$$

$$\delta S = \left\{ \underbrace{\left(\frac{\partial S}{\partial Ri} \delta Ri \right)^2}_{A} + \underbrace{\left(\frac{\partial S}{\partial Cap} \delta Cap \right)^2}_{B} + \underbrace{\left(\frac{\partial S}{\partial P} \delta P \right)^2}_{C} + \underbrace{\left(\frac{\partial S}{\partial D} \delta D \right)^2}_{D} + \right\}^{\frac{1}{2}}$$

Term A	$\dfrac{\partial S}{\partial Ri} = 12.85(Ri\,Cap)^{-\frac{1}{2}} Cap \dfrac{D}{P}$	Term B	$\dfrac{\partial S}{\partial Cap}$	$= 12.85(Ri\,Cap)^{-\frac{1}{2}} Ri \dfrac{D}{P}$
Term C	$\dfrac{\partial S}{\partial P} = -25.7(Ri\,Cap)^{\frac{1}{2}} \dfrac{D}{P^2}$	Term D	$\dfrac{\partial S}{\partial D}$	$= \dfrac{25.7(Ri\,Cap)^{\frac{1}{2}}}{P}$

A.4.6.4   Void fraction

$$\varepsilon = f(S, \rho_l, \rho_v, x)$$

$$\delta\varepsilon = \left\{ \underbrace{\left(\frac{\partial\varepsilon}{\partial S}\delta S\right)^2}_{A} + \underbrace{\left(\frac{\partial\varepsilon}{\partial \rho_l}\delta\rho_l\right)^2}_{B} + \underbrace{\left(\frac{\partial\varepsilon}{\partial \rho_v}\delta\rho_v\right)^2}_{C} + \underbrace{\left(\frac{\partial\varepsilon}{\partial x}\delta x\right)^2}_{D} \right\}^{\frac{1}{2}}$$

Term A $\qquad \dfrac{\partial\varepsilon}{\partial S} = -\left[1 + S\dfrac{\rho_v}{\rho_l}\left(\dfrac{1}{x} - 1\right)\right]^{-2}\left[\dfrac{\rho_v}{\rho_l}\left(\dfrac{1}{x} - 1\right)\right]$

Term B $\qquad \dfrac{\partial\varepsilon}{\partial \rho_l} = -\left[1 + S\dfrac{\rho_v}{\rho_l}\left(\dfrac{1}{x} - 1\right)\right]^{-2}\left[\dfrac{S}{\rho_l}\left(\dfrac{1}{x} - 1\right)\right]$

Term C $\qquad \dfrac{\partial\varepsilon}{\partial \rho_v} = -\left[1 + S\dfrac{\rho_v}{\rho_l}\left(\dfrac{1}{x} - 1\right)\right]^{-2}\left[\dfrac{-S\rho_v}{\rho_l^2}\left(\dfrac{1}{x} - 1\right)\right]$

Term D $\qquad \dfrac{\partial\varepsilon}{\partial x} = -\left[1 + S\dfrac{\rho_v}{\rho_l}\left(\dfrac{1}{x} - 1\right)\right]^{-2}\left[\dfrac{-S\rho_v}{\rho_l x^2}\right]$

A.4.7 Heat transfer coefficient

$$
h_o \;=\; \left[\frac{T_{wat} - T_{sat}}{q_o} - R_w - \frac{1}{h_i}\left(\frac{D_o}{D_i}\right)\right]^{-1}
$$

$$
h_o \;=\; f(T_{wat}, T_{sat}, q_o, R_w, h_i, D_o, D_i)
$$

$$
\delta h_o \;=\; \left\{
\begin{array}{c}
\underbrace{\left(\dfrac{\partial h_o}{\partial T_{wat}}\delta T_{wat}\right)^2}_{A} + \underbrace{\left(\dfrac{\partial h_o}{\partial T_{sat}}\delta T_{sat}\right)^2}_{B} + \\[2ex]
\underbrace{\left(\dfrac{\partial h_o}{\partial q_o}\delta q_o\right)^2}_{C} + \underbrace{\left(\dfrac{\partial h_o}{\partial R_w}\delta R_w\right)^2}_{D} + \\[2ex]
\underbrace{\left(\dfrac{\partial h_o}{\partial h_i}\delta h_i\right)^2}_{E} + \underbrace{\left(\dfrac{\partial h_o}{\partial D_o}\delta D_o\right)^2}_{F} + \\[2ex]
\underbrace{\left(\dfrac{\partial h_o}{\partial D_i}\delta D_i\right)^2}_{G}
\end{array}
\right\}^{\frac{1}{2}}
\tag{A.4}
$$

Term A
$$
\frac{\partial h_o}{\partial T_{wat}} = -\left[\frac{T_{wat}-T_{sat}}{q_o} - R_w - \frac{1}{h_i}\left(\frac{D_o}{D_i}\right)\right]^{-2}\left(\frac{1}{q_o}\right)
$$

Term B
$$
\frac{\partial h_o}{\partial T_{sat}} = \left[\frac{T_{wat}-T_{sat}}{q_o} - R_w - \frac{1}{h_i}\left(\frac{D_o}{D_i}\right)\right]^{-2}\left(\frac{1}{q_o}\right)
$$

Term C
$$
\frac{\partial h_o}{\partial q_o} = \left[\frac{T_{wat}-T_{sat}}{q_o} - R_w - \frac{1}{h_i}\left(\frac{D_o}{D_i}\right)\right]^{-2}\left(\frac{T_{wat}-T_{sat}}{q_o^2}\right)
$$

Term D
$$
\frac{\partial h_o}{\partial R_w} = \left[\frac{T_{wat}-T_{sat}}{q_o} - R_w - \frac{1}{h_i}\left(\frac{D_o}{D_i}\right)\right]^{-2}
$$

Term E
$$
\frac{\partial h_o}{\partial h_i} = -\left[\frac{T_{wat}-T_{sat}}{q_o} - R_w - \frac{1}{h_i}\left(\frac{D_o}{D_i}\right)\right]^{-2}\left(\frac{D_o}{D_i}\right)\left(\frac{1}{h_i^2}\right)
$$

Term F
$$
\frac{\partial h_o}{\partial D_o} = \left[\frac{T_{wat}-T_{sat}}{q_o} - R_w - \frac{1}{h_i}\left(\frac{D_o}{D_i}\right)\right]^{-2}\frac{1}{h_i D_i}
$$

Term G
$$
\frac{\partial h_o}{\partial D_i} = -D_o\left[\frac{T_{wat}-T_{sat}}{q_o} - R_w - \frac{1}{h_i}\left(\frac{D_o}{D_i}\right)\right]^{-2}\frac{1}{h_i D_i^2}
$$

A.4.7.1 Terms A and B (equation A.4)

Where δT_{wat} is known from the thermocouple calibration from a station averaging two thermocouples. The same type of thermocouple was employed to measure T_{sat} therefore δT_{sat} was also known.

A.4.7.2 Term C (equation A.4): Heat flux uncertainty in enthalpy gradient method

The enthalpy gradient method is defined in Chapter 3. The first possible method of defining the uncertainty for this method requires an approximation of the uncertainty of the gradient of the least squares solution to the second order temperature profile (T_{wat}).

$$q_o = \frac{\dot{m}c_p}{\pi D_o}\frac{dT_{wat}}{ds}$$

$$q_o = f(\dot{m}, c_p, D_o, \frac{dT_{wat}}{ds})$$

The uncertainty in $\dot{m}$ is known from the Coriolis flow-meter calibration and those of c_p from REFPROP and D_o has been stated previously in section A.2.4. T_{wat} was derived from a polynomial fit $T_{wat} = a.s^2 + b.s + c$. To calculate the uncertainties in the parameters a and b (δa and δb) required for $\delta\frac{dT_{wat}}{ds}$ is not a trivial matter. A possible method is discussed in literature by Cecchi (1991), Lira (2000), Lira *et al.* (2004) and Scarpa (1998). A basic understanding of the problem is given in Taylor (1997). However, this method was not pursued during this study.

Alternatively, for the specific case of a second order polynomial fit through the thermocouples at three equidistant locations (Gstöhl, 2004), the heat flux in the middle (s = L/2) of the tube can be re-written as :

$$q_o|_{s=L/2} = \frac{\dot{m}c_p}{\pi D_o L}(T_{wat,0} - T_{wat,L})$$

With this mean value theorem simplification for the middle point, the uncertainty in the heat flux can be computed as:

$$\delta q_o|_{s=L/2} = \left\{ \begin{array}{c} \left(\frac{\partial q_o}{\partial \dot{m}}\delta\dot{m}\right)^2 + \left(\frac{\partial q_o}{\partial c_p}\delta c_p\right)^2 + \\ 2\left(\frac{\partial q_o}{\partial T_{wat}}\delta T_{wat}\right)^2 + \left(\frac{\partial q_o}{\partial D_o}\delta D_o\right)^2 + \\ \left(\frac{\partial q_o}{\partial L}\delta L\right)^2 \end{array} \right\}^{\frac{1}{2}}$$

A.4.7.3 Term E (equation A.4): Internal heat transfer coefficient from the Wilson plot

The partial derivative of h_o to h_i is given as term E (equation A.4). It was assumed that the uncertainty in h_i was a result of the Wilson plot approximation used to define the internal heat transfer coefficient and the propagation of error. Therefore:

$$h_i = C_i h_{gni}$$

$$h_i = f(C_i, h_{gni})$$

$$\delta h_i = \left\{ \left(\underbrace{\underbrace{\frac{\partial h_i}{\partial C_i}}_{A} \cdot \underbrace{\delta C_i}_{\text{E1}}}_{A} \right)^2 + \left(\underbrace{\underbrace{\frac{\partial h_i}{\partial h_{gni}}}_{B} \underbrace{\delta h_{gni}}_{\text{E2}}}_{B} \right)^2 \right\}^{\frac{1}{2}}$$

Term A $\qquad \dfrac{\partial h_i}{\partial C_i} = h_{gni}$ $\qquad$ Term B $\qquad \dfrac{\partial h_i}{\partial h_{gni}} \qquad = C_i$

A.4.7.4 Term E1: Wilson plot multiplier

The technique to compute δC_i which was related to the Wilson plot method applied in the laboratory and is discussed in Appendix B.

$$\underbrace{\left[\frac{1}{U_o} - R_w \right] q_o^n}_{Y} = \underbrace{\frac{1}{C_i}}_{a} \underbrace{\left[\frac{q_o^n}{h_{gni}} \frac{D_o}{D_i} \right]}_{X} + \underbrace{\frac{1}{C_o}}_{b}$$

$$y = ax + b$$

The curve fits n pairs of observations (X_j, Y_j) and the objective is to determine δC_i. Each observation X_j and Y_j is subject to the propagation of error. A classic least squares approximation only minimizes the vertical (y) difference between the data point and the proposed fit. In our case the data were subject to errors in both the x and y directions. Therefore the error in each data point needed to be accounted for and the error in the proposed fit coefficients had to be provided.

$$C_i = \frac{1}{a}$$

$$\delta C_i = \left[\left(\frac{\partial C_i}{\partial a} \delta a \right)^2 \right]^{\frac{1}{2}} = \left| \frac{1}{a^2} \delta a \right|$$

The next step was to determine the uncertainty in the fitting coefficients: δa, δb. One method would be to determine these quantities numerically through mathematical software, as mentioned for the quadratic fit in term C.

A method related to linear least squares is presented in Cecchi (1991). For the case of linear regression, the analytical expressions of the uncertainties δa and δb are obtained. More details about the available methodologies are presented in Neri *et al.* (1989). The method proposed by York *et al.* (2004) provides the coefficient uncertainties for a linear regression, each datum weighted by its uncertainty and incorporating the x and y error of the data in the formulation of the regression. Before discussing this method the uncertainties in the observations X_j and Y_j are computed here.

For each data point, Y_j:

$$Y_j = \left[\frac{1}{U_o} - R_w\right] q_o^n$$

$$\delta Y_j = \left\{ \underbrace{\left(\frac{\partial Y_j}{\partial U_o}\delta U_o\right)^2}_{A} + \underbrace{\left(\frac{\partial Y_j}{\partial R_w}\delta R_w\right)^2}_{B} + \underbrace{\left(\frac{\partial Y_j}{\partial q_o}\delta q_o\right)^2}_{C} \right\}^{\frac{1}{2}}$$

Term A $\qquad \dfrac{\partial Y_j}{\partial U_o} = \dfrac{-1}{U_o^2}q_o^n$ $\qquad\qquad$ Term B $\qquad \dfrac{\partial Y_j}{\partial R_w} \qquad = -q_o^n$

Term C $\qquad \dfrac{\partial Y_j}{\partial q_o} = \left[\dfrac{1}{U_o} - R_w\right] n q_o^{n-1}$

For X_j:

$$X_j = \frac{q_o^n}{h_{gni}}\left(\frac{D_o}{D_i}\right)$$

$$\delta X_j = \left\{ \underbrace{\left(\frac{\partial X_j}{\partial q_o}\delta q_o\right)^2}_{A} + \underbrace{\left(\frac{\partial X_j}{\partial h_{gni}}\delta h_{gni}\right)^2}_{B} \right\}^{\frac{1}{2}} \tag{A.5}$$

Term A $\qquad \dfrac{\partial X_j}{\partial q_o} = n\dfrac{q_o^{n-1}}{h_{gni}}\dfrac{D_o}{D_i}$ $\qquad$ Term B $\qquad \dfrac{\partial X_j}{\partial h_{gni}} \qquad = (-1)\dfrac{q_o^n}{h_{gni}^2}\dfrac{D_o}{D_i}$

Although the method of York *et al.* (2004) provided the uncertainty for both coefficients it was δa that was required to compute δC_i. The weighting function was derived from the uncertainties in X_i and Y_i where the components $\omega(X_i)$ and $\omega(Y_i)$ were equated to $\frac{1}{\delta X_i}$ and $\frac{1}{\delta Y_i}$ respectively:

$$W_i = \frac{\omega(X_i)\omega(Y_i)}{\omega(X_i) + b^2\omega(Y_i)}$$

The following solution was minimized until b converged:

$$
\begin{aligned}
\overline{X} &= \frac{\sum(W_i X_i)}{\sum(W_i)} \\
\overline{Y} &= \frac{\sum(W_i Y_i)}{\sum(W_i)} \\
U_i &= X_i - \overline{X} \\
V_i &= Y_i - \overline{Y} \\
\beta &= W_i\left(\frac{U_i}{\omega(Y_i)} + b\frac{V_i}{\omega(X_i)}\right) \\
\overline{\beta} &= \frac{\sum(W_i \beta_i)}{\sum(W_i)} \\
b &= \frac{\sum(W_i \beta_i V_i)}{\sum(W_i \beta_i U_i)}
\end{aligned}
$$

Thereafter the remaining components were calculated

$$
\begin{aligned}
x_i &= \overline{X} + \beta_i \\
\overline{x} &= \frac{\sum(W_i x_i)}{\sum(W_i)} \\
u_i &= x_i - \overline{x}
\end{aligned}
$$

$$
a = \overline{Y} - b\overline{X}
$$

$$
\begin{aligned}
S &= \sum(W_i)(y - bx - a)^2 \\
\delta b &= \left(\frac{1}{\sum(W_i u_i^2)}\right)^{0.5} \\
\delta a &= \left(\frac{1}{\sum(W_i)} + \overline{x}^2 \delta b^2\right)^{0.5}
\end{aligned}
$$

A.4.7.5 Term E2: Gnielinski heat transfer prediction

The term δh_{gni} was calculated from the propagation of error in each variable in the equation similar to all the examples above. Details are not shown here.

$$
\delta h_{gni} = f(f, Re_{wat}, Pr_{wat}, k_l, D_h)
$$

A.4.8   Pressure drop uncertainty analysis

The uncertainty in the frictional pressure drop, in addition to being a function of the accuracy of the pressure transducers, is also a function of the vapour quality, void fraction and fluid properties that make up every component of the pressure drop.

$$\Delta p_{meas} = \Delta p_s + \Delta p_m + \Delta p_f$$

To isolate Δp_f the above equation is rearranged:

$$\Delta p_f = \Delta p_{meas} - \Delta p_m - \Delta p_s$$

A.4.8.1   Static pressure drop uncertainty

The static pressure drop was defined for incremental discretisations of the bundle as described in section 3.7.2. The uncertainty of the static component was defined as the mean static head of the bundle. The mean liquid and vapour densities were used because their values and uncertainty remain constant. The void fraction uncertainty for the inlet and outlet were used because they were dependent on the vapour quality whose uncertainty varied from the inlet to outlet.

$$\Delta p_s = [\rho_l(1 - \varepsilon_{mean}) + \rho_v(\varepsilon_{mean})] \, g\Delta h$$
$$\Delta p_s = f(\rho_l, \rho_v, \varepsilon_{in}, \varepsilon_{out}, \Delta h)$$

$$\delta\Delta p_s = \left\{ \underbrace{\left(\frac{\partial \Delta p_s}{\partial \rho_l}\delta\rho_l\right)^2}_{A} + \underbrace{\left(\frac{\partial \Delta p_s}{\partial \rho_v}\delta\rho_v\right)^2}_{B} + \underbrace{\left(\frac{\partial \Delta p_s}{\partial \varepsilon_{in}}\delta\varepsilon_{in}\right)^2}_{C} + \underbrace{\left(\frac{\partial \Delta p_s}{\partial \varepsilon_{out}}\delta\varepsilon_{out}\right)^2}_{D} + \underbrace{\left(\frac{\partial \Delta p_s}{\partial \Delta h}\delta\Delta h\right)^2}_{E} \right\}^{\frac{1}{2}}$$

This gives five terms in the calculation of uncertainty for the static pressure drop. Each of the uncertainties referred to for these terms can be found in the above sections. The derivatives of each term is given below:

Term A
$$\frac{\partial \Delta p_s}{\partial \rho_l} = (1 - \frac{1}{2}\varepsilon_{out} - \frac{1}{2}\varepsilon_{in})g\Delta h$$

Term B
$$\frac{\partial \Delta p_s}{\partial \rho_v} = (\frac{1}{2}\varepsilon_{out} + \frac{1}{2}\varepsilon_{in})g\Delta h$$

Term C
$$\frac{\partial \Delta p_s}{\partial \varepsilon_{in}} = (-\frac{1}{2}\rho_l + \frac{1}{2}\rho_v)g\Delta h$$

Term D
$$\frac{\partial \Delta p_s}{\partial \varepsilon_{out}} = (-\frac{1}{2}\rho_l + \frac{1}{2}\rho_v)g\Delta h$$

Term E
$$\frac{\partial \Delta p_s}{\partial \Delta h} = (\rho_l(1 - \frac{1}{2}\varepsilon_{out} - \frac{1}{2}\varepsilon_{in}) + \frac{1}{2}\rho_v(\varepsilon_{out} + \varepsilon_{in}))g$$

A.4.8.2 Momentum pressure drop uncertainty

The momentum pressure drop was defined in Section 3.7.2 for a constant cross-sectional area as:

$$\Delta p_m = G^2 \left\{ \left[\frac{(1-x)^2}{\rho_l(1-\varepsilon)} + \frac{x^2}{\rho_v\varepsilon} \right]_{out} - \left[\frac{(1-x)^2}{\rho_l(1-\varepsilon)} + \frac{x^2}{\rho_v\varepsilon} \right]_{in} \right\}$$

$$\Delta p_m = f(G, x_{in}, x_{out}, \rho_{in}, \rho_{out}, \varepsilon_{in}, \varepsilon_{out})$$

This equation is therefore a function of mass flux, vapour and liquid densities, vapour quality and void fraction, at the inlet and outlet. The derivatives of the momentum pressure drop in terms of its components are

$$\delta\Delta p_m = \left\{ \begin{array}{c} \underbrace{\left(\frac{\partial \Delta p_m}{\partial G}\delta G\right)^2}_{A} + \\[2ex] \underbrace{\left(\frac{\partial \Delta p_m}{\partial x_{in}}\delta x_{in}\right)^2}_{B} + \underbrace{\left(\frac{\partial \Delta p_m}{\partial x_{out}}\delta x_{out}\right)^2}_{C} + \\[2ex] \underbrace{\left(\frac{\partial \Delta p_m}{\partial \rho_{l,in}}\delta \rho_{l,in}\right)^2}_{D} + \underbrace{\left(\frac{\partial \Delta p_m}{\partial \rho_{l,out}}\delta \rho_{l,out}\right)^2}_{E} + \\[2ex] \underbrace{\left(\frac{\partial \Delta p_m}{\partial \rho_{v,in}}\delta \rho_{v,in}\right)^2}_{F} + \underbrace{\left(\frac{\partial \Delta p_m}{\partial \rho_{v,out}}\delta \rho_{v,out}\right)^2}_{G} + \\[2ex] \underbrace{\left(\frac{\partial \Delta p_m}{\partial \varepsilon_{in}}\delta \varepsilon_{in}\right)^2}_{H} + \underbrace{\left(\frac{\partial \Delta p_m}{\partial \varepsilon_{out}}\delta \varepsilon_{out}\right)^2}_{I} \end{array} \right\}^{\frac{1}{2}}$$

Term A $\qquad \dfrac{\partial \Delta p_m}{\partial G} = 2G \left\{ \left[\dfrac{(1-x)^2}{\rho_l(1-\varepsilon)} + \dfrac{x^2}{\rho_v \varepsilon} \right]_{out} - \left[\dfrac{(1-x)^2}{\rho_l(1-\varepsilon)} + \dfrac{x^2}{\rho_v \varepsilon} \right]_{in} \right\}$

Term B $\qquad \dfrac{\partial \Delta p_m}{\partial x_{in}} = G^2 \left[\dfrac{2(1-x)}{\rho_l(1-\varepsilon)} + \dfrac{2x}{\rho_v \varepsilon} \right]_{in}$

Term C $\qquad \dfrac{\partial \Delta p_m}{\partial x_{out}} = G^2 \left[\dfrac{2(1-x)}{\rho_l(1-\varepsilon)} + \dfrac{2x}{\rho_v \varepsilon} \right]_{out}$

Term D $\qquad \dfrac{\partial \Delta p_m}{\partial \rho_{l,in}} = \dfrac{G^2(1-x_{in})^2}{\rho_{l,in}^2(1-\varepsilon_{in})}$

Term E $\qquad \dfrac{\partial \Delta p_m}{\partial \rho_{l,out}} = -\dfrac{G^2(1-x_{out})^2}{\rho_{l,out}^2(1-\varepsilon_{out})}$

Term F $\qquad \dfrac{\partial \Delta p_m}{\partial \rho_{v,in}} = \dfrac{G^2 x_{in}^2}{\rho_{v,in}^2 \varepsilon_{in}}$

Term G $\qquad \dfrac{\partial \Delta p_m}{\partial \rho_{v,out}} = -\dfrac{G^2 x_{out}^2}{\rho_{v,out}^2 \varepsilon_{out}}$

Term H $\qquad \dfrac{\partial \Delta p_m}{\partial \varepsilon_{in}} = G^2 \left(-\dfrac{(1-x_{in})^2}{\rho_{l,in}(1-\varepsilon_{in})^2} + \dfrac{x_{in}^2}{\rho_{v,in}\varepsilon_{in}^2} \right)$

Term I $\qquad \dfrac{\partial \Delta p_m}{\partial \varepsilon_{out}} = G^2 \left(\dfrac{(1-x_{out})^2}{\rho_{l,out}(1-\varepsilon_{out})^2} - \dfrac{x_{out}^2}{\rho_{v,out}\varepsilon_{out}^2} \right)$

If the partial derivatives are available, the total uncertainty can be calculated by using the previously calculated values of the uncertainties in terms A through I.

A.4.8.3   Frictional pressure drop uncertainty

In the above two sections and section **A.2.3**, the uncertainty in the measured pressure drop, static pressure drop and in the momentum pressure drop were calculated. Using this, the frictional pressure drop's uncertainty was:

$$\delta \Delta p_f \;\; = \;\; f(\Delta p_{meas}, \Delta p_s, \Delta p_m)$$

$$\delta \Delta p_f \;\; = \;\; \left\{ \begin{array}{c} \left(\dfrac{\partial \Delta p_f}{\partial \Delta p_{meas}} \delta \Delta p_{meas} \right)^2 + \\[2mm] \left(\dfrac{\partial \Delta p_f}{\partial \Delta p_s} \delta \Delta p_s \right)^2 + \\[2mm] \left(\dfrac{\partial \Delta p_f}{\partial \Delta p_m} \delta \Delta p_m \right)^2 \end{array} \right\}^{\frac{1}{2}}$$

A.5   Uncertainty Results

The above equations were coded into a Matlab program that automatically calculated the uncertainties for all the data points during data reduction. The uncertainties are summarised in Tables

A.2 and A.3 and discussed thereafter. Since the heat transfer coefficient is mainly a function of heat flux, refrigerant and tube those combinations are presented. The uncertainties presented here are representative of the extremes of the test matrix. In general the uncertainties varied between the boundary values presented in Tables A.2 and A.3. Each mean is not based on the same number of data points, only on the available data for the conditions in the tables. For example, at a high refrigerant mass flux only a limited set of vapour qualities can be tested while more vapour qualities are achievable at lower mass fluxes.

The heat transfer coefficient is highly dependent on the applied heat flux. Higher heat fluxes generally bring about a lower outside heat transfer coefficient (increase in $(T_{wat} - T_{sat})$) and a larger water-side temperature difference $(T_{in} - T_{out})$. These two parameters are the dominant terms in the heat transfer uncertainty, both improve with higher heat flux in this case. Refrigerant mass flux did not have a large influence on the heat transfer and therefore the heat transfer coefficient uncertainty remained fairly constant over the mass flux range. The water mass flow rate (and Reynolds number) had no real effect because $(T_{in} - T_{out})$ was always the same for each tested heat flux.

The refrigerant mass flux did however have a significant effect on the pressure drop components. The static pressure uncertainty was only indicative of the propagation of error in the equations and the accuracy of the actual model (void fraction and data reduction assumptions) with respect to reality is not measurable. The lower refrigerant mass flux conditions had higher uncertainty for the static pressure drop and this could be related to the vapour quality and void fraction uncertainty. As the frictional pressure drop increased with mass flux the uncertainty therein also increased. The higher accuracy at higher heat fluxes stems from the fact that the heat flux could be more accurately determined and this reduced the overall error.

Table A.2: Experimental uncertainties for measurements during boiling heat transfer with *Wolverine Turbo-B5* in percentage

Measure	G kg/m^2s	R134a at 20 kW/m^2	R134a at 60 kW/m^2	R236fa at 20 kW/m^2	R236fa at 60 kW/m^2
q	4	$12.94 \, ^{(13.2)}_{(12.6)}$	No data	$14.13 \, ^{(14.3)}_{(14.0)}$	No data
	30	$14.29 \, ^{(15.5)}_{(13.2)}$	$4.11 \, ^{(4.2)}_{(4.0)}$	$13.93 \, ^{(15)}_{(13.2)}$	$4.33 \, ^{(4.4)}_{(4.3)}$
h_o	4	$37.28 \, ^{(38.3)}_{(36.4)}$	No data	$37.34 \, ^{(37.5)}_{(37.1)}$	No data
	30	$39.63 \, ^{(44.0)}_{(37.0)}$	$11.52 \, ^{(11.8)}_{(11.4)}$	$37.74 \, ^{(41.7)}_{(33.8)}$	$9.39 \, ^{(9.5)}_{(9.3)}$
x_{in}	4	$7.51 \, ^{(11.3)}_{(5)}$	No data	$7.95 \, ^{(10.2)}_{(5.7)}$	No data
	30	$6.13 \, ^{(10.3)}_{(3.6)}$	$6.28 \, ^{(10.8)}_{(3.6)}$	$6.80 \, ^{(10.6)}_{(5.1)}$	$9.23 \, ^{(11.8)}_{(6.6)}$
ε	4	$8.82 \, ^{(13.8)}_{(5.5)}$	No data	$8.95 \, ^{(11.9)}_{(6.1)}$	No data
	30	$4.97 \, ^{(6.5)}_{(2.3)}$	$5.13 \, ^{(10.2)}_{(2.3)}$	$4.88 \, ^{(9.0)}_{(3.1)}$	$7.30 \, ^{(10.1)}_{(4.5)}$
Δp_s	4	$11.56 \, ^{(14.8)}_{(8.8)}$	No data	$13.34 \, ^{(15.0)}_{(11.7)}$	No data
	30	$4.00 \, ^{(4.4)}_{(3.8)}$	$5.74 \, ^{(7.7)}_{(4.9)}$	$5.06 \, ^{(5.2)}_{(4.9)}$	$7.48 \, ^{(7.5)}_{(7.4)}$
Δp_f	4	$11.89 \, ^{(14.2)}_{(10.0)}$	No data	$14.91 \, ^{(16.4)}_{(13.5)}$	No data
	30	$11.43 \, ^{(19.6)}_{(5.9)}$	$9.31 \, ^{(13.7)}_{(6.1)}$	$17.70 \, ^{(31.2)}_{(11.0)}$	$20.35 \, ^{(27.5)}_{(13.2)}$

Presented as: mean $^{(max)}_{(min)}$

Table A.3: Experimental uncertainties for measurements during boiling heat transfer with *Wieland Gewa-B5* in percentage

Measure	G kg/m^2s	R134a at 20 kW/m^2	R134a at 60 kW/m^2	R236fa at 20 kW/m^2	R236fa at 60 kW/m^2
q	4	$13.52\ ^{(13.6)}_{(13.4)}$	No data	No data	No data
	30	$14.19\ ^{(14.3)}_{(14.1)}$	$4.09\ ^{(4.2)}_{(4.0)}$	$13.58\ ^{(14.0)}_{(13.2)}$	$4.06\ ^{(4.2)}_{(4.0)}$
h_o	4	$36.31\ ^{(36.5)}_{(36.0)}$	No data	No data	No data
	30	$32.79\ ^{(34.4)}_{(30.7)}$	$9.44\ ^{(9.7)}_{(9.2)}$	$25.18\ ^{(25.6)}_{(24.8)}$	$8.35\ ^{(8.5)}_{(8.2)}$
x_{in}	4	$6.87\ ^{(9.8)}_{(4.9)}$	No data	No data	No data
	30	$6.60\ ^{(9.4)}_{(4.5)}$	$6.03\ ^{(10.4)}_{(4.2)}$	$10.30\ ^{(12.7)}_{(7.9)}$	$8.77\ ^{(10.9)}_{(6.6)}$
ε	4	$8.13\ ^{(12.0)}_{(5.5)}$	No data	No data	No data
	30	$5.50\ ^{(8.7)}_{(3.2)}$	$4.93\ ^{(10.0)}_{(2.9)}$	$8.45\ ^{(11.1)}_{(5.8)}$	$6.90\ ^{(9.2)}_{(4.6)}$
Δp_s	4	$10.84\ ^{(13.4)}_{(8.4)}$	No data	No data	No data
	30	$3.82\ ^{(3.9)}_{(3.8)}$	$5.11\ ^{(5.5)}_{(4.8)}$	$5.35\ ^{(5.5)}_{(5.2)}$	$7.59\ ^{(7.9)}_{(7.3)}$
Δp_f	4	$10.92\ ^{(12.9)}_{(9.3)}$	No data	No data	No data
	30	$12.58\ ^{(18.6)}_{(8.2)}$	$8.94\ ^{(13.1)}_{(6.6)}$	$39.90\ ^{(46.5)}_{(33.3)}$	$21.51\ ^{(27.8)}_{(15.2)}$

Presented as: mean $^{(max)}_{(min)}$

A.6   Conclusion

The uncertainties presented here serve to quantify the quality of data captured. The uncertainties presented are only for the extremes of the test matrix but the uncertainty for every point was calculated and recorded.

The recommendation for future work with a focus on low heat flux data is that temperature measurement needs to be improved, either by more local thermocouples or by more advanced temperature measurement devices. Most important is to calibrate all measuring equipment to the highest standard possible.

Appendix B

Wilson plot method

B.1 Introduction

It is not possible to measure the wall temperature directly in the bundle boiling facility because of the thin tube wall thickness and the disturbance that a thermocouple fixation will cause in the local heat transfer. Without a wall temperature it is not possible to use Newton's law of cooling directly for a heat transfer coefficient evaluation. Thus, an indirect method is required. The Wilson plot method infers the heat transfer performance of the tested tube by running a carefully controlled set of experiments where the conditions of the two convective heat transfer coefficients involved are varied. This allows the water-side heat transfer coefficient (in this study) to be determined, and this provides a means to determine the boiling heat transfer coefficient on the outside surface of the tube.

A brief description of the Wilson plot method and its history, the LTCM modifications to this method and the validation results follow.

B.2 Heat transfer calculation principles

In general, the overall thermal resistance of a tubular heated surface can be expressed as:

$$\frac{1}{U_o A_o} = \frac{1}{h_o A_o} + r_w + \frac{1}{h_i A_i} \tag{B.1}$$

The heat transfer coefficient h_o measured on the external surface, the topic of interest of this study, can be found by rearranging equation B.1, for a reference area A_o:

$$h_o = \left(\frac{1}{U_o} - R_w - \frac{A_o}{h_i A_i} \right)^{-1} \qquad (B.2)$$

In the above equation, the heat transfer resistance through the wall is:

$$R_w = \frac{D_o ln |\frac{D_{or}}{D_i}|}{2k_w}$$

D_{or} is the outside root diameter of the enhanced tube, measured by removing the enhancement (the surface structure) on the outside. Any influence of fins on the outside surface, or ribs on the inside is assimilated into the internal and external heat transfer coefficients. The overall heat transfer coefficient U_o can be calculated from:

$$U_o = \frac{q_o}{T_{water} - T_{sat}}$$

where T_{water} is the temperature of the water measured in the middle of the tube. The heat flux, q_o is measured on the water-side.

In equation B.2 the external heat transfer coefficient h_o needs to be calculated. However, the heat transfer performance of the inner surface of the tube h_i is unknown leaving us with two unknowns in one equation. In the following sections, a brief summary of the different methods that have been proposed to close the calculation are presented, whereafter the method utilized in this study is described.

B.3 Origins of the Wilson plot method

B.3.1 Wilson plot method (1915)

In his original study, Wilson (1915) proposed a method for solving the issue of the undefined heat transfer resistances. Equation B.1 is modified and rewritten as:

$$U_o = \frac{1}{C_i h_i} \left(\frac{D_o}{D_i} \right) + R_w + \frac{1}{C_o h_o} \qquad (B.3)$$

In the above equation, there are five unknowns, namely, C_i, C_o, h_i, h_o, and R_w. In the method developed by Wilson (1915), four of these unknowns, C_o, h_i, h_o, and R_w are assumed to be known. The external heat transfer performance is kept constant, and is experimentally quantified by the Wilson (1915); thus the last two terms in equation B.3 can be grouped into a single known

constant C_2. Furthermore, Wilson (1915) characterizes the heat transfer performance of the inner surface of the tube as:

$$C_i h_i = C_i \left(k^{0.6} \rho^{0.82} c_p^{0.4} \mu^{-0.42} D_h^{-0.18} \right)_i v^{0.82} \tag{B.4}$$

where the only thing allowed to vary is the water velocity v. The rest of the terms in equation B.4 are grouped into a redefined C_i. Thus, the equation originally solved by Wilson (1915) is

$$\frac{1}{UA} = \frac{1}{C_i v^{0.82}} + C_o \tag{B.5}$$

Equation B.5 has a linear form of $Y = mX + b$, where $Y = (UA)^{-1}$, $b = C_o$, $X = v^{-0.82}$ and $m = C_i^{-1}$. This means that Wilson plotted $Y = (UA)^{-1}$ against $X = v^{-0.82}$ on a linear scale. Since both of these are known from the experimental data acquired during testing, both the slope $m = C_i^{-1}$ and intercept $b = C_o$ can be derived. Once C_i is known, the heat transfer coefficients of the fluid within the range of tests can be determined by the new correlation $h_i = C_i v^{-0.82}$.

However, the Wilson plot method does have several restrictions:

- Constant conditions have to be maintained on the shell-side (maintain C_o constant).

- The form or mathematical description of the heat transfer behaviour of both sides are assumed to be known.

- All test data must be in one flow regime, such as turbulent flow (*i.e.* the nature of the correlation cannot change).

- Calculated C_i is only valid for the outside condition tested.

Several authors have modified the original, single variable approach to allow for more complex problems, including ones in which there are three variables (Briggs and Young, 1969) and up to five variables (Khartabil *et al.*, 1988).

B.3.2   Modification by Briggs and Young (1969)

Starting with equation B.3, the modifications to the original Wilson plot method by Briggs and Young (1969) allow the calculation of three unknowns, namely the leading Wilson plot coefficients C_i and C_o, and one exponent in the heat transfer correlations. In the proposed method, the heat transfer coefficients on the tube- and shell-sides of a heat exchanger are:

$$h_i = C_i \frac{k_i}{D_i} Re_i^a Pr_i^{0.4} \left(\frac{\mu}{\mu_w}\right)_i^{0.14} \tag{B.6}$$

$$h_o = C_o \frac{k_o}{D_o} Re_o^p Pr_o^{\frac{1}{3}} \left(\frac{\mu}{\mu_w}\right)_o^{0.14} \tag{B.7}$$

In their text, Briggs and Young (1969) were interested in accurately calculating the heat transfer coefficient of the annulus-side (shell-side) in a simple tube-in-tube heat exchanger. They proposed that the exponent a of the inner tube's Reynolds number is equal to 0.8. Further, it is shown that the Prandtl number exponent should be 0.4 for cooling, and 1/3 for heating. Thus, their method attempts to calculate the leading coefficients of the tube-side and shell-side correlations and the Reynolds number exponent of the shell-side (*i.e.* the three variables, C_i, C_o and p). To do this, they introduce equations B.6 and B.7 into equation B.3, and by rearranging come to the tube-side formulation:

$$Y = mX + b \qquad \text{where}$$

$$Y = \left[\frac{1}{UA} - R_w\right] \left(C_o \frac{k_o}{D_o} A_o Re_o^p Pr_o^{0.4} \left(\frac{\mu}{\mu_w}\right)_o^{0.14}\right)$$

$$m = \frac{1}{C_i}$$

$$X = \left[\frac{\frac{k_o}{D_o} A_o Re_o^p Pr_o^{\frac{1}{3}} \left(\frac{\mu}{\mu_w}\right)_o^{0.14}}{\frac{k_i}{D_i} A_i Re_i^{0.8} Pr_i^{0.4} \left(\frac{\mu}{\mu_w}\right)_i^{0.14}}\right]$$

$$b = \frac{1}{C_o}$$

Assuming an initial value for p, and due to the linear form ($Y = mx + b$), a linear regression of Y on X allows the approximation of the heat transfer coefficient correlation constants, C_i and C_o. Applying a temperature correction step, they then rearrange equation B.3 to find the shell-side formulation:

$$
\begin{aligned}
Y &= mX + b \qquad \text{where} \\
Y &= \ln\frac{1}{y_s} \\
y_s &= \left[\frac{1}{UA} - R_w - \frac{1}{C_i \frac{A_i k_i}{D_i} Re_i^a Pr_i^{0.4} \left(\frac{\mu}{\mu_w}\right)_i^{0.14}} \right] \times \\
&\quad \left(A_o \frac{k_o}{D_o} Pr_o^{\frac{1}{3}} \left(\frac{\mu}{\mu_w}\right)_o^{0.14} \right) \\
m &= p \\
X &= \ln Re_o \\
b &= \ln C_o
\end{aligned}
$$

Hence, the shell-side empirical constant C_o and exponent p can be calculated. These results are then fed back into the tube-side formulation in an iterative scheme until the solution converges. To correctly implement this method, the shell-side conditions are held constant while the inside conditions are allowed to vary; then, the shell-side conditions are changed, and the inside conditions are repeated again for the test matrix involved. In the case mentioned above that means the experiments require a complete set of Re_o and Re_i data.

B.3.3   Modification by Khartabil (1988)

Khartabil *et al.* (1988) and Shah (1990) pointed out that the methods developed by Wilson (1915) and Briggs and Young (1969) are limited in scope and application to heat exchangers for which information regarding the heat transfer performance and wall thermal resistance are known in advance. Khartabil *et al.* (1988) proposed a new method that allows the determination of five variables in equation B.8 (C_i, C_o, a, b, R_w) from overall resistance measurements. In this method, the value of each resistance is obtained by subtracting the two remaining resistances from the overall resistance. From this point of view, the relative resistances have a significant effect on the accuracy of the resulting correlations. Shah (1990), showed that the only remaining limitation for this method is that the test data on each fluid side must be in a single flow regime (no change in the form of the correlation for the applied range). Furthermore, to accurately calculate the five unknowns, a sufficiently large experimental matrix is required.

$$
\begin{aligned}
U_o &= \frac{1}{C_i h_i}\left(\frac{D_o}{D_i}\right) + R_w + \frac{1}{C_o h_o} \qquad &\text{(B.8)}\\
h_i &= C_i Re^a\\
h_o &= C_o Re^b
\end{aligned}
$$

B.3.4 Rose's (2004) direct method

The method proposed by Rose (2004) considers the temperature differences between the two sides of a heat exchanger, rather than relying on the concept of thermal resistances. The overall temperature difference is:

$$
\Delta T_{oa} = \Delta T_o + \Delta T_w + \Delta T_i
$$

Neglecting any effect of axial conduction, a thermal balance can be described by:

$$
\begin{aligned}
\delta Q &= \pi D_i \delta L q_i = \pi D_o \delta L q_o\\
q_i &= q_o \frac{D_i}{D_o}
\end{aligned}
$$

and if it is considered that:

$$
\Delta T_i = \frac{q_i}{C_i h_i} \quad \Delta T_o = \frac{q_o}{C_o h_o} \quad \Delta T_w = q_o R_w
$$

Rearranging:

$$
\delta T_{oa} = \underbrace{\frac{1}{C_o}}_{a}\underbrace{\frac{q_o}{h_o}}_{x} + \underbrace{q_o R_w}_{y} + \underbrace{\frac{1}{C_i}}_{b}\underbrace{\frac{q_i}{h_i}}_{z}
$$

In the above equation, which is equation B.2 divided by q_o, the only two unknowns are a and b. It is implied that the form of the heat transfer correlation for the tube- and shell-side correlations is known, with the exception of the constant multipliers C_i and C_o. These two unknowns can be estimated by minimizing the residuals S as in linear least-squares:

$$
S = \Sigma \left(\Delta T_{oa,calc} - \Delta T_{oa,exp}\right)^2
$$

A particular advantage of this method is that the error in the quantities whose residuals are minimized (ΔT) is generally expected to be constant for each data point (Rose, 2004). Thus, the

assumption of constant uncertainty (for each point) is more feasible. This method is however just as susceptible to error when the temperature difference is small.

B.3.5 Styrylska and Lechowskia (2003) method

The Styrylska and Lechowska (2003) method analyzes the Wilson plot method as a least-squares adjustment problem, rather than a minimisation or least-squares fit problem. It is a constrained optimisation method, loosely based on the Newton gradient method. In this method the heat transfer correlations do not need to have a leading coefficient with exponent type form (Cx^n), but they can assume any form. This unified Wilson plot method separates the measurements into direct (temperature, heat flux, and mass flow) and indirect measurements (terms grouped together and calculated from the direct measurements: the overall heat transfer coefficient U, and the x_i expressions).

A governing equation (equation B.3) is differentiated by each of the terms in the vector of required unknowns, to create a Jacobian matrix of size z by j (z is the number of unknowns, and j the number of data points). The difference between the right-hand side and left-hand side will be equal to 0 when the solution is converged.

Of interest in this method is that the least-squares adjustment formulation not only allows one to iterate and find the unknowns (*i.e.* the coefficients of the heat transfer correlations), it also allows the user to iteratively find the uncertainty in each of the variables. This is done by utilizing an augmented covariance matrix, in which the main diagonal is filled by the calculated uncertainties of each overall heat transfer coefficient (U) data point and initial guesses for the unknowns' uncertainties.

At the beginning of each iterative step, the difference between each data point's calculated overall heat transfer coefficient U (left-hand side of equation B.3) and the sum of the heat transfer resistances (evaluated with the specific iteration's value of the unknowns) is saved into a vector. Finally, at the end of each iteration, the correction vector for the unknowns is evaluated; the *a priori* covariance matrix is also corrected. When the value of each component of the residual vector tends to 0, the solution is converged and the uncertainty in the variables is the square root of the terms in the main diagonal of the final *a posteriori* covariance matrix.

At each iteration, the unified Wilson plot method uses the change in gradient with respect to each variable, the residual vector and the current iteration's value of the variables to predict the following step's variables. This iterative solution method requires a robust scheme suitable to nonlinear solutions.

During the course of this study, this method was implemented using the experimental Wilson plot data gathered. However, due to the ill-conditioned nature of this particular covariance matrix (the relative sizes of the uncertainties) and the absence of a strong global minimum, it was not possible to find a converged solution independent of initial conditions. Further investigation into the solution method needs to be done and might refine this into a viable general solution tool for Wilson plot data without limitations on the form of equations.

B.4   LTCM implementation of the Wilson plot method

At the LTCM, an indirect method based on the Briggs and Young (1969) approach is implemented. In previous studies (Gstöhl, 2004, Roques, 2004), an attempt was made to use condensation on the outside of the tubes, but the external heat transfer coefficient was too small. As a consequence nucleate pool boiling is chosen as the test condition on the outside of the tube. Pool boiling is chosen for ease of testing, the fact that the external boiling heat transfer correlation could be represented by an exponential form and that the measured heat transfer coefficients are as high as possible. For a fixed saturation temperature, the outside pool boiling heat transfer coefficient is correlated using a nucleate pool boiling correlation of Cooper (1984) type with a single leading coefficient:

$$h_{o,pb} = C_o q_o^n$$

In this equation, both C_o and n are left variables, and are calculated in the Wilson plot.

For the form of the internal heat transfer correlation, the Gnielinski (1976) correlation is utilized. It is a modification of the Petukhov (1970) correlation, which extends its application to Reynolds numbers in the transition regime. The Gnielinski (1976) correlation is:

$$Nu_{gni} = \frac{(f/8)\left(Re_{water} - 1000\right)Pr_{water}}{1 + 12.7\left(f/8\right)^{\frac{1}{2}}\left(Pr_{water}^{\frac{2}{3}} - 1\right)}$$

The friction factor f is defined by Petukhov (1970):

$$f = (0.79 log Re_{water} - 1.64)^{-2}$$

and the water-side Reynolds number is:

$$Re_{water} = \frac{4\dot{m}_{water}}{\pi\left(D_i - D_{ss}\right)\mu_l}$$

The applicable range of this correlation is $3000 < Re_{water} < 10^6$, which covers flow closer to transition and the fully-turbulent regimes. Gnielinski (1976) quoted the prediction accuracy of this correlation to be within 10%. The Petukhov friction factor correlation is only valid for smooth tubes; nevertheless, this correlation can be used without any modification. The effect of all internal enhancement is taken into account by the leading coefficient C_i. Olivier (2008) showed that for Reynolds numbers larger than 10^4, internal enhancements proportionally increase the heat transfer performance rather than modify the slope of the correlation. This leading coefficient, determined experimentally, modifies the internal heat transfer correlation as follows:

$$h_i = C_i h_{gni} \qquad \text{when} \quad Re > 10^4$$

For the solution procedure we can rewrite equation B.3 as:

$$\frac{1}{U_o} = \frac{1}{C_i h_{gni}} \left(\frac{D_o}{D_i} \right) + R_w + \frac{1}{C_o q_o^n} \tag{B.9}$$

In equation B.9, we have three unknowns, C_i, C_o and n. The 2-step iterative modified Briggs and Young procedure is used to converge to a unique set of variables that satisfy the equality.

B.4.1 Step 1: Tube-side formulation

Rearranging equation B.9 gives:

$$\begin{aligned}
Y &= mX + c \text{ where} \\
Y &= \left(\frac{1}{U_o} - R_w \right) q_o^n \\
m &= \frac{1}{C_i} \\
X &= \left(\frac{q_o^n}{h_{gni}} \frac{D_o}{D_i} \right) \\
b &= \frac{1}{C_o}
\end{aligned} \tag{B.10}$$

An initial estimate for n is required to allow this method to work. In equation B.10, the terms labeled X and Y are known values, and m and c are the slope and intercept (found by linear regression). C_i and C_o are the inverse of m and c respectively. Once these values are calculated, the method proceeds to the shell-side formulation.

B.4.2   Step 2: Shell-side formulation

For the shell-side, equation B.9 is rearranged as

$$\underbrace{\left(\frac{1}{U_o} - R_w - \frac{1}{C_i}\left(\frac{1}{h_{gni}}\frac{D_o}{D_i}\right)\right)}_{1/y_s} = \frac{1}{C_o q_o^n}$$

$$y_s = C_o q_o^n$$

$$\underbrace{ln\,|y_s|}_{Y} = \underbrace{n}_{m}\underbrace{ln\,|q_o|}_{X} + \underbrace{ln\,|C_o|}_{c}$$

In this step, the calculated values of C_i and C_o are used to find the values of the shell-side X and Y. Once these are known, a linear regression may be performed to find the values of m and c. $C_o = e^c$ and n, the heat flux exponent in the nucleate boiling correlation, is equal to m.

Finally, a comparison can be made between the previous step's values of C_i, C_o and n. The convergence criteria for the LTCM method requires that all three vary by less than 0.01%. If this condition is not met, the values of the variables are updated and the tube- and shell-side calculations performed again.

B.4.3   Uncertainty propagation through the linear regression

In the previous section, it is mentioned that the slope and intercept of both the tube- and shell-side Wilson plots could be found through linear regression. This regression could be as simple as utilizing a least-squares minimisation algorithm. Such methods have been utilized successfully and are well-documented (Liebenberg, 2002). However, the least-squares linear regression method has several important drawbacks to consider. Firstly, it is difficult to propagate the experimental uncertainty through the method, and thus calculate the uncertainties in the resulting coefficients. Secondly, the calculated values of X and Y have experimental uncertainties associated with them which are not taken into account when performing a classic least-squares fit through the data. The classic method uses and minimizes the difference of the data points only in the y-axis. This means that the accuracy of the fit might suffer due to a method trying to fit data that are also subject to uncertainty in the x-axis and the data points are not weighted by their uncertainty.

York *et al.* (2004) presents a method that unifies the standard errors when both X and Y data are subject to propagation of error. The method proposed evaluates the least-squares estimation with a weighting parameter based on the uncertainty in X and Y. The sum of least-squares is calculated as the shortest perpendicular distance between the data points and the proposed fit.

Thereby including the data of the x-axis in the formulation. This method is adapted and utilized to perform the linear regression in the modified LTCM method. The use of this method allows for the propagation of experimental errors through the Wilson plot method, such that the final uncertainties in the measured heat transfer coefficients be accurately estimated (Appendix A).

B.4.4 Minimisation algorithm

In Section B.3.5, the method of Styrylska and Lechowska (2003) is discussed, in which the residuals (calculated as the difference between the measured overall heat transfer U and the sum of the iterative step's prediction of the sum of the heat transfer resistances) are minimized using a least-squares adjustment formulation. This served as the basis of a method developed in which an objective three-variable function f, had to be minimized subject to physical constraints imposed on the optimisation space.

$$f = \frac{1}{U_o} - \left(\frac{1}{C_i h_{gni}} \left(\frac{D_o}{D_i} \right) + R_w + \frac{1}{C_o q_o^n} \right) \Rightarrow 0 \tag{B.11}$$

The three variables, similar to the modified LTCM Wilson plot (Section B.4) are C_i, C_o and n. The minimisation is performed by a nonlinear least-squares algorithm, and the convergence criteria are based on the tolerance between two succeeding iterations being less than 0.01%. This type of implementation still follows the general methodology of the Wilson plot method (which essentially calculates values for the variables that minimize the difference between the left-hand and right-hand side of equation B.3 using successive first-order least-squares estimations), except that it uses a more direct method in which all the variables are solved simultaneously, and it directly minimizes the difference between the measured overall heat transfer resistance, and the sum of the predicted heat transfer resistances. The method can accommodate an unlimited number of variables; however, the larger the number of variables, the more uncertain and inaccurate the prediction will become. The drawback of this method is that the experimental uncertainties of the solution are not propagated through the method.

The minimisation algorithm utilized solves nonlinear least-squares (nonlinear data-fitting) problems of the form:

$$\min_x(f(x)) = f_1(x)^2 + f_2(x)^2 + ... + f_n(x)^2 \tag{B.12}$$

The functions are shown as functions only of x, while in reality they can be a function of several variables. Each f_i in equation B.12 is each data point's individual minimisation function

(equation B.11). Rather than compute the value $f(x)$ (the sum of squares), the algorithm requires the user-defined function to compute the vector-valued function as follows:

$$
\mathbf{F}(x) =
\begin{bmatrix}
f_1(x) \\
f_2(x) \\
... \\
f_n(x)
\end{bmatrix}
$$

The algorithm utilized is based on the interior-reflective Newton method (Coleman and Li, 1996, 1994). To compute the Jacobian, which is the transpose of the gradient of the vector **F**, a finite difference method is utilized. Each iteration involves the approximate solution of a large linear system using the method of preconditioned conjugate gradients (Snyman, 2005). The algorithm does not solve underdetermined systems; it requires that the number of equations (*i.e.*, the number of elements of **F**) be at least as great as the number of variables being optimized.

B.5 Water-to-water tests

Further experimental validation is done by comparison against direct heat transfer coefficient measurements performed on a simple tube-in-tube water-to-water test section. A simplified diagram of the test section is presented in Figure B.1.

B.5.1 Description of the water-to-water test facility

The water-to-water test facility was a simple tube-in-tube counterflow heat exchanger, in which the outside enhancement of the inner tube had been machined off. After machining, the measured outer diameter was 17.73 mm (the root diameter of the enhancement). The tube was 1027 mm long. A 1 mm-thick wire was wrapped around the exterior of the tube to both enhance mixing of the flow, and to act as a centering mechanism. The inside diameter of the outer tube was 20 mm. Three 0.25 mm thick thermocouples were installed in machined slots on the inner tube wall at 120° intervals. Other thermocouples were installed at the inlet and outlet of both the inner tube and the annulus to directly measure the local temperatures of the water. The instrumented rod used to measure local water profile temperatures (Chapter 3) was installed inside the inner tube. This rod used three stations, at three locations along the heat transfer length, with two thermocouples each to measure the water temperature profile. The water mass flow rates of both the inner tube and the annulus were measured with Coriolis flow meters. The temperature

of both mass flows were computer-controlled by exchanging heat with two reservoirs. The first exchanged heat with the laboratory's heat supply and the second with water from Lake Geneva (constant 7°C throughout the year).
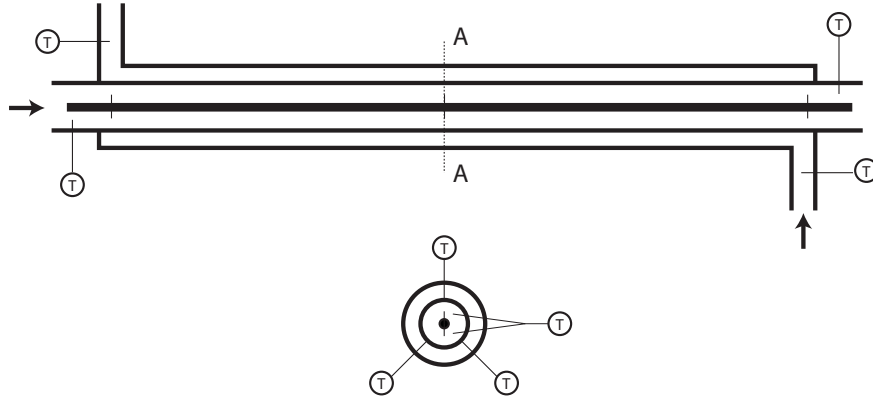
Figure B.1: Schematic of the counter flow tube-in-tube test section. The inner tube water is cooled by the outer annulus and thermocouples are installed in the middle

The experimental conditions for the water-to-water tests detailed in this section mimicked the water-side conditions found both when performing the Wilson plot testing and the heat transfer experiments during bundle boiling. These conditions are summarised in Table B.1. The annulus side conditions were varied such that the heat flux measured at the central temperature measuring station in the inner tube coincided with the required experimental conditions. Using the thermocouple measurements at the inner-tube and annulus inlets and outlets coupled to the two measured mass flow rates, the energy balance ($|Q_{in} - Q_{ann}/Q_{avg}|$) was never found to differ by more than 1% (*i.e.* less than 1% of the heat transferred was lost to ambient).

Table B.1: Experimental conditions tested for Wilson plot experiments

	T_{water}	
	5°C	15°C
q	20–60 kW/m^2	20–60 kW/m^2
Re_{water}	8–17.5$\cdot$10^3	8–16$\cdot$10^3

B.5.2 Water-to-water results

The heat transfer coefficients measured directly using the wall temperatures were compared directly to the heat transfer performance as predicted by the Wilson plot method ($h_i = C_i h_{gni}$). The direct method was not used to create a new correlation. The results are presented in Figures B.2 and B.3 for the Turbo-B5 and the Gewa-B5 respectively. It is clear that all of the results are within the experimental uncertainties of each other, and there is never more than 10% deviation between the two methods. The heat transfer measurements at higher Reynolds numbers for the Turbo-B5 (Figure B.2b) tend to over-predict; the thermocouples embedded in the inner tube's wall may have been affected by convective effects due to the increased mass flow rate in the narrow annulus.

(a) h_i vs. Re

(b) $h_{i,direct}$ vs. $h_{i,WP}$
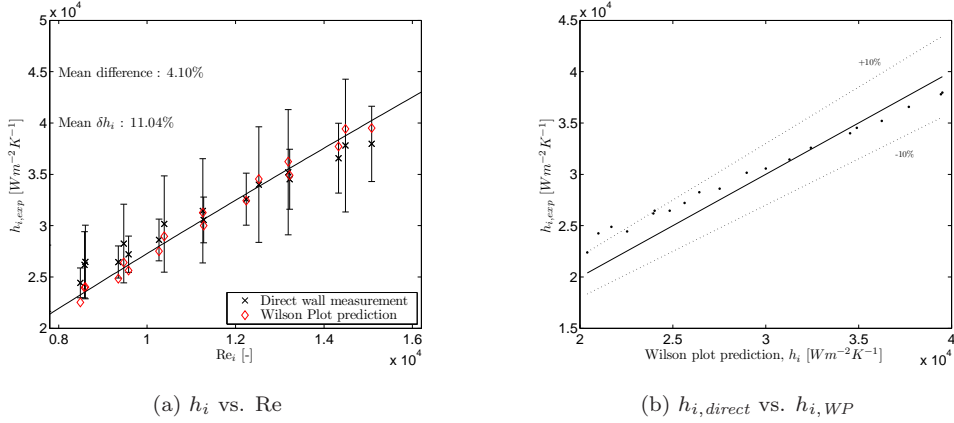
Figure B.2: Comparison of the direct wall temperature heat transfer coefficient measurements and the Wilson plot correlation for the Wolverine Turbo-B5. (The error bars for the Wilson plot results are not plotted for clarity reasons. At best the uncertainty in these results is on the order of 15%)

(a) h_i vs. Re

(b) $h_{i,direct}$ vs. $h_{i,WP}$
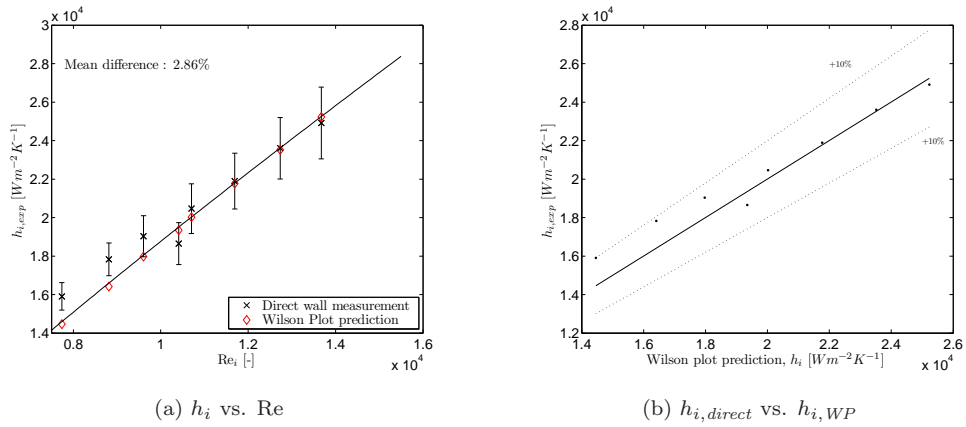
Figure B.3: Comparison of the direct wall temperature heat transfer coefficient measurements and the Wilson plot correlation for the Wieland Gewa-B5. (The error bars for the Wilson plot results are not plotted for clarity reasons. At best the uncertainty in these results is on the order of 15%)

In conclusion, it has been shown that the water-to-water experimental setup resulted in heat transfer coefficient measurements that were reproducible and it validated the Wilson plot method utilized to predict the relative size of the internal heat transfer resistance. The correlations resulting from thorough Wilson plot experiments can be used with confidence.

Appendix C

Enhanced boiling and mechanisms

In this section a brief overview of the considerations regarding enhanced tube boiling mechanisms are presented. The existing mechanistic models are described briefly and possible limitations and improvements are presented.

C.1 Boiling enhancement and mechanisms

The literature on this subject lacks a proven detailed explanation of the thermal-fluidic phenomena that creates the complex relationship between h_o, ΔT and q. The considerable differences in the shapes of boiling curves can be attributed to the specific features of heat transfer in various kinds of enhanced structures (Thome, 1990, Mitrovic, 2006).

Thome (2004) mentions the advantages of enhancement through surface modifications of tubes and states that most effort is put into making mechanically deformed helical fins to create re-entrant passageways. The primary factors contributing to the enhancement are identified as:

- nucleation superheat temperature reduction due to the re-entrant tunnels (so that the higher performance boiling process with respect to natural convection in liquid is started earlier);

- a 2 to 4 times increase in heat transfer area as a result of deformation of the tube surface;

- promotion of thin film evaporation on the tunnel passageways;

- capillary evaporation through menisci in the corners of tunnel passageways;

- internal convection resulting from the liquid being pumped/sucked through the tunnels by the bubble growth and departure cycle; and

- external convection through flow and bubble movement over the surface provides latent and sensible contributions.

Poniewski and Thome (2008), in their recent book, emphasized the importance of vapour generation in enhanced structures (mainly capillary-porous structures) and described vapour bubble formation in detail providing extensive references. Vapour bubble generation is an important factor in boiling and they stated that it is a function of: surface geometry at the nucleation site, density of sites, wetting angle hysteresis and heat flux. Most of these factors are extremely varied and difficult to quantify universally and therefore no general theory for vapour bubble generation currently exists (Poniewski and Thome, 2008). According to them, heat transfer enhancement is a function of the:

- number of active sites on the surface;

- frequency of bubble departure from the sites;

- the fluid characteristics;

- convection effects; and

- micro-structures on the surface.

The existence of a nucleus of vapour is of foremost importance to initiate the heterogeneous boiling process, since the creation of vapour without such an initial nucleus requires excessive energy input, which is not the case on most surfaces. The density of active nucleation sites was found to be higher for enhanced surface tubes which directly leads to higher heat transfer coefficients (Dhir, 2001).

Vapour is generated in the tunnel by high rates of evaporation from the thin films and menisci. The thin film results from the liquid that is pushed into the cavity after a bubble leaves (Dhir, 1998). After vapour generation, which is aided by the sensible heating provided by the structure (due to high convective heat transfer in the microchannels for laminar inlet, non-fully developed flow (Thome, 1990)), the vapour escapes but the structure retains vapour which allows rapid follow-on liquid film formation and bubble growth. Thus, enhanced structures provide more nucleation sites where the vapour escapes due to higher evaporation rates. If the tunnel is flooded with liquid, the thin films and menisci responsible for the high evaporation are replaced by thick

liquid films or single phase liquid-only flow. This liquid-only flow is not as effective as thin film evaporation.

On enhanced tubes the existence of outer surface nucleation sites are less important for the evaporation process. The vapour will escape through a pore somewhere on the tube but the vapour could have been generated by a combination of thin film evaporation, menisci evaporating in the corners of microchannels and nucleate boiling.

There are many different processes occurring and interacting on the surface during boiling. Some of these are: evaporation, convection, conduction and hysteresis mechanisms. In combination with the evaporation contributions mentioned above, a summary of expected mechanisms of heat transfer present on/in enhanced surfaces are:

- evaporation from liquid-vapour menisci (capillaries) inside the tunnel structure;

- evaporation from the liquid microlayer surface with the resulting vapour carried away to a pool of liquid;

- thin film evaporation inside tunnels of the capillary-porous structure;

- sliding bubbles with thin film evaporation on the outer wall side;

- evaporation to the externally growing bubbles;

- transient heat transfer in the disturbed field around growing and sliding bubbles;

- convection inside the tunnel; and

- sensible heat transfer at various locations: external convection and liquid pumping in and out of tunnels.

The bubble growth is not limited to the superheated layer because the vapour is generated elsewhere (Chien and Webb, 1998a) and only liquid inertia balances the bubble growth (Chien and Webb, 1998b). The vapour generation at the microlayer on the external surface is neglected by most models (Thome, 1990). The performance drops off as the liquid intake phase shortens as the heat flux in the tunnels increases and dryout commences. Depending on the fluid and heat flux, external convection effects might influence mainly the outer surface mechanisms or outer and inner surface mechanisms. In general, enhanced surfaces are less susceptible to imposed convection or tube proximity (Kim *et al.*, 2002, Liu and Qiu, 2002). The liquid pumping through the tunnels observed by Chien and Webb (1998d) and the outside surface, agitated by bubbles, are responsible for the large fraction of sensible heating.

The abundance of saturated and superheated liquid in and around an enhanced tube is responsible for the low superheat required for boiling incipience (Poniewski and Thome, 2008). Saturation pressure also affects the boiling process to a considerable extent (Nakayama *et al.*, 1980b). The combination of elevated pressure and appropriate pore dimensions makes it possible for boiling incipience to take place at very small superheats (as low as 0.1-0.2 K). The occurrence of boiling at very small superheats can be explained due to the contact of the saturated liquid with the heat transfer surface inside the pores, which causes the evaporation of the liquid sucked into the re-entrant channels. Capillary superheating, resulting from menisci formation in the pores, can partially explain why the boiling curves show different trends at different distributions of pore dimensions. An appropriate proportion of the number of active and inactive pores may constitute an important factor affecting the shape of the boiling curves.

C.2   Mechanistic studies of enhanced geometries

The evolution of enhanced structures and mechanistic models have been summarised in Webb (2004). For example, Nakayama *et al.* (1980b,a) used an enhanced surface fabricated by joining a thin plate with pores over a low-fin type of tube to create a dense re-entrant channel substructure. Different geometries were investigated and the following conclusions were drawn from their work:

- the density and diameter of pores determined the character of the boiling process at heat fluxes larger than 3×10^4 to 4×10^4 W/m^2;

- on surfaces with different pore diameters, the pores with the highest density controlled the level of heat transfer enhancement;

- at low heat fluxes, the largest pore determines the heat transfer performance;

- at low heat flux, the tubes having smaller total open areas (that is, the sum of the cavity areas) give higher heat transfer coefficients;

- at high heat fluxes, tubes having larger total open areas yielded higher heat transfer performance (Chien and Webb, 1998c);

- if the total open area was too large at low heat flux, the re-entrant tunnels became flooded by liquid and the heat transfer coefficient decreased; and
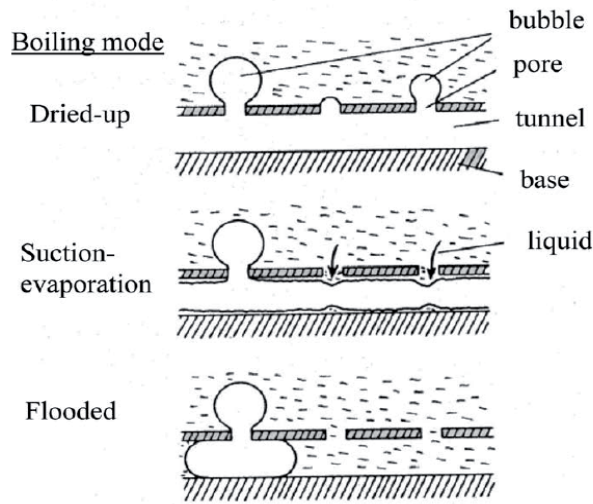
Figure C.1: Main modes of heat transfer in subsurface tunnel structures

- if the total open area was too small at high heat fluxes, the tunnels dried out due to inadequate liquid supply.

Arshad and Thome (1983) and Chien and Webb (1998a) also performed visualisation studies that supported these trends and film dynamics. In the first study bubble nucleation in the re-entrant channels was shown to rapidly create thin liquid films on the channel walls with vapour ejection through open pores. In the second study, the basic mechanisms and liquid inlet criteria were empirically correlated to some geometric parameters to match the heat transfer of the model and data.

C.3 Mechanistic models

Three types of boiling regimes were identified in the substructure: flooded, suction-evaporation and dryout (Figure C.1). The mechanistic study of Nakayama *et al.* (1980a) set the basis for later work done by Chien and Webb (1998b) which was also based on a comprehensive experimental study.

C.3.1 Ramaswamy *et al.* (2003) model

The recent studies of Ramaswamy *et al.* (2003) and Pastuszko and Poniewski (2008) added to the model while still retaining the same basic framework. The Ramaswamy *et al.* (2003) model for suction-evaporation will be discussed here with reference to the Chien and Webb (1998b) model on which it was based. The latest Pastuszko and Poniewski (2008) model that improves the liquid suction theory will also be referred to, although the geometry differs from the Ramaswamy *et al.* (2003) model.

The enhanced surface models also make use of bubble dynamics data for their predictions, as for smooth tubes. The basis of vapour generation is, however, completely different since it occurs inside the re-entrant channel structure and not on the surface. An important distinction must be made between nucleation of bubbles from cavities and a bubble emerging from a pore in an enhanced surface.

Moss and Kelly (1970) found a stable vapour film inside the porous layer and measured the film thickness as a function of the heat flux density. They revealed that the frequency of bubble formation inside the capillary-porous structure was much lower than in nucleate boiling on a smooth surface. This might infer a lesser importance of nucleation inside the tunnels because meniscus and thin film evaporation are more likely mechanisms.

The mechanistic model can be described by using the presently accepted stages of the boiling cycle for enhanced surfaces in suction-evaporation mode (Figure C.2): waiting time, growth time and suction time (Nakayama *et al.*, 1980b). The first mode of heat transfer considered in this model is internal evaporation from the menisci contributing vapour to the bubble during the waiting time and the growth time. The second component is the external heat flux attained through a semi-empirical correlation. Each of these stages have been characterised by specific processes that occur during them.

Usually for such a model the wall superheat (T_w-T_{sat}) of the system is specified and from the modelled mechanisms a heat flux can be predicted. The essential overall cycle parameters for such models are: departure diameter, departure frequency and nucleation site density.

Present models of suction evaporation do not include the sensible heat from liquid being pumped through the tunnels as pointed out in Thome (1990).

C.3.1.1 Bubble departure

Ramaswamy *et al.* (2003) uses a comprehensive force model including unsteady growth, buoyancy, surface tension, lift, bubble inertia and liquid inertia forces. The force balance is solved for the
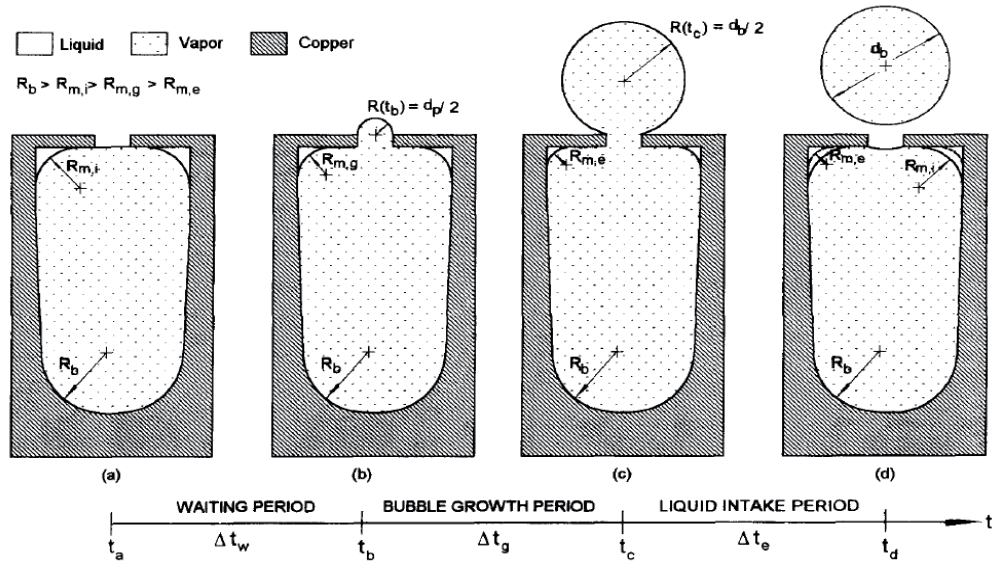
Figure C.2: Boiling cycle for suction-evaporation mode as proposed in Chien and Webb (1998b)
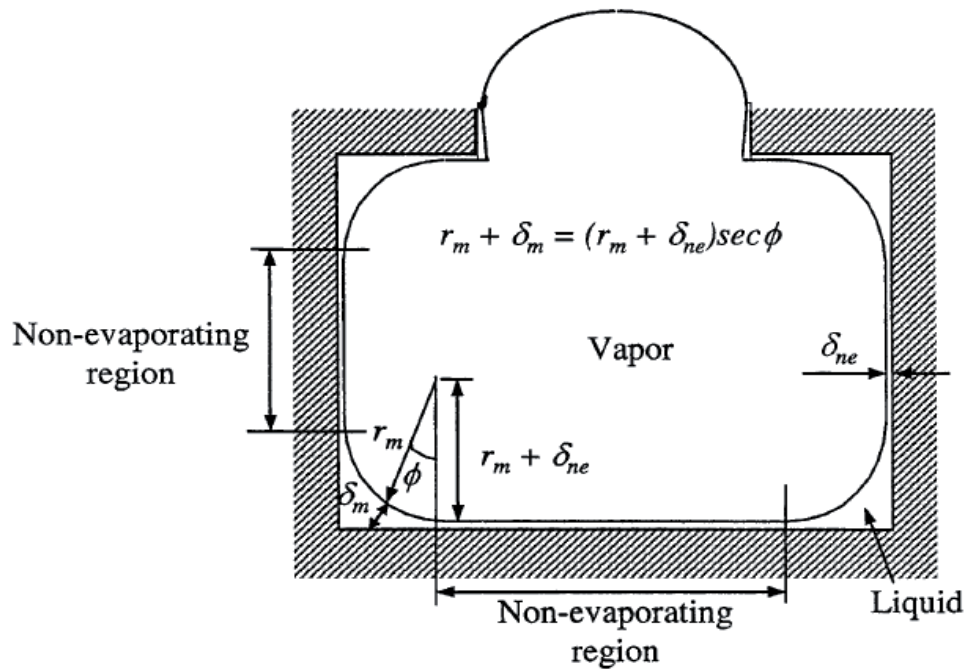
Figure C.3: Geometry assumed for the boiling model of Ramaswamy *et al.* (2003)

instantaneous diameter of the bubble to determine the departure diameter when the attaching forces are overcome. The buoyancy and lift forces tend to pull the bubble from the surface while the other forces keep the bubble on the surface.

C.3.1.2 Waiting time

At the beginning of the waiting time the meniscus thickness is needed as input for the model. At this time the vapour is saturated and corresponds to the system pressure. The tunnel evaporation heat flux can then be modelled by conduction through the meniscus and keeping track of the liquid film thickness as it evaporates over time (Figure C.3). The evaporation is an ongoing process that is limited by the elevation of the saturation temperature due to capillary pressure and disjoining pressure (DasGupta et $al.$, 1993) when the film thickness becomes very small (δ_{ne}).

$$T_{int} = T_{sat,bulk}\left(1 + \frac{\sigma/r_m + A/\delta^3}{h_{lv}\rho_l}\right)$$

$$\delta_{ne} = \left(\frac{AT_{sat}}{\rho_l h_{lv}\Delta T_{super}}\right)^{\frac{1}{3}} \tag{C.1}$$

Conduction is assumed across the liquid film:

$$q_t = \frac{k_l}{\delta(\phi)}(T_w - T_{int}) \tag{C.2}$$

The tunnel heat transfer rate is tracked taking into account the variation of film thickness over time and position and limited by a minimum film thickness described by the relationship in equation C.1:

$$dQ_t = \frac{dE_t}{dt} = \int_0^{A_m} \frac{k_l(T_w - T_{int})}{\delta(t,\phi)}dA \tag{C.3}$$

This relationship is dependent on the Hamaker constant. Although this constant is not known precisely, the results are a strong function of it (Ramaswamy et $al.$, 2003):

The end of the waiting time is marked by the internal vapour pressure rising to the level where it is possible to overcome the surface tension at the pore keeping the vapour inside. It is assumed that the vapour behaves like an ideal gas. The initial conditions of the waiting time state: $p_{v0} = p_{sat}$, $T_{v0} = T_{sat}$, $\rho_{v0} = \rho_v$ and finally $p_{v1} = p_{v0} + \frac{4\sigma}{D_p}$. The volume and density are assumed to vary linearly over time and the heat balance is used to evaluate the waiting time:

$$\frac{dE_t}{dt} = h_{lv}\frac{dm_v}{dt} = h_{lv}\left(V_{v,mean}\frac{d\rho_v}{dt} + \rho_{v,mean}\frac{dV_v}{dt}\right)$$

The limits and equations mentioned above are then used to evaluate the waiting time and estimate the amount of energy needed to generate the required pressure.

C.3.1.3   Growth phase

Evaporation continues during the growth phase as described in the waiting phase. Chien and Webb (1998b) used a modified form of the bubble growth model of Mikic *et al.* (1970) to evaluate the growth rate. This requires a curve fit to their bubble growth data to estimate an empirical constant C_{tg}:

$$\frac{dr}{dt} = C_{tg} \sqrt{\left(\frac{\pi}{7} \frac{h_{lv} \rho_v (T_w - T_{sat})}{\rho_l} \right) \left(\frac{D_d - D_p}{D_d + D_p} \right)} \tag{C.4}$$

A good correlation was found between the mentioned correlation and experimental data and it was used by Ramaswamy *et al.* (2003). If the bubble departure diameter is predicted from a force balance and the final bubble diameter is known, this equation is integrated for time steps from the initial pore size to the final departure diameter to find the growth time.

In their model Pastuszko and Poniewski (2008) quantify the volume changes during the waiting and growth periods to find a mean volume. This mean volume is then used do define a mean triangular liquid meniscus that is responsible for the latent heat flux.

C.3.1.4   Intake phase

Chien and Webb (1998b) found that the intake time was very short. Therefore the intake time was normally ignored when calculating the frequency. The study of Ramaswamy *et al.* (2003) found that the intake time overlaps with the final moments of the growth phase.

In the procedure of Ramaswamy *et al.* (2003), which is similar to that of Chien and Webb (1998b), an initial meniscus radius is estimated and the procedure is followed to predict the heat flux from the tunnel as the meniscus evaporates. This heat flux value is then compared to the experimental data and the initial meniscus radius estimate is updated until the heat fluxes match, albeit empirically. A non-evaporating minimum meniscus was defined. The liquid intake is then backed out from the calculated data. The empirical correlation defined by Ramaswamy *et al.* (2003) is a function of wall superheat and other geometric parameters:

$$\Delta A_{cyc} = C \delta \left(T_w - T_{sat} \right)^a \left(D_p^2 \right)^b P_p^c H_t^d N_m^e$$

Therefore, the intake period is the source of a major unknown in the mechanistic models. There is no known method of mechanistically modelling or predicting the amount of liquid sucked in. The problem has thus far been circumvented by specifying a correlation for the liquid intake and using the experimental data to determine the correlation coefficients so that the prediction method works. This method is biased to the mechanism selected in the tunnels and forces the solution to work correctly based only on this mechanism. This also has implications for cases with convection over the tubes since the added dynamic pressure could increase the liquid intake and thereby increase flooding or delay the onset of dryout inside the subsurface channels. The external convection also adds a force to the balance of forces on the growing bubble. This additional force could modify the bubble dynamics which in turn affect the liquid intake and resulting subsurface evaporation.

C.3.1.5 Consolidation

The total internal heat flux is calculated by the integral of latent heat exchange over the waiting and growth time. The waiting time and the growth time are now used to establish the departure frequency. The heat flux attributed to evaporation inside the tunnels together with the vapour volume, frequency and departure diameter is used to establish the nucleation site density that will be used for the external heat flux prediction:

$$
\begin{aligned}
N_b &= \frac{Q_t}{\rho_v h_{lv} f (\pi D_d^3/6)} \\
N_a &= \frac{N_b}{A_o}
\end{aligned}
$$

The external heat flux needs to be predicted to conclude the total heat flux prediction. The model of Mikic and Rohsenow (1969) is based on the intermittent nature of the boiling process. They assumed the departing bubble removes some of the superheated layer within an area twice the bubble diameter. Hence the problem was considered to be one-dimensional transient conduction through a semi-infinite solid. Haider and Webb (1997) considers steady state convection with the transient conduction term. Their model contained coefficients that were determined empirically and in the study of Ramaswamy *et al.* (2003), correlated as a function of superheat to predict the data of Haider and Webb (1997) and their own within 40%. The area of influence was reduced as the number of nucleation sites increased over the limit where nucleation will occur within the two diameter areas:

$$q_o = 2\sqrt{\pi k_l \rho_l c_p f} d_d^2 N_a \Delta T_{super} \left\{ 1 - \left(\frac{0.66\pi C}{Pr^{\frac{1}{6}}} \right)^2 \right\}^{\frac{1}{2}}$$
$$C = 6.58 - 1.1612(\Delta T) + 0.0782(\Delta T)^2 - 0.0018(\Delta T)^3$$

The total heat flux is the sum of internal and external heat fluxes:

$$q_{total} = q_t + q_o \tag{C.5}$$

Departing bubbles are assumed to be isolated in this model because the dynamics of coalescence are not dealt with. The occurrence of lateral or vertical coalescence is set as upper limits for the validity of the model.

C.3.2 Murthy *et al.* (2006) model for flooded boiling regime

The Murthy *et al.* (2006) model for flooded evaporation is also discussed because the flooded regime evaporation was observed during experimentation. The flooded regime could be present in the structure due to low heat fluxes and the added liquid intake caused by the external convection filling the tunnels with liquid. The visualisation studies of Chien and Webb (1998d) also observed flooding in horizontal tubes at high heat fluxes although normally only for a limited fraction of the tunnels (10-20%).
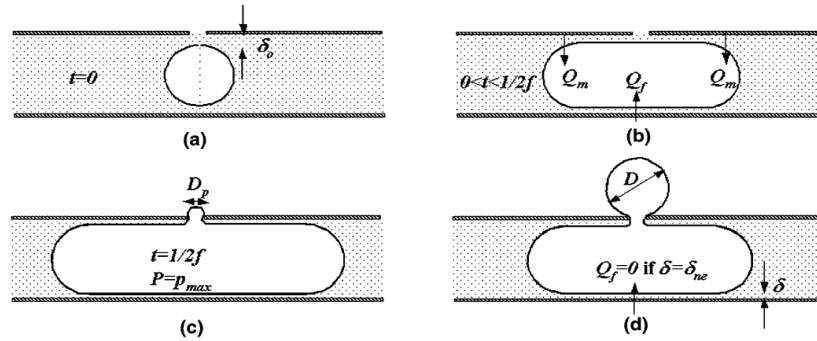
Figure C.4: Stages of the flooded regime boiling model used by Murthy *et al.* (2006)

The flooded regime of boiling can also be divided into several phases or time periods during which several mechanisms are active (Figure C.4). The cycle of flooded regime boiling starts with a spherical bubble. This bubble grows from evaporation at the menisci at either end of the bubble

and from the intermediate thin liquid film in-between. The vapour expansion continues inside the tunnel until the pressure is greater than the surface tension retaining pressure at the pore. After this point the vapour expansion continues outside the tunnel until the bubble departs. The main difference between this regime and the suction-evaporation regimes are the mechanisms inside the tunnel since the departure and external heat transfer is essentially similar in both regimes.

C.3.2.1   Tunnel heat transfer

The tunnel heat flux is calculated based on the liquid evaporation from the thin film and the two menisci at either end of a vapour plug in the tunnel. Evaporation from the thin film occurs until the non-evaporating film thickness is reached. This non-evaporating film thickness is defined as previously mentioned (equation C.1).

The model uses heat conduction through the thin film and the meniscus to obtain the heat flux. The film thickness is tracked by stepwise integration of small time increments, assuming latent heat evaporation. The pressure fluctuation in the tunnel during a cycle is used to predict the velocity of the meniscus oscillating in the tunnel. The length of vapour expansion is tracked using these relations. The heat flux over one time period is divided into the expansion and contraction parts and results in a bubble with the departing volume:

$$\int_0^{0.5/f} (2Q_m + Q_f)_{exp}dt + \int_{0.5/f}^{1/f} (2Q_m + Q_f)_{con}dt = \frac{\pi}{6}\rho_v h_{lv} d_d^3$$

The initial film thickness is modelled using lubrication theory and by assuming that the expanding menisci would result in a thin liquid film. The result is an iterative prediction method for the size of the initial bubble diameter. This method was derived for circular tunnel structures but it remains applicable in other geometries according to Murthy *et al.* (2006).

C.3.3   Convective mechanism effects

On a smooth tube a combination of mechanisms act on the surface. These mechanisms are: convection over the surface, nucleation of bubbles (latent heating), thin film evaporation (latent), microlayer evaporation and liquid superheating (sensible heating). These mechanisms are directly affected by imposed convection over the tube and the presence of other tubes in a bundle. The vapour generation is from the microlayer evaporation. The bubble growth is limited to the thickness of the superheated layer and inertia from the fluid.

For enhanced tubes the mechanisms inside the tube might remain largely unaffected when convection is imposed, except for the change in bubble dynamics. The convection would affect the mechanisms on the external surface directly and by changing the bubble departure diameter and frequency of the components due to bubble agitation, internal effects, such as thin film evaporation and thereby the entire bubble cycle, would also be affected.

The convective effect on enhanced tubes has been studied by several researchers (Kim *et al.*, 2002, Robinson and Thome, 2003) and includes studies from single tubes in a pumped flow (Ribatski *et al.*, 2008), bubbles rising (Cornwell, 1990) to convective bundle boiling and falling film evaporation (Christians, 2010). The geometry, heat flux, mass flux, fluid properties and saturation temperature seem to have an effect, although in general, the enhanced geometries are less affected by convection. The relation of convective heat transfer to pool boiling is often used as metric (bundle factor or k_{BB}). This factor is lower for enhanced tubes compared to smooth tubes. At high heat fluxes the convective effect tended to disappear and the performances became comparable to those in pool boiling (Kim *et al.*, 2002, Christians, 2010). The bundle factor is also subject to high uncertainty and comparing fractional changes might not be significant.

Interaction between mechanisms could decrease some heat flux mechanisms whereas others increase with the overall effect being neutral. A complete understanding could facilitate optimisation of geometries for specific tube and refrigerant combinations.

C.3.4 External heat transfer

Several methods have been proposed for the external heat transfer prediction. They are mostly based on assumptions regarding bubble dynamics on a surface and have been used for plain and enhanced surfaces. Models have assumed fluid replacement by departing bubbles (Mikic and Rohsenow, 1969), stagnation flow-bubble rise similarity (Tien, 1962), additional convection (Haider and Webb, 1997) and local fluid convection as part of a compound heat flux (Moghaddam and Kiger, 2009a).

Mikic and Rohsenow (1969) developed a model based on the intermittent bubble departure process removing a part of the superheated boundary layer. The superheated fluid is immediately replaced with saturated fluid and the amount of fluid flow is determined by the area of influence. One-dimensional transient heat conduction into the semi-infinite solid (the fluid) is assumed. Averaging over the time period of bubble departure gives:

$$q_o = 2\sqrt{\pi k_l \rho_l c_p f} D_d^2 N_a \Delta T \tag{C.6}$$

Haider and Webb (1997) added a convection term to the model of Mikic and Rohsenow (1969) after finding that the latter underpredicts and that convection can be important. They called this mechanism transient convection and it occurs in the wake of departing bubbles. To fit their model they changed the weight factors of each mechanism and found transient convection to be dominant:

$$q_o = 2\sqrt{\pi k_l \rho_l c_p f} D_d^2 N_a \Delta T \{1 + \left(\frac{0.66\pi c}{Pr^{\frac{1}{6}}}\right)^n\}^{\frac{1}{n}} \tag{C.7}$$

Moghaddam and Kiger (2009a) measured local heat fluxes during a bubble cycle and found that all the proposed mechanisms could be significant. They discarded any model assuming a single heat flux to be dominant and proceeded to develop their own model from composite mechanisms. The research was based on a single bubble, but clearly states that better mechanistic models should be based on getting the physics right.

The final composite model proposed by Moghaddam and Kiger (2009a) includes mechanisms of microlayer evaporation from under the bubble with sensible energy taken into account. The transient conduction term proposed by Mikic and Rohsenow (1969) was elaborated to include a gradual surface coverage condition as the saturated fluid washes into the space occupied by the bubble as it departs. Thus, the transient conduction does not occur over the entire zone at once, but progressively as the fluid moves in to replace the departing bubble. The third component was microconvection outside the bubble contact area and within the projected area of the bubble on the heater surface. This component was sufficiently predicted by Rohsenow (1952).

Although this method was not developed for a large surface, it includes a full set of probable mechanisms and interactions. A future model for large surfaces can be composed from components such as these that were measured and verified individually without arbitrarily adapting the area of influence parameters that can bias the model.

C.3.5 Limitations

Theories or models needed for boiling mechanistic models that are presently unavailable include the following:

- vapour bubble generation process on a surface and inside re-entrant tunnels;

- number of active nucleation sites on a surface;

- bubble interaction;

- inception of bubble growth;

- liquid intake and vapour escape through pores;

- liquid distribution inside the tunnel;

- external heat flux components on full scale enhanced tubes; and

- convective effects on boiling on tubes.

Moghaddam and Kiger (2009b) state that better boiling models can be built by a bottom up approach to first develop a proper understanding of the microscale physics of the nucleate boiling process and then to sort out the existing models to develop new models based on the actual physics of the boiling processes. They have shown in their study that combining unsubstantiated models and fitting them to integral experimental data often results in misrepresentation of the true nature of some of the boiling subprocesses. For example, one can readily fit a composite model to experimental data by varying parameters such as influence area of different mechanisms and their time period of activation and find incorrect values for each parameter. Instead, efforts to relate these parameters to explicitly known boiling conditions (i.e. surface and liquid conditions) might be more fruitful.

Currently, there exists no general theory explaining the reasons for heat transfer coefficient increase, the lowering of the surface initial superheating or the intensity and quantity of boiling hysteresis phenomena on developed microsurfaces (Poniewski and Thome, 2008). The effect of evaporation into the bubbles growing and sliding on the outside are also not dealt with in the present models. The liquid intake and all aspects of liquid supply versus geometry are dealt with empirically and remain too complex to model.

Furthermore, the above models assume that the process is cyclic (Figure C.2) while it is quite likely a continuous process, with some pores providing a continuous liquid supply to the film while other pores provide a continuous exit for the vapour generated to escape (Das *et al.*, 2007). A continuous process implies diverse bubble departure characteristics as observed in this study (Chapter 4). Sections of the tunnel maintain a thin evaporating film supplied by liquid. Additionally, some parts of the tunnel might become flooded due to the excessive liquid intake or slight wall temperature drop after significant evaporation took place. These flooded parts of the tunnel then experience single phase heat transfer while the wall heats up and then trapped vapour bubbles begin to grow once again or the liquid is displaced with vapour from other parts of the tunnel where evaporation is taking place. A tube structure that can maintain continuous

thin film evaporation and avoids "flooded" and "dried up" regimes is going to be much higher in performance. An example illustrates the concept of such a multipore interacting process (Figure C.5).

Process: Buoyancy forces, inertial forces, surface tension forces, pressure forces, shear forces
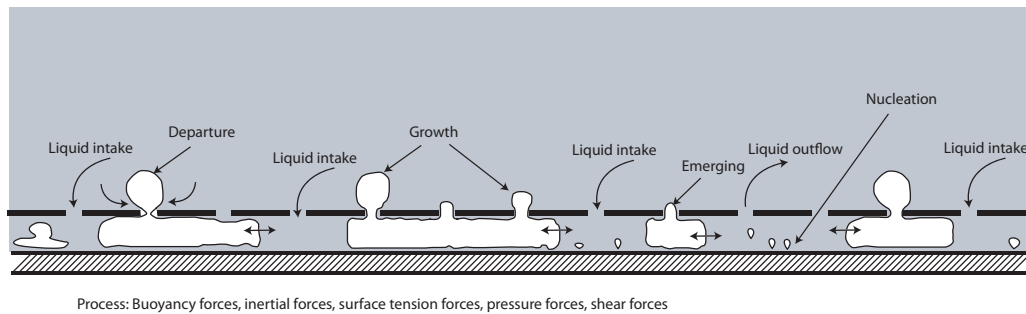
Figure C.5: Interaction between liquid and vapour phases during evaporation in a subsurface tunnel enhanced boiling tube

C.4   Conclusion

Heat transfer on enhanced surfaces is a complex thermodynamic process in which phase change, heat transport and liquid and vapour dynamics are all interconnected. Knowledge of the evaporation process inside enhanced structures is limited. Explanations of experimental trends in heat flux or heat transfer coefficients are mostly of empirical nature.

Appendix D

Pressure drop data reduction

D.1 Introduction

The pressure drop in the bundle is made up of three components: static, momentum and friction. Of these three, the static component is generally the largest and the momentum component is almost negligible. The method of reducing data for pressure drop is subject to a large amount of uncertainty and assumptions. Some of these factors can be mitigated while others are, for the moment, left unchanged. The following section describes the evaluation and modification to the data reduction methods used for this study.

D.1.1 Past data reduction

The previous data reduction methods were developed for the pressure drop measurements taken over the entire bundle. The instrumentation was mounted at three locations along the length of the bundle and was used to validate the distribution of the flow by the perforated plate. The perforated plate was found to work exceptionally well (Robinson and Thome, 2003).

The assumptions made for the data reduction were:

- a single void fraction model from bottom to top

- use of only the mass flux calculated with the reference gap (minor restriction) of the bundle

- no acceleration between the "no tubes" sections and the bundle

The static component, calculated for each vertical subsection, was made with the two-phase density using the Feenstra *et al.* (2000) void fraction model.

The frictional component was found negative in some cases indicating an overestimation of the static and momentum components. This was later validated by the fourth pressure transducer, which measured over half the bundle. The uncertainty analysis also supports this conclusion by indicating the probable limits of error. This included the uncertainty in the static and momentum components and allowed a propagation of error to be estimated for the frictional component. The uncertainty in this case indicated that the error in the negative frictional predictions were larger than could be attributed to measurement error alone. It must be stated that this does not include the possible error in the void fraction model and other possibly incorrect assumptions, only the propagation of the error through the calculation. The data for the fourth differential pressure transducer indicated a poor assumption regarding the pressure components in the bundle up to the height of this new pressure tap. The shortcomings for the pressure data reduction were addressed by a meticulous re-evaluation of the pressure data reduction.

(a) Bundle discretisation *a priori*   (b) Bundle discretisation *a posteriori*
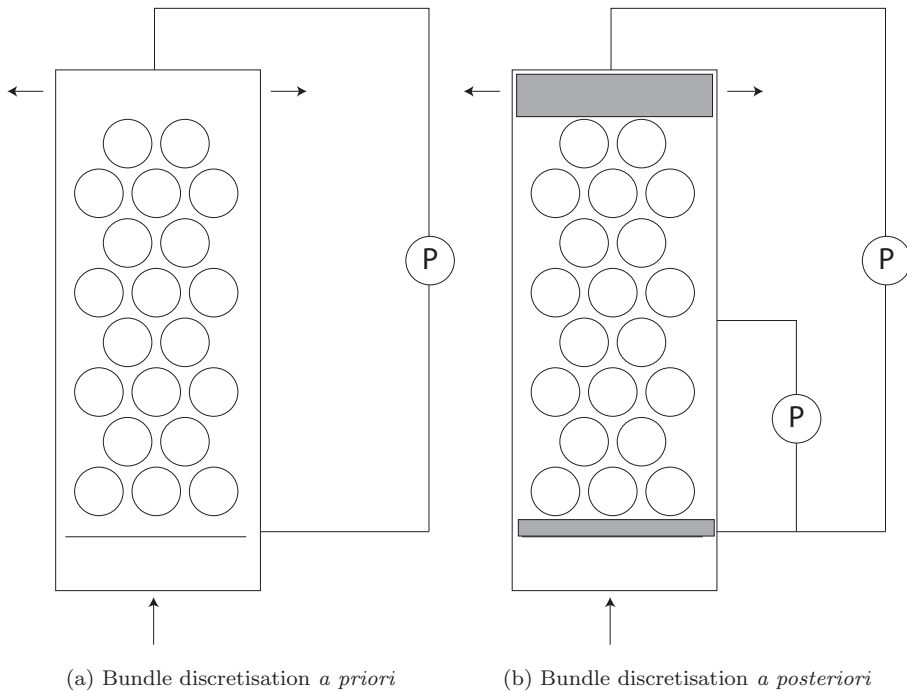
Figure D.1: The development of bundle data reduction with new instrumentation, zones and assumptions for flow entering from the bottom and leaving to the sides

D.1.2 Evaluation of data reduction

The measurements of pressure in the bundle was augmented by a new (fourth) differential pressure transducer over the diabatic section of the bundle. This new measurement was added to increase the accuracy of measurements over the diabatic section of the bundle. The new measurement allowed the evaluation of the frictional pressure drop of the two sections making up the diabatic and adiabatic parts of the bundle in relation to the entire bundle. The major difference in the new split evaluation is the separation of the inlet and outlet sections of the bundle (Figure D.1). These sections were not dealt with in the assumptions of the original data reduction, but no reason was found for further investigation at that stage.

Equation D.1 presents the total measured pressure drop as the sum of the measured diabatic pressure drop and the remaining pressure drop in the adiabatic section. Equation D.2 is used for the total and diabatic sections with the measured pressure drop value obtained directly from a transducer. The adiabatic section uses the difference between the total and diabatic measurements ($\Delta p_{adiab,calc}$), with the associated increase in uncertainty. It is clear that the calculated frictional pressure drop of the various sections does not indicate a realistic result when using the previous data reduction method (Figure D.2). The expected result for adiabatic flow is similar friction factors for each section with a possibility of a slight inlet effect but no negative friction factors.

$$\Delta p_{t,meas} \quad = \quad \Delta p_{diab,meas} + \Delta p_{adiab,calc} \qquad (D.1)$$

$$\Delta p_f \quad = \quad \Delta p_{t,meas} - \Delta p_s - \Delta p_m \qquad (D.2)$$

A closer investigation of the data reduction highlights various aspects that could possibly be improved on *i.e.*: a finer discretisation, subdivisions in the bundle, the void fraction model, the static component, the momentum component, the mass flux and friction factor definition.

D.1.3 Updated method

In the new data reduction methodology the bundle is divided into three sections and each part is treated with appropriate assumptions. The bundle can be subdivided into three sections between the pressure taps *i.e.*: a "no tubes" inlet section with flow area of 1.027 x 0.067 m, then through the tube bundle where the flow area is defined by the minor restriction followed by an outlet "no tubes" section. The reference area, mass flux and void fraction in each consecutive section are
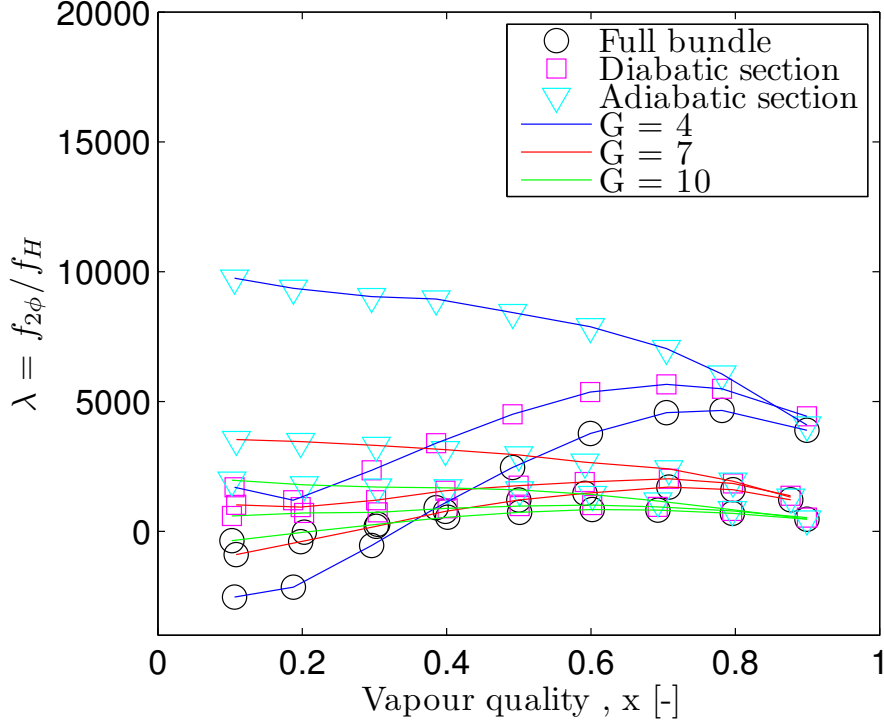
Figure D.2: Friction factor ratio data for pressure drops in all sections of the bundle indicating the apparent deviation from expected behaviour

different. The new data reduction method involves a more rigorous treatment of each component to improve the accuracy of the resulting frictional pressure drop data.

The bundle has always been discretised vertically into subsections where the local properties and conditions such as vapour quality and void fraction are evaluated locally at the tube centerline of each second row. This practice allows for easy implementation of the new method. When evaluating the components of the pressure drop we can define the correct parameters: mass flux, vapour quality, void fraction and area for every subsection. Firstly, the momentum term is affected by the acceleration and deceleration of the flow to and from the "no tubes" sections by a two-phase nozzle/diffuser term added to the momentum component (equation D.3).

$$\frac{dp_m}{dz} = \frac{d}{dz}\left(\frac{m_v u_v + m_l u_l}{A}\right) \tag{D.3}$$

This accounts for the restriction in the flow area from 1.027 x 0.067 m to approximately 3 x (0.0033 x 1.027) m. Since the outlets are horizontal they do not contribute to the momentum pressure drop at the outlet of the last element. When evaluating only the diabatic section, only
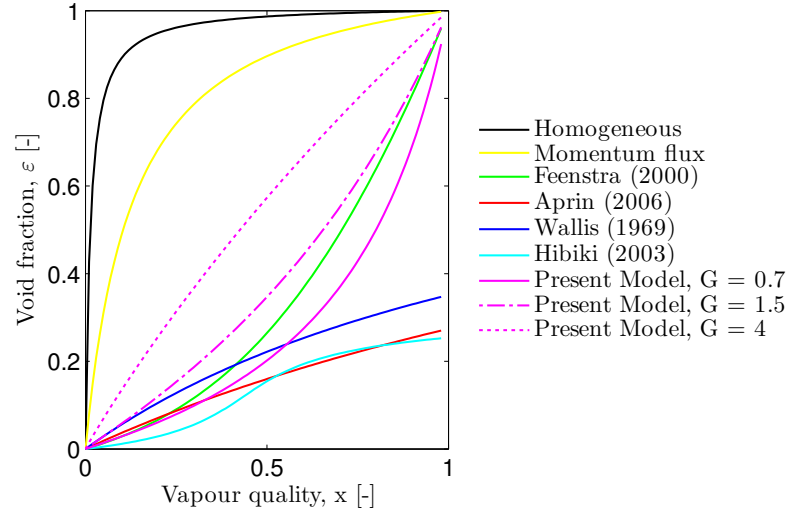
Figure D.3: Large tube drift flux model in comparison with Feenstra *et al.* (2000) model and the new large duct model for R134a at G = 1.5 kg/m^2s

the inlet nozzle term is included in the momentum pressure drop. When evaluating the entire head in the bundle the inlet momentum pressure drop is slightly recovered by the expansion at the outlet diffuser, but if evaporation occurred in between, the momentum change of the high velocity vapour at the outlet section is larger than for the inlet nozzle.

Secondly, the implementation of the void fraction prediction method of Feenstra *et al.* (2000) in tube bundles is not valid for the "no tubes" section. An attempt was made to approximate the void fraction in the "no tubes" section with void fraction models for bubbly flow in large tubes or ducts (Hibiki and Ishii, 2002, Schlegel *et al.*, 2009). These models were exclusively formulated for low vapour quality flow with discrete bubbly flow and did not predict the void fraction for larger vapour qualities, nor did it maintain the limit $\varepsilon(x = 1) = 1$ (Figure D.3). Another mismatch in conditions was the mass flux, which was less than 3 kg/m^2s for most conditions when no tubes were present. A void fraction model for bubbly-type flow in ducts at low mass flux was required. Some of the predicted void fractions from a variety of models for bubbly flow in large ducts at low mass fluxes are presented for R134a at 1.5 kg/m^2s (Figure D.3).

D.2 Low mass flux void fraction

A void fraction model is defined for the low mass flux conditions and bubbly flow after leaving the perforated plate. The model uses a bubble rise velocity correlation and the drift flux formulation to define a void fraction and slip ratio valid for the conditions in the "no tubes" section.

The basic assumptions of the model allow for an understanding of its use and limitations. Mass fluxes in the "no tubes" section or for any large duct of less than $5 \ kg/m^2 s$ are assumed. Bubbles can vary in size depending on conditions, but possible bubble coalescence after departure from the perforated plate was not taken into account. Buoyancy forces are dominant in describing the bubble rise velocity. The terminal velocity of bubbles rising in quiescent fluid is used for the vapour velocity (v_i). The liquid velocity is very low for all cases (u_l). It is hypothesized that the vertical velocity of the liquid does not affect the rise of the bubble and that the two components can be superimposed.

$$u_v = u_l + v_i$$

The slip ratio in the void fraction definition is defined as follows:

$$\varepsilon = \left[1 + S\left(\frac{1-x}{x}\right)\frac{\rho_v}{\rho_l}\right]^{-1} \quad and \quad S = \frac{u_v}{u_l}$$

The drift flux model defines drift velocities in relation to a plane moving at the sum of the superficial vapour and liquid velocity. Therefore all the velocities of the phases need to be known or predicted by the model to estimate the slip ratio and void fraction. The velocity of the reference plane is $[U = U_v + U_l]$. The drift velocities of the phases relative to the plane are:

$$U_{gu} = u_v - U \qquad and \qquad U_{lu} = u_l - U$$

We assume cross-sectional averages in all terms. The weighted mean drift velocity U_{gu} can be equated to U_{gl}/ε. Substituting the definition of U_{gu} and U and manipulating we get:

$$U_{gu} = v_i(1 - \varepsilon) \tag{D.4}$$

The void fraction as defined by the drift flux method is defined with a distribution parameter and a drift velocity. C_o is the distribution parameter that corrects one-dimensional homogeneous flow to separated flow theory, because void concentrations and velocity profiles can vary independently. Wallis (1969) set $C_o = 1$ for bubbly flow with small isolated bubbles so that here:

$$\varepsilon = \frac{x}{\rho_v}\left(C_o\left(\frac{x}{\rho_v} + \frac{1-x}{x}\right) + \frac{U_{gu}}{\dot{m}}\right)^{-1} \tag{D.5}$$

The next step is to solve the vapour rise velocity to predict the void fraction. The solution is used to define a slip ratio as defined previously and the slip ratio is easily correlated to π-groups defined by dimensional analysis following the principle in Feenstra *et al.* (2000). The empirical correlation of slip ratio is chosen to avoid solving the entire model to obtain a prediction.

D.2.1 Components of the model

The void fraction model with its assumptions mentioned in the section above depends on several other models or correlations explained below, each with their own assumptions.

The rise velocity of single bubbles has been correlated by various researchers including: Tomiyama *et al.* (1998, 2002), Fan and Tsuchiya (1990) and Celata *et al.* (2004). The Fan and Tsuchiya (1990) method compared well with experiments in Celata *et al.* (2004) and was chosen to predict v_i. The input required for the rise velocity model is the diameter of the bubbles leaving the perforated plate. Bubble departure diameters after perforated plates or sieve plates have been investigated by several researchers (Kulkarni and Joshi, 2005) and the model of Loimer *et al.* (2004) was chosen after evaluation.

The model is developed for R134a and R236fa at 5 and 15°C for vapour qualities ranging from 0.05 to 0.95 and mass flux ranges as defined with the bundle gap of 3 to 40 kg/m^2s. The true mass flux in the duct is below 5 kg/m^2s. Discrete points are solved, beginning with a prediction of the bubble diameter after the perforated plate. Each void fraction was converted to a slip ratio that could be empirically correlated.

D.2.2 Model

Feenstra *et al.* (2000) describe the Richardson number and Capillary number as the two dimensionless groups for bundle void fraction. These two numbers relate the buoyancy/inertial and viscous/surface tension forces. In a large duct with low mass flux and discrete bubbles the same force relationships should provide a correlation. A nonlinear solution scheme was used to fit the equation defined below for slip ratio to the results from the model described above. The final correlation is a pure empirical relation that satisfies the solutions of the model (Table D.1). The coefficient of determination for the final solution was, $R^2 = 0.974$.

$$
\begin{aligned}
S &= 1 + aRi^{b}(Cap\,x)^{c} \\
Cap &= \frac{\mu x G}{\sigma \rho_v} \\
Ri &= \frac{\Delta\rho^2 g a}{G^2}
\end{aligned}
$$

Table D.1: Empirical coefficients for the low mass flux void fraction model

Coefficient	Value
a	2.36386
b	0.4902
c	0.0142

D.2.3 Method inspection

The model can be compared to numerical results and other available models. The correlations of Zuber *et al.* (1967) and Wallis (1969) for bubbly flow in large ducts correspond at low vapour qualities but do not respect the obvious solution when the flow is only vapour. Several other void fraction models for bubbly flow in large tubes were considered (Hibiki and Ishii, 2002, Schlegel *et al.*, 2009).

As mass flux varies for a constant vapour quality the major effect is the increase in liquid velocity (Figure D.4a). In this case the vapour velocity, due to the buoyancy, is almost constant. As the liquid mass flux nears zero the slip ratio tends to infinity. These effects can be seen by looking at how the slip ratio and the void fraction reacts.

As the vapour quality increases, a difference in bubble rise velocity is noted because the diameter changes (Figure D.4b). This results in small changes in slip ratio since the liquid velocity remains fairly constant.
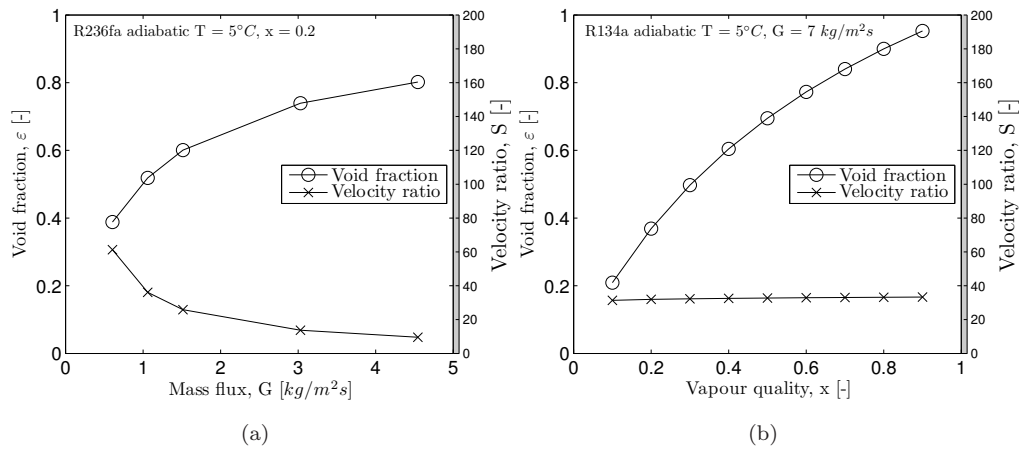
Figure D.4: Characteristics of the model for sample condition of low mass flux with R134a for (a) x = 0.2 and (b) G = 1 kg/m^2s

References

Abu-Eishah, S. I. (2001). Correlations for the thermal conductivity of metals as a function of temperature. *International Journal of Thermophysics*, 22:1855–1868.

Agostini, F. (2008). *Boiling on a tube bundle: Heat transfer, Pressure drop and Flow patterns.* PhD thesis, LTCM, École Polytecnique Fédérale de Lausanne.

Ajaev, V. S. (2005). Spreading of thin volatile liquid droplets on uniformly heated surfaces. *Journal of Fluid Mechanics*, 528:279–296.

Ajaev, V. S. and Homsy, G. M. (2001). Steady vapor bubbles in rectangular microchannels. *Journal of Colloid and Interface Science*, 240(1):259–271.

Akagawa, K., Hamaguchi, H., Sakaguchi, T., and Ikari, T. (1971a). Studies on the fluctuation of pressure drop in two-phase flow (1st report, experimental study). *Bulletin of JSME*, 14(71):447–454.

Akagawa, K., Hamaguchi, H., Sakaguchi, T., and Ikari, T. (1971b). Studies on the fluctuation of pressure drop in two-phase flow (2nd report, theoretical analysis). *Bulletin of JSME*, 14(71):455–461.

Akagawa, K., Hamaguchi, H., Sakaguchi, T., and Ikari, T. (1971c). Studies on the fluctuation of pressure drop in two-phase flow (3rd report, pressure recovery behind a bubble, and lengths of bubble and liquid slug). *Bulletin of JSME*, 14(71):462–469.

Aprin, L. (2003). *Etude expérimentale de l'ébullition d'hydrocarbures sur un faisceau de tubes horizontaux. Influence de la nature du fluide et de l'état de surface.* PhD thesis, Université de Provence Aix–Marseille.

REFERENCES

Aprin, L., Mercier, P., and Tadrist, L. (2007). Experimental analysis of local void fractions measurements for boiling hydrocarbons in complex geometry. *International Journal of Multiphase Flow*, 33(4):371–393.

Arshad, J. and Thome, J. R. (1983). Enhanced boiling surfaces: Heat transfer mechanisms and mixture boiling. *Proc. ASME-JSME Therm. Eng. Joint Conf.*, 1:191–197.

Bell, K. J. (1981). *Delaware method for shell side design.*, volume Heat exchangers: Thermal-hydraulic fundamentals and design. Hemisphere/McGraw–Hill, Washington, DC.

Bennett, D. L., Davis, M. W., and Hertzler, B. L. (1980). Suppression of saturated nucleate boiling by forced convective flow. *AIChE Symposium Series*, 76(199):91–103.

Bertola, V. (2003). Experimental characterization of gas–liquid intermittent subregimes by phase density function measurements. *Experiments in Fluids*, 34(1):122–129.

Briggs, D. and Young, E. (1969). Modified wilson plot technique for obtaining heat transfer correlations for shell and tube heat exchangers. *Chemical Engineering Progress Symposium Series*, 65:35–45.

Browne, M. W. and Bansal, P. K. (1999). Heat transfer characteristics of boiling phenomenon in flooded refrigerant evaporators. *Applied Thermal Engineering*, 19:595–624.

Burnside, B. M., Miller, K. M., McNeil, D. A., and Bruce, T. (2005). Flow velocities in an experimental kettle reboiler determined by particle image velocimetry. *International Journal of Heat and Mass Transfer*, 48(5):1000–1016.

Burnside, B. M. and Shire, N. F. (2005). Heat transfer in flow boiling over a bundle of horizontal tubes. *Chemical Engineering Research and Design*, 83(5 A):527–538.

Casciaro, S. and Thome, J. R. (2001). Thermal performance of flooded evaporators, part 1: Review of boiling heat transfer studies. *ASHRAE Transactions*, 107 PART. 1:903–918.

Cecchi, G. (1991). Error analysis of the parameters of a least–squares determined curve when both variables have uncertainties. *Measurement Science and Technology*, 2:1127–1128.

Celata, G. P., Cumo, M., D'Annibale, F., and Tomiyama, A. (2004). The wake effect on bubble rising velocity in one-component systems. *International Journal of Multiphase Flow*, 30:939–961.

Chen, J. C. (1966). Correlation for boiling heat transfer to saturated fluids in convective flow. *IandEC Process Design and Development*, 5(3):322–329.

Cheung, K., Ohadi, M. M., Dessiatoun, S., and Singh, A. (1997). EHD-enhanced boiling coefficients and visualization of R-134a over enhanced tubes. *Journal of Heat Transfer*, 119(2):332–338.

Cheung, K., Ohadi, M. M., and Dessiatoun, S. V. (1996). Boiling heat transfer enhancement of R-134a in a tube bundle utilizing the EHD technique. *Journal of Enhanced Heat Transfer*, 3(4):301–309.

Chien, L. H. and Webb, R. L. (1998a). Measurement of bubble dynamics on an enhanced boiling surface. *Experimental Thermal and Fluid Science*, 16(3):177–186.

Chien, L. H. and Webb, R. L. (1998b). A nucleate boiling model for structured enhanced surfaces. *International Journal of Heat and Mass Transfer*, 41(14):2183–2195.

Chien, L. H. and Webb, R. L. (1998c). A parametric study of nucleate boiling on structured surfaces, part ii: Effect of pore diameter and pore pitch. *Journal of Heat Transfer*, 120(4):1049–1054.

Chien, L. H. and Webb, R. L. (1998d). Visualization of pool boiling on enhanced surfaces. *Experimental Thermal and Fluid Science*, 16(4):332–341.

Chien, L. H. and Wu, J. S. (2004). Convective evaporation on plain tube and low–fin tube banks using R-123 and R-134a. In *ASHRAE Transactions*, volume 110 PART 1, pages 101–108.

Christians, M. (2010). *Heat transfer and visualization of falling film evaporation on a tube bundle*. PhD thesis, LTCM, École Polytecnique Fédérale de Lausanne.

Coetzee, S. (2000). The development of an experimental set-up to investigate heat transfer enhancement in tube-in-tube heat exchangers. Master's thesis, Rand Afrikaans University, Department of Mechanical Engineering.

Coleman, T. F. and Li, Y. (1994). On the convergence of reflective newton methods for large–scale nonlinear minimization subject to bounds. *Mathematical Programming*, 67:189–224.

Coleman, T. F. and Li, Y. (1996). An interior, trust region approach for nonlinear minimization subject to bounds. *SIAM Journal on Optimization*, 6:418–445.

REFERENCES

Consolini, L., Robinson, D., and Thome, J. R. (2008). Void fraction and two-phase pressure drops for evaporating flow over horizontal tube bundles. *Heat Transfer Engineering*, 27(3):5–21.

Cooper, M. G. (1984). Heat flow rates in saturated nucleate pool boiling. a wide–ranging examination using reduced properties. *Advances in Heat Transfer*, 16:157–239.

Cornwell, K. (1990). The influence of bubbly flow on boiling from a tube in a bundle. *International Journal of Heat and Mass Transfer*, 33(12):2579–2584.

Cornwell, K., Duffin, N. W., and Schöller, R. B. (1980). Experimental study of the effects of fluid flow on boiling within a kettle reboiler tube bundle. *American Society of Mechanical Engineers*, 80-HT-45:7.

Cornwell, K. and Einarsson, J. G. (1990). Influence of fluid flow on nucleate boiling from a tube. *Experimental Thermal and Fluid Science*, 3(2):101–116.

Cornwell, K., Einarsson, J. G., and Andrews, P. R. (1986). Studies on boiling in tube bundles. In *Studies on boiling in tube bundles.*, volume 5, pages 2137–2141.

Cornwell, K. and Houston, S. D. (1994). Nucleate pool boiling on horizontal tubes: A convection-based correlation. *International Journal of Heat and Mass Transfer*, 37(SUPPL. 1):303–309.

Cornwell, K. and Schöller, R. B. (1982). A study of boiling outside a tube bundle using high speed photography. *International Journal of Heat and Mass Transfer*, 25:683–690.

Cornwell, K. and Scoones, D. J. (1988). *Analysis of low quality boiling on plain and low-finned tube bundles.* Bury St. Edmunds, U.K., Mech. Eng. Publications Ltd.

Cotchin, C. and Boyd, E. (1992). Boiling of refrigerant and refrigerant/oil mixtures in a flooded evaporator. In *Institution of Chemical Engineers Symposium Series*, volume 1 (129), pages 131–137.

Cumo, M., Farello, G. E., Gasiorowski, J., Iovino, G., and Naviglio, A. (1980). Quality influence on the departure from nucleate boiling in cross flows through bundles. *Nuclear Technology*, 49(3):337–346.

Das, A. K., Das, P. K., Bhattacharyya, S., and Saha, P. (2007). Nucleate boiling heat transfer from a structured surface - effect of liquid intake. *International Journal of Heat and Mass Transfer*, 50(7-8):1577–1591.

Das, A. K., Das, P. K., and Saha, P. (2006). Heat transfer during pool boiling based on evaporation from micro and macrolayer. *International Journal of Heat and Mass Transfer*, 49(19–20):3487–3499.

Das, S. K. and Roetzel, W. (2004). A composite heat transfer model for pool boiling on a horizontal tube at moderate pressure. *Canadian Journal of Chemical Engineering*, 82(2):316–322.

DasGupta, S., Schonberg, J. A., and Wayner Jr., P. C. (1993). Investigation of an evaporating extended meniscus based on the augmented young–laplace equation. *Journal of Heat Transfer*, 115(1):201–208.

Dhir, V. K. (1998). Boiling heat transfer. *Annual Review of Fluid Mechanics*, 30:365–401.

Dhir, V. K. (2001). Numerical simulations of pool–boiling heat transfer. *AIChE Journal*, 47(4):813–834.

Dhir, V. K. (2006). Mechanistic prediction of nucleate boiling heat transfer–achievable or a hopeless task? *Journal of Heat Transfer*, 128(1):1–12.

Diehl, J. (1957). Calculate condenser pressure drop. *Petroleum Refiner*, 36(10):147–153.

Doo, G., McNaught, J. M., and Dempster, W. M. (2004). Shellside evaporation in a TEMA E-shell: Flow patterns and transitions. *Applied Thermal Engineering*, 24(8–9):1195–1205.

Doo, G. H., Dempster, W. M., and McNaught, J. M. (2008). Improved prediction of shell side heat transfer in horizontal evaporative shell and tube heat exchangers. *Heat Transfer Engineering*, 29(12):999–1007.

Dowlati, R., Kawaji, M., and Chan, A. M. (1990). Pitch-to-diameter effect on two-phase flow across an in-line tube bundle. *AIChE Journal*, 36(5):765–772.

Dowlati, R., Kawaji, M., and Chan, A. M. C. (1996). Two-phase crossflow and boiling heat transfer in horizontal tube bundles. *Journal of Heat Transfer*, 118(1):124–131.

Dowlati, R., Kawaji, M., Chisholm, D., and Chan, A. (1992). Void fraction prediction in two-phase flow across a tube bundle. *AIChE Journal*, 38(4):619–622.

Fair, J. R. and Klip, A. (1982). Thermal design of horizontal–type reboilers. In *Thermal design of horizontal–type reboilers.*

REFERENCES

Fan, L. S. and Tsuchiya, K. (1990). *Bubble Wake Dynamics in Liquids and Liquid–Solid Suspensions*. Butterworth–Heinemann, Oxford.

Feenstra, P. A., Weaver, D. S., and Judd, R. L. (2000). An improved void fraction model for two-phase cross-flow in horizontal tube bundles. *International Journal of Multiphase flow*, 26(11):1851–1873.

Fujita, Y., Bai, Q., and Hidaka, S. (1997). Heat transfer and flow pattern in horizontal tube bundles under pool and flow boiling conditions. *Convective Flow and Pool Boiling Conference, Kloster Irsee, Germany*, May 18–23.

Gaddis, E. S. and Gnielinski, V. (1985). Pressure drop in cross flow across tube bundles. *International Chemical Engineering*, 25(1):1–15.

GAW (2006). Scientific assessment of ozone depletion. *Scientific Assessment Panel of the Montreal Protocol on Substances that Deplete the Ozone Layers*, August:1–3.

Gnielinski, V. (1976). New equations for heat and mass transfer in turbulent pipe and channel flow. *Advances in Heat Transfer*, 16(2):359–368.

Gorenflo, D. (1993). *Pool Boiling, VDI–Heat Atlas, VDI–Verlag*. Düsseldorf (English version).

Gorenflo, D., Kaupmann, P., Koester, R., and Buschmeier, M. (1995). Pool boiling heat transfer of propane/i-butane/n-butane mixtures: example for other ternary mixtures as new refrigerants. In *Proceedings of 19th International Congress of Refrigeration, Den Haag, NL, volume IVa, pp. 238–245*.

Gorgy, E. and Eckels, S. (2010). Average heat transfer coefficient for pool boiling of R-134a and R-123 on smooth and enhanced tubes (RP-1316). *HVAC and R Research*, 16(5):657–676.

Grant, I. and Chisholm, D. (1979). Two-phase flow on the shell-side of a segmentally buffled shell-and-tube heat exchanger. *Journal of Heat Transfer*, 101:38–42.

Grant, I. and Murray, I. (1972). Pressure drop on the shell-side of a segmentally baffled shell-and-tube heat exchanger with vertical two-phase flow. Technical report, National Engineering Laboratory, East Kilbride, Glasgow.

Grant, I. and Murray, I. (1974). Pressure-drop on the shell-side of a segmentally buffled shell-and-tube heat exchanger with horizontal two-phase flow. Technical report, National Engineering Laboratory, East Kilbride, Glasgow.

Gstöhl, D. (2004). *Heat transfer and flow visualization of falling film condensation on tube arrays with plain and enhanced surfaces.* PhD thesis, LTCM, École Polytecnique Fédérale de Lausanne.

Gupta, A. (2005). Enhancement of boiling heat transfer in a 5 x 3 tube bundle. *International Journal of Heat and Mass Transfer*, 48(18):3763–3772.

Gupta, A., Saini, J. S., and Varma, H. K. (1995). Boiling heat transfer in small horizontal tube bundles at low cross-flow velocities. *International Journal of Heat and Mass Transfer*, 38(4):599–605.

Gupte, N. S. and Webb, R. L. (1995a). Shell-side boiling in flooded refrigerant evaporators part I: integral finned tubes. *HVAC and R Research*, 1:35–47.

Gupte, N. S. and Webb, R. L. (1995b). Shell-side boiling in flooded refrigerant evaporators part II: enhanced tubes. *HVAC and R Research*, 1(1):48–60.

Habert, M. (2009). *Falling film evaporation on a tube bundle with plain and enhanced tubes.* PhD thesis, LTCM, École Polytecnique Fédérale de Lausanne.

Hahne, K., Spindler, K., Chen, Q., and Windisch, R. (1990). Local void fraction measurements in finned tube bundles. *Heat Transfer 1990, Proceeding of the 9th International Heat Transfer Conference*, 6:41–46.

Haider, S. I. and Webb, R. L. (1997). A transient micro-convection model of nucleate pool boiling. *International Journal of Heat and Mass Transfer*, 40(15):3675–3688.

Heng, Y., Mhamdi, A., Wagner, E., and Marquardt, P. S. W. (2010). Estimation of local nucleate boiling heat flux using a three–dimensional transient heat conduction model. *Inverse Problems in Science and Engineering*, 18(2):279–294.

Hibiki, T. and Ishii, M. (2002). Distribution parameter and dfift velocity of drift-flux model in bubbly flow. *International Journal of Heat and Mass Transfer*, 45:707–721.

Hristov, Y., Zhao, D., Kenning, D. B. R., Sefiane, K., and Karayiannis, T. G. (2009). A study of nucleate boiling and critical heat flux with EHD enhancement. *Heat and Mass Transfer/Waerme- und Stoffuebertragung*, 45(7):999–1017.

Huang, X., Wang, L., and Jia, F. (2008). Study of two-phase flow regime identification in horizontal tube bundles under vertical upward cross-flow condition using wavelet transform. *Frontiers of Energy and Power Engineering in China*, 2(3):333–338.

REFERENCES

Hwang, T. H. and Yao, S. C. (1986). Forced convective boiling in horizontal tube bundles. *International Journal of Heat and Mass Transfer*, 29(5):785–795.

Ibrahem, K., Rabbo, M. F. A., Gambaryan-Roisman, T., and Stephan, P. (2010). Experimental investigation of evaporative heat transfer characteristics at the 3-phase contact line. *Experimental Thermal and Fluid Science*, 34(8):1036–1041.

Ishihara, K., Palen, J. W., and Taborek, J. (1980). Critical review of correlations for predicting two-phase flow pressure drop across tube banks. *Heat Transfer Engineering*, 1(3):23–32.

Israelachvili, J. N. (1985). *Intermolecular and surface forces*. Academic Press.

Iwaki, C., Cheong, K., Monji, H., and Matsui, G. (2005). Vertical, bubbly, cross–flow characteristics over tube bundle. *Experiments in Fluids*, 39(6):1024–1039.

Jabardo, J. M. S., Silva, E. F. D., Ribatski, G., and Barros, S. F. D. (2004). Evaluation of the rohsenow correlation through experimental pool boiling of halocarbon refrigerants on cylindrical surfaces. *Journal of the Brazilian Society of Mechanical Sciences and Engineering*, 26(2):218–230.

Jain, P. and Roy, R. (1983). Stochastic characteristics of vapor and wall pressure fluctuations in boiling flows. *International Journal of Multiphase flow*, 9(5):463–489.

Jensen, M. K. and Hsu, J.-T. (1988). A parametric study of boiling heat transfer in a horizontal tube bundle. *Journal of Heat Transfer*, 110:976–81.

Jensen, M. K., Trewin, R. R., and Bergles, A. E. (1992). Crossflow boiling in enhanced tube bundles. *Proc. Engineering Foundation Conference on Pool and External Flow Boiling*, 1:373–379.

Jones Jr., O. C. and Zuber, N. (1975). The interrelation between void fraction fluctuations and flow patterns in two-phase flow. *International Journal of Multiphase Flow*, 2(3):273–306.

Khartabil, H., Christensen, R., and Richards, D. (1988). A modified Wilson-plot technique for determining heat transfer correlations. *Proceedings of the Second UK National Conference on Heat Transfer*, 11:1331–1357.

Khushnood, S., Khan, Z., Malik, M., Koreshi, Z., and Khan, M. (2004). A review of heat exchanger tube bundle vibrations in two-phase cross-flow. *Nuclear Engineering and Design*, 230(1–3):233–251.

Kim, N.-H., Cho, J.-P., and Youn, B. (2002). Forced convective boiling of pure refrigerants in a bundle of enhanced tubes having pores and connecting gaps. *International Journal of Heat and Mass Transfer*, 45(12):2449–2463.

King, M. P. and Jensen, M. K. (1995). Local heat transfer and flow pattern distributions in a kettle reboiler. *Two-Phase Flow Modelling and Experimentation*, Vol. 2, Edizioni ETS Pisa:1289–1296.

Kline, S. and McClintock, F. (1953). Describing uncertainties in sinlge–sample experiments. *ASME Mechanical Engineering*, 75(1):3–8.

Kolev, N. I. (1995). How accurately can we predict nucleate boiling? *Experimental Thermal and Fluid Science*, 10(3):370–378.

Kondo, M. (1984). Experimental investigation of air–water two phase upflow across horizontal tube bundles (Part II, pressure drop. *Bull. of JSME*, 27(230):1616–1624.

Kondo, M. and Nakajima, K. (1980). Experimental investigation of air-water two-phase upflow across horizontal tube bundles (Part I, flow pattern and void fraction). *Bull. of JSME*, 23(177):385–393.

Kramer, W., Marvillet, C., and Auracher, H. (1997). Cross flow and pool boiling of ethanol–water mixtures on the outside of horizontal enhanced tubes. *Convective Flow and Pool Boiling Conference, Kloster Irsee, Germany*, May 18–23.

Kulkarni, A. A. and Joshi, J. B. (2005). Bubble formation and bubble rise velocity in gas–liquid systems: A review. *Industrial and Engineering Chemistry Research*, 44(16):5873–5931.

Lemmon, E. (2006). Refprop 7 enthalpy uncertainty. Private e–mail conversation 08–Nov–06.

Lian, H. Y., Chan, A. M. C., and Kawaji, M. (1992). Effects of void fraction on vibration of tubes in tube bundles under two-phase cross flow. *Symposium on flow–induced vibration and noise, ASME*, 230:109–118.

Liao, L. and Liu, Z.-H. (2007). Enhanced boiling heat transfer of the compact staggered tube bundles under sub–atmospheric pressures. *Heat Transfer Engineering*, 28(5):444–450.

Liebenberg, L. (2002). *A Unified Prediction Method for Smooth and Microfin Tube Condensation Performance.* PhD thesis, Rand Afrikaans University, Department of Mechanical Engineering.

REFERENCES

Lin, P. Y. and Hanratty, T. J. (1987). Detection of slug flow from pressure measurements. *International Journal of Multiphase Flow*, 13(1):13–21.

Lips, S., Lefèvre, F., and Bonjour, J. (2011). Physical mechanisms involved in grooved flat heat pipes: Experimental and numerical analyses. *International Journal of Thermal Sciences*, 50(7):1243–1252.

Lira, I. (2000). Curve adjustment by the least–square method. *Metrologia*, 37:677–681.

Lira, I., Cordero, R., François, M., and Vial–Edwards, C. (2004). The uncertainty of experimental derivatives: application to strain measurements. *Measurement Science and Technology*, 15:2381–2388.

Liu, Z. H. and Liao, L. (2006). Enhancement boiling heat transfer study of a newly compact in-line bundle evaporator under reduced pressure conditions. *Chemical Engineering and Technology*, 29(3):408–413.

Liu, Z. H. and Qiu, Y. H. (2002). Enhanced boiling heat transfer in restricted spaces of a compact tube bundle with enhanced tubes. *Applied Thermal Engineering*, 22(17):1931–1941.

Liu, Z.-H. and Qiu, Y. H. (2004). Boiling characteristics of R-11 in compact tube bundles with smooth and enhanced tubes. *Experimental Heat Transfer*, 17(2):91–102.

Loimer, T., Machu, G., and Schaflinger, U. (2004). Inviscidbubble formation on porous plates and sieve plates. *Chemical Engineering Science*, 59:809–818.

Longtin, J. P., Badran, B., and Gerner, F. M. (1994). A one-dimensional model of a micro heat pipe during steady-state operation. *ASME Journal of Heat Transfer*, 116(3):709–715.

Lowe, D. and Rezkallah, K. (1999). Flow regime identification in microgravity two-phase flows using void fraction signals. *International Journal of Multiphase Flow*, 25(3):433–457.

Luke, A. and Gorenflo, D. (2000). Heat transfer and size distribution of active nucleation sites in boiling propane outside a tube. *International Journal of Thermal Sciences*, 39(9–11):919–930.

Marto, P. J. and Anderson, C. L. (1992). Nucleate boiling characteristics of R-113 in a small tube bundle. *Journal of Heat Transfer*, 114(2):425–433.

Matsushima, H., Nakayama, W., Daikoku, T., and Osawa, Y. (1986). Shell–side single–phase flows and heat transfer in shell–and–tube heat exchangers (1st report, experimental study on local heat transfer coefficients). *Heat Transfer – Japanese Research*, 15(2):60–74.

Matsushima, H., Nakayama, W., and Kudo, T. Y. A. (1987). Shell-side single-phase flows and heat transfer in shell-and-tube heat exchangers (Part II: Effects of inlet nozzle diameter on flow patterns and local heat transfer coefficients). *Heat Transfer – Japanese Research*, 16(2):1–14.

Matsushima, H., Nakayama, W., and Kudo, T. Y. A. (1988). Shell-side single-phase flow and heat transfer in shell-and-tube heat exchangers (Part III: Transfer coefficients in a tube bundle). *Heat Transfer – Japanese Research*, 17(6):60–73.

McNeil, D. A., Bamardouf, K., and Burnside, B. M. (2010)). A one-fluid, two-dimensional flow simulation model for a kettle reboiler. *International Journal of Heat and Mass Transfer*, 53:825–835.

Memory, S. B., Akcasayar, N., Eraydin, H., and Marto, P. J. (1995). Nucleate pool boiling of R-114 and R-114-oil mixtures from smooth and enhanced surfaces-II. Tube bundles. *International Journal of Heat and Mass Transfer*, 38(8):1363–1376.

Memory, S. B., Chilman, S. V., and Marto, P. J. (1994). Nucleate pool boiling of a TURBO-B bundle in R-113. *Journal of Heat Transfer*, 116(3):670–678.

Mikic, B. B. and Rohsenow, W. M. (1969). A new correlation of pool-boiling data including the effect of heating surface characteristics. *Journal Heat Transfer*, 91:245–250.

Mikic, B. B., Rohsenow, W. M., and Griffith, P. (1970). On bubble growth rates. *International Journal of Heat and Mass Transfer*, 13(4):657 – 666.

Mitrovic, J. (2006). How to create an efficient surface for nucleate boiling? *International Journal of Thermal Sciences*, 45(1):1–15.

Moghaddam, S. and Kiger, K. (2009a). Physical mechanisms of heat transfer during single bubble nucleate boiling of FC-72 under saturation conditions-I. experimental investigation. *International Journal of Heat and Mass Transfer*, 52(5–6):1284–1294.

Moghaddam, S. and Kiger, K. (2009b). Physical mechanisms of heat transfer during single bubble nucleate boiling of FC-72 under saturation conditions. II: Theoretical analysis. *International Journal of Heat and Mass Transfer*, 52(5–6):1295–1303.

Moss, R. A. and Kelly, A. J. (1970). Neutron radiographic study of limiting planar heat pipe performance. *International Journal of Heat and Mass Transfer*, 13(3):491–502.

Murthy, S., Joshi, Y., Gurrum, S., and Nakayama, W. (2006). Enhanced boiling heat transfer simulation from structured surfaces: Semi-analytical model. *International Journal of Heat and Mass Transfer*, 49(11–12):1885–1895.

Nakajima, K. (1978). Boiling heat transfer outside horizontal multitube bundles. *Heat Transfer - Japanese Research*, 7(2):1–24.

Nakayama, W., Daikoku, T., Kuwahara, H., and Nakajima, T. (1980a). Dynamic model of enhanced boiling heat transfer on porous surfaces. *Journal of Heat Transfer*, 102(3):451–456.

Nakayama, W., Daikoku, T., Kuwahara, H., and Nakajima, T. (1980b). Dynamic model of enhanced boiling heat transfer on porous surfaces. *Journal of Heat Transfer*, 102(3):445–450.

NEL report (1975). Advances in thermal and mechanical design of shell–and–tube heat exchangers. Technical Report NEL Report No 590, National Engineering Laboratory, East Kilbride, Glasgow.

Neri, F., Saitta, G., and Chiofalo, S. (1989). An accurate straighforward approach to line regression analysis of error-affected experimental data. *Journal of Physics: Scientific Instruments*, 22:215–217.

Nishikawa, K., Fujita, Y., Uchida, S., and Ohta, H. (1984). Effect of surface configuration on nucleate boiling heat transfer. *International Journal of Heat and Mass Transfer*, 27(9):1559 – 1571.

NIST (2007). *NIST Thermodynamic Properties of Refrigerants and Refrigerant Mixtures Database*. ver 8.0, Gaithersburg, MD.

Noghrehkar, G. R., Kawaji, M., and Chan, A. M. C. (1999). Investigation of two-phase flow regimes in tube bundles under cross-flow conditions. *International Journal of Multiphase Flow*, 25(5):854–874.

Olivier, J. (2008). *Single–phase heat transfer and pressure drop inside Horizontal Circular Smooth and Enhanced Tubes with different inlet configurations for transitional flow*. PhD thesis, University of Pretoria, Department of Mechanical and Aeronautical Engineering.

Palen, J. W. and Small, W. M. (1964). Kettle and internal reboilers. *Hydrocarbon Processing*, 43:199–208.

Palen, J. W. and Yang, C. (1983). Circulation boiling model for analysis of kettle and internal reboilier performance. In *Circulation boiling model for analysis of kettle and internal reboilier performance*, volume 27, pages 55–61.

Pastuszko, R. and Poniewski, M. E. (2008). Semi-analytical approach to boiling heat fluxes calculation in subsurface horizontal and vertical tunnels. *International Journal of Thermal Sciences*, 47(9):1169–1183.

Pettigrew, M. J., Taylor, C. E., and Kim, B. S. (1989a). Vibration of tube bundles in two-phase cross-flow: Part 1-hydrodynamic mass and damping. *Journal of Pressure Vessel Technology*, 111:466–477.

Pettigrew, M. J., Tromp, J. H., Taylor, C. E., and Kim, B. S. (1989b). Vibration of tube bundles in two-phase cross-flow: Part 2-fluid-elastic instability. *Journal of Pressure Vessel Technology*, 111:478–487.

Pettigrew, M. J., Tromp, J. H., Taylor, C. E., and Kim, B. S. (1989c). Vibration of tube bundles in two-phase cross-flow: Part 3-turbulence-induced excitation. *Journal of Pressure Vessel Technology*, 111:488–500.

Petukhov, B. (1970). Heat transfer and friction in turbulent pipe flow with variable physical properties. *Advances in Heat Transfer*, 6:503–564.

Pioro, I. L., Rohsenow, W., and Doerffer, S. S. (2004). Nucleate pool-boiling heat transfer. I: Review of parametric effects of boiling surface. *International Journal of Heat and Mass Transfer*, 47(23):5033–5044.

Polley, G. T., Ralston, T., and Grant, I. D. R. (1980). Forced crossflow boiling in an ideal in-line tube bundle. *American Society of Mechanical Engineers*, 80 -Ht-46.

Poniewski, M. E. and Thome, J. R. (2008). *Nucleate Boiling on Micro-Structured Surfaces*. Heat Transfer Research, Inc. (HTRI), TX, USA.

Qiu, Y. H. and Liu, Z. H. (2004). Boiling heat transfer of water on smooth tubes in a compact staggered tube bundle. *Applied Thermal Engineering*, 24(10):1431–1441.

Quiben, J. M. and Thome, J. R. (2007). Flow pattern based two-phase frictional pressure drop model for horizontal tubes, part II: New phenomenological model. *International Journal of Heat and Fluid Flow*, 28(5):1060–1072.

REFERENCES

Rajković, M., Riznić, J., and Kojasoy, G. (1996). Dynamical characteristics of flow pattern transitions in horizontal two-phase flow. *2nd European Thermal–Science and 14th UIT National Heat Transfer Conference, Rome, Italy, Ed. ETS*, pages 1403–1408.

Ramaswamy, C., Joshi, Y., Nakayama, W., and Johnson, W. B. (2003). Semi-analytical model for boiling from enhanced structures. *International Journal of Heat and Mass Transfer*, 46(22):4257–4269.

Rebrov, P. N., Bukin, V. G., and Danilova, G. N. (1989). Correlation for local coefficients of heat transfer in boiling of R12 and R22 refrigerants on multirow bundles of smooth tubes. *Heat transfer. Soviet research*, 21(4):543–548.

Revellin, R., Dupont, V., Ursenbacher, T., Thome, J. R., and Zun, I. (2006). Characterization of two-phase flows in microchannels: Optical measurement technique and flow parameter results for R-134a in a 0.5 mm channel. *International Journal of Multiphase Flow*, 32(7):755–774.

Ribatski, G., Saiz Jabardo, J. M., and da Silva, E. F. (2008). Modeling and experimental study of nucleate boiling on a vertical array of horizontal plain tubes. *Experimental Thermal and Fluid Science*, 32(8):1530–1537.

Ribatski, G. and Thome, J. R. (2007). Two-phase flow and heat transfer across horizontal tube bundles - A review. *Heat Transfer Engineering*, 28(6):508–524.

Robinson, D. and Thome, J. R. (2003). Flooded evaporation heat transfer performance for tube bundles including the effects of oil using R-410a and R-507a. *ASHRAE*, Research Project RP–1089.

Rohsenow, W. M. (1952). A method of correlating heat transfer data for surface boiling liquids. *Journal of Heat Transfer*, 74:969–976.

Roques, J.-F. (2004). *Falling Film Evaporation on a single tube and on a tube bundle*. PhD thesis, LTCM, École Polytecnique Fédérale de Lausanne.

Rose, J. (2004). Heat-transfer coefficients, Wilson plots and accuracy of thermal measurements. *Experimental Thermal and Fluid Science*, 28:77–86.

Roser, R., Thonon, B., and Mercier, P. (1999). Experimental investigations on boiling of n-pentane across a horizontal tube bundle: two-phase flow and heat transfer characteristics. *International Journal of Refrigeration*, 22:536–547.

Sateesh, G., Das, S. K., and Balakrishnan, A. R. (2005). Analysis of pool boiling heat transfer: effect of bubbles sliding on the heating surface. *International Journal of Heat and Mass Transfer*, 48:1543–1553.

Scarpa, F. (1998). Evaluation of reliable bounds for sensor calibration curves. *Metrologia*, 35:1–5.

Schlegel, J. P., Sawant, P., Paranjape, S., Ozar, B., Hibiki, T., and Ishii, M. (2009). Void fraction and flow regime in adiabatic upward two-phase flow in large diameter vertical pipes. *Nuclear Engineering and Design*, 239:2864–2874.

Schrage, D. S., Hsu, J. T., and Jensen, M. K. (1988). Two-phase pressure drop in vertical cross flow across a horizontal tube bundle. *AIChE Journal*, 34:107–115.

Shah, M. M. (2007). A general correlation for heat transfer during saturated boiling with flow across tube bundles. *HVAC&R Research*, 27(10):20–29.

Shah, R. K. (1990). Assessment of modified Wilson plot techniques for obtaining heat exchanger design data. *Journal of Heat Transfer*, 5:51–56.

Shklover, G. G. and Gusev, S. E. (1988). Natural convection heat transfer in horizontal tubular bundles. *Heat transfer. Soviet research*, 20(6):746–758.

Snyman, J. (2005). *Practical Mathematical Optimization: An Introduction to Basic Optimization Theory and Classical and New Gradient-Based Algorithms*. Springer, 1st edition.

Stephan, K. and Abdelsalam, M. (1980). Heat–transfer correlations for natural convection boiling. *International Journal of Heat and Mass Transfer*, 23(1):73–87.

Stephan, P. and Kern, J. (2004). Evaluation of heat and mass transfer phenomena in nucleate boiling. *International Journal of Heat and Fluid Flow*, 25(2):140–148.

Stephan, P. and Wondra, F. (2008). Nucleate pool boiling on tubes with subsurface mini and micro channels. In *Proceedings of the 6th International Conference on Nanochannels, Microchannels, and Minichannels, PART B*, pages 1759–1769.

Styrylska, T. and Lechowska, A. (2003). Unified wilson plot method for determining heat transfer correlations for heat exchangers. *Journal of Heat Transfer*, 125(4):752–756.

Sutherland, L. and Murray, I. (1969). Pressure-drop and heat-transfer on the shell-side of model heat exchanger with two-phase flow. Technical Report NEL Report No 395, National Engineering Laboratory, East Kilbride, Glasgow.

REFERENCES

Tatara, R. A. and Payvar, P. (2000a). Effects of oil on boiling of replacement refrigerants flowing normal to a tube bundle - part I: R-123. In *ASHRAE Transactions*, volume 106.

Tatara, R. A. and Payvar, P. (2000b). Effects of oil on boiling of replacement refrigerants flowing normal to a tube bundle - part II: R-134a. In *ASHRAE Transactions*, volume 106.

Taylor, J. (1997). An introduction to error analysis: the study of uncertainties in physical measurements. *University Science Books*.

Thome, J. R. (1990). *Enhanced boiling heat transfer*. Hemisphere Publishing Corp., New York.

Thome, J. R. (2004). *ENGINEERING DATABOOK III*. Wolverine. Web-based reference book available for free at: http://www.wlv.com/products/databook/db3/DataBookIII.pdf.

Thome, J. R. and Robinson, D. (2006). Prediction of local bundle boiling heat transfer coefficients: pure refrigerant boiling on plain, low fin, and Turbo-BII HP tube bundles. *Heat Transfer Engineering*, 27(10):20–29.

Tien, C. L. (1962). A hydrodynamic model for nucleate pool boiling. *International Journal of Heat and Mass Transfer*, 5(6):533–540.

Tomiyama, A., Celata, G. P., Hosokawa, S., and Yoshida, S. (2002). Terminal velocity of single bubbles in surface tension force dominant regime. *International Journal Multiphase Flow*, 28:1497–1519.

Tomiyama, A., Kataoka, I., Zun, I., and Sakaguchi, T. (1998). Drag coefficients of single bubbles under normal and microgravity conditions. *JSME International Journal, Series B: Fluids and Thermal Engineering*, 41:472–479.

Ulbrich, R. and Mewes, D. (1994). Vertical, upward gas-liquid two-phase flow across a tube bundle. *International Journal of Multiphase Flow*, 20(2):249–272.

UNEP (2000). Montreal Protocol on Substances that Deplete the Ozone Layer. *United Nations Environmental Program*, Kenya.

U.S. Environmental Protection Agency (2010). http://www.epa.gov/ozone/science/ods/index.html.

Van Rooyen, E., Agostini, F., Borhani, N., and Thome, J. R. (2011a). Boiling on a tube bundle: Part II – heat transfer and pressure drop. *Heat transfer engineering*, 33:XX–XX.

Van Rooyen, E., Christians, M., and Thome, J. R. (2011b). Modified wilson plots for enhanced heat transfer experiments: Current status and future perspectives. *Heat transfer engineering*, 33(3-4):XX–XX.

Vince, M. A. and Lahey Jr., R. T. (1982). On the development of an objective flow regime indicator. *International Journal of Multiphase Flow*, 8(2):93–124.

Žukauskas, A. and Ulinskas, R. (1983). *Heat Exchanger Design Handbook*. Hemisphere Publishing Corp. New York.

Wallis, G. B. (1969). *One Dimensional Two-Phase Flow*. McGraw–Hill, New York.

Wang, H., Garimella, S. V., and Murthy, J. Y. (2007). Characteristics of an evaporating thin film in a microchannel. *International Journal of Heat and Mass Transfer*, 50(19–20):3933–3942.

Watanabe, K. (2003). Uncertainties in enthalpy for the IAPWS formulation 1995 for the thermodynamic properties of ordinary water substance for general and scientific use (IAPWS-95) and the IAPWS industrial formulation 1997 for the thermodynamic properties of water and steam (IAPWS-97). Technical Report 1, The International Association for the Properties of Water and Steam.

Wayner Jr., P. C., Kao, Y. K., and LaCroix, L. V. (1976). The interline heat-transfer coefficient of an evaporating wetting film. *International Journal of Heat and Mass Transfer*, 19(5):487–492.

Webb, R. L. (2004). Odyssey of the enhanced boiling surface. *Journal of Heat Transfer*, 126(6):1051–1059.

Webb, R. L. and Chien, L.-H. (1994a). Correlation of convective vaporization on banks of plain tubes using refrigerants. *Heat Transfer Engineering*, 15:57–69.

Webb, R. L. and Chien, L. H. (1994b). Correlation of convective vaporization on banks of plain tubes using refrigerants. *Heat Transfer Engineering*, 15(3):57–69.

Webb, R. L. and Pais, C. (1992). Nucleate pool boiling data for five refrigerants on plain, integral-fin and enhanced tube geometries. *International Journal of Heat and Mass Transfer*, 35(8):1893–1904.

Wege, M. E. and Jensen, M. K. (1984). Boiling heat transfer from a horizontal tube in an upward flowing two-phase crossflow. *Journal of Heat Transfer*, 106(4):849–855.

REFERENCES

Wilson, E. (1915). A basis for rotational design of heat transfer apparatus. *ASME transactions*, 37:47–82.

Xu, G. P., Tou, K. W., and Tso, C. P. (1998a). Two-phase void fraction and pressure drop in horizontal crossflow across a tube bundle. *Journal of Fluids Engineering*, 120:140–145.

Xu, G. P., Tso, C. P., and Tou, K. W. (1998b). Hydrodynamics of two-phase flow across a horizontal tube bundle. *International Journal of Multiphase Flow*, 24(8):1317–1342.

Yilmaz, S. and Palen, J. W. (1984). Performance of finned tube reboilers in hydrocarbon service. In *American Society of Mechanical Engineers*.

York, D., Evensen, N. M., Martinez, M. L., and Delgado, J. D. B. (2004). Unified equations for the slope, intercept, and standard errors of the best straight line. *American Journal of Physics*, 72(3):367–375.

Zuber, N., Staub, F. W., Bijwaard, G., and Kroeger, P. G. (1967). Steady state and transient void fraction in two-phase flow systems. *GEAP report*, 5417.

Curriculum Vitae

Personal information

Name	Eugene van Rooyen
Date of birth	December 28$^\text{th}$, 1982
Nationality	South African

Education

2007–2011	Doctoral Student and Assistant, Laboratory of Heat and Mass Transfer, Swiss Federal Institute of Technology Lausanne (EPFL), Switzerland
2007	Master of Engineering in Mechanical Engineering, *cum laude*, University of Pretoria, South Africa
2006	B.Eng.(Honors) in Mechanical Engineering, *cum laude*, University of Pretoria, South Africa
2005	Bachelor of Engineering in Mechanical Engineering, *cum laude*, University of Pretoria, South Africa

Professional experience

2007–2010	Swiss Federal Institute of Technology (EPFL), Laboratory of Heat and Mass Transfer, Lausanne, teaching assistant, research project developments, laboratory activities.
2003–2007	University of Pretoria, Dept. of Mechanical Engineering, South Africa, Lecturer for Thermodynamics, various T.A. positions and internship.

Journal publications

1. E. van Rooyen, M. Christians, L. Liebenberg, J.P. Meyer. Probabilistic flow pattern-based heat transfer correlation for condensing intermittent flow of refrigerants in smooth horizontal tubes.

International Journal of Heat and Mass Transfer, 53:1446–1460, 2010.

2. H. Canière, C. T'joen, A. Willockx, M. De Paepe, M. Christians, E. van Rooyen, L. Liebenberg, J.P. Meyer. Horizontal two-phase flow characterization for small diameter tubes with a capacitance sensor. *Measurement Science and Technology*, 18:2898–2906, 2007.

3. E. van Rooyen, M. Christians, J.R. Thome. Modified Wilson plots for enhanced heat transfer experiments: Current status and future perspectives. *Heat Transfer Engineering, accepted for publication*, Vol 33 Issues 3-4, 2012.

4. E. van Rooyen, F. Agostini, N. Borhani, J.R. Thome. Boiling on a tube bundle: Part I - Flow visualization and onset of dryout. *Heat Transfer Engineering, accepted for publication*, Vol 33 Issue 11 , 2012.

5. E. van Rooyen, F. Agostini, N. Borhani, J.R. Thome. Boiling on a tube bundle: Part II - Heat transfer and pressure drop. *Heat Transfer Engineering, accepted for publication*, Vol 33 Issue 11 , 2012.

Conference articles

1. M. Christians, E. van Rooyen, L. Liebenberg, J.P. Meyer. Probabilistic flow pattern-based heat transfer for condensing intermittent flow in smooth horizontal tubes. *14th International Heat Transfer Conference*, August 8–13, Washington D.C., 2010.

2. M. Christians, E. van Rooyen, L. Liebenberg, J.P. Meyer. Flow pattern-based heat transfer correlation for R-22 in a smooth tube. *5th HEFAT conference*, July 1–4, Sun City, 2007.

3. E. van Rooyen, M. Christians, L. Liebenberg, J.P. Meyer. Optical measurement technique for predicting time fractions in two-phase flow. *5th HEFAT conference*, July 1–4, Sun City, 2007.

4. H. Canière, C. T'joen, A. Willockx, M. De Paepe, M. Christians, E van Rooyen, L. Liebenberg, J.P. Meyer. Refrigerant flow regime detection with a capacitance void fraction sensor, *9th AIAA/ASME joint Thermophysics and Heat Transfer Conference*, 3–8 June, San Francisco, 2006.